EPFL

Thèse n° 8002

Growth and viability of microorganisms in bentonite and their potential activity in deep geological repository environments

Présentée le 26 mars 2021

Faculté de l'environnement naturel, architectural et construit
Laboratoire de microbiologie environnementale
Programme doctoral en génie civil et environnement

pour l'obtention du grade de Docteur ès Sciences

par

Niels BURZAN

Acceptée sur proposition du jury

Prof. D. Licina, président du jury
Prof. R. Bernier-Latmani, directrice de thèse
Dr A. Cherkouk, rapporteuse
Dr I. Gaus, rapporteuse
Prof. M. Lever, rapporteur

École
polytechnique
fédérale
de Lausanne

2021

Ich kann freilich nicht sagen, ob es besser wird wenn es anders wird;
aber so viel kann ich sagen, es muss anders werden, wenn es gut werden soll.
— Georg Christoph Lichtenberg (1742-1799)

I cannot say whether things will get better if we change;
what I can say is that they must change if they are to get better.
— Georg Christoph Lichtenberg (1742-1799)

This work is dedicated to my grandmothers Ingeborg and Hannelore, who stand for an entire generation that had to endure the struggles of the Second World War in their childhood. Their generation shared the dream of a better world by building a new society and witnessed its rise and fall. Their strength, Their love, Their devotion I am viewing as desirable characteristics.

Acknowledgements

First and foremost my thanks go to Rizlan Bernier-Latmani for offering me the opportunity to work on this important topic. Doing a PhD in a field with immediate need has provided me a constant motivation in the past years. Especially for introducing me to the vast world of life in the deep subsurface and for all the amazing things I learned about planet Earth during the past 5 years. For example, I particularly enjoyed the numerous scientific conferences Rizlan sent me to attend.

Of course, such a thesis is not the exclusive achievement of one person, I am grateful for the advice and practical help from Olivier Leupin, Nikitas Diomidis and the several days spent underground with Yanick Lettry. Big thanks go to Joël Stoudmann and Michel Teuscher who helped me to design and built for me quality experimental modules. Working with great people like Manon Frutschi is a pleasure I was lucky to enjoy on several trips to the laboratories of Jacobs Engineering in Harwell (UK), where we did good work and spend nice times with Bharti Reddy and Andrew Rance.

I really enjoyed my time at the Environmental Microbiology Laboratory thanks to the amazing people I had the chance to work with: Aislinn, Ash, Andrew (UNIL), Barbora, Carla, Conny, Edu, Emma, Gabrielle, Karen, Karin, Luca, Lyne, Manon (aka 'mon amour'), Matthew Reeves, Matthew Reid, Mapi, Margaux, Solenne, Simiao and Zezhen. I would also like to mention the great help of our secretaries Maria and Tania. Furthermore, I would like to mention the three students I co-supervised during my thesis, Roberta Murad-Lima, Vincent Berweiler and Victor Pahon.

My path into the academic world would have been a lot different without the help and mentorship of Wolfgang Souffrant and Artur Braun. The younger Niels learned a lot during the times in Dummerstorf also thanks to Walter, Vladimir and Marie, who became valuable friends.

In Lausanne, I am happy I had the chance to spend an awesome time with Åsa, Robert, Emma, Andrew, Solenne, Oscar, Marta, Conny, Dani, Karen, Oh-Hyeon, Grace, Helena, Elisa, David, Julien, Aryan, Dorsa, Nicolas, Masoud, Marie, Mathilde and Tobias Borgmeyer. Special thanks to Arnaud for the many late-night and weekend hours spent together.

During the past years, the famous Poulet Express in Renens developed from a simple protein provider to an institution for me. The excellent taste of the Portuguese grilled chicken is something I would expect to enjoy if there is a paradise Afterlife. Of course, it is the monthly gathering with the 'Fellowship of the Wing' that makes this such a good dinner with Anh Chi,

Matt, Lucía and Tomás, Hugo and Ximena.
Every time I am back in Germany, I am grateful for the welcoming and open arms of Danilo, Georg, Till, Olga, Christiane, Kevin, André and Caro. I would also like to thank my friends from study times in Basel, who supported my path as well, especially Muriel but also Flo, Tobi (aka 'Patreon'), Matias, Kamil, Thomas, Markus, Nadja, Eddi, Darja, Max, Gregor and Ekoe.
The unconditional support and trust from my parents Ute and Ekki, my brother Olaf and my grandmothers Hannelore and Ingeborg can be viewed as the backbone of my achievements. Thank you!
Finally I would like to express my gratitude to Anh Chi for being such a supportive and loving partner, having you by my side during this thesis was an invaluable contribution.

Lausanne, 24 Février 2021 N. B.

Abstract

Radioactive waste is among the most dangerous anthropogenic waste and its safe disposal is a challenging multi-generational task. Many nations have sought for the peaceful application of nuclear fission for the reliable production of electric energy to power their societies. The increasing volumes of radioactive waste generated are, however, proving an increasingly urgent problem to tackle. Deep geological disposal is deemed our best option for the safe long-term disposal of radioactive waste. Different host rocks are being considered for deep geological disposal, depending on the nation's geology. Switzerland favours the Opalinus Clay Formation due to its very low hydraulic conductivity and good radionuclide retention capabilities. Microorganisms in the deep subsurface are active and must be considered as their activity will influence a deep geological repository for radioactive waste. On one hand, the microorganism's activity represents a safety concern due to the possibility of enhanced corrosion, when considering the metallic waste canister encapsulating spent fuel from nuclear power plants. In other cases, however, they can contribute to the safety of a deep geological repository, when considering the gas balance of a Swiss low- and intermediate-level repository. Anoxic corrosion of metallic radioactive waste poses risks to the structural integrity of the host rock. Harnessing the activity of naturally occurring microorganisms at a safe distance from the waste itself can result in the net reduction of gases and thus their activity can be viewed as beneficial and worth exploring. In this thesis, both the positive and negative aspects of the microbial presence are explored. Wyoming bentonite is a back-fill material and an important engineered barrier system for spent nuclear fuel and high-level waste. Within the framework of an *in-situ* corrosion experiment, the presence and growth of microorganisms in Wyoming bentonite are investigated. The results show that the activity of corrosion enhancing sulfate-reducing bacteria in Wyoming bentonite is inhibited during the critical bentonite saturation phase but other microorganisms were able to grow. The second *in-situ* research project explores the potential implementation of a microbial gas sink, a natural biofilm composed of hydrogen-oxidizing sulfate-reducing bacteria and methanogenic archaea. Indeed, under the right conditions, a microbial gas sink can fulfil its intended design purposes and consume all hydrogen-gas evolving from the anoxic corrosion of the waste. This thesis contributes to our understanding of the near-field processes of a Swiss radioactive waste repository within the Opalinus Clay Formation through the contribution of experimental insight obtained under

in-situ conditions.

Key words: *Deep geological repository, Opalinus Clay, Radioactive waste, Hydrogen oxidation, Wyoming bentonite, Deep subsurface, Microorganisms, Sulfate-reducing bacteria, Methanogenesis, Microbial gas sink*

Résumé

Les déchets radioactifs comptent parmi les déchets anthropiques les plus dangereux et leur élimination en toute sécurité est une tâche multigénérationnelle difficile. De nombreux pays ont cherché à utiliser la fission nucléaire à des fins pacifiques pour produire de manière fiable de l'énergie électrique afin d'alimenter leurs sociétés. Les volumes croissants de déchets radioactifs générés s'avèrent toutefois être un problème de plus en plus urgent à résoudre. Le stockage en couches géologiques profondes est considéré comme notre meilleure option pour l'élimination sûre à long terme des déchets radioactifs. Différentes roches d'accueil sont envisagées pour le stockage en couches géologiques profondes, en fonction de la géologie du pays. La Suisse privilégie la formation Argiles à Opalinus en raison de sa très faible conductivité hydraulique et de ses bonnes capacités de rétention des radionucléides. Les microorganismes du sous-sol profond sont actifs et doivent être pris en compte car leur activité influencera un dépôt géologique profond pour les déchets radioactifs. D'une part, l'activité des microorganismes représente un problème de sûreté en raison de la possibilité d'une corrosion accrue, si l'on considère le conteneur de déchets métalliques encapsulant le combustible irradié des centrales nucléaires. Dans d'autres cas, cependant, ils peuvent contribuer à la sûreté d'un dépôt géologique profond, si l'on considère le bilan gazeux d'un dépôt suisse de faible et moyenne activité. La corrosion anoxique des déchets radioactifs métalliques présente des risques pour l'intégrité structurelle de la roche d'accueil. L'exploitation de l'activité des micro-organismes naturels à une distance sûre des déchets eux-mêmes peut entraîner une réduction nette des gaz et leur activité peut donc être considérée comme bénéfique et méritant d'être explorée. Dans cette thèse, les aspects positifs et négatifs de la présence microbienne sont explorés. La bentonite du Wyoming est un matériau de remblayage et un important système de barrière technique pour le combustible nucléaire irradié et les déchets de haute activité. Dans le cadre d'une expérience de corrosion *in-situ*, la présence et la croissance de microorganismes dans la bentonite du Wyoming sont étudiées. Les résultats montrent que l'activité des bactéries sulfato-réductrices de la corrosion dans la bentonite du Wyoming est inhibée pendant la phase critique de saturation de la bentonite, mais que d'autres micro-organismes ont pu se développer. Le second projet de recherche *in-situ* explore la mise en œuvre potentielle d'un puits de gaz microbien, un biofilm naturel composé de bactéries sulfato-réductrices oxydant l'hydrogène et d'archées méthanogènes. En effet, dans de bonnes conditions, un puits de gaz microbien peut remplir les fonctions pour lesquelles il a été conçu et consommer tout

l'hydrogène gazeux provenant de la corrosion anoxique des déchets. Cette thèse contribue à notre compréhension des processus en champ proche d'un dépôt de déchets radioactifs suisse au sein de la formation Argiles à Opalinus grâce à l'apport de connaissances expérimentales obtenues dans des conditions *in-situ*.

Mots-clefs : *Dépôt géologique profond, Argiles à Opalinus, Déchets radioactifs, Oxydation de l'hydrogène, Bentonite du Wyoming, Sous-sol profond, Micro-organismes, Bactéries réductrices de sulfate, Méthanogénèse, Puits de gaz microbien*

Zusammenfassung

Radioaktive Abfälle gehören zu den gefährlichsten anthropogenen Abfällen und ihre sichere Entsorgung ist eine herausfordernde Mehrgenerationenaufgabe. Viele Nationen haben sich für die friedliche Anwendung der Kernspaltung zur zuverlässigen Erzeugung von elektrischer Energie für ihre Gesellschaften entschieden. Die zunehmenden Mengen an radioaktivem Abfall erweisen sich jedoch als ein immer dringender zu lösendes Problem. Die geologische Tiefenlagerung gilt als unsere beste Option für die sichere Langzeitlagerung radioaktiver Abfälle. Für die geologische Tiefenlagerung kommen je nach Geologie des Landes unterschiedliche Wirtsgesteine in Frage. Die Schweiz favorisiert die Opalinuston-Formation aufgrund ihrer sehr geringen hydraulischen Leitfähigkeit und ihres Rückhaltevermögens für Radionuklide. Mikroorganismen im tiefen Untergrund sind aktiv und müssen berücksichtigt werden, da ihre Aktivität ein geologisches Tiefenlager für radioaktive Abfälle beeinflussen wird. Einerseits stellt die Aktivität der Mikroorganismen aufgrund der Möglichkeit einer verstärkten Korrosion ein Sicherheitsrisiko dar, wenn man die metallischen Abfallbehälter betrachtet, welche die abgebrannten Brennelemente aus Kernkraftwerken einschliessen. In anderen Fällen können sie jedoch zur Sicherheit eines geologischen Tiefenlagers beitragen, wenn man beispielsweise die Gasbilanz eines Schweizer Lagers für schwach- und mittelaktive Abfälle betrachtet. Die anoxische Korrosion von metallischen radioaktiven Abfällen stellt ein Risiko für die strukturelle Integrität des Wirtsgesteins dar. Die Nutzung der Aktivität natürlich vorkommender Mikroorganismen in einem sicheren Abstand zum Abfall selbst kann zu einer Netto-Reduktion von Gasen führen und daher kann ihre Aktivität als vorteilhaft und erforschenswert angesehen werden. In dieser Dissertation werden sowohl die positiven als auch die negativen Aspekte der mikrobiellen Präsenz betrachtet. Wyoming-Bentonit ist ein Verfüllmaterial und ein wichtiges technisches Barrieresystem für abgebrannten Kernbrennstoff und hochradioaktiven Abfall. Im Rahmen eines *in-situ* Korrosionsexperiments werden die Präsenz und das Wachstum von Mikroorganismen in Wyoming-Bentonit untersucht. Die Ergebnisse zeigen, dass die Aktivität von korrosionsfördernden sulfatreduzierenden Bakterien in Wyoming-Bentonit während der kritischen Bentonitsättigungsphase gehemmt wird, andere Mikroorganismen jedoch wachsen konnten. Das zweite *in-situ* Forschungsprojekt erforscht die mögliche Implementierung einer mikrobiellen Gassenke, eines natürlichen Biofilms, der aus wasserstoffoxidierenden, sulfatreduzierenden Bakterien und methanogenen Archaeen besteht. In der Tat kann eine mikrobielle Gassenke unter den richtigen Bedingungen den beabsichtigten Konstruktionszweck erfüllen

und das gesamte Wasserstoffgas verbrauchen, welches bei der anoxischen Korrosion des Abfalls entsteht. Diese Arbeit trägt zu unserem Verständnis der Prozesse im Nahfeld eines Schweizer Endlagers für radioaktive Abfälle in der Opalinuston-Formation durch den Beitrag experimenteller Erkenntnisse bei, die unter *in-situ* Bedingungen gewonnen wurden.

Schlüsselwörter: *Geologisches Tiefenlager, Opalinuston, Radioaktiver Abfall, Wasserstoffoxidation, Wyoming-Bentonit, Tiefer Untergrund, Mikroorganismen, Sulfatreduzierende Bakterien, Methanogenese, Mikrobielle Gassenke*

русский

Радиоактивные отходы относятся к числу наиболее опасных антропогенных отходов, и их безопасное удаление представляет собой сложную задачу нескольких поколений. Многие страны выбрали мирное использования ядерной энергии в целях надежного производства электрической энергии для своего населения. Вместе с тем растущий объем образующихся радиоактивных отходов свидетельствует о том, что эта проблема становится все более насущной. Глубокое геологическое захоронение считается самым предпочтительным вариантом безопасного долгосрочного хранения радиоактивных отходов. Для глубокого геологического захоронения рассматриваются различные горные породы в зависимости от строения почвы. Швейцария отдает предпочтение опалиновым глинистым породам в силу их очень низкой гидравлической проводимости и хорошей способности удерживать радионуклиды. Микроорганизмы в глубоких подповерхностных слоях являются активными и следует учитывать, что их активность будет влиять на глубокое геологическое хранилище радиоактивных отходов. С одной стороны, активность микроорганизмов представляет угрозу безопасности из-за вероятности ускорения процесса коррозии металлических контейнеров, в которых храниться отработанное топливо атомных электростанций. Однако в других случаях они могут способствовать обеспечению безопасности глубокого геологического хранилища, если учитывать к примеру газовый баланс швейцарского хранилища низкого и среднего уровня. Аноксическая коррозия металлических радиоактивных отходов создает опасность для структурной целостности вмещающей породы. Использование активности автохтонных микроорганизмов на безопасном расстоянии от самих отходов может привести к чистому сокращению выбросов газов, и поэтому их активность можно рассматривать как полезную и заслуживающую изучения. В этой диссертации исследуются как положительные, так и отрицательные аспекты микробного присутствия. Вайомингский бентонит является материалом для обратной засыпки и важной инженерной барьерной системой для отработавшего ядерного топлива и высокоактивных отходов. В рамках in situ эксперимента по коррозии исследуется присутствие и рост микроорганизмов в бентоните Вайоминга. Результаты показывают, что активность сульфатоснижающих бактерий, усиливающих коррозию в бентоните Вайоминга, ингибируется на критической фазе насыщения бентонитом, однако другие микроорганизмы смогли вырасти. Второй исследовательский in situ

проект исследует возможность внедрения микробного газопоглотителя - естественной биопленки, состоящей из окисляющих агрессивных сульфатредуцирующих бактерий и метаногенных археи. При правильных условиях поглотитель микробных газов может выполнять свои проектные задания и потреблять весь водородный газ, образующийся в результате аноксической коррозии отходов. Этот тезис вносит свой вклад в обеспечение более глубокого понимания процессов происходящих в ближней зоне швейцарского хранилища радиоактивных отходов в опалиновой глине, благодаря вкладу экспериментальных данных, полученных в условиях in situ.

Ключевые слова: Глубокое геологическое хранилище, Опалиновая глина, Радиоактивные отходы, Окисление водорода, Бентонит Вайоминга, Глубокая подпочва, Микроорганизмы, Сульфат-редуктирующие бактерии, Метаногенез, Микробный газопоглотитель

Contents

List of Figures

List of Tables

1 Introduction

1.1 Terrestrial deep subsurface

The deep subsurface is an ill-understood environment that is receiving increasing public attention. Evident to the importance of the deep subsurface is the discussion of how humanity is tackling the climate crisis: Storing carbon-dioxide emissions in the deep subsurface is an integral part of the future emission scenarios outlined by the Intergovernmental Panel on Climate Change (IPCC) to limit the global temperature rise to 1.5°C. Alongside, there is the renaissance of nuclear power in some regions. Nuclear energy is projected to increase its global share in primary energy production by between 98 up till 501% (depending on the scenario) by 2100 (based on 2010 levels) (Masson-Delmotte et al., 2018).

But what do we understand by the deep subsurface? The dictionary defines the noun subsurface as "earth material (such as rock) near but not exposed at the surface of the ground" (Merriam-Webster, 2020). Thus the deep subsurface could be defined as the earth material below the "near but not exposed" rocks. However, this is a vague definition. Within the recent literature, the deep subsurface was defined as the combination of all the marine sub-seafloor sediments, the oceanic crust and all terrestrial mass deeper than 8 meters below the surface, excluding soil (Bar-On et al., 2018; Whitman et al., 1998). The definition of the deep subseafloor is established by Jørgensen and Boetius, who "define the seafloor as the top metre of the seabed that is bioturbated by animals [...] whereas the deep subsurface [...] comprises the sediment and rock that is deeper than 1 metre beneath the seafloor" (Jørgensen & Boetius, 2007). The terrestrial deep subsurface thus contains only the portion of the deep subsurface belonging to the thick continental crust.

1.1.1 Terrestrial subsurface applications

Anthropogenic use of the terrestrial subsurface is mostly limited to the extraction of natural resources, mainly groundwater from shallow aquifers, as well as hydrocarbons (oil and gas), coal, and a wide variety of ores from (sometimes) great depths. Novel applications are the

abovementioned carbon sequestration, where the first commercial projects are ramping up both in the terrestrial deep subsurface and the deep sub seafloor bed (Collins & Watts, 2020; Equinor, 2020). Similarly, the emerging expected widespread use of hydrogen as a fuel or for fuel storage has created the need for suitable storage solutions, which are for example met by artificially created caverns in salt-rock formations in The Netherlands (Energystock, 2020). Geothermal energy is viewed as an ideal replacement for fossil fuels, thus research and development in that field is increasing, for example in Switzerland (SFOE, 2020). Other applications concern the remediation of contaminated sites from ore mining, processing, or the accidental spill of hazardous waste in the surface and the subsurface, e.g., for uranium (Fox et al., 2012; IAEA, 2004), or for chromate (Wanner et al., 2012). Furthermore, deep geological repositories are considered for the safe storage for radioactive wastes from nuclear power plants and other applications of radioactivity (Ewing et al., 2016). Infrastructure projects such as metropolitan railways and highway tunnels crossing mountain ranges, rivers or bays are popular examples of daily applications within the part of the lithosphere defined as the terrestrial deep subsurface.

1.1.2 Microbiology in the terrestrial deep subsurface

Microbiology of this particular biosphere is an challenging endeavour for the obvious reason that it is difficult to access and thus, expensive. The easiest access for scientific investigations is provided by partnering with commercial interests. However, the requirements of scientific and financial interests may differ substantially. There are two main techniques to sample the terrestrial deep subsurface: drilling from the surface or drilling from existing galleries (e.g., highway tunnels). From a microbiologist's perspective, both techniques suffer from the same problem: the almost unavoidable contamination with exogenous microorganisms (Pedersen et al., 1997). Underground research facilities were established to serve the scientific community, one such example is the project 'Mont Terri' in St.-Ursanne, Canton Jura, Switzerland (discussed further below). Additionally, the low overall biomass density presents an additional challenge to investigations of the terrestrial deep subsurface investigations. Thus, experiments have to be designed carefully and to take these limitations into account.

Deep biosphere

In recent years, the deep subsurface has been investigated in many studies, showing a surprising diversity despite the extreme conditions. The potential of microorganisms to modify the chemical composition of minerals, the groundwater and pollutants has been recognized. However, the size of the deep (prokaryotic) biomass remains uncertain due to limited access. The estimates differ widely and state that between 20% and 70% of the total Earth biomass may be located in the terrestrial deep subsurface (McMahon & Parnell, 2014; Parkes et al., 2014; Whitman et al., 1998). But a more recent study of the terrestrial (continental) deep subsurface biomass points to "roughly 4 to 10 times less than previous estimates" with a "total global prokaryotic biomass is approximately 23 to 31 Pg of carbon C (PgC)" (Magnabosco et al.,

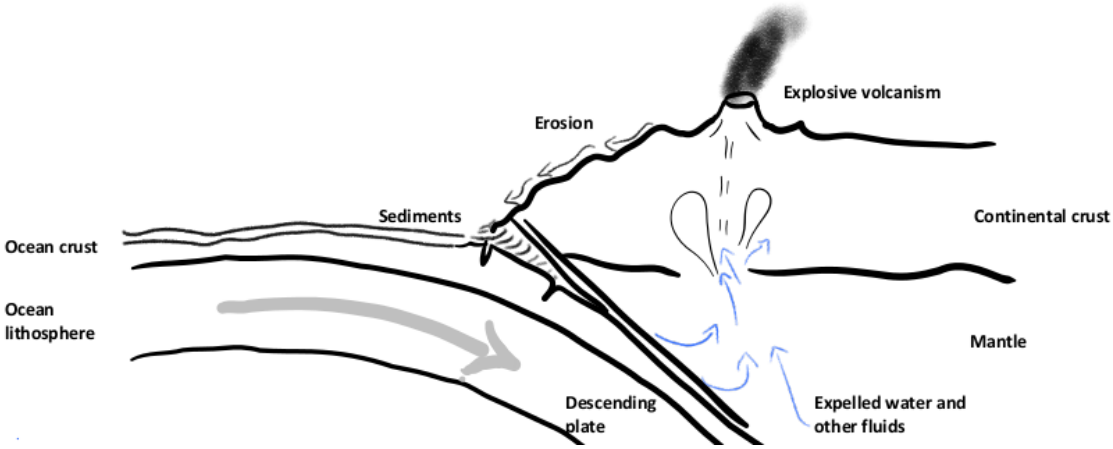

Figure 1.1 – Subduction zones generate water-containing rocks. Ocean crusts migrating downwards, take water-soaked sediments with them. Under high pressure and temperature, water and other fluids are pushed out into the overlaying continental crust.

2018).

The deep biosphere extends from 8 m below the surface down to at least 2.5 km below the surface. However, microbial signatures have even been detected down to 4-km-deep oil reservoirs (Inagaki et al., 2015) and up to 3.4-km-deep fractures, accessed via gold- and diamond mines in South Africa (Kieft et al., 2018). Terrestrial communities dwell in the dark, independently from photosynthesis and photosynthesis-derived compounds transported from the surface down to deep subsurface (in contrast to the deep sea, where organic matter falls down onto the seabed). Much less energy is available in the absence of light and, as a result, the microbial populations have remarkably long generation times, up to thousands of years (Jørgensen & D'Hondt, 2006; Jørgensen & Marshall, 2016), and remain, under the right conditions, viable trapped within groundwaters over long times of millions to billions of years (Lollar et al., 2019).

On Earth, a steady supply of water to the deep subsurface is provided by the rock formation at subduction zones, where the upper part of a descending plate of the ocean lithosphere is saturated with water-bearing sediments, 1.1. This water is initially squeezed out but considerable amounts of water are brought further down, where the increasing heat and pressure transforms minerals from their hydrous to their anhydrous forms. This process can happen so rapid as to cause earthquakes. The water migrates upwards, partly melting the overlaying continental crust, which results in the formation of silica-rich basalt (Zalasiewicz, 2016). Such processes create a water reservoir for the various hydrogen-forming processes.

Most of the deep subsurface microbial life belongs to the lithotrophic category, utilizing soluble inorganic compounds, hydrogen, reduced sulfur, methane or simple organic molecules as electron donors. Dead biomass can be oxidized by heterotrophic microorganisms using nitrate, manganese (IV), iron (III), sulfate or carbon dioxide as electron acceptors. Oxidation of

molecular hydrogen by chemolithoautotrophs is considered to be one of the major oxidative processes for deep subsurface life, enabling microbial communities to sustain life basically indefinitely as long as they are fueled by geological processes (Lin et al., 2006).

Several potential H_2 sources were proposed:

- outflow of hydrogen, from the mantle (Fredrickson & Balkwill, 2006; Zgonnik, 2020), e.g., due to the transport of water at subduction zones, Figure 1.1.
- radiolysis of porewater (Barr & Allen, 1959; Curie, 1910)
- serpentinization reaction of mafic and ultra mafic rock (Stevens & McKinley, 1995; Twing et al., 2017)
- seismogenic hydrogen (cataclasis) (Gregory et al., 2019; McMahon et al., 2016), resulting from rock-water interactions at seismic active zones, like fault zones, by frictional grinding, creating a highly reactive silicon radical species: $2(\equiv Si\cdot) + 2H_2O \rightarrow 2(\equiv SiOH) + H_2$
- hydrogen produced by other microorganisms, e.g. via the degradation of organic matter (necromass cycled within the deep biosphere) (Bagnoud, de Bruijn, et al., 2016), or via fermentation of other organics, via nitrogen fixation, via anaerobic carbon monoxide oxidation, via posphite oxidation, via acetate oxidation (Gregory et al., 2019)

Other potential sources of low redox potential electrons for microbial metabolism include groundwater rich in organic matter or organic matter deposited in sedimentary rocks. Finally, the deep biosphere is also considered a very likely environment for life in the Solar System, e.g., on Mars (S. L. Nixon et al., 2013; Stamenković et al., 2020), and thus any knowledge gained about the Earth's deep biosphere will help future exploration of life in the Solar System.

1.2 Opalinus Clay rock

The Opalinus Clay Formation is the preferred host rock formation for deep geological disposal of radioactive waste in Switzerland and has been extensively studied during the past two decades. Opalinus Clay rock belongs to the group of sedimentary rocks and features a very low hydraulic conductivity even though it is saturated with 8-18% of water (Gaucher et al., 2003). An Underground Research Laboratory (URL), the project 'Mont Terri', was set up in St.-Ursanne, Canton Jura, Switzerland, to investigate this rock formation: mechanical, physical and (bio)geochemical properties of Opalinus Clay are studied, it is however not considered as a future repository site.

Sedimentary rock diagenesis The Opalinus Clay rock formation was formed 174 million years ago by sedimentation, when the area spanned by today's cities Bern-Zurich-Munich-Stuttgart-Strasbourg was a shallow sea. Three different sedimentation conditions lead to three

different facies of Opalinus Clay: a shaly, a sandy and a carbonate-rich sandy clay, composed of similar minerals but in different ratios, Table 1.1. Differences in the marine sedimentation conditions during the mid-Jurassic until the late-Cretaceous period are responsible for the formation of three facies (Pearson et al., 2003).

Table 1.1 – Mineralogical analysis of the three Opalinus Clay rock facies. Table modified from (Pearson et al., 2003)

	Opalinus Clay shaly facies	**Opalinus Clay calc-sandy**	**Opalinus Clay sandy facies**
n° of samples	9	2	4
Calcite	5–28	36–42	7–17
Dolomite/ankerite	0.2–2	2.1–3.3	0.3–2
Siderite	1–4	1.1–2.4	1.1–3
Pyrite	0.6–2	0.2–1.3	0.7–3.2
Organic C	<0.1–1.5	0.2	0.2–0.5
Quartz	6–24	27–31	16–32
K-feldspar	1–3.1	3–5	2.5–5
Albite	0.6–2.2	1.1–2.4	0.8–2.2
$\sum$ clays	58–76	25	45–70
Illite	16–40	6–9	15–35
Illite-smectite	5–20	3–6	5–20
Chlorite	4–20	2.2–4	4.4–15
Kaolinite	15–33	8–13	13–35

Upon burial, the marine sediment layers were exposed to increasing pressure, heat and a changing chemical environment as subsequent layers are deposited on top. In the case of Opalinus Clay rock at Mont Terri, which is expected to have reached burial temperatures of 55-85°C, the rock has a low degree of crystallisation (Mazurek et al., 2006). Temperatures around 80-90°C have been shown to have a sterilizing effect (paleo-pasteurisation) in oil reservoirs as signatures of microbial activity are only proven for colder oil reservoirs (Bell, 2016; Head et al., 2003). Therefore, an indigenous microbial community should exist within the Opalinus Clay rock formation of Mont Terri. In addition to the increase in temperature, another process taking part in the formation of a sedimentary rock is the pressure increase, resulting in the loss of water and the migration of the sediment particles from high-pressure contact points to adjacent areas of lower pressure. The once porous seafloor sediment turns into a low porosity rock. Opalinus Clay rock has 10-20 nm pores, is mainly composed of clay minerals, quartz and carbonates, Table 1.1. In addition, marine organic matter is deposited and represents about 1% weight (Gaucher et al., 2003). 36% of the soluble fraction of this organic matter is mainly composed of acetate but also of formate and lactate (Courdouan

et al., 2007) - suitable electron and carbon sources for microbial metabolism.

The small pore size also comes with poor pore interconnectivity, precluding extensive microbial activity despite the presence of organic matter. Prokaryotes are typically micrometers in size (Moran et al., 2010). Thus, the small Opalinus Clay rock pore size restricts their ability to grow. Furthermore, the small pores result in low hydraulic conductivity in the range of $10^{-13} - 10^{-14} \frac{m}{s}$, and is a feature of this rock. It is also a major reason for its selection as a host rock for radioactive waste. It will act as an effective barrier preventing the migration of dissolved radionuclides (Bagnoud, 2015; Gaucher et al., 2003; Pearson et al., 2003).

1.2.1 Microbial studies in Opalinus Clay rock

Studying the porewater of Opalinus clay rock is a challenging task due to the aforementioned low hydraulic conductivity (Pearson et al., 2003). Therefore boreholes are drilled and either filled with artificial porewater or slowly fill with the surrounding rock due to the pressure gradient established by a borehole. A microbial influence was detected in several experiments, for instance, the hydrogen transfer (HT) experiment (Vinsot et al., 2014). Recently, the influence of microbially-mediated (bio-)geochemical processes is garnering increasing attention from the national radioactive waste authorities. In Switzerland, studies of microorganisms in Opalinus Clay rock started in 2007 (O. X. Leupin et al., 2017), where phospholipid fatty acids belonging to the genera *Desulfobulbus* and *Desulfovibrio* were detected. Later, enrichment cultures revealed seven species, among them the genera *Sphingomonas* and *Alicyclobacillus*, but most attempts for direct DNA extraction failed, except for a round-robin study with four partner laboratories. DNA extraction was only successful for two of the four partners and the 16S rRNA gene sequences pointed to a diverse microbiota: *Sphingomonas*, *Bdellovibrio*, *Ralstonia*, Procabacteriaceae, Methylophilaceae, Rhizobiales (O. X. Leupin et al., 2017). However, the results from the two labs exhibited limited overlap. Additionally, contamination could not ruled out as the source of the microbial signatures. Still, Opalinus Clay rock was proposed to harbor an indigenous microbiome marked by large spatial heterogeneity in biomass concentration.

More insight have been obtained from disturbed Opalinus Clay in the form of porewater-filled, sealed boreholes. A comprehensive metagenomic study of a single borehole has shown that providing space is a sufficient requirement to allow a microbial community to thrive. The microbiome was mainly composed of two microorganisms. One was a *Pseudomonas* sp., shown to ferment organic macromolecules (from Opalinus clay rock) and producing low molecular weight organic acids. The second most abundant bacterial group, belonging to the family Peptococcaceae, found to oxidize hydrogen or organic acids to carbon dioxide and using sulfate as the electron acceptor (sulfate reduction) (Bagnoud, de Bruijn, et al., 2016). This system, labelled a "minimalistic microbial food web" (Bagnoud, de Bruijn, et al., 2016), can serve as an analogue to the expected excavation-disturbed zone in a radioactive waste repository. Such zones are located along excavated galleries and extend radially towards the pristine host rock, Figure 1.2. They exhibit increased pore space and fractures extending. The

formation of a excavation-disturbed zone creates favorable conditions for microbial live in Opalinus Clay rock, in relatively close proximity to the radioactive waste.

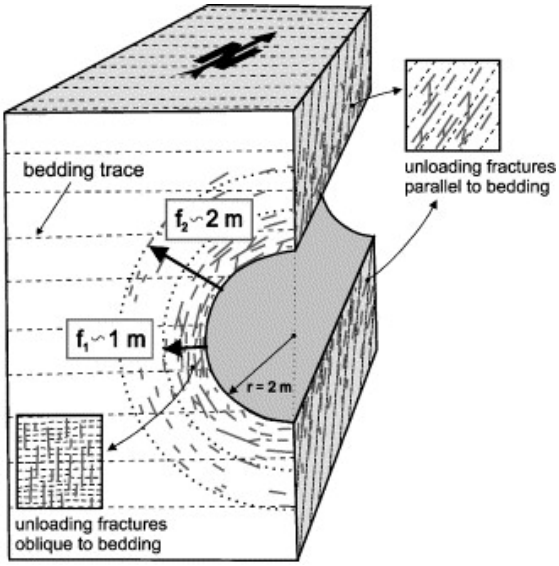

Figure 1.2 – Illustration of the excavation-disturbed zone, fractures extending about two meters into the surrounding host rock, radially from a excavated tunnel. The outer two-meter zone "consists of partially porewater-saturated unloading fractures". Figure from (Bossart et al., 2002)

Considering the scarcity of hydrogen within the deep biosphere, it is expected that a Opalinus Clay rock borehole community would thrive upon stimulation with hydrogen, thus hydrogen evolving from the anoxic corrosion of metallic waste is considered for a deep geological repository in this type of host rock. For Opalinus Clay rock, studies of the hydrogen-oxidizing potential of the microbiota in disturbed Opalinus Clay have revealed a subsurface metabolic web in the geological setting for the Swiss repository, describing a full carbon cycling in a subsurface environment, fueled by hydrogen. Metagenome binning has uncovered the metabolic web composed of seven species: Two hydrogenotrophic species transforming CO_2 to biomass (one of them a sulfate-reducing bacteria), one fermenting bacterium degrading the necromass, which is providing acetate to four heterotrophic sulfate-reducing bacteria and producing CO_2. The hydrogen and sulfate consumption rates of the adapting microbiome were determined to be 1.13-1.93 $\frac{\mu mol\, H_2}{cm^3\, day}$ and 0.14-0.2 $\frac{\mu mol\, SO_4^{2-}}{cm^3\, day}$, in a planktonic microbiome setting (a porewater-filled borehole) (Bagnoud, Chourey, et al., 2016; Bagnoud, Leupin, et al., 2016). Most importantly, this detailed study proved that microbial life within Opalinus Clay will play an important role in the gas balance of the repository (details in the sections below). The experiment performed by (Bagnoud, Chourey, et al., 2016) serves as analogue for the excavation-disturbed zone, filled with porewater and provided with diffusive hydrogen from the anoxic corrosion of the radioactive waste canister and the metallic waste itself.

A microcosm study (Boylan et al., 2019), followed and showed that porewater microorganisms

and Opalinus Clay rock, amended with hydrogen, resulted in the formation of iron-sulfide minerals, such as pyrite (FeS_2. The activity of sulfate-reducing bacteria led to the leaching of iron(II) (from siderite) and sulfate (from celestite) into porewater. This illustrates the biogeochemical influence microorganisms can exert onto the host rock.

1.3 Radioactive waste repository concept

Geological processes have trapped radioactive elements and hydrocarbons within the Earth crust for millions of years, until eventually, humans developed the technology to exploit uranium ores and hydrocarbons for industrialization. By storing radioactive waste and carbon dioxide in the deep subsurface, is akin to returning them to their source. In addition, the deep subsurface is the only place in our reach to enclose our most dangerous anthropogenic waste type: radioactive waste. All known Earth-based higher life forms are extremely sensitive to radioactivity (Wells, 1976), only some fungi and specialized bacteria have been found to resist (Mattimore & Battista, 1996) or even exploit radioactivity (Dadachova et al., 2007). Therefore, it is an obligation, to isolate radioactive waste from the surface and oceanic biosphere. Guidelines on how to handle radioactive waste were established and the nations utilizing nuclear power have set up their own radioactive waste management organization (IAEA, 1995). The qualification of the deep subsurface as the place to dispose of radioactive waste is supported by worldwide assessments, by the fact that it effectively hinders access to radioactive material for malicious intentions, as well as by observations of natural systems, e.g., natural nuclear fission reactors (Gauthier-Lafaye, 2002). A disposal system for radioactive waste must ensure the long-term security and safety at three levels:

- Isolation of the waste from human environments. This is best ensured by a repository deep underground, with all access routes sealed and backfilled. Furthermore, the area should not host any currently recognised valuable natural resources and should not interfere with future infrastructure projects. The site must be considered as stable, i.e., not prone to disruptive events (Nagra, 2002).
- Long-term confinement and radioactive decay within the disposal system. Most activity shall decay while the radioactive waste is still encapsulated within the primary waste containers/canisters. That is especially the case for spent fuel and high-level waste. After canister and containers fail, engineered barrier systems and the host rock shall keep radionuclides in place such that further decay can take place, for example via immobilisation and due to high barriers to diffusion (Nagra, 2002).
- Attenuation of release to the environment. Because confinement cannot be ensured for all radionuclides over all relevant times, the attenuation of their transport towards the surface environment needs to be considered and evaluated (Nagra, 2002).

Radioactive waste is divided into three categories according to its activity level: High-level

radioactive waste (high-level waste), α-toxic waste[I] (waste that emits more than 20.000 Bq[II] radiation per gram conditioned waste), and low- and intermediate-level radioactive waste (low-/intermediate-level waste). A subclass of the intermediate-level waste is the long-lived intermediate-level radioactive waste.

Within these activity classifications, 5 different kinds of wastes have been categorised:

- Operational waste from nuclear power plants [III] compromises ion-exchange resins, concentrates, filter materials and other overhaul waste. Further operational waste sources are the interim storage [IV], surface facilities of the prospective deep geological repositories, the prospective deep geological repository itself and waste from industrial, medical and scientific applications.
- Decommissioning waste from nuclear power plants, interim storage, surface facilities and from scientific facilities[V], i.e., their dismantling.
- Reactor equipment waste[VI]
- Waste from the reprocessing of fuel rods.
- Spent fuel rods from power plants and research reactors[VII].

The Swiss Federal Nuclear Safety Inspectorate (ENSI) has defined the relevant time period for safety considerations as follows: 1 million years for high-level and long-lived intermediate-level waste and 100'000 years for low- and intermediate-level waste repositories (Nagra, 2014b). Additionally, the following repository requirements have been set by ENSI (Nagra, 2016):

- Limitation of the vertical extent of the storage chambers to minimize the deterioration of the low vertical transport mobility of radionuclides in Opalinus Clay (for spent fuel/high-level waste) or the host rock in the Swiss north-west region (for low-/intermediate-level waste). Because the considered Opalinus Clay formations are not very thick, the storage chambers should not be of a too large vertical extent. This makes sure that the very low vertical diffusivity for radionuclides of Opalinus Clay rock can fulfil its safety purpose.
- Avoidance of perforation of the host rock in vertical direction in close proximity to the storage chambers.

[I] ${}^{4}_{2}He^{2+}$, the α particle
[II] Bequerel Bq, s^{-1}, the SI unit of radioactivity, nucleus decays per second
[III] Beznau 1 & 2, Goesgen, Leibstadt, Muehleberg.
[IV] ZWILAG Wuerelingen AG
[V] Particle accelerators at Paul Scherrer Institute (PSI) and European Organization for Nuclear Research (CERN)
[VI] Replacement components which have been activated, e.g., measuring rods
[VII] SAPHIR (1957-1994), DIORIT (1960-1977), University Basel AGN-211-P (1959-2013) whereas in 2015 the US National Nuclear Security Administration the highly enriched uranium fuel rods brought back to the USA, EPFL-CROCUS (since 1983), PSI-PROTEUS (1968-2011), University Geneva AGN 201 P (1958-1987)

- Use of spent fuel/high-level waste canisters that ensure a complete inclusion for at least 1,000 years.

- Limitation of the heat output derived from the spent fuel/high-level waste containers to prevent unwanted heat-related processes in the host rock.

- Verification of retrievability of canisters, without large costs until the end of the observation period.

- Special requirements for a Swiss low-/intermediate-level waste repository:

  – Avoidance of concepts that require monitoring and maintenance of any kind.

  – Avoidance of concepts that are not suitable for great depths (several 100's of meters below surface)

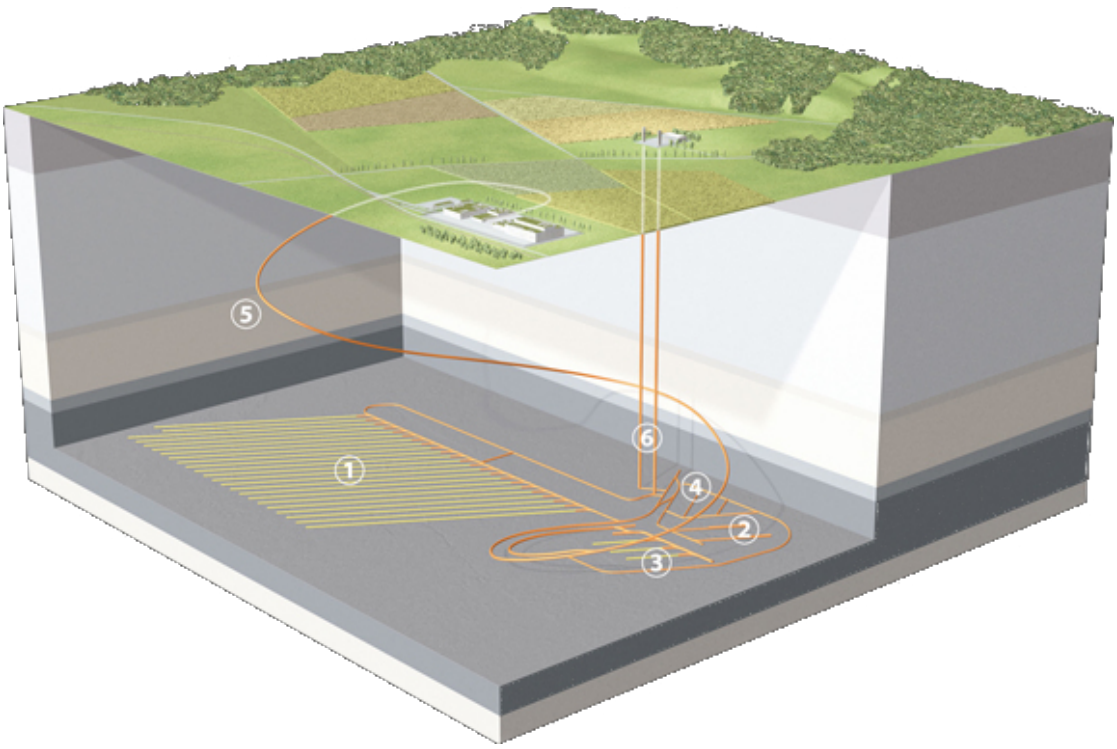

Figure 1.3 – Rendering of a prospective spent fuel, high-level waste and long-lived intermediate level waste repository in Swiss Opalinus Clay rock formation. The following repository parts are planned at a maximum depth of 900 meters: 1 - Storage tunnels for spent fuel and high-level waste; 2 - Long-lived intermediate-level waste storage cavern (a smaller cross section layout is necessary due to the large overburden, see Figure 1.7a; 3 - Pilot repository; 4 - Testing area; 5 - Access tunnel; 6 - Ventilation and construction shafts. Rendering by Infel AG, Claudio Köppel, obtained from (Nagra, 2020a)

1.3.1 Swiss concept for spent fuel and high level waste

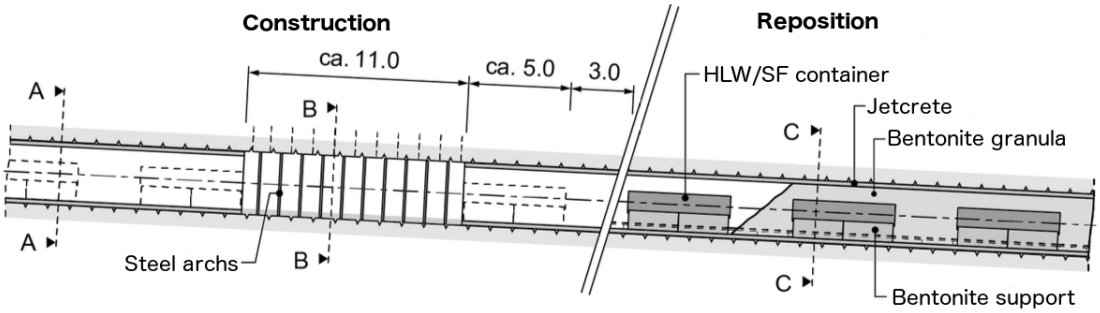

(a) Spent fuel (SF) & high-level waste (HLW) storage chamber, viewed as lengthwise cut.

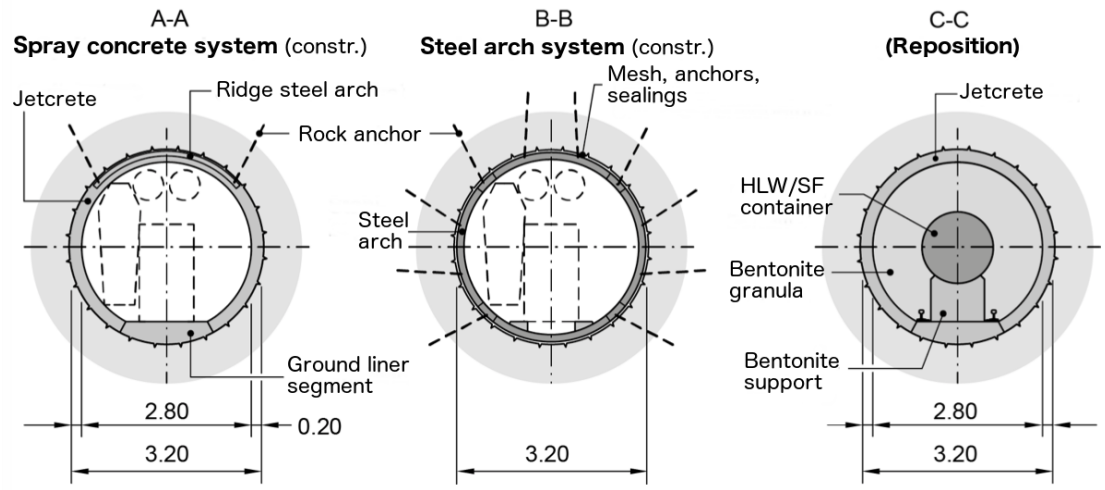

(b) Spent fuel (SF) & high-level waste (HLW) storage chamber, viewed as normal profile, the three presented cross sections correspond to the indicated cross sections A-A, B-B and C-C in subfigure (a).

Figure 1.4 – Spent fuel (SF) & high-level waste (HLW) storage chamber design with two construction layouts. Requirements for the layouts are: A-A The jetcrete layer shall not exceed 30 cm, B-B the amount of steel shall be small enough to not contribute significantly to gas evolution from anoxic corrosion, C-C final reposition of high-level waste (HLW), and spent fuel (SF) container residing on a bentonite support and the gallery backfilled with a bentonite granulate. Figures modified from (Nagra, 2016).

A deep geological repository within a sufficiently thick and mechanically stable Opalinus Clay rock formation is the most likely final disposal for spent fuel from Swiss nuclear power plants and other high-level radioactive wastes. This repository will be placed in depth of not more than 900 meters, Figure 1.3. The concept for spent fuel and high-level waste envisions long horizontal storage chambers parallel to the bedding with a diameter of 3 m and lengths of several 100's of meters, Figure 1.3 and Figures 1.4a and 1.4b. The relatively small diameter (3 m) of the storage chamber is chosen to minimise risks related to the rock integrity because of the relative weak mechanical properties of Opalinus Clay. Further weakening the host rock

is the expected heat load, originating from the radioactive waste. Certain space requirements have to be met: Long storage chambers with a high number of canisters disposed together will require more separation space to the next storage chamber (Nagra, 2016).

Canister design The two types of storage canister that best meet the requirements are: carbon steel without any coating and an inner canister made out of carbon steel or cast iron combined with a copper coating. However, the reference design is a carbon steel canister and a copper, nickel, titanium or ceramic coating option is kept as an alternative if an improved canister is deemed necessary (Diomidis et al., 2016; Nagra, 2016). The waste canister for high level nuclear waste will contain two high-level waste flasks, Figure 1.3. Each waste canister for spent fuel will either contain 4 fuel rods from pressurized water reactors or 9-12 fuel rods[VIII] from boiling water reactors (BWR). The spent fuel rods are stored as is, decreasing the complexity of their handling and keeping the mantle integrity of the rod itself. Therefore, the final length of a spent fuel canister is 5 m with a diameter of 1 m and a weight of 20'000 kg. The maximal heat load per canister will be below the limit of 1'500 W (Nagra, 2016). Finally, the canister will be placed on a highly compacted bentonite support and the remaining space backfilled with a bentonite granulate, see C-C in Figure 1.4a and 1.4b. Achieving a minimum dry-density is key to this concept. Bentonite is chosen due to its swelling capacity (its small pore size inhibits microbial activity), transport properties (low diffusion constants, low solubility and high sorption capacity of radionuclides), and low corrosion rates of steel and waste matrices (whether fuel rod or glass based matrix). The alternative version for the waste canisters, copper-coated steel combined with highly compacted bentonite offers the longest expected canister lifetimes. Additionally, a cementitious-based back-fill is kept as an alternative solution for cases where the conditions for a sufficiently dense bentonite back-filling is not achieved and thus, microbial activity can not be ruled out (Nagra, 2016). The storage chamber will be constructed using limited amounts of jetcrete (maximum 30 cm thickness), with the additional advantage of enabling the transformation of sodium-bentonite to calcium-bentonite adjacent to the jetcrete (Nagra, 2016). The usage of construction steel should be limited and not significantly increase the expected gas evolution from disposal canisters. However, concealed cavities (from the jetcrete) and loose rock may lead to microbial activity near and within the back-fill bentonite buffer as a result of reduced swelling capacity due to a lower dry density. In such a case, the weakened bentonite barrier and the spatially adjacent microbial activity may lead to increased corrosion rates. This scenario is of particular interest when assessing a copper-coated disposal canister design (Nagra, 2016).

[VIII] Depending on the final host rock formation's heat load capacity, the heat load can be tuned using 9 or 12 fuel rods from BWR

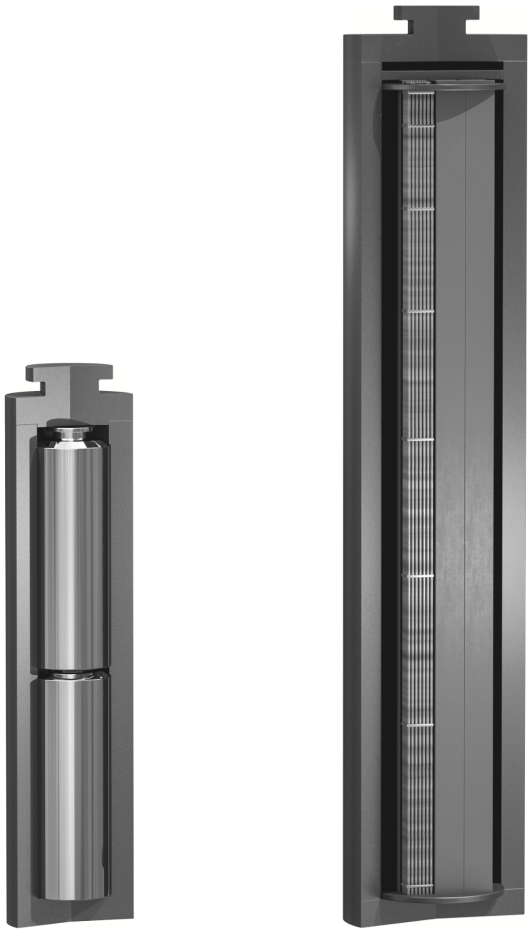

Figure 1.5 – Rendering of a schematic cross section showing the reference design for a high-level waste canister (left) and a spent fuel canister (right). The reference design expects the disposal of 317 canisters for high-level waste and of 1894 canisters for spent fuel. Additional data and dimensions are provided in Table 1.2. Figure from (Diomidis et al., 2016)

Table 1.2 – Spent fuel and high-level waste canister data (Diomidis et al., 2016)

Canister type	HLW	SF
Outer diameter [mm]	720	1050
Inner diameter [mm]	440	770
Approximate external length [mm]	3000	5000
Wall thickness body [mm]	140	
Wall thickness base [mm]	150	180
Wall thickness lid [mm]	170	180
Approximate unloaded weight [kg]	6400	19500
Number of canisters	317	1894
Reference lifetime [a]	10000	

Context to Chapter 2 Within Chapter 2 of this thesis, the microbial activity in the proposed bentonite buffer/backfill is investigated under *in-situ* conditions within a porewater-filled borehole in Opalinus Clay rock. The test allows to evaluate the extent of microbial activity within Wyoming bentonite at the reference dry-densities and formulations as a function of time after deployment in the borehole. Highly compacted bentonite modules of 1.55 g/cm^3 are used to simulate the canister support. A mixture of pellets and powders of MX-80 Wyoming bentonite is used to simulate the storage gallery back-fill. The microbiology results obtained could be combined with carbon-steel and copper corrosion rates (not part of this thesis) from identical test modules and thus will allow a complete assessment of expected canister corrosion.

Context to Chapter 3 In Chapter 3, using a similar *in-situ* approach as presented in Chapter 2, we investigated the potential microbial influence on the *in-situ* corrosion of reference canister materials. With the performed experiment we explored the role of microorganisms highly active on the surface of the engineered barrier system Wyoming bentonite (backfill material). Furthermore, we utilized sterile bentonite such that we could exclude the impact of microorganisms in direct contact with the metallic test coupons resembling the spent fuel and high-level waste canister surface in one setup. The other setup was supposed to create a high activity of sulfate-reducing bacteria in direct contact with the test materials, by seeding sulfate-reducing bacteria into sterile bentonite. Our results show that bentonite-sourced sulfate-reducing bacteria, seeded into sterile bentonite and Opalinus Clay rock microorganisms are unsuccessful colonizers of Wyoming bentonite at early timepoints of the bentonite saturation. The sterile bentonite used had a dry-density of 1.45 g/cm^3, appeared free of bacteria other than from experimental contamination, whereas the bentonite surface, in direct contact with the porewater, was shown to be colonised by Opalinus Clay rock porewater microorganisms.

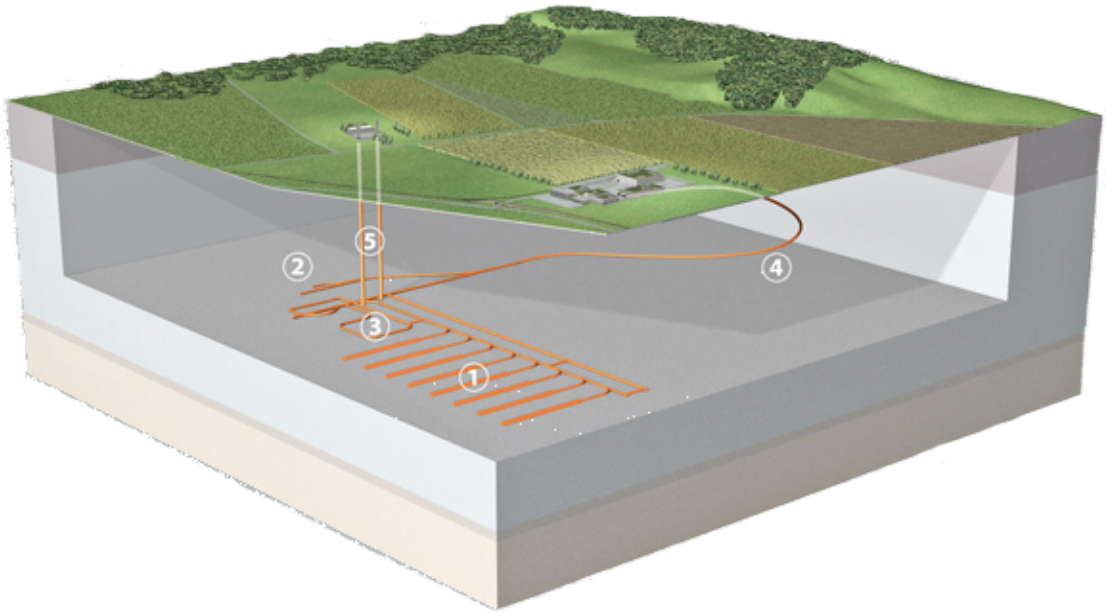

Figure 1.6 – Rendering of a prospective low- and intermediate-level waste repository in Swiss Opalinus Clay rock formation. In a maximum depth of 600 meters are the following repository parts: 1 - Storage caverns; 2 - Pilot repository; 3 - Testing area; 4 - Access tunnel; 5 - Ventilation and construction shafts. Rendering by Infel AG, Claudio Köppel, obtained from (Nagra, 2020a)

1.3.2 Swiss concept for low- and intermediate-level waste and long-lived intermediate-level waste

Disposal of low-/intermediate-level waste and long-lived intermediate-level waste[IX] is conceptualised in a repository in Opalinus Clay at a depth not deeper than 600 meters below the surface and, unlike other repository concepts, it will be instantaneously back-filled after disposal. In general, the deeper the low-/intermediate-level waste repository, the smaller the cross section[X] and thus, the layout of the disposal chamber changes(1.7a).

[IX] Long-lived intermediate-level waste will be most likely stored within the repository of spent fuel and high level waste, but due to the waste composition, the disposal design is similar to that of the low-& intermediate-level waste

[X] A smaller cross section leads to longer storage chambers, total tunnel lengths: K04a 10'962 m, K04 8'770 m, K06 6'264 m, K09 3'986 m.

K04a	K04	K06	K09
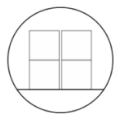	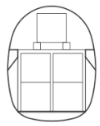	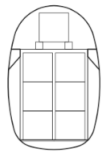	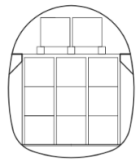
LRF: 58 m^2 LØ: 8.6 m	LRF: 58 m^2 LH: 9.5 m LB: 7.3 m	LRF: 77 m^2 LH: 11.9 m LB: 7.6 m	LRF: 110 m^2 LH: 12.6 m LB: 10.4 m
4 storage containers	5 storage containers	7 storage containers	11 storage containers

(a) Cross section of options for storage chambers of low- and intermediate-level waste and long-lived intermediate-level waste, several hundreds of meter in length, parallel to the bedding. With the cross sections, the proposed number of disposal containers increases from 4, 5, 7 up to 11. long-lived intermediate-level waste will be placed within the high-level waste repository, thus a small cross section, e.g., K04a, might be necessary because of the greater overburden in a high-level waste repository. Figure modified from (Nagra, 2016)

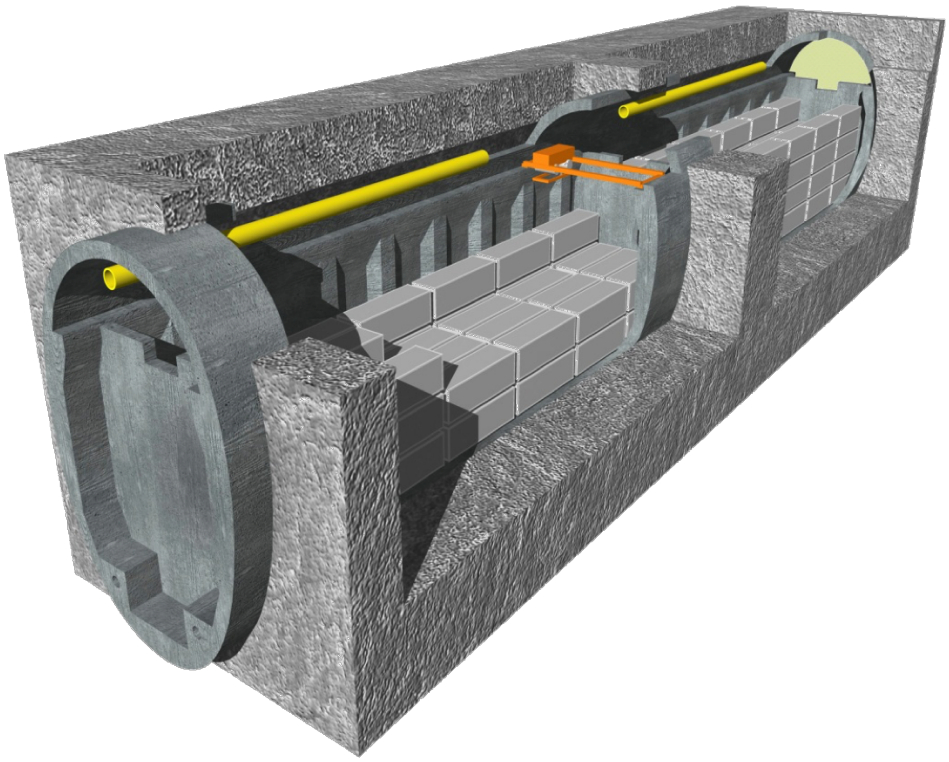

(b) Illustration of the storage cavern, design option K09: The concrete containers containing barrels of low- and intermediate-level waste are stacked upon each other to use the available space in the most efficient way. The hallow space will be back-filled with a cement mortar featuring a high pH, a radionuclide sorption capacity, and gas conductivity. Figure modified from (**leupin_research_2017**)

Figure 1.7 – Low- and intermediate-level waste storage chamber layout option.

(a) Low-level waste is conditioned into a slow-degrading waste matrix and placed in barrels.

(b) Assemblies of waste barrels are then placed in concrete disposal containers and filled with mortar. The waste will be contained for about 100 years.

Figure 1.8 – Low- and intermediate-level waste conditioning and packing into disposal containers (O. Leupin et al., 2016), Figures modified from (Nagra, 2016).

For low-level and intermediate level waste, different waste containers are planned, Figure 1.8b. Barrels placed in concrete containers are not considered to be an engineered barrier, which is in contrast to the waste canister concept for spent fuel & high-level waste. The geometry of the waste container, the shielding from radiation and handling aspects are requirements already given from interim storage and transport needs. For example, a maximum weight per container will be set. The overall goal is to achieve the most uniform waste container distribution with the most efficient use of the space available. It has been concluded that concrete containers meet the aforementioned requirements best because the usage of concrete allows variable dimensions, although a maximum of unification is targeted, Figure 1.7a (Nagra, 2014a, 2014b). A cement mortar back-fill is proposed due to its ability to immobilize radionuclides by sorption. Due to the high pH of cement, steel corrosion is reduced and thus lowers the H_2 gas evolution rate from anaerobic steel corrosion as long as the pH remains elevated. In this concept, the host rock Opalinus Clay is the main barrier because the barrels and concrete container have expected lifetimes of about 100 years (O. Leupin et al., 2016). Opalinus Clay is a very good hydraulic barrier (exclusion of groundwater flow) and offers good retention (radionuclide sorption capacity) and self-healing properties (closure of fractures) (Jaeggi et al., 2017). It is expected that corrosive processes are delayed because of the elevated pH-values in the evolving porewater of a cementitious backfill, however, anoxic corrosion and the degradation of organic waste will inevitably lead to increased gas evolution. The porous cementitious back-fill is designed to conduct the evolved gases from the storage cavern to outside the cavern, towards the backfilled service tunnels and operational tunnels.

Waste degradation leading to gas evolution

The metals used for tunnel support, the waste containers, and the metals and metal oxides in the waste itself, will ultimately corrode and lead to the evolution of hydrogen because of the absence of oxygen and presence of saline water. Additionally, carbon dioxide, methane, and other gases are expected from the degardation of higher molecular organic waste. These gaseous products will be consumed by chemical reactions and microbial activity. However, a discrete gas phase will be formed when the gas evolution rate is high and the production of gases exceeds the consumption of dissolved gases. The gas phase is expected to accumulate until the pressure is high enough to escape through engineered gas transport systems (EGTS) and the excavation disturbed zone (EDZ) into the host rock (O. Leupin et al., 2016). The base scenario predicts that 96% of the Swiss radioactive waste (valid for both mass and volume) will be disposed in the low- and intermediate-level waste repository, leaving 3% of spent fuel and high-level waste and 1% of long-lived intermediate-level waste for a high-level waste repository. Low- and intermediate-level waste and long-lived intermediate-level waste can be subjected to methods to reduce the waste volume such as burning, melting and pyrolysis (Nagra, 2014b). According to calculations (Diomidis et al., 2016), the total gas produced at standard atmospheric pressure and temperature for the waste in the low- and intermediate-level waste repository will be composed of:

- $2.59 \cdot 10^7$ m ^{3} hydrogen (H_2) (≈ 87.3% of total gas)
- $2.18 \cdot 10^6$ m^3 methane (CH_4) (≈7.3%)
- $1.38 \cdot 10^6$ m ^{3} carbon dioxide (CO_2) (≈4.6%)
- $1.06 \cdot 10^5$ m ^{3} ammonia (NH_3) (≈0.4%)
- $9.30 \cdot 10^4$ m^3 hydrogen sulfide (H_2S) (≈0.4%)

A visualization of the amounts on a log scale can be seen in Figure 1.9, for comparison the volume of evolving H_2 within the low- and intermediate-level repository, $2.59 \cdot 10^7 m^3$ H_2 ≈ 0.96 × volume of concrete used in the construction of the Three Gorges Dam (≈ $2.72 \times 10^7 m^3$) (WolframAlpha, 2020b).

Context to Chapter 4 Given the high amount of H_2 expected to evolve, the structural integrity of the host rock may be compromised at the same time as the radionuclides are released for the waste containers due to corrosion. The potential creation of fractures due to a change in the stress regime mediated by a gas phase displacing the porewater, represents a concern. Within Chapter 4 of this thesis, we study the feasibility of a microbial gas sink placed at a safe distance from the storage caverns of a low- and intermediate-level repository. The work was performed using a well-characterized 80/20% w/w mixture of quartz-Wyoming bentonite as the porous matrix for the formation of a hydrogen-oxidizing biofilm. Previously, the 80/20%

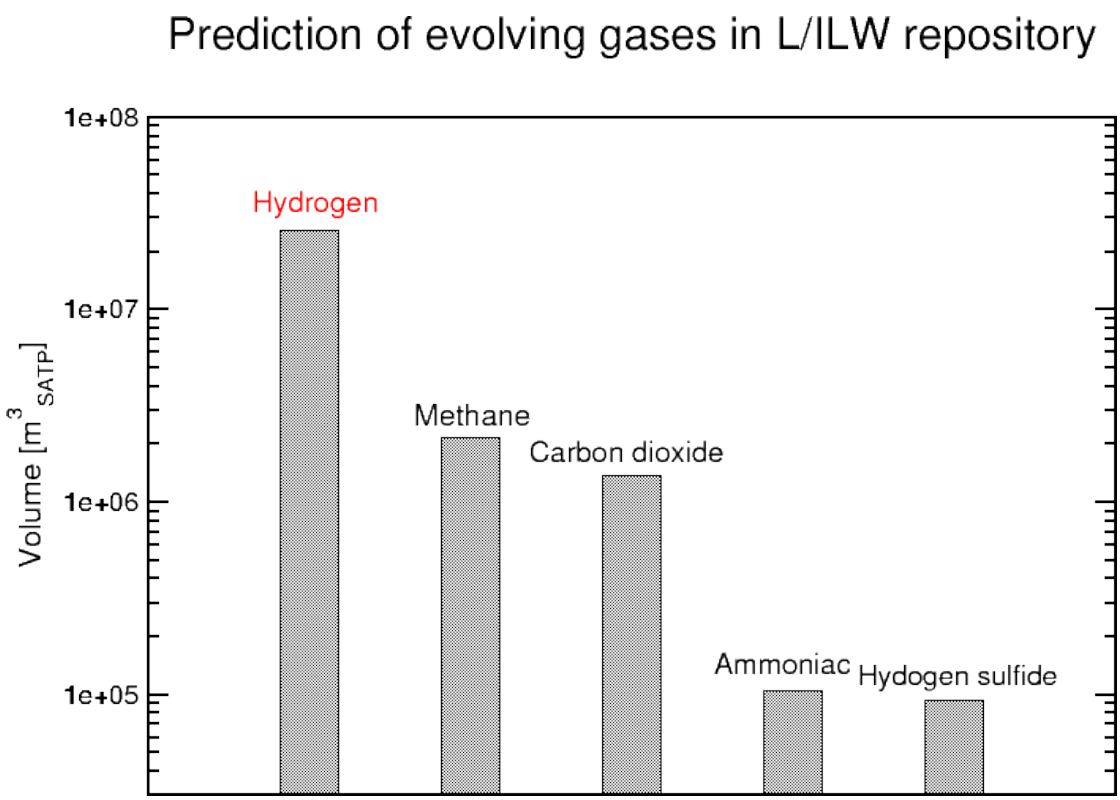

Figure 1.9 – Gas evolution prediction for low- and intermediate-level waste repositories in the Swiss concept. Most of the evolving gas will be hydrogen, followed by methane and carbon dioxide. Modified from (Diomidis et al., 2016)

w/w quartz-Wyoming bentonite mixture was studied as plug-material of the storage caverns and as access tunnel backfill (Manca, 2015). The biofilm forms naturally in the presence of excess hydrogen, and oxidizes hydrogen coupled to sulfate reduction, with sulfate provided by Opalinus Clay porewater. In addition, the consumption of hydrogen via methanogenesis, leading to a net-decrease of the gas-pressure, is also observed.

1.4 Conclusion and thesis goals

The design of a structure capable of enclosing radioactive waste until its radioactivity has decayed to harmless levels is a challenging engineering task for several reasons: (1) Due to the long time frame (100,000 - 1,000,000 years) needed for radionuclide decay, many possible events need to be considered, i.e., any current design is inherently afflicted with large uncertainty. Therefore, models predicting the behavior of the repository need to be characterized thoroughly. (2) The preferred host rock formation is subject to natural changes over time; microbial activity plays an important role and is likely to be accelerated and broadened because of the construction of the repository and the introduction of exogenous microorganisms. (3) The repository near-field is governed by the interplay of the hostrock geochemistry,

the chemical characteristics of the engineered barrier systems, the physical and chemical characteristics of the diversity of waste matrices, and by the biosphere (microorganisms). The combined effects of these are not understood in full detail. (4) Repositories are subject of important concern by inhabitants of the chosen areas and therefore, it is also a major sociological and ethical issue. This thesis addresses knowledge gaps (2) and (3) concerning the microbial influence on the geochemical evolution of the host rock. It contributes to the understanding of the near-field evolution of the repository by investigating the microbial influence under repository relevant *in-situ* conditions. In more detail, the relevant knowledge gaps that are addressed are: (a) consideration of the potential beneficial effect of microbial activity on the long term safety of deep geological repositories; (b) constraining uncertainty about the biogeochemical influence of the present microbiota on the long term evolution of the repository. Previous studies have pointed to sulfate reduction as the most probable metabolism in a deep geological repository within Opalinus Clay rock formations (Bagnoud, 2015; O. X. Leupin et al., 2017), but these studies could not decipher the consumption rates of hydrogen and sulfate in biofilms under repository relevant *in-situ* conditions. That is of importance as many gaseous waste degradation products are expected and biofilms within porous backfill materials have not been investigated thus far. To reliably model the long-term biogeochemical evolution repository-wide, more knowledge about relevant consumption rates are required for hydrogen and sulfate, with sulfate being the major limiting factor in hydrogen consumption (O. Leupin et al., 2016). Until this work, methanogenesis had not been observed in a repository-relevant setting in Opalinus Clay rock, but is now expected once the accessible sulfate pool is depleted.

The engineered barrier system for the spent fuel and high-level waste storage tunnel backfill, compacted and pelletized bentonite, is expected to prevent microbial activity. However, the material is marked with high heterogeneity which may allow microorganisms to thrive in close vicinity of the storage canisters, potentially leading to microbial induced/enhanced corrosion. Thus, *in-situ* corrosion rates of carbon steel under repository relevant conditions remain to be determined to consolidate the modelled and required canister lifetimes.

2 Growth and persistence of an aerobic community in Wyoming bentonite MX-80 despite anoxic *in-situ* conditions

Niels Burzan

Environmental Microbiology Laboratory (EML), Ecole Polytechnique Fédérale de Lausanne (EFPL), Switzerland

Experimental work mainly performed by the student with help during sampling by Manon Frutschi. Cultivation work was partially performed by Roberta Murad Lima in connection with a Master thesis, co-supervised by the student. BET analysis were performed by Lionel Sofia, IC and ICP-MS analysis of water samples were performed by Karine Vernez Thomas and Sylvain Coudret, EPFL, Lausanne, Switzerland. 16S rRNA gene-library sequencing was performed by the team of the Lausanne Genomics Technologies Facility (University of Lausanne, Switzerland). The content of this chapter is under manuscript preparation for submission to Environmental Science and Technology with contributions by the following co-authors in addition to the student: Rizlan Bernier-Latmani, Roberta Murad Lima, Nikitas Diomidis, Manon Frutschi, Andrew Janowczk.

Abstract

Microbial activity may enhance the corrosion of high-level radioactive waste canisters, which, in the Swiss case, will be embedded in bentonite and placed in Opalinus Clay host rock. Thus, it is important to investigate potential microbial contributions to the corrosion under *in-situ* conditions. Twelve bentonite-bearing modules were deployed into a borehole in Opalinus Clay rock for up to 5.5 years. Individual modules were retrieved after 1, 1.5, 2.5 and 5.5 years. Enumeration of aerobic and anaerobic heterotrophs and sulfate-reducing bacteria (SRB) revealed an initial growth of microorganisms followed by a decline of microbial viability after

5.5 years. Lower microbial viability was observed for higher bentonite dry densities. Aerobic heterotrophs are shown to thrive and persist in bentonite, supported by detectable amounts of oxygen trapped within bentonite whereas SRB stay inactive but viable. DNA extraction at 1, 2.5 and 5.5 years confirmed the presence of aerobes and relative low contributions of anaerobes to the bentonite microbiome. The interface between bentonite and anoxic borehole harbors a community influenced by the borehole, composed of SRB and the Pseudomonadaceae family. Bentonite dry-density, *in-situ* exposure time and a gradient of bioavailable trapped oxygen are observed to shape the bentonite microbial community.

2.1 Introduction

The safe storage of radioactive waste produced from nuclear power plants is an important environmental challenge faced by societies utilizing electricity from nuclear fission. Deep geological repositories are envisioned by many countries as the most promising path for a safe long-term disposal (Ewing et al., 2016). The discovery of the natural nuclear reactor Oklo and its subsequent characterization confirm the suitability of geological disposal (Gauthier-Lafaye, 1986, 2002).

Nagra (National Cooperative for the Disposal of Radioactive Waste, Switzerland) is considering Opalinus Clay rock formations as the host rock for high-level waste and spent fuel. Carbon steel is considered for the canister material, and the current design plans a gallery back-fill with Wyoming bentonite at a dry density of 1.45 g/cm^3 around the canisters. In this concept (Nagra, 2009), the cylindrical canister will rest on a base of compacted bentonite blocks at a dry density of 1.55 g/cm^3.

This study builds on an *in-situ* experiment of the corrosion of carbon steel embedded in Wyoming bentonite and deployed in Opalinus clay rock (Smart et al., 2017). An initial time point included limited microbial investigations (Smart et al., 2017). Here, we report on three additional time-points (1 year, 2.5- [in the Chapter Appendix] and 5.5-years) and the DNA-based characterization of the microbial community. Bentonite buffers, due to their significant swelling potential when in contact with water, are expected to create conditions unsuitable for microbial growth, such as a low water content, small pore space and a nutrient availability restricted by diffusion processes (Pedersen et al., 2000; Rättö & Itävaara, 2012; Stroes-Gascoyne et al., 2010).

Three dry-densities of bentonite were employed in this study. The goal was to provide *in-situ* corrosion rates (not part of this thesis) and information about the viability and persistence of microorganisms in bentonite. Of particular interest are sulfate-reducing bacteria, whose activity has been shown to lead to microbially-induced corrosion of carbon steel (Černoušek et al., 2020). It is expected that a considerable number of bacterial cells will remain viable despite the harsh conditions after repository closure despite increased pressure, heat and irradiation (Haynes et al., 2018). Recently, an *in-situ* study (Engel, Ford, et al., 2019), featuring identical test modules but deployed within a granite host rock environment, reported a persistent

microbial community organized along a spatial gradient between the surrounding anoxic rock porewater and the bentonite in the test modules. The borehole water was dominated by sulfate-reducing bacteria belonging to *Desulfosporosinus* and *Desulfovibrio*. The surface of the module was reported to be dominated by *Pseudomonas stutzeri*, while the bentonite itself was dominated by *Streptomyces* sp. and *Xanthomonas* sp. The interpretation was that there was little growth of these organisms and that they may represent remnant (extracellular) DNA adsorbed to clay particles in bentonite. The authors suggested further studies should include cultivation and activity assays to confirm the viability of microorganisms within deployed bentonite cylinders.

Here, employing classical cultivation techniques, known to capture only a fraction of the viable microbiome, we were able to establish confidence in a bentonite-microenvironment dominated by aerobic heterotrophic microorganisms, with a closer relation to the bentonite community before deployment than to the surround anoxic borehole community. Thus, we demonstrate the presence of a viable aerobic community in bentonite deployed in an anoxic environment, showing both growth and persistence over all tested timeframes and bentonite dry-densities.

2.2 Materials & Methods

2.2.1 Experimental design

Experimental modules were designed as a stainless steel cylinder (25 cm high and 12.6 cm of outer diameter) in which test coupons[I] of carbon steel and copper are embedded in Wyoming bentonite of three different dry-densities, either as a MX-80 power/pellet mix or as pre-compacted blocks, Figure 2.1 and Figure 2.2. The modules were submerged into a porewater-filled borehole (BIC-A) within the Opalinus Clay rock at the Mont Terri URL in St-Ursanne, Switzerland. This low-temperature (14°C), anoxic and saline environment is expected to resemble the long-term conditions of a repository built into Opalinus Clay rock. The microbial community of the porewater at the beginning of the experiment was previously analyzed by (Bagnoud, de Bruijn, et al., 2016). The stainless-steel modules are designed to allow the free exchange of water with the borehole water and remained in the borehole for approximately 1-, 1.5-, 2.5- and 5.5-years, Figure 2.3 shows the experimental timeline. The 1.5-year results were previously published (Smart et al., 2017). Additionally, changes in experimental details of the preparation of the modules deployed for 2.5- years precluded direct comparison with other years. The elimination of that time point led to the selection of the 1-year, 1.5-year (Smart et al., 2017). and 5.5-year modules to conduct a comparison of enumerated viable heterotrophic aerobes and anaerobes and sulfate-reducing bacteria. Cultivation-independent 16S rRNA gene V4-region microbiome profiling was performed and is presented for the 1-year and 5.5-year modules.

[I] carbon steel (20 mm of diameter, thickness of 10 mm) and copper coupons (20 mm of diameter, thickness of 3 mm)

2.2.2 Experimental setup

At the onset of the experiment (Jan. 2013), a set of 12 modules was deployed in the borehole (modules 1 – 12), Figure 2.3. After ~1.5 years (Sept. 2014), 3 modules (1-3) were removed and the results of the corrosion and microbial cultivation published (Smart et al., 2017). The 3 modules removed at ~1.5 years were replaced with a second set of modules (modules 13-15) and exposed for ~2.5 years (from Sept. 2014 to July 2017). However, it is important to note that, for modules 13-15, the deployment started around 1.5 years into the overall experiment, not at the same time as the modules removed at ~1.5 years (modules 1-3). After removal of that second set (modules 13-15), a third set of modules (16-18) was deployed for 1 year (from July 2017 to July 2018). Again, their exposure began not at the onset of the experiment but rather around 4 years into the overall experiment. In July 2018, that third set of modules (16-18), deployed for 1 year, and a subset of the first set of modules (4-6), deployed for ~5.5 years (Jan 2013 to July 2018), were removed for analysis.

Figure 2.1 – Stainless steel experimental module of the IC-A experiment. Cylinder of 25 cm high and 12.6 cm of outer diameter, top lid and two rows of five water exchange holes are shown.

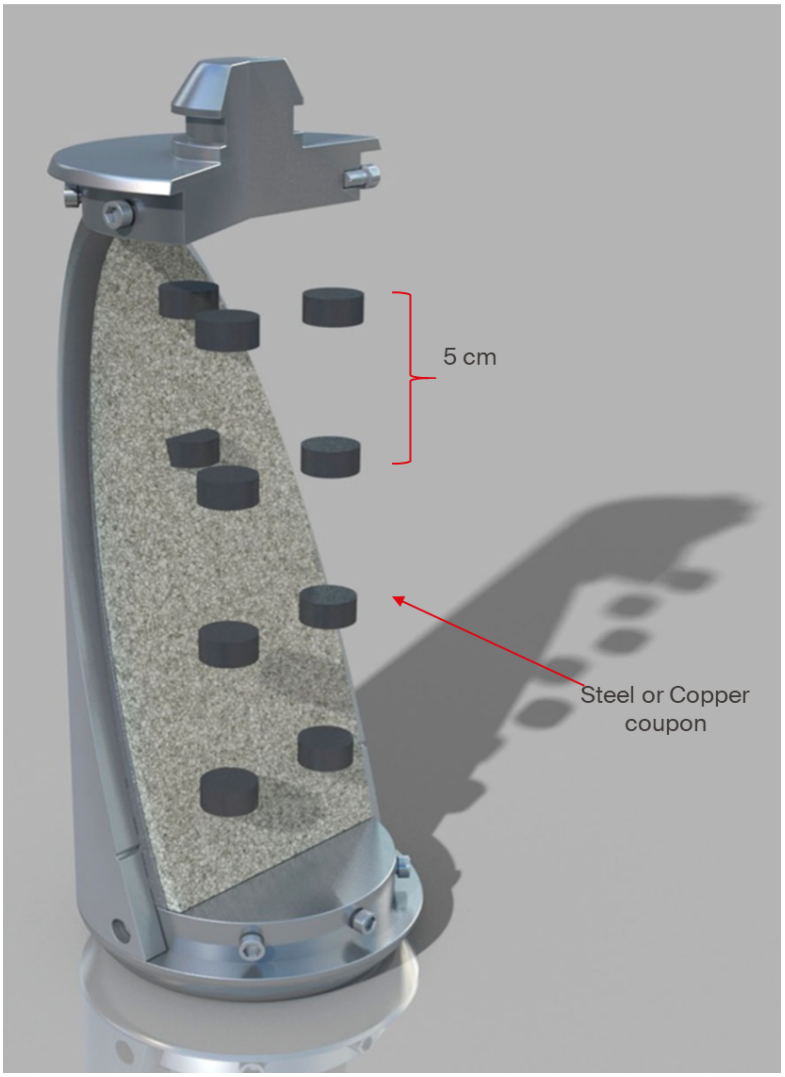

Figure 2.2 – Stainless steel experimental module of the IC-A experiment, filled with bentonite and embedded corrosion test coupons. Figure modified from (Smart et al., 2017).

2.2.3 Bentonite preparation

Corrosion coupons and preparation of modules filled with bentonite was carried out by the commercial laboratories of Jacobs Engineering Group Inc, located in Harwell, Oxfordshire, United Kingdom, in the same way as previously described (Smart et al., 2017). Bentonite was sourced from Wyoming, United States of America, and purchased as Volclay® MX-80 from Minerals Technologies, New York, U.S.A., and used to set up all modules. Compaction into pre-formed blocks of 100 mm diameter of bentonite, maintaining space for the incorporation of the corrosion coupons, was performed by Clay Technology AB, Lund, Sweden, and the following dry-densities were produced: 1.25, 1.45 or 1.55 g/cm^3. The compaction mold was flushed with nitrogen to prevent the trapping of excess air and the compaction of the bentonite was carried out while under vacuum at increased moisture. These measures were taken in

order to minimize residual oxygen in the compacted bentonite. Bentonite blocks were sealed in Mylar bags within a nitrogen atmosphere and transported to Jacobs Engineering Group Inc in Harwell, Oxfordshire, United Kingdom. Upon arrival, the bentonite blocks were stored in an argon gas filled glovebox until further processing. The assembly of the modules with blocks and corrosion coupons was performed in a controlled argon atmosphere. The second formulation, a mix of pellets and powders of Wyoming bentonite, were provided at a dry density of 1.45 g/cm and stored under oxic conditions until assembly.

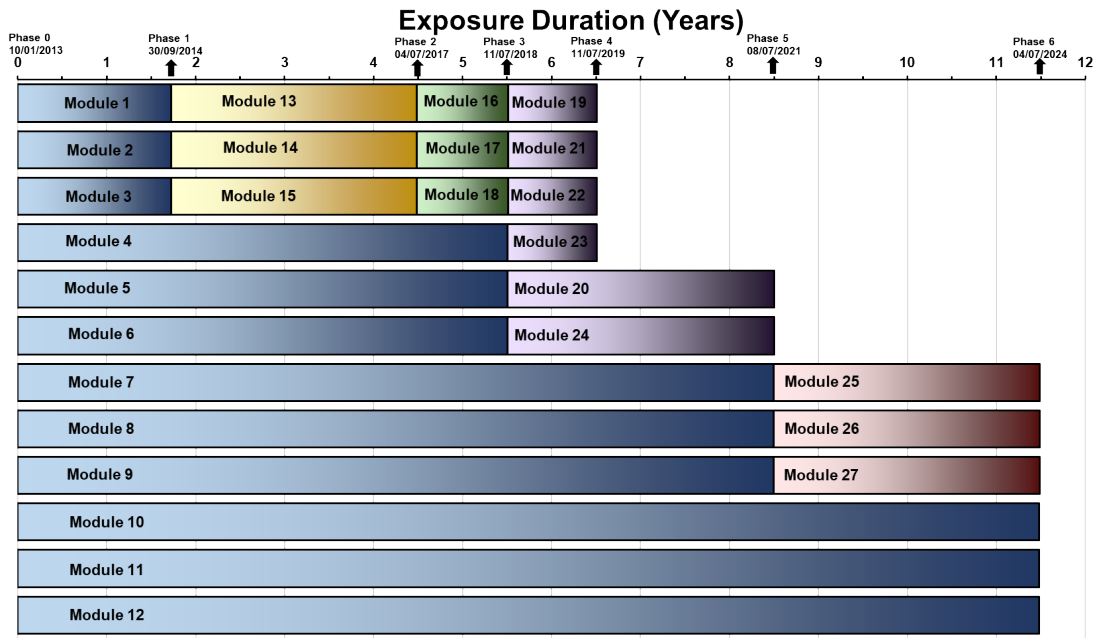

Figure 2.3 – Schematic of the deployment and retrieval schedule for the modules. In this study, we discuss modules 1-6, 13-15, and 16-18. Cultivation-based enumeration of microorganisms was performed for all modules, DNA extraction and analysis were performed for all modules retrieved except modules 1-3.

2.2.4 Assembly of corrosion test modules

A sintered stainless-steel filter (outer diameter of 106 mm with a wall thickness of 3 mm, porosity of 30% with average pore size of 18 µm) was inserted as a support for bentonite and to prevent its leakage through the water-exchange holes of the module. Prior to assembly, all parts were cleaned with acetone and deionized water. All bentonite block-bearing modules were assembled in the absence of oxygen, within an argon-filled glovebox. However, for bentonite pellet and powder-bearing modules, varying protocols were utilized for module assembly, depending on the batch. For the first set of modules (specifically modules M1, M4 and M10), bentonite pellet and powder-bearing modules were assembled in an air atmosphere. For each module, four layers of 3 coupons were positioned within the bentonite, see Figure 2.2 and (Smart et al., 2017), for details. The coupons were 5 mm away from the outer circumference of

the bentonite and positioned at 120°angles. After assembly, all modules were pre-saturated with non-sterile, anoxic artificial Opalinus Clay porewater for two days (bentonite blocks) or ten days (bentonite powder-pellet) within an argon-filled glovebox. Because the first set of bentonite pellet and powder-bearing modules were assembled outside the glovebox, they were transferred into the glovebox for pre-saturation, with four cycles of vacuum and argon flushing applied to the assembled modules prior to being placed into the pre-saturation solution. The prepared and pre-saturated modules were packed in three layers of Mylar™ to exclude oxygen exposure during shipping to the URL 'Mont Terri'.

Starting with the second set of modules, M13, M14 and M15, all modules were assembled within the glovebox. For this, the bentonite pellet-powder mix was weighed in oxic conditions, transferred to the glovebox with four cycles of vacuum and argon flushing and left to equilibrate for 3 to 5 days within the glovebox prior to module assembly. The two modules M14 and M15, which contained bentonite blocks were stored for 18 months within the argon-gas filled glovebox. Pre-saturation and packing of the module were carried out as described for the first set of modules.

Assembly of the third set of modules, M16, M17 and M18, was more similar to the first set of modules: Bentonite blocks were produced by Clay Technology AB immediately before module assembly within the glovebox, i.e., no interim storage of blocks in anoxic conditions. However, the bentonite pellet-powder mix modules were prepared in the same manner as the second set of modules: bentonite was weighed in air and placed within the glovebox for 3-5 days. Pre-saturation and packing of the modules were performed in the same way as for previous sets of modules.

2.2.5 *In-situ* exposure

The modules were deployed in a 15 m deep borehole in Opalinus Clay rock at the URL 'Mont Terri', St Ursanne, Switzerland. The borehole was drilled in March 2012, flushed with argon gas four times and sealed with a hydraulic packer. Additional argon gas was supplied until an overpressure of 3.5 bars was achieved (to maintain anoxic conditions). It was estimated that Opalinus Clay porewater filled the borehole at a rate of 44 mL per day. The first set of 12 modules was deployed on January 10th 2013 and the natural porewater accumulated since drilling was sampled and analyzed (Bagnoud, de Bruijn, et al., 2016). Additional 9 L of nonsterile anoxic artificial porewater was added in order to submerge all 12 modules completely.

2.2.6 Removal of test modules

The first set of three test modules (Modules 1-3) was removed for analysis on 30 September 2014 after 20 (~1.5 y) months of exposure. The second set of three modules (Modules 13-15) was removed for analysis on 4 July 2017 (after 33 months (~2.5 y). The third set of six

modules (Modules 16-18 and Modules 4-6) was removed in July 2018 after respectively 12 and 66 months (1 y and ~5.5 y) of exposure, Figure 2.3. During removal, porewater samples were obtained from the borehole for microbial community and chemical analysis. The modules were removed from the borehole while purging with 0.2µm-filtered argon gas and put into custom-built stainless-steel transfer flasks that were filled with water from the borehole and purged with argon before transport to the U.K. for analysis. In the U.K., the modules were placed into a pre-cleaned and sterilized (wiped with a 70% isopropyl alcohol solution) argon-purged glove box for dismantling.

2.2.7 Porewater analysis

Upon opening the borehole to retrieve the modules, the borehole porewater was sampled. A sterile 1-liter glass bottle was attached to an eight-meter long aluminum rod (70% ethanol disinfected) and lowered into the borehole several times to obtain enough porewater for the following analyses. On-site, a Hach multimeter, HQ30D (Hach, Loveland, Colorado, U.S.A.) was used, equipped with electrodes MTC101 and PHC201 to measure pH and redox potential (Eh). Porewater was syringe-filtered through sterile 0.2 µm membranes and samples were obtained for subsequent chemical analysis of sulfide, iron(II) and iron (III), using a UV-2501PC spectrophotometer (Shimadzu, Kyoto, Japan). Sulfide was analyzed using the Cline method (Cline, 1969) and iron(II) using the ferrozine assay (Stookey, 1970). Major anions and cations were detected and quantified by ion chromatography: An IonPac® CS12A-5µm cation-exchange column (Thermo Fisher Scientific Inc., Waltham, Massachusetts, U.S.A.) and eluent 20 mM methanesulfonic acid were used for major cations, whereas an IonPac® AS18-4µm anion-exchange column (Thermo Fisher Scientific Inc., Waltham, Massachusetts U.S.A.) with a gradient eluent KOH (from 0.0 to 30mM) was used for major anions. Trace metals Co, Cu, Sr, Ni, Mn, Cr, Zn and Al were measured using inductively coupled plasma mass spectrometry (ICP-MS), Agilent 8900 Triple Quadrupole (Agilent Technologies Inc., Santa Clara, California, U.S.A.), whereas all samples for trace elemental analysis were prepared in dilutions with 0.1 M HNO_3 (final concentration, ultra-pure grade, MilliporeSigma, Burlington, Massachusetts, U.S.A.).

The sampled porewater was filtered on site for DNA analysis, using a sterile filtration device equipped with 0.2 µm polycarbonate membranes (MilliporeSigma, Burlington, Massachusetts, U.S.A.). For the first timepoint (removal in September 2014) the following method was used (Bagnoud, de Bruijn, et al., 2016; Smart et al., 2017):

"Four filtrations of 250 mL each were performed. DNA was extracted from filtered water samples using a slightly modified protocol from the DNA Spin kit for Soil (MP Biomedicals LLC, Irvine, California, U.S.A.) and then purified using the Genomic DNA Clean & Concentrator purification kit (Zymo Research Corp., Irvine, California, U.S.A.). The total amount of DNA extracted was 19.5 ng and the final suspension had a concentration of 0.195 ng/µL." ((Smart et al., 2017))

Subsequent porewater samples were processed similarly but with the following differences: Three filtrations of 200 mL each were performed and the DNA was extracted using a phenol/chloroform approach as reported by (Bagnoud, Chourey, et al., 2016). However, the polycarbonate filter was not removed prior to the phenol treatment, because polycarbonate is soluble in phenol, thus a potentially higher DNA yield could be achieved. All used reagents for the DNA extraction are of molecular biology grade and care was taken to not introduce any contaminant DNA. Low amounts of recovered DNA can be attributed to two effects: a) the low biomass as starting point and b) the presence of Opalinus Clay particles that scavenge DNA (Engel, Coyotzi, Vachon, et al., 2019).

(a)

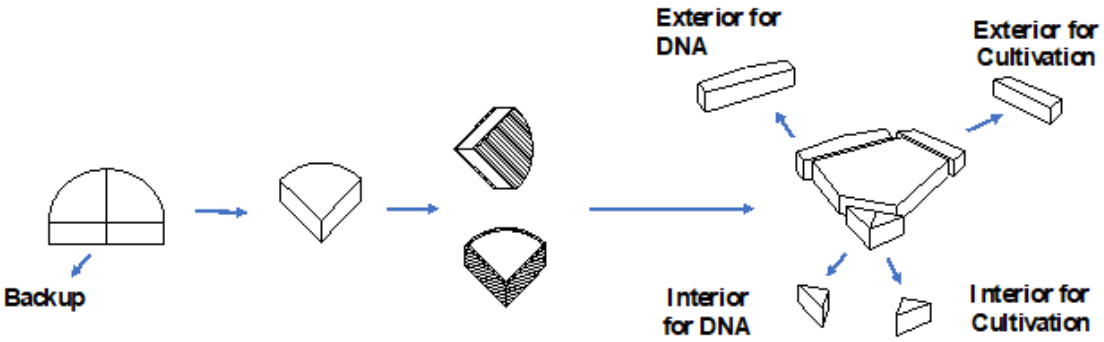

(b)

Figure 2.4 – Bentonite core sampling. a) Slicing of a retrieved core into 6 slices; slices 1 to 5 are used for microbial investigations whereas the sixth slice is used for the determination of the bentonite dry density. b) Subsampling of the bentonite half-cylinder slices within a disinfected glovebox: (from left to right) a quarter is left as backup, the other one is cut with sterile scalpel blades to remove potentially contaminated areas. The remaining slice was cut into 4 subsamples, representing an interior and an exterior part of the bentonite core, for each a sample for cultivation (enumeration of microorganisms) and a subsample for DNA extraction. Figures from M. Frutschi with permission.

2.2.8 Enumeration of bentonite microorganisms and amplicon sequencing

Bentonite samples were obtained within an anoxic atmosphere and kept at 4°C for enumeration and -20°C for gDNA extraction. Details of the bentonite cylinder sampling procedure are shown in Figure 2.4. The retrieved bentonite core was cut and sampled with disinfected knives and spatulas (70% ethanol) packed in sterile sampling bags, then packed in two layers of Mylar^{TM} bags with an argon gas atmosphere and kept at 4°C (enumeration). To see any variation in the distribution of microbial activity in the bentonite and around the corrosion coupons, samples were taken at various locations (interior and exterior parts of the bentonite core). The samples were transferred to the laboratories of EPFL, Lausanne, Switzerland, and stored at 4°C until analysis. The samples were cut into smaller pieces, using disinfected knives within a disinfected, nitrogen-filled glovebox, with the aim to remove potentially contaminated areas at the surface of the bentonite core.

Bentonite microbial analyses

The following procedure is based on the work instruction of the Atomic Energy of Canada Limited (AECL) / Énergie atomique du Canada limitée (EACL), Chalk River, Ontario, Canada, for the 'Analysis of rock, soil and clay for microbes' (Hamon, 2006): A representative sample is weighted (wet weight) and chopped into small pieces which were placed in a volume of sterile, anoxic phosphate-buffered saline solution (1xPBS, volume depended on mass of bentonite such that a ten-fold dilution per mass is reached) to release microbial cells by shaking at 300 rpm for 60 minutes on a horizontal shaker plate within a sealed, anoxic, sterile serum bottle (mounted horizontally). A sample for cultivation was obtained from the middle of the suspension after one minute of sedimentation. The obtained suspension was then diluted in anoxic, sterile 1xPBS in 10-fold dilution steps up to a final dilution of 10^{-6} of the initial weight and used as an inoculum for the enumeration of microbial cells. Each dilution was plated in triplicates once for the enumeration of aerobic heterotrophic microorganisms and for anaerobic heterotrophic microorganisms using the following procedure: 1 ml of the dilution was pipetted into a sterile culture dish and 12-15 mL semi-solid R2A medium (Reasoner & Geldreich, 1985), cooled down to 45-50°C, was added. The composition of the R2A medium is summarized in Table 2.1. The liquids were mixed by carefully swirling in all possible directions without spilling. After about 10 minutes, the R2A medium was solid and the triplicate plates were grouped together, inverted and the plates designated for the enumeration of anaerobic microorganisms transferred into an anaerobic jar to be transported to a heated glovebox (30°C) and were incubated for three weeks. Plates designated for aerobic microorganisms were transferred to an incubation room (30°C) and allowed to grow for three days. Enumeration of sulfate-reducing bacteria (SRB) was performed with the most probable number (MPN) method, as described by (Hamon, 2003). Hungate tubes were filled with 9 mL of sterile, anoxic Postgate's Medium B as described by DSMZ (of Microorganisms and Cell Cultures, 2018), Table 2.2 and serial dilutions from 10^{-1} to 10^{-5} were made (in triplicates), using the same inoculum as for heterotrophic (an-)aerobes. The tubes were sealed to maintain anoxic

conditions during seven weeks of incubation at 30°C. The MPN method used is described by (Hamon, 2003) and the MPN table used is published by the U.S. Food and Drug Administration in the Bacteriological Analytical Manual (Nutrition, 2019)).

Table 2.1 – R2A medium for anaerobic and aerobic heterotrophs (Reasoner & Geldreich, 1985). A total volume of 3.6 liters was aliquoted in 500 mL bottles, pH=7.2±0.1, and the anoxic medium flushed with sterile filtered nitrogen for 20 min.

Mass [g]	Substance
1.80	Yeast-Extract
1.80	Bacto-peptone
1.80	Vitamin Assay Casamino Acids
1.80	Glucose (D-glucose)
1.80	Soluble starch
1.08	K_2HPO_4
1.08	$MgSO_4 \cdot 7H_2O$
0.18	Na-pyruvate
6.00 per 500 mL aliquot	Agar

Table 2.2 – Postgate's Medium B for sulfate-reducing bacteria, composition according to (of Microorganisms and Cell Cultures, 2018). Total volume of 2 liters, pH=7-7.5

Mass [g]	Substance
7.0	Na-lactate
4.0	$MgSO_4 \cdot 7H_2O$
2.0	NH_4Cl
2.0	$CaSO_4$
2.0	Yeast Extract
1.0	KH_2PO_4
1.0	$FeSO_4 \cdot 7H_2O$
0.2	Ascorbic acid
0.2 (add as 20 mL solution)	Thioglycolic acid
0.0008 (or 7mL of 0.025% solution)	Resazurin

DNA extraction from bentonite modules

gDNA extraction from bentonite and forensic swab samples (Sarstedt AG & Co KG, Nümbrecht, Germany) was performed according to recommendation by (Engel et al., 2018; Engel, Coyotzi, Vachon, et al., 2019; Engel, Ford, et al., 2019) utilizing a modified protocol of the DNeasy PowerSoil Kit and DNeasy PowerMax Soil Kit (QIAGEN NV, Venlo, The Netherlands).

DNA extraction from bulk bentonite samples

Representative samples of the interior and the exterior of the bentonite core, adjacent to the samples obtained for the enumeration were used for DNA extraction using the DNeasy® PowerMax® Soil Kit (QIAGEN NV, Venlo, The Netherlands) with a slightly modified protocol:

samples of 2 ± 0.1 grams of bentonite were vortexed for 1 minute in 15ml PowerBead® solution, containing beads. 1.2 mL of Solution C1 was added and the samples were again vortexed for 30 seconds. After 30 minutes incubation at 65°C, the samples were homogenized for 10 minutes at 30 Hz using a Mixer Mill MM 400 (Retsch GmbH, Haan, Germany). The following steps of the DNA extraction were carried out as suggested by QIAGEN. The extracted DNA was eluted in 2.1 mL of solution C6. The obtained DNA was further purified and concentrated using an isopropanol-ethanol precipitation method: 4µL/mL co-precipitant linear polyacrylamide GenElute® (molecular biology grade, MilliporeSigma, Burlington, Massachusetts, U.S.A.) was added to the eluted DNA, along with 0.1 volumes of 5 M NaCl (molecular biology grade, Merck KGaA, Darmstadt, Germany) and 1 volume of isopropanol (molecular biology grade, MilliporeSigma, Burlington, Massachusetts, U.S.A.) and gently mixed, left overnight at -20°C to incubate. The precipitation was performed by 30 minutes centrifugation at 13'000 g at 4°C using an Avanti® J-26 XP centrifuge (Beckman Coulter Inc., Brea, California, U.S.A.). The obtained DNA-polyacrylamide pellet was washed with sterile, -20°C cold ethanol, 80 vol.%. This ethanol solution was prepared by mixing autoclaved MilliQ water (80-minutes, 121°C) and molecular biology grade ethanol (Merck KGaA, Darmstadt, Germany). The DNA and ethanol solution was centrifuged for another 30 minutes at 13'000 g at 4°C. Within a sterile laminar flow hood, the washed DNA pellet was air-dried for 10-20 minutes before elution in 125 µL of elution buffer (solution C6). After one-hour incubation at 4°C, the eluted DNA was briefly centrifuged and transferred to 2 mL Soreson™ Dolphin tubes for storage at -20°C until DNA analysis.

DNA extraction from coupon bentonite samples

DNA from coupon imprints were extracted in the same way with the only difference being that only bentonite close to the metal coupons was collected by scraping off a sample using new, sterile scalpel blades for each sample, within a sterile laminar flow box, thus the amount of bentonite varied between 0.1 and 1.9 grams of bentonite.

DNA extraction from module and bentonite swab samples

DNA from forensic swabs (Sarstedt AG & Co KG, Nümbrecht, Germany) and bentonite cuts were also extracted following the recommendations by (Engel et al., 2018; Engel, Coyotzi, Vachon, et al., 2019): A slightly modified protocol of the DNeasy® PowerSoil® Kit (OIAGEN NV, Venlo, The Netherlands) was used: Within a sterile laminar flow hood the tips of swabs were cut with flame-sterilized scissors into PowerBead® tubes and briefly vortexed. Cuts of bentonite point-of-interests were added similarly within the laminar flow hood and the mass was recorded, varying between 0.003 and 0.182 grams. After addition of solution C1, the samples were briefly vortexed and incubated for 10 minutes at 70°C. Homogenization was carried out with a Precellys 24 homogenizer (Bertin Technologies SAS, Montigny-le-Bretonneux, France), for 45 seconds at 6'000 rpm. The following steps are carried out as indicated in the kit manual, except for the elution of the extracted DNA: 65 µL of elution buffer

C6 were applied to the center of the DNA binding membrane of a MB Spin Column. After a centrifugation step, 1 min at 8'000 g, the DNA was collected in a 2mL Soreson™ Dolphin tube and stored at -20°C until DNA analysis.

gDNA quantification

All DNA was quantified using the Qubit® ds-DNA HS Assay Kit (Thermo Fisher Scientific Inc., Waltham, Massachusetts, U.S.A.) according to the manufacturer's protocol. The fluorescence signal was measured with a Qubit® 2.0 Fluorometer (Thermo Fisher Scientific Inc., Waltham, Massachusetts, U.S.A.).

DNA amplification from borehole porewater

Borehole porewater was sampled for chemical analsyes, Table 2.5, and DNA microbiome profiling, Tables 2.3 and 2.4. 16S rRNA V4 region gene amplicons were generated used the PCR reaction mix KOD Hot Start (Merck KGaA, Darmstadt, Germany), Table 2.3, which contains the following: a 1x concentration of a proprietary Buffer for KOD Hot Start DNA polymerase, 1.5 mM MgSO4, 0.2 mM of each dNTP's, 0.3 µM of each 515F-MiSeq and Pro806bR-MiSeq primers and 0.02 U/µL KOD Hot Start polymerase and 10µL of a DNA template to amplify the V4 region of the 16S rRNA gene from DNA extracted from the borehole porewater. Below, the primer sequences are shown in bold along with the overhang sequence for Illumina MiSeq (not in bold):

515F-MiSeq (Parada et al., 2016)

5'-TCG TCG GCA GCG TCA GAT GTG TAT AAG AGA CAG **GTG CCA GCM GCC GCG GTA A**-3'

Pro806bR-MiSeq (Apprill et al., 2015)

5'-GTC TCG TGG GCT CGG AGA TGT GTA TAA GAG ACA G**GG ACT ACN VGG GTW TCT AAT**-3'

The obtained PCR products were sent to the commercial sequencing laboratory Research and Testing Laboratory (RTL Genomics, Lubbock, Texas, U.S.A.) for sequencing on an Illumina MiSeq platform with a 2 x 250 bp paired-end read configuration to obtain a approx. 200 bp overlap. The bioinformatic pipeline used for porewater is different than for bentonite and module samples to enable comparison with previously published results. Raw sequencing reads were preprocessed (merging, quality filtering) with USEARCH (Edgar, 2010) version 11, allowing a maximum of 10 bases of differences between the paired-end reads. Operational taxonomic units (OTUs) were assigned with UPARSE (Edgar, 2013), and chimeras were removed utilizing UNOISE2 (Edgar, 2016c). The taxonomies to the OTUs were assigned using the RDP classifier (Cole et al., 2009), in QIIME (Caporaso et al., 2010), using the Silva 128 database (Quast et al., 2013).

Table 2.3 – Composition of PCR solution used to amplify the V4 region of the 16S rRNA gene from DNA extracted from the borehole porewater.

	50 µL reaction = 40 µL mastermix + 10 µL DNA	
	µL per sample	**Final concentration**
DEPC H2O	20	-
10 x Buffer	5	1 x
2 mM dNTP mix	5	0.2 mM
25 mM MgSO4	3	1.5 mM
5 µM forward primer	3	0.3 µM
5 µM reverse primer	3	0.3 µM
KOD Hot Start polymerase	1	0.02 U/µL
Total volume	40	

Table 2.4 – Temperature cycles of PCR program used to amplify the V4 region of the 16S rRNA gene from DNA extracted from the borehole porewater.

Temperature °C	**Duration**	
95	2 min	
95	25 sec	
55	15 sec	x34
70	15 sec	
70	3 min	

DNA amplification from bentonite and module samples

DNA from bentonite and swabs was amplified using a quantitative PCR (total samples n=377). We used a modified protocol based on the *Quick*-16S NGS Library Prep Kit (Zymo Research Corp., Irvine, California, U.S.A.). The utilization of SYBR Green fluorescence signals during the PCR limits the generation of chimeric DNA amplicons, thus greatly improving the control over the amplification process. The provided kit allows the amplification of the V4 region of the 16S rRNA gene and allow the multiplexing of up to 376 samples into a single MiSeq lane. We decided to sequence on two MiSeq lanes (lane 1: 280 uniquely barcoded samples, lane 2: with 243 uniquely barcoded samples, the total number is higher than the total samples n=377 due to additional standards and controls, as described below). Additionally, we took advantage of the fluorescence signal to a semi-quantitative assessment of the 16S rRNA gene copy number. It is semi-quantitative because of two major limitations: i) no amplification replicates instead of the usual triplicates needed and ii) employing a standard curve method, using a pGEM-T plasmid (Promega Corp. Madison, Wisconsin, U.S.A.) containing a E. coli 16S rRNA gene copy as a standard. The latter is known to perform poorly for the quantification of environmental microbial communities (Brankatschk et al., 2012). Nevertheless, qPCR provided insight into the relative quantities of rRNA, and thus improved the robustness of the DNA sequencing interpretation. The 6-point standard curve was performed from 10^7 copies per µL,

down to 100 copies per µL in ten-fold dilution steps. Together with a positive control (Zymo Microbial Community Standard®) and a negative control, each 96-well plate of the *Quick*-16S NGS Library Prep Kit could be used to amplify 88 samples. The amplification was carried out on a LightCycler® 480 Instrument (F. Hoffmann-La Roche AG, Basel, Switzerland) using LightCycler® 480 Multiwell plats (96-well, white, F. Hoffmann-La Roche AG, Basel, Switzerland). For this system, the fluorescence threshold was determined at 24.63, which indicates the onset of an exponential increase of the fluorescence signal based on the amplification of a targeted DNA sequence. The amplification, barcoding and 16S-library generation of DNA samples from bentonite, modules swabs and contamination controls swabs were carried out as suggested from Zymo Research Corp. PCR efficiencies were calculated using LinRegPCR (Ruijter et al., 2009), and the 16S rRNA gene copy number for the samples on each plate were calculated based on the standard curve method with the values obtained on the same plate (Brankatschk et al., 2012). The 16S-library was sequenced on an Illumina MiSeq (Illumina Inc., San Diego, California, U.S.A.) platform at the Lausanne Genomics Technologies Facility (University of Lausanne, Switzerland), applying 10 pM of the 16S-library with 15% Phi-X spike in a paired-end 300bp mode.

The bioinformatic pipeline used for bentonite and module samples is slightly different than that for the porewater samples. The processing of raw reads was carried out as recommended in the USEARCH v 11 manual: Raw sequencing reads were preprocessed (merging, quality filtering) with USEARCH (Edgar, 2010) version 11, allowing a maximum of 10 bases difference between the paired-end reads. Operational taxonomic units (OTUs) were assigned with UPARSE (Edgar, 2013), and chimeras were removed utilizing UNOISE2 (Edgar, 2016c). Taxonomies of OTUs were assigned using SINTAX (Edgar, 2016a), based on the published and curated 16S RDP database version 16, training set (2016) (Edgar, 2016b), release 11. The number of high-quality reads was rarefied to 2,500 and imported to ampvis2 (Andersen et al., 2018), which was used to analyze the dataset for similarities and explanatory variables. Results are visualized using the R-package (core team, 2014), gplot2 (Wickham, 2009), to create balloon plots representing major OTUs on the family level for each sample, where the balloon size is indication of the relative contribution within the respective sample (in %) and samples obtained from similar locations were averaged for each module.

2.2.9 Bentonite humidity, dry-densities, oxygen detection, specific surface area

Bentonite humidity, dry-densities were calculated by recording the wet weight, wet volume and the dry weight after drying for 7 days at 105°C. The presence of oxygen bound/trapped within 300 g of as-received bentonite, isolated within gas-tight glass bottles, was determined by gas chromatography of the gas phase using a Varian GC-450 (Agilent Technologies, Santa Clara, California, U.S.A.) equipped with a molecular sieve column (CP81071: 1.5m*1/8” ultimetal molsieve 13 9 80-100 mesh) and a thermal conductivity detector (TCD).

Details about each method are given below.

Water content and observed dry density of bentonite

For each bentonite core, one slice of bentonite was used to determine the water content and the dry density, Figure 2.4. A cheese knife was used to cut the bentonite slice into six approximately equal parts. The dimensions of the slices were measured with a ruler and the wet weight ($m_{\text{sample wet}}$) was rapidly recorded using an analytical scale before drying had impacted the weight. The bentonite was dried in a laboratory oven at 105°C. Dry weights of cooled down samples (in moisture-free conditions) were recorded after 24 hours, 48 hours and after seven days. The lowest weights were recorded for all samples after seven days and the mass of water (m_{water}) was calculated on that basis. The wet moisture was calculated using

$$\%\text{moisture}_{\text{dry}} = \frac{m_{\text{water}} \cdot 100}{m_{\text{sample dry}}} \tag{2.1}$$

Similarly, the bentonite dry densities were obtained by

$$\rho_{\text{dry}} = \frac{m_{\text{sample wet}} - m_{\text{water}}}{V_{\text{wet}}} \tag{2.2}$$

Oxygen desorption from Wyoming bentonite and specific surface area

Eight serum glass bottles (V=1220 mL) were filled with 300 grams of as-received MX-80 Wyoming bentonite and sealed with rubber stoppers. Five additional bottles were sealed without bentonite and used as control for the bottle and stopper tightness. The air trapped within the sealed bottles was removed during 30 min flushing with nitrogen at atmospheric pressure, the bottle containing bentonite were shaken every 5 minutes to ensure removal of air trapped between bentonite grains. The bottles were stored in the dark at room temperature. 10 mL of the gas phase (a total of approx. 1000 mL), were sampled at each day in approx. 24h intervals for oxygen detection in an gas chromatography system. The removed gas volume was replaced by anoxic nitrogen. The gas chromatography system Varian GC-450 (Agilent Technologies, Santa Clara, CA, U.S.A.) used is equipped with a molecular sieve column (CP81071: 1.5m*1/8” ultimetal molsieve 13 9 80-100 mesh) and the detection of oxygen was performed using a thermal conductivity detector (TCD). After the experiment, three bentonite samples were sieved for particles smaller than one millimeter, dried in an oven for two hours at 200 degrees Celsius and analyzed for their specific surface area (BET-analysis) using a TriStar II Plus system (Micromeritics Instrument Corporation, Norcross, Georgia, U.S.A.). The BET-analysis was carried out by the Laboratory of Construction Material at EPFL, Lausanne, Switzerland.

2.3 Results & Discussion

We considered the spatially-resolved distribution of microorganisms in the microbiome from the outside (the porewater) progressively towards the inside of the module: the steel module surface, the water exchange holes, the sintered steel filter, the surface of the bentonite cylinder, the bulk bentonite and the bentonite adjacent to the test coupons. The goal was to determine whether some microorganisms thrived in the bentonite under long-term, near-repository conditions and if so, which. Cultivation of microorganism was performed from bulk bentonite samples obtained from the inner (interior) part and the outer (exterior) part of the bentonite cylinder with the goal to detect the potential colonization of bentonite by porewater microorganisms.

2.3.1 The microbial community in Opalinus Clay rock porewater

The chemical composition of the BIC-A borehole water was assayed over time from 2013 to 2018, Table 2.5. The results indicate that it is consistently anoxic: reduced iron is detected most years, except 2017, suggesting microbial iron reduction. Sulfide is only detectable in the 2013 sample, suggesting the activity of sulfate-reducing bacteria (SRB) which is consistent with the high concentration of sulfate (15.6 to 23.3 mM). Its lack of detection in other years could be related to its precipitation with iron. The porewater microbiome was also characterized prior to deployment of the modules (Bagnoud, de Bruijn, et al., 2016), and at regular time intervals (Smart et al., 2017), and with the results presented here.

- The pristine borehole porewater microbiome (January 2013) was dominated by taxa from the Peptococcaceae family (~68%) and by SRB (~66%) (Bagnoud, de Bruijn, et al., 2016), and two of the most abundant genera were *Desulfotomaculum* and *Desulfosporosinus*, both Gram-positive SRB, Table 2.6. Additionally, a genus identified as *Pseudomonas sp.* represented approximately 26% of the community, Table 2.6.

- The porewater microbiome 1.5-years post-deployment (July 2014), revealed a significant change in composition, Table 2.6 and Figure 2.8, epitomized by a large increase in the relative abundance of *Pseudomonas* (~87%) and a stark decrease in the sulfate-reducing genera (~4%). The reason for this change is unknown but could be due to the disturbance caused by the deployment of the experiment in the borehole. Organic carbon leached out of the bentonite cylinders placed within the modules, (representing 0.20-0.28 % of the bentonite by weight (Karnland & AB, 2010)) could also have caused a shift in the community.

- In July 2017, 4.5-years into the experiment, the community had shifted again, as evidenced by the lower abundance of *Pseudomonas* (~31%) and higher contribution of SRB (~19%) to the community.

- Finally, after 5.5 years (July 2018), the community appeared to have reached a steady-state as its composition resembled that of the year before.

Table 2.5 – Samples of filtered porewater were collected on 4 timepoints and the chemical composition was investigated.

Component	January 2013 (Bagnoud, de Bruijn, et al., 2016)	September 2014	July 2017	July 2018	Unit
Fe(II)	1.3	76.32	0.3	31.6	µM
H_2S	7.4		<0.1	<0.1	µM
Co	<10		<50	<500	µg L-1
Cu	13		<50	<500	µg L-1
Sr	60.657		18.387	26.467	mg L-1
Ni	<10		69.3	<500	µg L-1
Mn	53		125.9	<500	µg L-1
Cr	31		<50	<500	µg L-1
Zn	<10		<50	<500	µg L-1
Al	<10		<50	<500	µg L-1
Na^+	313.6	267.1	257.9	258.7	mM
NH_4^+	0.3		4.6	0.9	mM
Mg^{2+}	15.0	3.0	13.0	9.8	mM
K^+	1.9	9.00	3.8	3.4	mM
Ca^{2+}	18.8	15.3	12.3	13.4	mM
F^-	0.1		0.03	<0. 5	mM
Cl^-	290.3	226.5	264.6	274.8	mM
NO_2^-	<0.005		<0.05	<0.5	mM
SO_4^{2-}	15.6	23.3	21.8	22.5	mM
Br^-	0.5		<0.05	<0.5	mM
NO_3^-	<0.005		0.16	0.09	mM
PO_4^{3-}	<0.005		0.04	<0.5	mM
pH	8.2		8.30	8.45	
EH	-88	-88	-271.8	-230.1	mV

Table 2.6 – Operational taxonomical units (OTUs) of the BIC-A porewater microbial community. Contributions larger than 1% to the community for at least one timepoint are listed. A detailed investigation of the initial timepoint, January 2013, was reported in (Bagnoud, de Bruijn, et al., 2016). The contribution of sulfate-reducing bacteria decreases from the first to the second timepoint, but increases again from 2017 onward. Generally, the 2017 and 2018 samples exhibit a more diverse microbial community in the porewater than earlier timepoints.

Taxonomy	**01/2013** (Bagnoud, de Bruijn, et al., 2016) **Rel. %**	**09/2014 Rel. %**	**07/2017 Rel. %**	**07/2018 Rel. %**
Pseudomonas	25.9	87.3	30.9	24.9
Desulfotomaculum	58.9	2.4		
Desulfosporosinus	7.4	1.7	9.3	2.0
Natronincola anaerovirgula	2.3		1.7	2.0
Peptococcaceae	1.0		2.5	22.1
Sporotomaculum			4.8	4.4
Hydrogenophaga			15.3	5.0
Desulfitobacter			1.6	5.5
Desulfococcus			1.0	2.5
Desulfobulbaceae			3.4	5.9
Acidobacteria iii1-8 DS-18			1.0	1.5
Thiobacillus			2.5	
Desulfurispora			1.3	
Dethiobacter				1.1
Devosia				1.0
Gracilibacter		2.2		
Poseidonocella		1.3		
Natranaerobiales	2.2			
Beijerinckiaceae			1.5	
Rhodobacteraceae				1.3
Clostridia			3.8	6.8
Bacteria			6.9	

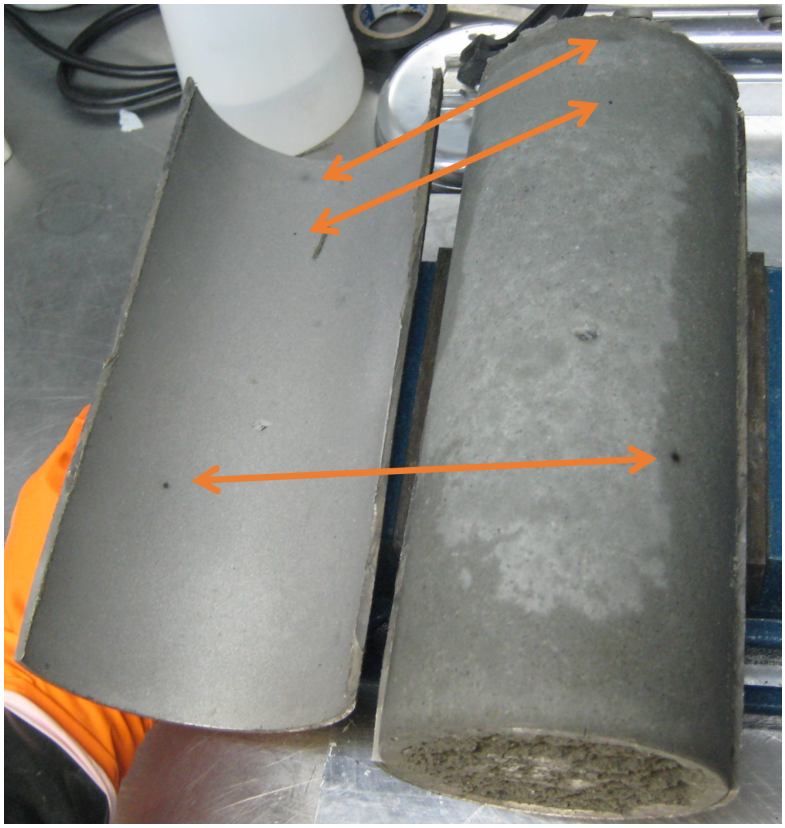

Figure 2.5 – Bentonite core (M13, 2.5-years, 1.45 g/cm^3 powder/pellets), the surface features localized black spots which are also observed on sintered steel filter opposite.

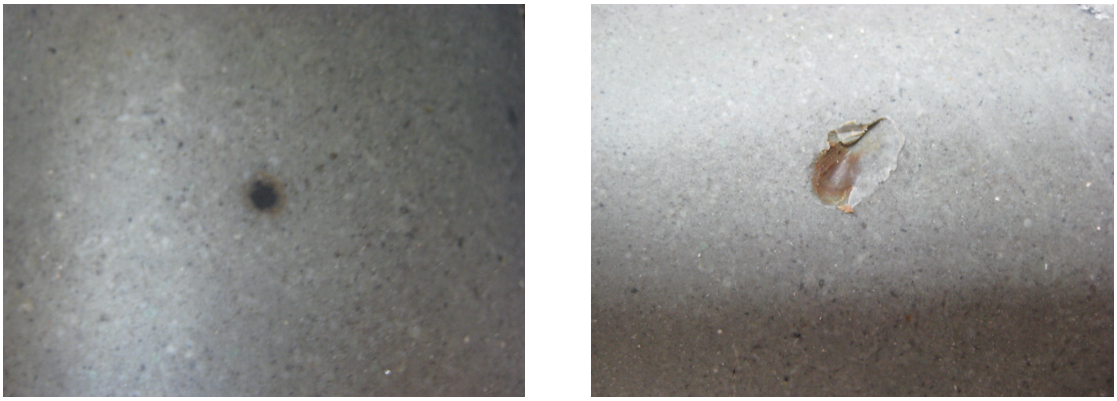

(a) (b)

Figure 2.6 – Black spots (a) observed on the bentonite core surface are potentially made-up by iron-sulfide minerals, Iron(II) may be leaching out of the sintered steel filter and react with sulfide within the porewater (black precipitates) or with bentonite-trapped oxygen, forming iron-oxides (brown precipitates). (b) Below the black spot, in approximately 2 mm depth we observed a brown coloration of bentonite.

2.3.2 The microbial community on the stainless-steel module, the sintered steel filter and the bentonite surface

At early deployment times, we observed isolated black spots on the surface of the bentonite cylinders, Figures 2.5 and 2.6. As time proceeded, the spots grew and the entirety of the cylinders' surface turned black, Figure 2.7. Similarly, with longer deployment times, an increase in the black coloration of the sintered filter material was observed, suggesting that the stainless-steel sintered filter was reacting with dissolved sulfide. Furthermore, DNA-based microbiome profiling revealed that the porewater microbial community colonizes the module surface, which is in direct contact with the borehole fluid, but also water exchange holes and the sintered stainless-steel filter, as evident in Figure 2.15 (in Chapter Appendix). Indeed, the microbiomes observed on these surfaces are dominated by Pseudomonadaceae as well as Peptococcaceae, Natranaerobiaceae, Desulfobalbaceae, Desulfobacteriaceae, which are typically observed in the BIC-A borehole water. The bentonite cylinder surface and darker shades observed on that surface, as well as the aforementioned black spots are also shown to harbor a microbiome closely related to the borehole community.

In addition to considering the microbial community on surfaces and in the porewater, we also characterized the microbial community and enumerated microorganisms within the bentonite.

Figure 2.7 – Bentonite core (M6, 5.5-years, 1.55 g/cm^3) after sintered filter removal (upper half, lower half used as support during sampling), showing strong black coloration on the surface, except for the places the metal test coupons are placed within the bentonite, indicating an interaction between coupons and sulfide-rich borehole water at the bentonite-borehole water interface.

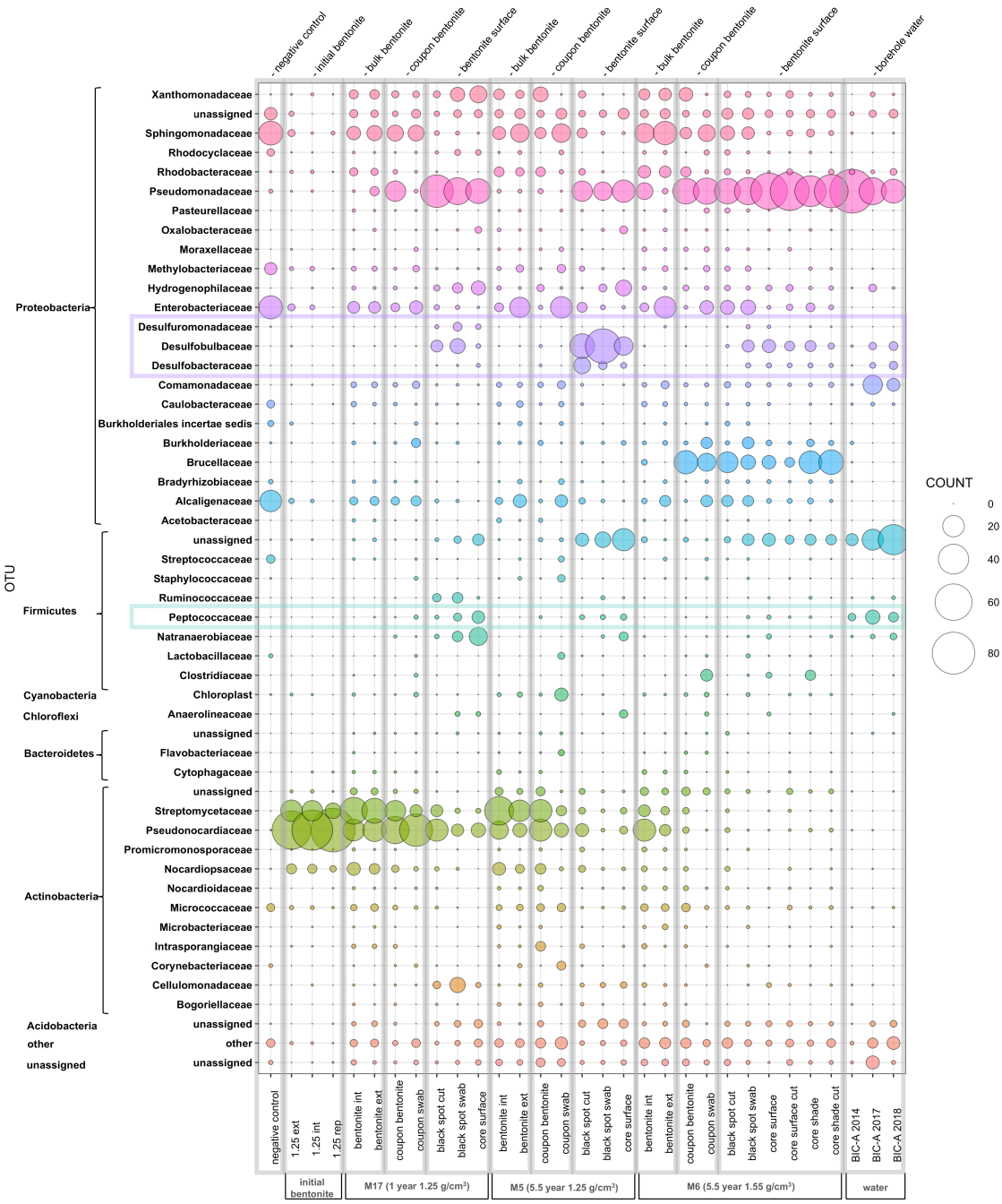

Figure 2.8 – 16S rRNA gene V4 region amplicon profile of bentonite from three modules: M17 (1-year), M5 (5.5-years) both featuring low-density bentonite blocks (1.25 g/cm^3), and M6 (5.5-years) including high-density bentonite block (1.55 g/cm^3). The bentonite cylinders were exposed to *in-situ* conditions within the BIC-A borehole. The x-axis lists the samples, while major contributions of operational taxonomic units (OTUs), at the phylum and family level, are listed on the y-axis. Each OTU is color-coded according to its Phylum and the size of the circle corresponds to its normalized (percent) occurrence within a given sample. Only OTUs > 1% relative abundance within a sample and including three observations (above threshold) are shown; the remaining minor OTUs are represented within 'other'. Shown are averages of sample groups: Control sample (negative control) (n=1); initial undeployed bentonite

Figure 2.8 *(previous page)* – blocks (initial bentonite) (n=3); for each module (M17, M5 and M6), bentonite bulk interior (bentonite int) and exterior (bentonite ext) (n=5); bentonite adjacent to coupons (coupon bentonite) (n=4); swabs of bentonite in contact with coupons (coupon swab) (n=4), cuts/extractions of black spots on the bentonite cylinder surface (black spot cut) (M17 n=3, M5 n=4, M6 n=3); swabs of black spots (black spot swab) (M17 n=4, M5 n=7, M6 n=5); swabs of bentonite cylinder surface without visible features (core surface) (M17 n=1, M5 n=1, M6 n=1); cut/extract of bentonite cylinder surface (core surface cut) (M6 n=1); swab of discolored area on bentonite cylinder surface (core shade) (M6, n=4); cut/extract of discolored area on bentonite cylinder surface (core shade cut) (M6, n=2), borehole water community (n=3). The porewater samples from BIC-A are labeled according to the year of their sampling.

2.3.3 Microbial viability in bentonite

The average number of viable cells, as colony-forming units (CFU), were enumerated over the entire bentonite cylinder (n=10 per module, n=2 for undeployed bentonite), as a function of bentonite dry weight for both anaerobic and aerobic heterotrophs, Figure 2.9c, and for sulfate-reducing bacteria (SRB), Figure 2.9d. The same results are presented in Figure 2.10, highlighting the change in viable cell counts over time and as a function of dry density. Additional results can be found in the Chapter Appendix for aerobic heterotrophs in Figures 2.16 and 2.17, for anaerobic heterotrophs in Figures 2.18 and 2.19, for sulfate-reducing bacteria in Figures 2.20 and 2.21 and bentonite moisture content in Table 2.9 and dry densities in Figure 2.14.

The growth of both aerobic and anaerobic heterotrophs is observed in the deployed bentonite as compared to the initial bentonite in the blocks with a dry density of 1.25 g/cm^3. We observe significant growth of both aerobic and anaerobic heterotrophs when comparing undeployed bentonite (CT) to the one deployed in the borehole for 1.5-years (M2), Figure 2.9c. However, the comparison of 5.5 years of deployment (M5) to the initial sample (CT) reveals a significant decrease in the number of aerobic heterotrophs. This finding is confirmed when comparing aerobic counts for 1-year (M17), 1.5-years (M2), and 5.5 years (M5) using one-factor analysis of variance (ANOVA), Table 2.7: the *p-value* is significant when time is considered as the ANOVA explanatory variable, confirming that the increase from M17 to M2 and suggesting that the decrease from M2 to M5 is statistically significant. The anaerobic CFU/g count decreases to a lesser extent than the aerobic count when comparing 1.5 to 5.5 years and is barely statistically significant with an ANOVA *p-value* of 0.028.

The change in aerobic heterotroph counts as a function of deployment time in the higher density blocks (1.55 g/cm^3) illustrates the increasingly challenging conditions for microbial life posed by the higher density. Indeed, there is a steady decrease in viable counts from initial (CT) to 1.5-years (M3) and further to 5.5-years (M6). More rigorously, we tested the explanatory variables time and density as driving forces for microbial viability in bentonite by performing a two-factor ANOVA on the dataset containing the 1.25 g/cm^3 low density

(M2, M5) and 1.55 g/cm^3 high density (M3, M6) modules, at 1.5- and 5.5-years. The analysis revealed both time and density as significant explanatory variables for aerobic and anaerobic heterotrophs, Table 2.7. Thus, for 1.55 g/cm^3 dry density, there is a small but significant decrease in the number of cultivable aerobes during the first 1.5 year, but followed by only an insignificant decrease between 1.5 and 5.5 years, highlighting the persistence of aerobes. Similarly, the number of cultivable anaerobes did not change significantly, based on a pairwise comparison (Student's t-Test), Table 2.7.

Comparison of the change in CFU/g between low- and high-density modules indicates a strong inhibitory effect on the viability of aerobes due to increased density at both short (1.5-years) and long (5.5-years) deployment times. Anaerobes are shown to be affected by dry-density as well, because the higher the density, the fewer viable microorganisms reported, Figure 2.10.

Finally, there is no profound difference in the viable counts when comparing the exterior and the interior of the bentonite cylinder (n=5 for each per module), Figures 2.17 and 2.19 in Chapter Appendix, hinting at the fact that bulk bentonite microorganisms may originate from the sourced bentonite rather than from the borehole porewater.

In summary, we observe a similar trend for both aerobes and anaerobes at the lower dry density. Thus, provided sufficient pore space is available (i.e., the low dry density), the number of viable heterotrophs increases up until 1.5-years, but decreases at longer deployment times. As expected and previously reported (Smart et al., 2017; Stroes-Gascoyne et al., 2013; Stroes-Gascoyne et al., 2010), the 1.25 g/cm^3 bentonite dry density appears to create better conditions for microbial life than the higher, 1.55 g/cm^3 dry densities. For the higher density (1.55 g/cm^3), the anaerobes display the same transient increase up until 1.5 years followed by a decrease from 1.5 to 5.5 years. However, the number of cultivable aerobes decreases from the initial time point to 1.5 years and remain stable thereafter, despite exposure to an anoxic environment. Additionally, it was surprising to observe that the number of cultivated aerobes always exceeded that of cultivated anaerobes, Figure 2.9. Thus, the persistence of aerobic heterotrophic CFUs cannot be attributed solely to facultative anaerobes, although at least a fraction is likely to be. For example, at 5.5 years, for the high density 1.55 g/cm^3, the counts of aerobic compared to anaerobic heterotrophs has become significantly larger, despite the long exposure into an anoxic borehole, Table 2.7.

Table 2.7 – Significance values for comparison of (an)-aerobic heterotrophs and SRB, Figure 2.9 and Figures 2.16, 2.18 & 2.20 in this Chapter's Appendix. Significance indicated in **bold** when p<0.05. nd=not defined due to insufficient number of observations.

Module	Analysis	p_{time}			$p_{density}$			$p_{interaction}$		
		aerobes	anaerobes	SRB	aerobes	anaerobes	SRB	aerobes	anaerobes	SRB
M2 (1.25 g/cm^3, 1.5-yrs) M3 (1.55 g/cm^3, 1.5-yrs) M5 (1.25 g/cm^3, 5.5-yrs) M6 (1.55 g/cm^3, 5.5-yrs)	Two-factor ANOVA: time & dry-density	$4.5 \cdot 10^{-8}$	**0.039**	**0.047**	$1.7 \cdot 10^{-4}$	$3.9 \cdot 10^{-6}$	0.142	$1.3 \cdot 10^{-7}$	0.178	0.3718
M17 (1.25 g/cm^3, 1-yr) M2 (1.25 g/cm^3, 1.5-yrs) M5 (1.25 g/cm^3, 5.5-yrs)	One-factor ANOVA: time	$3.4 \cdot 10^{-6}$	**0.028**	0.430						
M3 (1.55 g/cm^3, 1.5-yrs) M6 (1.55 g/cm^3, 5.5-yrs)	Student's t-test: time	0.110	0.056	0.081						
t=0 CT (1.55 g/cm^3, 0-yr), M3 (1.55 g/cm^3, 1.5-yrs)	Student's t-test: time, initial growth	**0.009**	0.133	nd						
M3 (1.55 g/cm^3, 1.5-yrs)	Student's t-test: aerobes vs. anaerobes count	0.067								
M6 (1.55 g/cm^3, 5.5-yrs)		**0.010**								

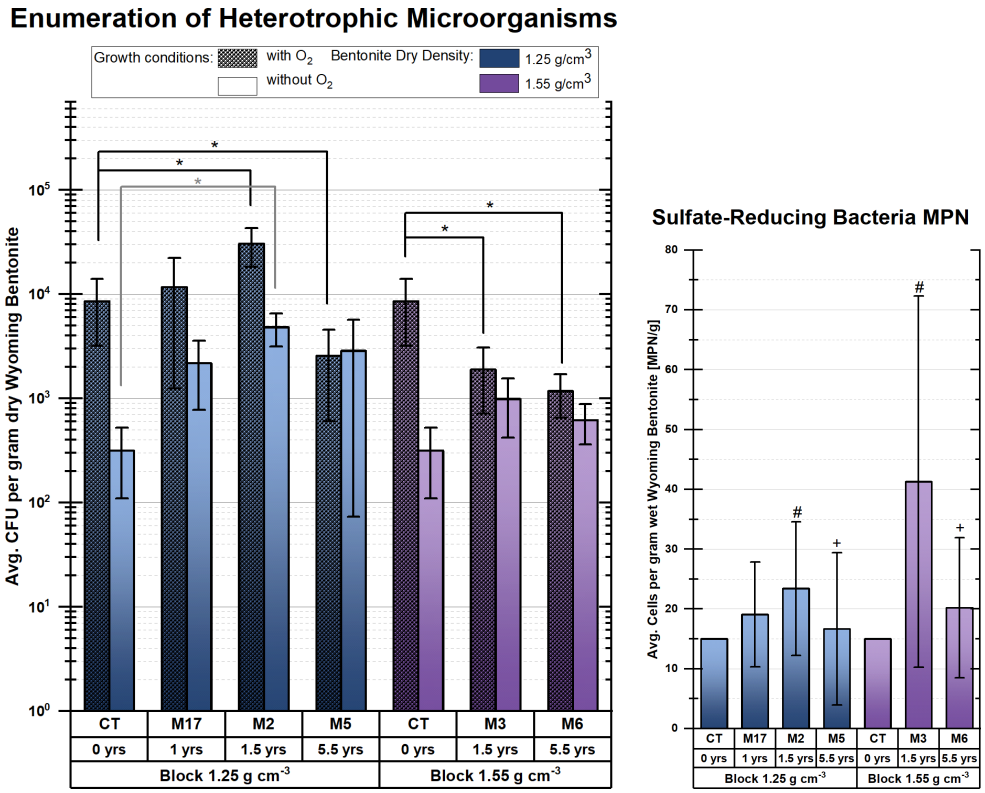

(c) (d)

Figure 2.9 – Colony-forming units (CFU) per gram dry bentonite. (a) absolute counts in log scale, aerobic (dark) and anaerobic heterotrophs (light), averaged over the entire bentonite cylinder as a function of dry density and time; error bars represent one standard deviation. Initial, undeployed sample labelled CT (bentonite powder-pellet mix used to produce blocks). (b) Sulfate-reducing bacteria enumerated by most probable number (MPN) per gram bentonite. Two-way ANOVA of the SRB MPN/g counts exposed time as explanatory variable but not density, # indicates the identified 1.5 year and + the 5.5-year condition, Table 2.7.

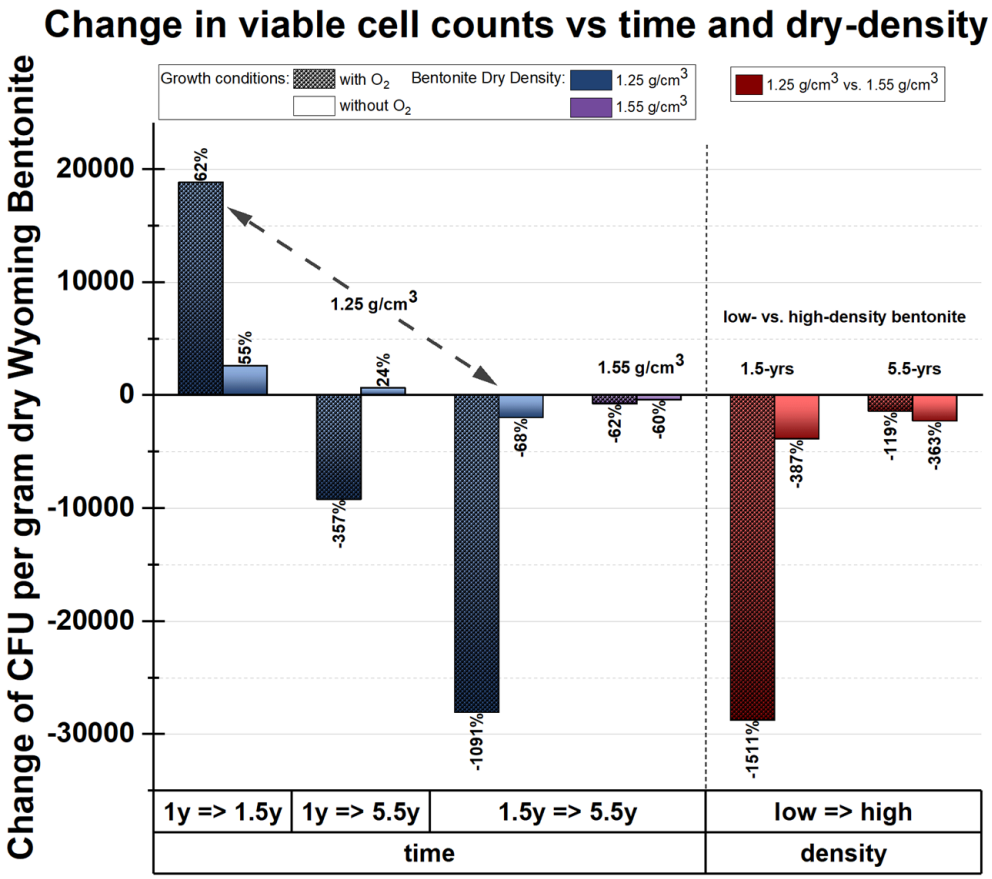

Figure 2.10 – Change of viable heterotrophs observed against time and dry-density for selected timepoints of modules with similar bentonite dry density (blue, purple) and of modules with different dry density (red).

The enumeration of SRB by the MPN method revealed very low numbers of viable cells counts compared to (an)-aerobic heterotrophs, in the range of 10-100 cells/g bentonite for SRB, Figures 2.9 and 2.16, compared to up to 31,000 cells/g bentonite for aerobic heterotrophs, Figure 2.9. Surprisingly, no trend based on increasing dry-density could be discerned for SRB, but a trend towards lower MPN/g for the longer deployment times was apparent (1.5 vs. 5.5-years, ANOVA, Table 2.7 and Figure 2.9). Amongst the deployed modules, the highest number of SRB was found after 1.5-years in M3 despite the fact that the bentonite has the highest dry density (1.55 g/cm^3). Additionally, in contrast to heterotrophic anaerobes, SRB show no increase in numbers between the initial bentonite and the first time point. However, from 1.5 to 5.5 years, the abundance of sulfate-reducing bacteria (SRB) decreases as revealed by time being an explanatory variable in the two-factor ANOVA, Table 2.7.

This suggests that SRB do not grow during the bentonite saturation period while other anaerobic microorganisms (and aerobes in the case of 1.25 g/cm^3) do, Figure 2.9. Comparing the

location within the bentonite cylinder, interior vs. exterior, we could not observe any trend, Figure 2.21, suggesting no colonization of the bentonite bulk by borehole water SRB, even though the sintered stainless-steel filter offers large enough pores to enable the migration of microorganisms (18 µm avg. pore size). Had such a colonization taken place, a gradient of SRB abundance would have been expected. These observations lead to the conclusion that the SRB found in the modules' bentonite cylinders are likely to be bentonite-derived. However, they remain inactive under the given conditions, as no growth was observed. Possible explanations for the absence of porewater-derived SRB are that: a) the bentonite has swelled sufficiently from pre-deployment saturation to preclude the inward migration of porewater microorganisms once deployed in the borehole; or b) the conditions for growth of porewater microorganisms are too challenging within the bentonite – at least for the tested timeframes, or c) both. The latter option may be supported by the fact that aerobes grow at early timepoints, which means that the influence of introduced microorganisms might be more evident at later timepoints when the conditions turn into favor for anaerobic microorganisms, including SRB.

2.3.4 Bulk bentonite microbiome

The amplified V4 region of the 16S rRNA gene allows the detection of both Archaea and Bacteria. However, we observed only bacteria among the major contributors to the microbial community. Fungal microorganisms are excluded as they do not carry the 16S rRNA gene. When assessing the microbiome based on a DNA profile, one has to recognize the stabilization of DNA on clay (Engel, Coyotzi, Vachon, et al., 2019; Greaves & Wilson, 1969); thus, the signature of inactive, non-viable microorganisms is included in the microbiome. The 16S rRNA gene semi-quantification results can be found in the Chapter Appendix in Figure 2.22.

Dry density and deployment into the borehole shapes the bentonite microbiome

This is most clearly evidenced in Figure 2.11 by the canonical correspondence analysis (CCA) of Hellinger transformed 16S rRNA amplicon data presented in Figure 2.8. First, the growth-related change in the microbial community upon saturation with porewater is revealed by the separation between the initial bentonite samples and the deployed samples. This finding, combined with the cultivation data, suggests that there is growth and change in the microbiome composition. Additionally, the distinct distribution of the low- and high-density samples indicates a differentiation in the microbial community that is associated with the density. In essence, while starting from an identical initial inoculum, the communities develop in different directions at the two densities. Furthermore, the two deployed bentonite communities are vastly different from the borehole community point to an incompatibility of the aquatic borehole microbiome to colonize the bentonite within the sampled timeframes (5.5-years). Finally, the clustering of samples from the 1-year deployment and the 5.5-year deployment indicate a temporally stable bentonite community.

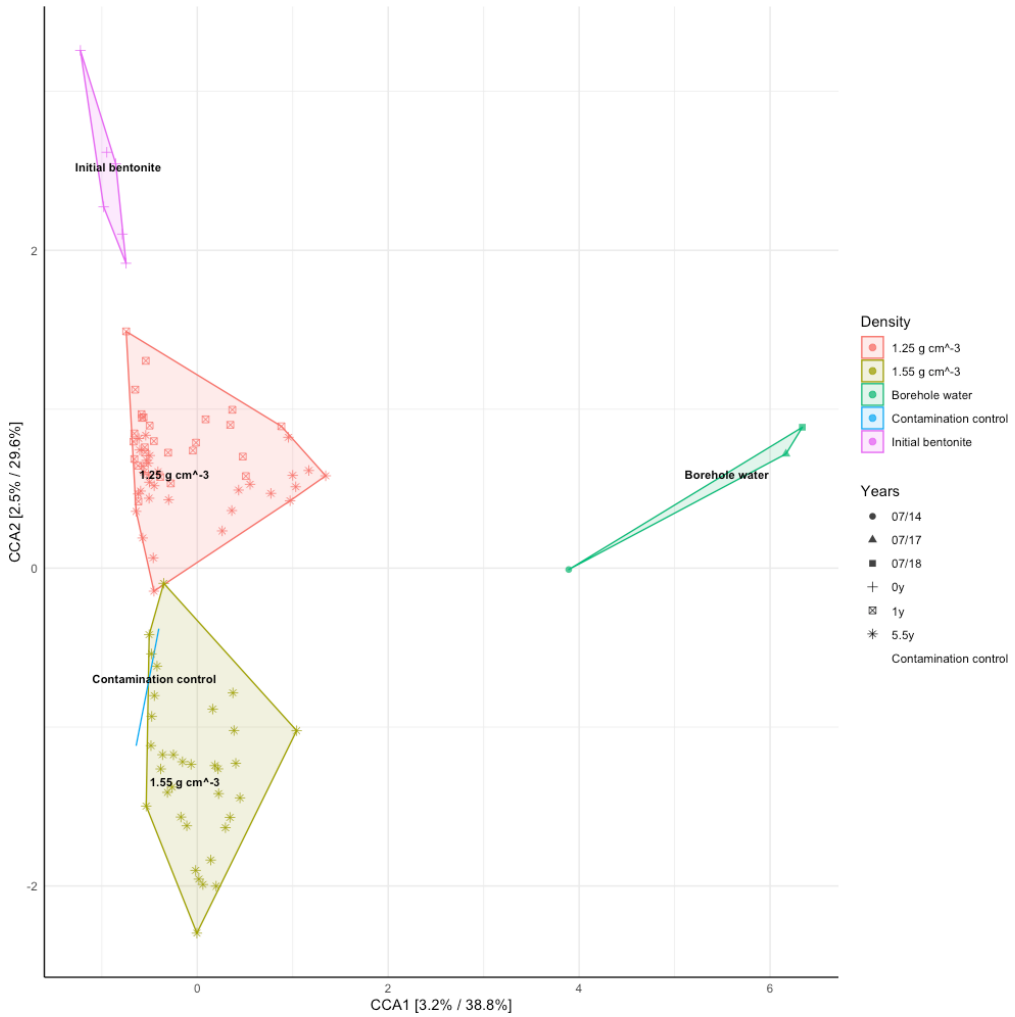

Figure 2.11 – Canonical Correspondence Analysis (CCA, Hellinger transformed data) of modules M17, M5 and M6, as presented in Figure 2.8, constrained for the bentonite dry density as the explanatory variable. The time-dependent dependence is represented by the shape of the data markers (see legend).

Spatial distribution of the microbiomes

The microbial communities are separated along a spatial gradient from the inside of the bentonite cylinder to the surface of the module, Figures 2.8 and 2.12. The balloon plot shows the community composition in the initial bentonite and in the three modules (M17, M5, and M6) as a function of location, inside to outside (left to right) in comparison to the no-template qPCR control and undeployed bentonite samples, representing the starting community within bentonite blocks. The latter was evidenced as a low-diversity community with aerobic heterotrophs dominating: Streptomycetaceae, Pseudonocardiaceae and Nocardiopsaceae. In comparison, the community associated with samples from M17, bentonite deployed for 1 year (int, ext, coupon and coupon swab), reflects the growth of an aerobic community,

with major contributions by OTUs related to: Streptomycetaceae, Pseudonocardiaceae and Nocardiopsaceae (the three families present in the undeployed bentonite), as well as, the emergence of families such as Xanthomonadaceae and Comamonadaceae, and Burkholderiaceae. Sphingomonadaceae, Enterobacteriaceae, and Alcaligenaceae were not considered as contributions as they were also detected in the negative control. Thus, despite the anoxic borehole environment, it is evident that aerobic microorganisms were able to grow, Figure 2.8.

Comparing low- (M5) and high-density (M6) bentonite (deployed for 5.5 years), we observe a lower relative abundance of Streptomycetaceae and Pseudonocardiaceae for the higher-density bentonite as well as the emergence of Brucellaceae and Pseudomonadaceae, Figure 2.8. This difference in community composition may be attributed to a lower initial growth of the aerobic community in the high-density bentonite as compared to the low-density one, thus leading to increased relative contributions by anaerobic groups, Figure 2.9.

In contrast, the porewater is dominated by sulfate-reducing bacteria such as Desulfobulbaceae and Desulfobacteraceae and by OTUs belonging to Peptococcaceae, as well as Pseudomonadaceae, Figure 2.8. OTUs found in the porewater are also dominating the interface with the bentonite, thus indicating the boundary between oxic and anoxic environments, with OTUs belonging to Desulfobulbaceae and Pseudomonadaceae colonizing the observed black spots on the bentonite cylinder surface.

- Within the bulk bentonite (int, ext and coupon bentonite), we observe that the microbial community is changing over time (from 1 year to 5.5 years of deployment of the 1.25 g/cm^3 bentonite modules). However, the contribution of aerobes does not appear to decrease with prolonged deployment times and no SRB are detected among the major contribution OTUs in bulk bentonite, Figure 2.15 in the Chapter Appendix. This observation confirms the results from enumeration of a viable aerobic community and a muted presence of SRB.

- The microbial community observed near the coupons, Figure 2.8, appears to be governed by the surrounding bentonite, i.e., the proximity to the metallic coupons has not impacted the microbial community.

- Furthermore, the interface between the bentonite cylinder and sintered stainless steel filter harbors a different microbiome than within the bentonite (samples denoted as black spot (cut), cylinder surface (cut), cylinder shade (cut)), Figure 2.8. The appearance of SRB families belonging to OTUs of Peptococcaceae, Desulfobulbaceae and Desulfobacteraceae and of an OTU related to Pseudomonadaceae indicate an established anoxic environment, highly influenced by the surrounding borehole water.

- The borehole signature become increasingly evident the further away the sampling location is from the bentonite cylinder, as shown for module hole (H) and module surface (S) samples in Figure 2.15 in the Chapter Appendix.

The spatial differences of the microbiome are observed throughout all sampled timeframes and densities. This general trend is exemplified in an unconstrained principal component analysis (PCA), Figure 2.12, with Hellinger-transformed data from Figure 2.8. It shows the segregation of the microbial communities according to their location along the cross-sectional gradient spanning the bulk bentonite to the borehole water. The clustering occurred along a three-OTU axis: (i) aerobes Pseudonocardiaceae and Streptomycetaceae; (ii) (an)-aerobes Enterobacteriaceae and Sphingomonadaceae; and (iii) borehole-derived anaerobic Pseudomonadaceae and Desulfobulbaceae. Evident is the divide between the microbiomes of initial and deployed bentonite, with interior and exterior bentonite samples clustering closer to the initial states than the samples obtained from the surface or the outside of the bentonite cylinder, towards the borehole. Bentonite cylinder surface, cylinder discolored surface, and black spot swab samples cluster more closely with the borehole water samples, characterized by OTUs related to Pseudomonadaceae and Desulfobulbaceae, than with the bulk bentonite. Inclusion of coupon samples and black spot cut samples in the PCA analysis reveals a community more closely related to the bentonite or the borehole water, depending on the amount of bentonite obtained for the respective sample, Figure 2.12b.

It is notable that in the number of microorganisms grown from bulk bentonite under oxic conditions exceeds that grown under anoxic conditions. This suggests that there is at least a fraction of the aerobic microorganisms that are strict aerobes. The growth of strict aerobes under anoxic conditions up until 1.5 years (for the low-density condition) and their persistence for up to 5.5 years (under both densities) suggests that oxygen may also persist to some extent in the bentonite. We hypothesize that oxygen trapped in macropores and adsorbed to the clay mineral surfaces may facilitate the survival of these microorganisms. Additionally, the growth of anaerobes, but not SRB, at both densities supports the possibility that many of the cultivated anaerobes are indeed facultative anaerobes. This is supported by the DNA-based analyses showing the emergence of Pseudomonadaceae and Rhodobacteraceae, both of which harbor some facultatively anaerobic genera.

The fact that significant growth is observed for heterotrophic anaerobes but not for SRB bolsters the case of a delayed onset of SRB growth in bentonite due to the presence of bioavailable oxygen. In order to probe the potential for oxygen to be present in bentonite, we conducted a desorption test of ambient-humidity dry bentonite at room temperature and observed detectable oxygen (0.05 vol.%) within the gas phase at around 7 to 9 days after isolation in a nitrogen atmosphere, Figure 2.13 and Table 2.8. However, it is likely that this oxygen will be consumed over time, allowing for the potential for the increase in the relative abundance of SRB in bulk bentonite for longer deployment times. It remains an open question whether the SRB present in low numbers within the bentonite would be able to grow. If that were the case, we would expect an increase in SRB in the bulk bentonite at least within the 1.25 g/cm^3 module at the next sampling point (7.5 years). Current data does not suggest the possibility that borehole water SRB (or other borehole water microorganisms) will be able to colonize the bentonite.

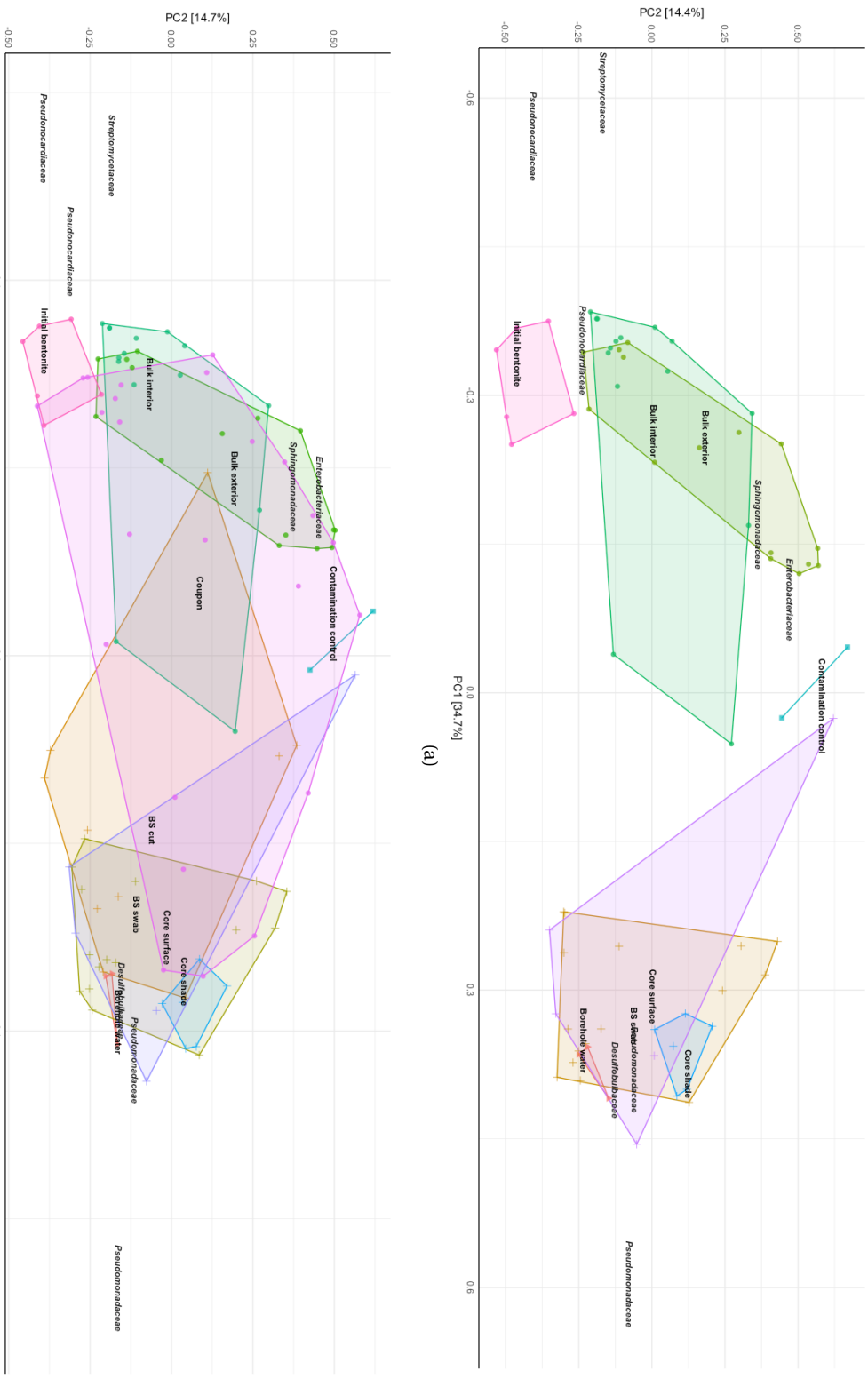

Figure 2.12 – Unconstrained Principal Component Analysis (PCA, Hellinger transformed data) of modules M17, M5 and M6, as presented in Figure 2.8, shows the microbial community composition for the two densities and timepoints, the initial bentonite, the borehole water and the contamination control. The samples are color-coded according to their location. BS swab = Black spot swab sample; BS cut = black spot bentonite removed to a few mm depth; Core shade = discolored bentonite cylinder surface. Subfigure (a) shows all sampling locations except BS cut and Coupon samples. Subfigure (b) includes these two sample types, which can contain both bentonite and borehole communities, depending on the individual sample.

Table 2.8 – Oxygen quantification from gas phases of bentonite sealed within gas-tight glass bottles, desorption started within 10 days upon sealing within a nitrogen atmosphere.

Time [days]	Oxygen [%]	Oxygen [%]	Oxygen [%]	Oxygen [%]	Oxygen [%]	Oxygen [%]	Oxygen [%]	Oxygen [%]	Mean [%]	Standard Deviation [%]
	1	**2**	**3**	**4**	**5**	**6**	**7**	**8**	**Mean**	**Std Dev**
0	0	0	0	0	0	0	0	0	**0**	0
1	0	0	0	0	0	0	0	0	**0**	0
2	0	0	0	0	0	0			**0**	0
3	0.10069	0.05747					0	0	**0.03954**	0.04895
4	0.14873	0	0	0.05813	0	0	0	0	**0.02586**	0.05365
5	0.21036	0	0	0.05356	0	0	0	0	**0.03299**	0.07408
6	0.2553	0	0	0.06516	0	0	0	0	**0.04006**	0.08991
7	0.10544	0.10502	0	0.07336	0.0649	0.0607	0	0	**0.05118**	0.04547
9			0	0.08627	0	0.05682	0.0868	0.12098	**0.05848**	0.04965
10	0.06742	0	0	0.06459	0.07861	0	0.05818	0.05965	**0.04106**	0.03455

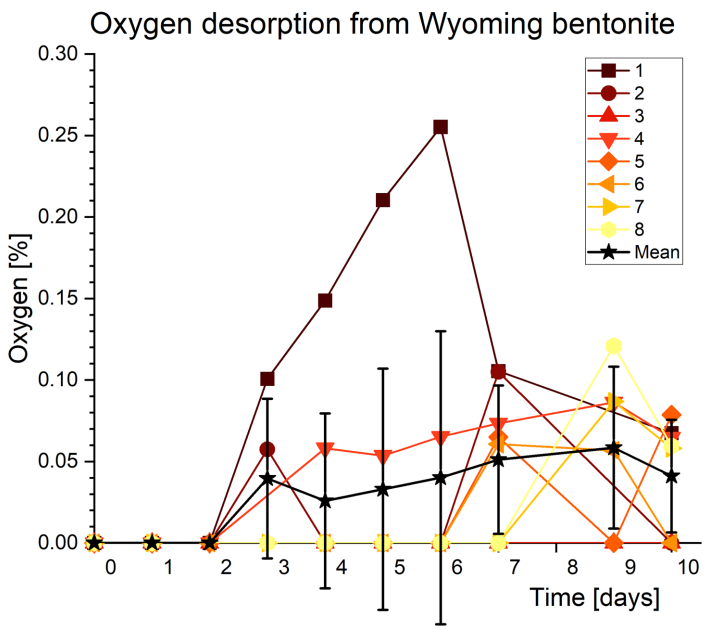

Figure 2.13 – Oxygen quantification from bentonite gas phases, desorption within 10 days upon sealing within a nitrogen atmosphere. The results indicate desorption of oxygen from bentonite starting at earliest after three days (dark brown) but we observe that between 7 and 9 days (orange to yellow) are necessary to be able to detect approx. 0.05% oxygen (limit-of-detection).

2.4 Conclusion

From this experiment, we can conclude that full bentonite saturation with porewater is a process accompanied with the growth of a heterotrophic microbiome and that bioavailable oxygen remains trapped within the bentonite (e.g., via adsorption) for long periods of time. These findings reshape our understanding of the predominant microbial processes upon repository gallery closure. Microorganisms will increase in numbers until full saturation is reached and will stay at stable numbers over extended periods, with the possibility to take advantage of any anomaly showing up over time in the engineered barriers. The possibility of a resurgence of microbial activity after several years of exposure to a repository-relevant environment cannot be excluded and must be considered in the safety case for deep geological storage of radioactive wastes. However, with the data available to date, there is no direct evidence of sulfate reduction occurring within the bentonite. Longer-term exposure to the Opalinus Clay rock environment is needed to make conclusive statements.

Chapter 2 - Appendix

Table 2.9 – Deployed bentonite moisture content calculated from wet and dry weights. Water activity data are only available for the first set of modules (1-3). [a]Water weight x 100/weight of original sample. [b]Water weight x 100/weight of dried sample. Table modified from (Smart et al., 2017) with added moisture values for the second, third and fourth set of test modules.

Module ID	Deployment time [years]	Target dry bentonite density before emplacement [kg m^{-3}]	Moisture [%] wet weight[a]	Moisture [%] dry weight[b]	Water activity a_w
1	1.5	1450	24.3	32.1	0.956 (±0.0104)
2	1.5	1250	28.9	40.6	0.984 (±0.027)
3	1.5	1550	22.6	29.3	0.950 (±0.014)
4	5.5	1450	22.3	29.7	-
5	5.5	1250	28.0	38.9	-
6	5.5	1550	23.0	29.8	-
13	2.5	1450	27.2	37.4	-
14	2.5	1550	24.0	31.6	-
15	2.5	1450	26.5	36.2	-
16	1.0	1450	23.8	31.5	-
17	1.0	1250	29.9	40.9	-
18	1.0	1450	24.6	32.6	-

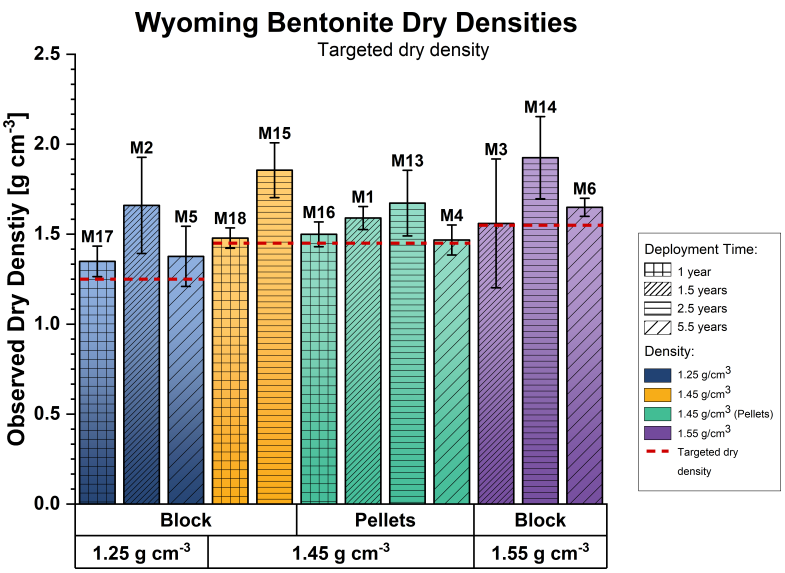

Figure 2.14 – Observed dry-densities of all deployed bentonite modules, including data from the first phase (Smart et al., 2017).

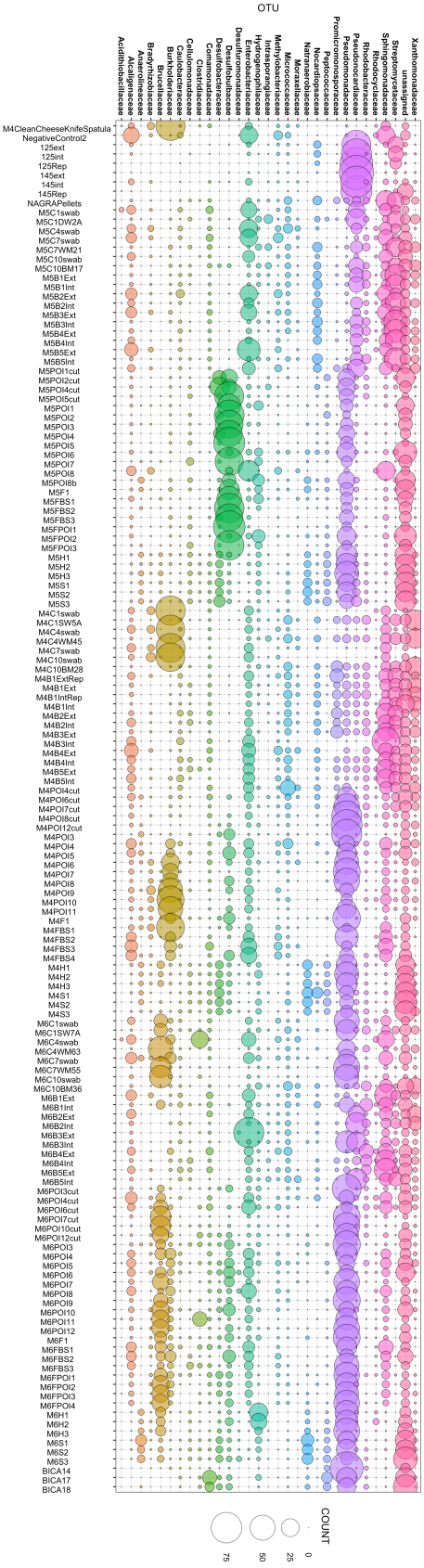

Figure 2.15 – Balloon plot of three 5.5-year modules, M5 (block bentonite at 1.25 g/cm^3), M4 (pellet-powder bentonite at 1.45 g/cm^3), M6 (block bentonite at 1.55 g/cm^3). Major OTUs on family level (more than 1% rel. abundance) for individual samples from all sampled locations are plotted: C = coupon bentonite or coupon swab, F = sintered filter inside(in)/outside(ex), POI = Point of interest on bentonite core surface e.g. black spots or shades on the bentonite core, H = module case holes for water exchange with the borehole, S = module case surface outside, exposed to the borehole, BICA14/17/18 are filtered borehole water samples. Only for the highest dry-density module M6 (1.55 g/cm^3), the coupon bentonite shares an OTU belonging to Brucellaceae with the bentonite core surface and the module holes and surface but not with the bulk bentonite. This effect was only observed in one module and thus needs confirmation from future longer timepoints and might be related to a temporary disturbance in the borehole system as it is only observed in a porewater sample of 2014, however it should be noted that the module design places the coupons relatively close to the bentonite core surface.

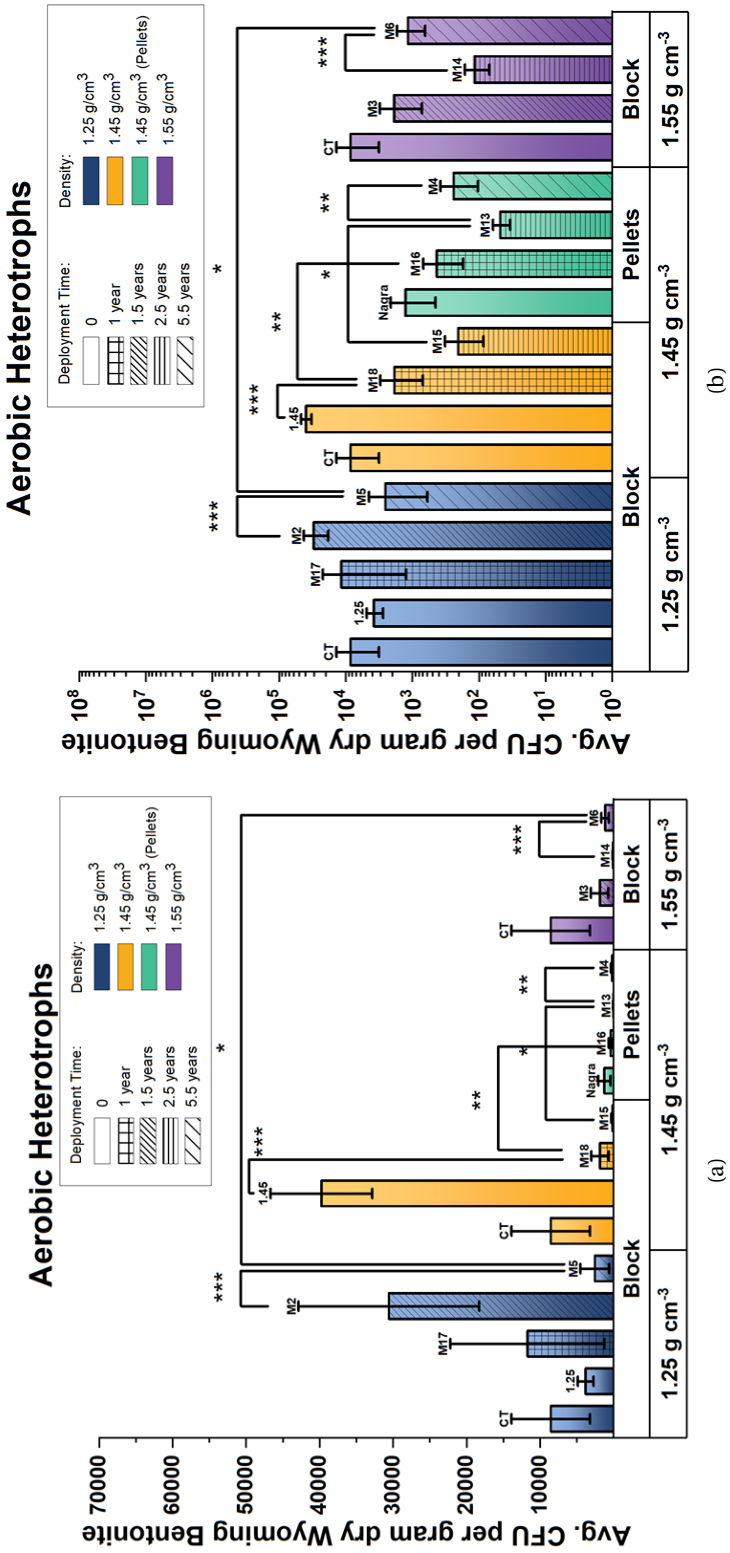

Figure 2.16 – Aerobic heterotrophs, averaged over the entire bentonite core (except for M13 for which one layer resulted in an CFU number 10-times higher than the other 9 samples of that module and was excluded), as a function of dry density, formulation and time. Data presented on a linear scale (a) and a log scale (b). Viable aerobic heterotrophs were averaged over all samples (interior and exterior bentonite core for all five layers), error bars represent standard deviation among all samples. Initial, undeployed samples are represented by solid bars (no pattern). CT pellets is the powder-pellet mix used to produce all blocks (blue, yellow, purple), Nagra denotes the undeployed time zero sample of the investigated powder-pellet mix, which was provided from Nagra (green). The highest counts of aerobic heterotrophs are found for the initial states (undeployed bentonite), 1.45 vs M18 ***p=$5.4 \cdot 10^{-4}$. Also, more counts were found for the lowest dry density (M5 (1.25 g/cm^3) vs. M6 (1.55 g/cm^3) *p=0.047). Furthermore, lower counts were found for the pellet-powder mix as compared to the blocks at the same dry density (M18 vs. M16 **p=0.002 and M15 vs. M13 *p=0.006). When comparing the deployment times, we observe only a significant decrease of aerobic CFU/g from 1.5- to 5.5-year modules for the 1.25 g/cm^3 blocks: M2 (1.5-years) vs. M5 (5.5-years) ***p=$2.5 \cdot 10^{-6}$, but no significant differences for the highest dry density blocks: M3 (1.5-years) vs. M6 (5.5-years) p=0.110, nor for the powder-pellet mix: M1 (1.5-years) vs. M4 (5.5-years) p=0.054. However, the 2.5-year modules are reported with very low CFU/g numbers, which increase significantly when compared with the following 5.5-year modules: M13 (2.5-years) vs. M4 (5.5-years) **p=0.001, and M14 (2.5-years) vs. M6 (5.5-years) ***p=$1.03 \cdot 10^{-6}$.

Remarks

We note that the modules representing the 2.5-year samples (modules 13-15) were assembled later than the modules representing the 1.5-year and 5.5-year samples (modules 1-6). Later assembly may have changed the microbial community, for example because of the different storage conditions of the bentonite blocks used for modules 14 and 15 and a different module assembly method for module 13. It cannot be ruled out that the decrease in viable microorganisms observed for the 2.5-year samples are due to the 18-month storage in a controlled argon atmosphere in case of M14 and M15, and for M13 and M16 due to a 5-day storage within argon prior to assembly, which was not the case for the pellets used to assembly M4. It is also possible that the decrease reported for the 2.5-year deployment is an artefact of the deployment time, due to different assembly procedures (the modules deployed for 1.5 and 5.5 years (and in the future, 8.5 years) were prepared and deployed at the same time). Confirmation of either trend will be sought from the upcoming 8.5-year samples. Modules 16-18, representing the one-year time point, were prepared even later than modules 13-15 and exhibit a more abundant viable cell count, however the bentonite blocks were produced immediately before the modules were assembled, similar to the modules 1-12, representing the 1.5- and 5.5-year samples and six modules to be investigated at later timepoints. Therefore, we can hypothesize that anoxic storage of bentonite for 18 months has drastically decreased the starting population of heterotrophic microorganisms (both aerobic and anaerobic). Similar, the higher CFU counts for the 5.5-years pellet module M4 compared to the 1- and 2.5-year pellet modules can be explained by the modified module assembly, leaving only the upcoming 8.5-year sample comparable to module M4. Currently, the only two sets of samples for which we have modules that were prepared at the same time and that represent the same dry density are low dry density modules M2 (1.5 years) and M5 (5.5 years) and the other represents the high dry density modules M3 (1.5 years) and M6 (5.5 years) which were discussed in the main text. Further timepoints will help to conclude whether this observed trend is sustained or a result of a potential artefact.

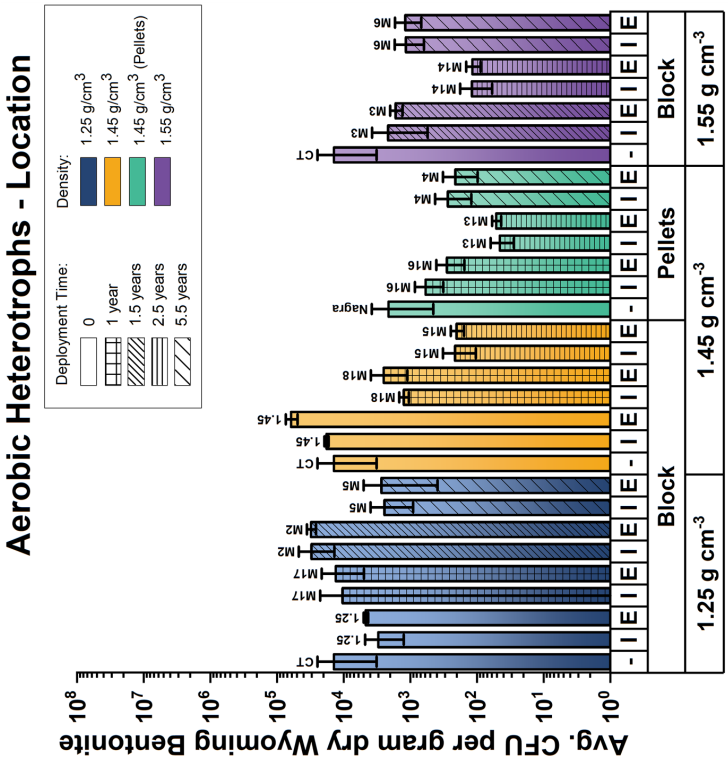

Figure 2.17 – Aerobic heterotrophs, separated between the interior and exterior samples of the core, as a function of dry density, formulation and time. Viable aerobic heterotrophs were averaged over all sampled layers but separated into the interior and the exterior of the bentonite core, error bars represent standard deviation amongst layers. Initial, undeployed samples are represented by solid bars (no pattern). The highest counts of aerobic heterotrophs are found for 1.5-year modules. Interestingly in the case of the lowest dry density (1.25 g/cm^3, blue) the counts after 1- and 1.5- year of deployment into an oxic environment are higher than the initial counts, indicating growth of aerobes enabled by bioavailable oxygen in bentonite. Similarly, the powder-pellet formulation showed comparable counts of aerobes to the initial state after 1.5-years of exposure to the borehole fluid. Only in the case of the 1.45 g/cm^3 blocks (yellow), the expected decrease in aerobe counts is observed. No initial bentonite block for the highest density could be investigated. The persistence of aerobes within bentonite, even after 5.5 years of exposure indicates possible bioavailable oxygen within the bentonite cores.

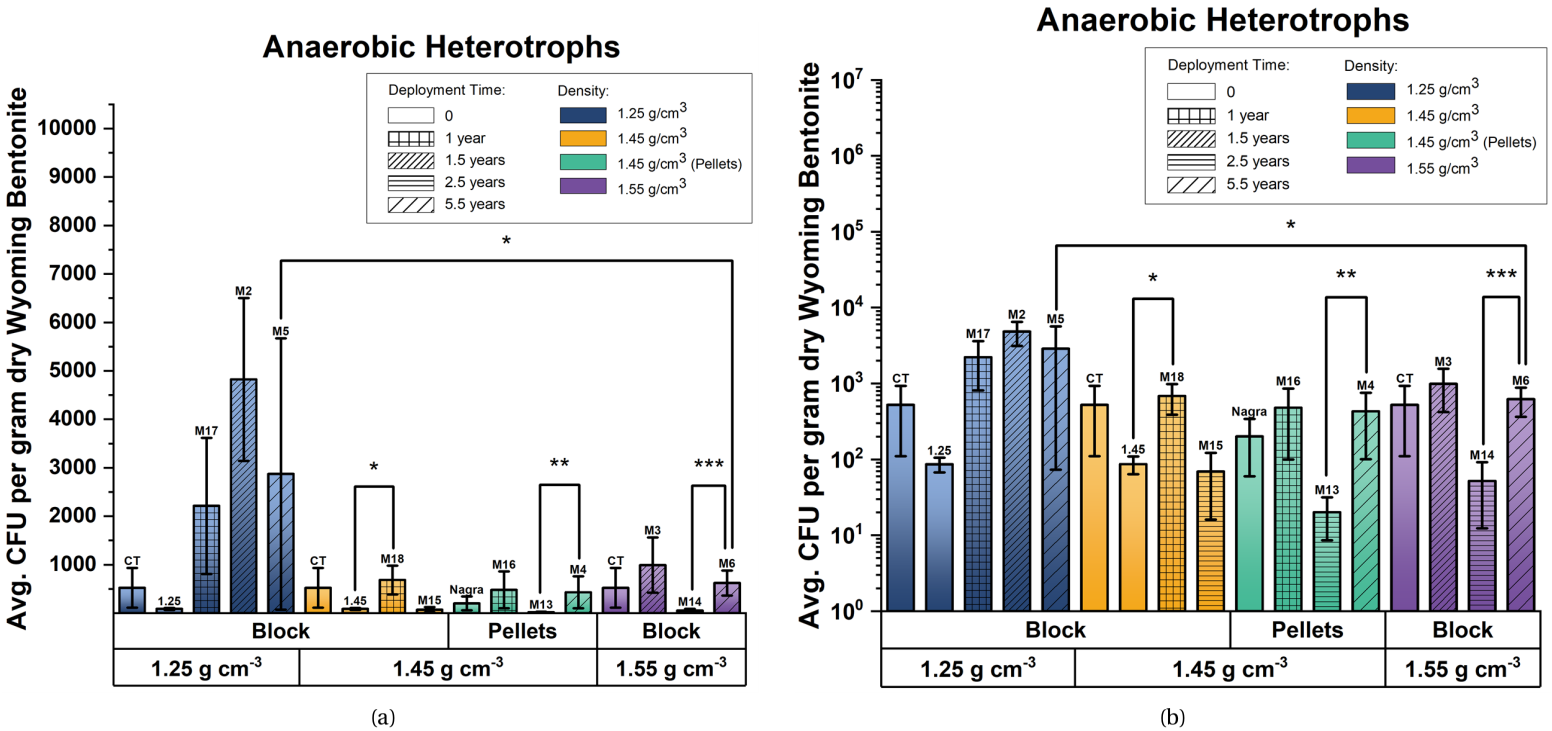

Figure 2.18 – Anaerobic heterotrophs, averaged over the entire bentonite core (except for M17 and M13 for which one layer resulted in an outlier CFU number 10-times higher than the other 9 samples of that module and was removed), as a function of dry density, formulation and time. Data presented on a linear scale (a) and a log scale (b). Viable anaerobic heterotrophs were averaged over all samples (interior and exterior bentonite core for all five layers), error bars represent standard deviation among all samples. Initial, undeployed samples are represented by solid bars (no pattern). They are represented by blocks labeled with the dry density achieved (the 1.55 g/cm^3 block sample is missing) and pellets. CT pellets is the powder-pellet mix used to produce all blocks (blue, yellow, purple), Nagra denotes the undeployed time zero sample of the investigated powder-pellet mix, which was provided from Nagra (green). The 1- and 1.5-year modules exhibit higher counts of anaerobic heterotrophs than the 2.5-year modules. However, there is no significant difference between the 1- or 1.5-year modules and the 5.5-year modules, indicating a persistent anaerobic community in bentonite. M3 (1.5-years) vs. M6 (5.5-years) p=0.056; M2 (1.5-years) vs. M5 (5.5-years) p=0.090. Significant is the increase from 2.5 to 5.5 years, M13 (2.5-years) vs. M4 (5.5-years) **p=0.0026; M14 (2.5-years) vs. M6 (5.5-years) ***p=$3.9 \cdot 10^{-6}$. The lowest dry density bentonite blocks (1.25 g/cm^3, blue, module M5) shows significantly more viable heterotrophic anaerobes than the highest dry density bentonite blocks (1.55 g/cm^3, purple, module M6) after 5.5 years of deployment, *p=0.027. Significant is the growth of anaerobes from undeployed bentonite 1.45 g/cm^3 (yellow) to the 1-year sample, 1.45 vs M18 (1-year) *p=0.027.

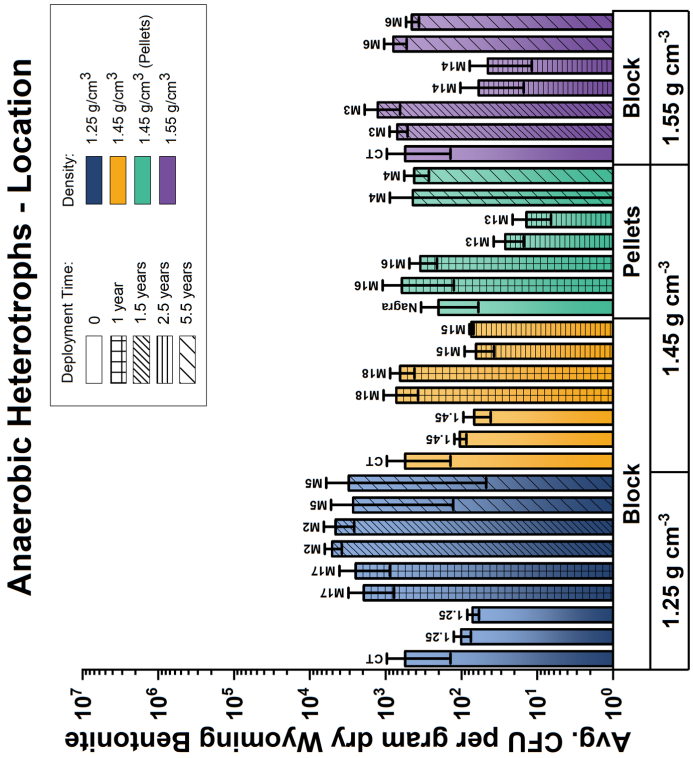

Figure 2.19 – Anaerobic heterotrophs, separated between the interior and exterior samples of the core, as a function of dry density, formulation and time. Viable anaerobic heterotrophs were averaged over all sampled layers but separated into the interior and the exterior of the bentonite core, error bars represent standard deviation amongst layers. Initial, undeployed samples are represented by solid bars (no pattern). The highest counts of anaerobic heterotrophs are found for 1- and 1.5-year modules. No significant differences between interior and exterior of the bentonite core could be discerned.

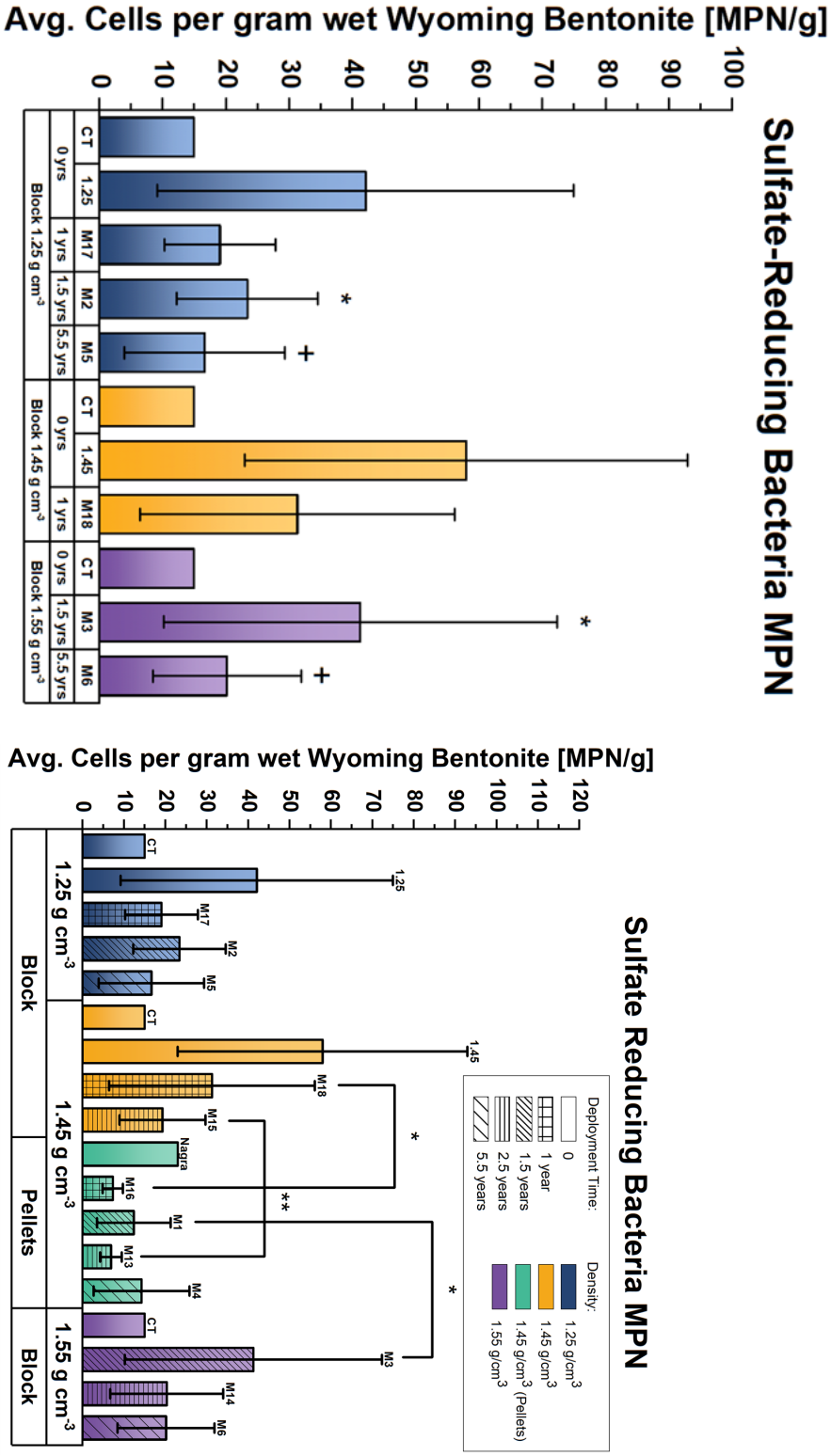

Figure 2.20 – Sulfate-reducing bacteria (SRB) (a); only block modules, (b), including powder-pellet modules, averaged over the entire interior and exterior bentonite core, presented on a linear scale, as a function of dry density and time. SRB most-probable numbers per gram bentonite were averaged over all sampled layers, error bars represent standard deviation amongst layers. Initial, undeployed samples are denoted CT (pellets used to produce blocks), 1.25 and 1.45 represents undeployed bentonite blocks. Due to the higher variance of the data for not-deployed bentonite, no significant differences could be discerned. ANOVA analysis of the 1.5, 5.5-year 1.25, 1.55 g/cm^3 four module dataset revealed no significant differences based on the bentonite density, but a significant difference due to deployment time, as the number of SRB decreased towards the 5.5-year timepoint.

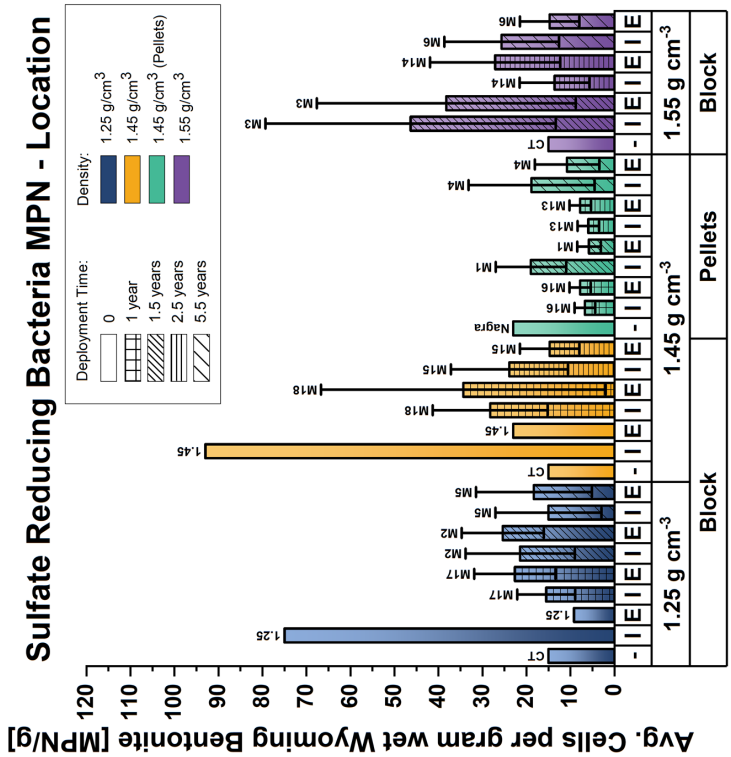

Figure 2.21 – Sulfate-reducing bacteria (SRB), separated between the interior and exterior samples of the core, as a function of dry density, formulation and time. SRB most-probable numbers per gram bentonite were averaged over all sampled layers but separated into the interior and the exterior of the bentonite core, error bars represent standard deviation amongst layers. Initial, undeployed samples are represented by solid bars (no pattern). The highest number of SRB were observed in the interior part of undeployed blocks, showing SRB counts 3-4 times higher than the SRB counts observed in the pellet-powder material (CT Pellets, yellow) which was used to press the blocks. This indicates that the block pressing procedure is a source of additional SRB. Comparing the deployed modules, no significant differences in the number of SRB from the interior vs the exterior of the bentonite core could be found.

DNA semi-quantification from bentonite gave only limited insight into the abundance of microbial life because many quantification attempts failed due to the very low biomass and thus low starting DNA material. A significant decline in 16S rRNA copy number can be observed from the initial bentonite samples for the lowest dry density blocks (1.25 g/cm^3) when compared with the modules deployed for one year (M17, *p=0.022) and for 5.5 years (M5, *p=0.026), Figure 2.22. Similarly, for the medium dry density a significant decline in 16S rRNA copy number was observed when comparing the initial sample (1.45 g/cm^3, yellow) with the modules deployed for one year (M18, yellow, *p= 0.017) and for 2.5 years (M15, yellow, *p=$5 \cdot 10^{-6}$). As already observed from the cultivation of viable microorganisms, a significant increase of the number of 16S rRNA genes are observed from the 2.5-year to 5.5-year modules for 1.55 g/cm^3 blocks (M14&M6, purple, *p=0.041) but not for powder/block from 2.5-year to 5.5-year modules (M13&M4, green, p=0.080). Also, for the lowest dry density block (blue), no significant difference could be discerned when comparing 1-year to 5.5-year 16S rRNA gene copies, (M17&M5, p=0.393). DNA amplification, Figure 2.22, shows a decrease of 16S rRNA gene copies from the initial, unexposed bentonite, compared to the 1-year block modules, but no difference is observed for the pellet-powder formulation. This is in contrast with the enumeration of (an-)aerobic heterotrophs, which are shown to increase, see Figures 2.16 and 2.18. Confirmed is the increase of microorganisms from the 2.5-year modules to the longer deployed 5.5-year modules. However, the amount of 16S genes appears relatively stable over all sampled modules (1 year, 2.5 and 5.5 years), which is not surprising as the detection of DNA does not allow conclusions about the microbe viability. For example, dead bacterial cells lyse, liberating their DNA which then can be adsorbed by bentonite clays and thus stabilized over long timeframes, nevertheless, their signature is picked up in a molecular biological analysis (Engel, Coyotzi, Vachon, et al., 2019; Greaves & Wilson, 1969).

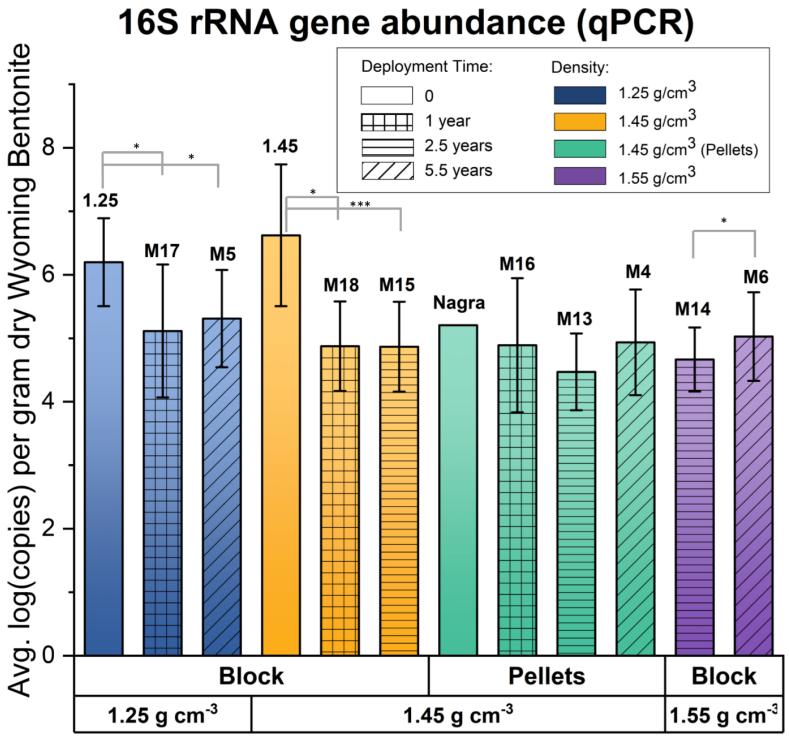

Figure 2.22 – 16S rRNA gene semi-quantification of bulk bentonite samples from all 1 year, 2.5 and 5.5 years bentonite modules.

3 Growth inhibition of sulfate-reducing bacteria in sterilized Wyoming bentonite under *in-situ* conditions

Niels Burzan

Environmental Microbiology Laboratory (EML), Ecole Polytechnique Fédérale de Lausanne (EFPL), Switzerland

Experimental work was performed by the student with help by Manon Frutschi during sampling. BET analysis were performed by Lionel Sofia, IC and ICP-MS analysis of water samples were performed by Karine Vernez Thomas and Sylvain Coudret, EPFL, Lausanne, Switzerland. 16S rRNA gene-library sequencing was performed by the team of the Lausanne Genomics Technologies Facility (University of Lausanne, Switzerland). The content of this chapter is under manuscript preparation for submission to Frontiers in Microbiology, Section Terrestrial Microbiology with contributions by the following co-authors in addition to the student: Rizlan Bernier-Latmani, Nikitas Diomidis, Manon Frutschi, Barbora Bartova, Bharti Reddy and Andrew Rance.

Abstract

A follow-up experiment (Phase 4) within the framework of the Iron-Corrosion experiment A (IC-A), which was presented in the previous Chapter 2, was conducted and revealed a strong inhibitory effect on sulfate-reducing bacteria within pre-sterilized Wyoming bentonite MX-80. The results highlight the challenging environment for microorganisms within an important engineered barrier for the Swiss radioactive waste repository. Artificially amended, bentonite-derived sulfate-reducing bacteria were not able to colonize powder-pellet MX-80 Wyoming bentonite of a 1.45 g/cm^3 dry-density likely due to the known swelling of bentonite clays upon saturation with natural Opalinus Clay rock porewater as well as due to the presence of O_2 trapped on bentonite. In this experiment, even in the absence of an indigenous bentonite microbiome, the borehole microorganisms did not grow into the bentonite cylinder within 365 days of exposure. Instead, they thrived on the surface of the cylinder, presumably due to the leaching of organic compounds from the irradiated bentonite, and the release of H_2 produced from the radiolysis of water during the gamma irradiation process and adsorbed

to the clay. A borehole water-derived microbiome composed of sulfate-reducing bacteria and fermenting microorganisms such as *Pseudomonas* was shown to colonize the bentonite surface. Additionally, these microorganisms likely catalyzed sulfate reduction, leading to the precipitation of mackinawite and pyrite near or at the bentonite surface. The results obtained from the fourth phase provide further insights into the co-evolution of the bio- and geosphere in the near field of a high-level waste repository, novel findings on radiation-mediated enhancement of microbial activity at the bentonite interface, and further indication of the inhibition of sulfate-reducing bacteria.

3.1 Introduction

The iron-corrosion experiment (IC-A) focuses on *in-situ* corrosion rates of carbon steel and copper, both potential canister materials for spent nuclear fuel and high-level radioactive waste. These materials are to be embedded in Wyoming bentonite MX-80 and saturated with Opalinus Clay porewater. More specifically, spent fuel packed within a carbon steel canister will rest on pre-compacted blocks of bentonite (at a dry-density of 1.55 g/cm^3) within a gallery excavated in Opalinus Clay rock and backfilled with bentonite pellets (1.45 g/cm^3). The host rock-bentonite interface will potentially contain areas of lower density such that porewater can accumulate and space and nutrient availability may allow the indigenous and anthropogenically-introduced microorganisms to grow.

The experimental setup of the IC-A experiment aims to mimic the conditions expected upon closure of a deep geological repository for radioactive waste in Switzerland. It consists of metal coupons embedded in Wyoming bentonite of different dry densities (1.25, 1.45, 1.55 g/cm^3) and two formulations (pre-compacted blocks or powder/pellet mix). Test coupons and bentonite are placed within stainless steel modules and submerged in a borehole drilled vertically down from the gallery of the Underground Research Laboratory (URL) 'Mont Terri', Saint-Ursanne, Switzerland. The bentonite-filled modules are in diffusive exchange with Opalinus Clay porewater that accumulated in the borehole. The module deployment schedule for IC-A is shown in Figure 3.1.

3.1.1 Previous findings

The experiment was initiated in October 2013 and is composed of five phases (including phases zero prior to any module deployment) so far, Figure 3.1. Previous phases (1-3) were reported on earlier within peer-reviewed journals (Frutschi et al., 2016; Smart et al., 2017) and as reports from EPFL to Nagra (Burzan et al., 2018; Burzan et al., 2020), and is presented within this thesis, as Chapter 2. For the context, a short summary of the findings to date is provided below.

Phase 1: 1.5 years post-deployment, consists of microbial analysis of modules M1, M2, and M3 and concluded that the microbial viability decreases as the bentonite dry density increases

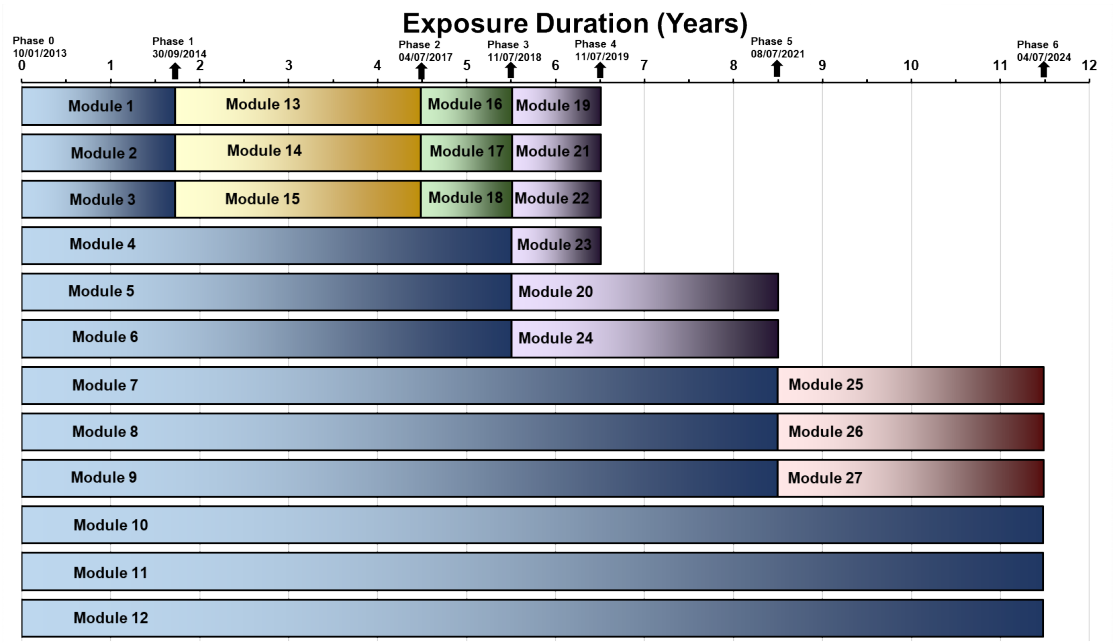

Figure 3.1 – Experimental time plan with 12 modules (1 to 12) initially deployed. Phase 1: Three modules (M1, M2 and M3, blue) are retrieved after 1.5 years and replaced with another set of three modules (M13, M14 and M16, yellow) which were prepared in a different way. Phase 2: One set of modules (M13, M14 and M15) are removed and replaced by another set (M16, M17, and M18, green). Phase 3: a set of six modules was removed and consisted of three green (M16, M17, and M18) and three blue (M4, M5, and M6) modules and were replaced by six phase-4 modules (purple, M19-M24). Phase 4: four of the phase-4 modules (M19, M21, M22, and M23) were retrieved after one year.

and that no sulfate-reducing bacteria (SRB) growth was observed (Smart et al., 2017) and as report from EPFL to Nagra by (Frutschi et al., 2016).

Phase 2: 2.5 years post-deployment (modules M13, M14, and M15) resulted in the lowest number of viable microorganisms reported and a microbiome that diverges from that of previous years, most likely due to distinct module preparation. The findings are presented within Chapter 2 of this thesis.

Phase 3: consists of the 1-year (M16, M17, and M18) and 5.5-year modules (M4, M5, and M6). The block sample preparation was identical to that in Phase 1 for both the 1- and 5.5-year samples but occurred at different times. The blocks for the 5.5-year deployment were prepared immediately prior to deployment in 2013 while the blocks for the 1-year deployment were prepared in 2017, immediately prior to that deployment. Because the deployment of the 1-year and the 5.5-year blocks occurred 4.5 years apart, it might have resulted in their exposure to distinct microbiomes on the bentonite core surface and all module surfaces (see below).

Additionally, the powder/pellet sample preparation was modified for each phase, resulting in

the inadequacy of side-by-side comparisons of modules with this bentonite formulation over time.

Thus, it was only possible to directly compare the 5.5-year block bentonite modules (Phase 3) with the 1.5-year block bentonite modules from Phase 1, as presented in Chapter 2. The moment of deployment is of critical importance due to the observed dynamics of the borehole water microbiome from 2013 to 2017: Initially dominated by SRB genera such as *Desulfotomaculum*, there was a shift in the community to the vast dominance of a heterotrophic genus related to *Pseudomonas stuzeri*. This shift in the community could have been due to the depletion of readily available electron donors such as hydrogen and low-molecular weight organic acids which may have led to the decrease of the SRB population. Alternatively, organic compounds leaching out of the deployed modules might have favored *Pseudomonas*, which tend to be able to degrade complex organics. Indeed, Wyoming bentonite has been shown to leach complex, recalcitrant organic molecules (Maanoja et al., 2020). Within the following three years, up to 2017, the community composition continued to change, increasing in diversity, and appearing to stabilize based on the DNA profiles obtained for 2018 and 2019. Phase 3 revealed that the bentonite microbiome is composed of aerobic and anaerobic heterotrophs and that bioavailable oxygen, trapped within bentonite, could be a reason for the persistence and viability of aerobes and the inactivity and decreasing viability of sulfate-reducing bacteria, which is a beneficial outcome in terms of potential microbially-enhanced corrosion. The results are presented in Chapter 2 of this thesis.

Phase 4: This Chapter presents the results from Phase 4.

3.1.2 Goals of the phase 4 study

As established in previous publications related to the IC-A experiment (see (Bagnoud, de Bruijn, et al., 2016; Frutschi et al., 2016; Smart et al., 2017) and Chapter 2 of this thesis) there are two major pools of microorganisms under *in-situ* conditions: The microorganisms originating from the host rock and those originating from the bentonite. Here, we present the results of Phase 4 of the IC-A experiment. The goal of this study was to discern the relative influence of the two pools of microorganisms.

The specific questions posed were:

(1) Do the communities observed within bentonite during Phases 1 to 3 originate exclusively from the sourced bentonite?

(2) Is the colonization of bentonite with porewater microorganisms possible and, if so, to what extent? That is, will Opalinus Clay rock microorganisms play an important role in a long-term potential microbially-enhanced corrosion?

(3) Will an active microbial community at the vicinity of bentonite enhance corrosion for instance by diffusion of sulfide into the bentonite?

3.2 Materials & Methods

Details of module preparation are provided in the module and deployment report by Wood PLC (now Jacobs Engineering Group) and EPFL to Nagra (Reddy & Burzan, 2018). A summary of the used materials and methods is proved in the subsections below.

3.2.1 Bentonite sterilization and module assembly

Nagra provided bentonite from their stock of MX-80 Wyoming bentonite (power/pellet mixtures) used for the Full-Scale Emplacement (FE) experiment (Müller et al., 2017). A batch of this bentonite was gamma-irradiated with a Cobalt-60 source at the laboratories of Wood PLC/Jacobs Engineering Group at Harwell, Oxfordshire, UK. A minimum dose of 50 kGy was selected to ensure sterility of the bentonite based on work conducted on soil (McNamara et al., 2003). This dose was applied to individual bentonite samples in closed borosilicate glass bottles containing between 222.8 *g* and 533.4 *g* of bentonite. For all modules, the targeted bentonite dry-density is 1.45 g/cm^3. A sample of bentonite pre-amended with a culture of SRB (see origin of culture in section below) was also subjected to the same irradiation. After the irradiation, the glass bottles with sterile bentonite were shipped to Switzerland.

Cultivation efforts from irradiated bentonite with and without the microbial amendment showed no growth for anaerobic/aerobic heterotrophs nor for sulfate-reducing bacteria, confirming that 50 kGy successfully sterilized the bentonite. Module assembly took place within a sterile laminar flow box. All metallic parts of the module and the sintered steel filter were wrapped in autoclavable plastic bags and autoclaved (80 minutes) and dried for 24h at 60°C. Any residual water evaporated during the module assembly in a sterile laminar air flow.

The module layout is presented in Figure 3.2 and a summary of the discussed modules and their individual modifications in Table 3.1. All modules received sterile bentonite but each had a specific feature to probe a specific question. Module 19 (M19) was open to the borehole water, potentially allowing colonization of bentonite by those microorganisms. M21 contained sterile bentonite amended with a microbial community obtained from unirradiated bentonite (see details below). This module was also open to borehole water and was intended to represent the impact from both pools of microorganisms. M22 did not receive a microbial amendment and included a membrane that was intended to block the transport of microorganisms from the borehole water towards the bentonite. Lastly, M23 received the microbial amendment post-sterilization and included the membrane. It was designed to isolate the role of the bentonite community.

All module lids were fitted with water-tight rubber rings such that water-tight sealing of the modules was achieved – with the only possible water exchange path being the water entrance holes along the cylindrical module, Figure 3.3. These rubber rings, the steel and copper test coupons, tools and gloves were disinfected with 70% ethanol on a regular basis during preparation and prior to emplacement to minimize potential contamination.

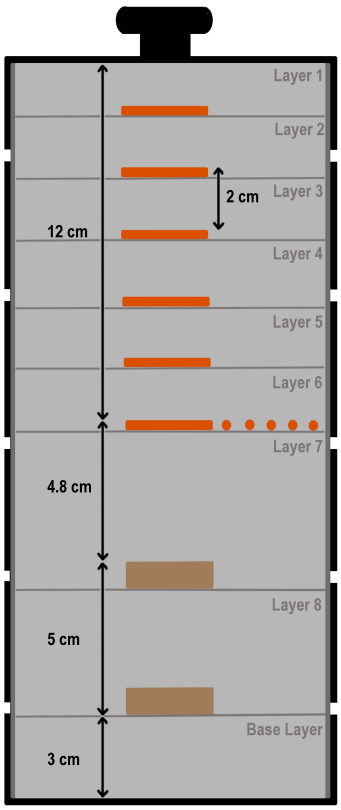

Figure 3.2 – Module layout: two carbon steel coupons (brown) at the interface of the base layer and layer 8 and of layer 8 and layer 7. For the SRB-spiked modules, no SRB were added to layers 6 and 7 in order not to influence the H_2S-Cu diffusion experiment (Cu-balls, orange circles), performed in parallel to the microbial analysis and not part of this thesis. The remaining layer were equipped with copper coupons (orange).

3.2.2 Bentonite humidity, free swelling test, dry-density

Bentonite water content was determined by obtaining the bentonite wet and dry mass (the latter after 24h in an oven at 105°C). Similarly, for representative pieces of bentonite obtained from the modules after exposure, the volume and mass while moist was measured in order to determine the dry density as explained in Chapter 2 of this thesis and in the report to Nagra by (Burzan et al., 2020). Free swelling tests were performed on irradiated bentonite and compared with non-irradiated bentonite of the same Nagra batch. The free-swelling test procedure was previously described in (D. J. Nixon et al., 2015).

3.2.3 Membrane modules to control influx of microorganisms

As mentioned above, some modules received a membrane with the goal to exclude borehole-derived microorganisms while maintaining the diffusive exchange of soluble substances between bentonite and Opalinus Clay rock. Strips of DURAPORE® Membrane Filter (0.22 µm

Table 3.1 – Module setup with added bacteria, membrane, glue and amount of bentonite. The bentonite around the copper coupons did not received a bacterial amendment not to interfere with sulfide-diffusion observations (not part of this thesis).

Module number	Experimental setup	Sulfate-reducing bacteria (MPN/g)	DURAPORE® membrane	ARALDITE rapid®	Total mass of bentonite [g]
19	Biotic, borehole communities	0	No	Yes	2561.7
21	Biotic, bentonite & borehole communities	2.57×10^3 - 2.57×10^5	No	Yes	
22	Abiotic, sterile control	0	Yes	Yes	
23	Biotic, bentonite communities	2.57×10^3 - 2.57×10^5	Yes	Yes	

poresize) made of hydrophilic and autoclavable polyvinylidene fluoride (PVDF) (Merck KGaA, Darmstadt, Germany), were glued to the inner part of the module for three of six modules. A pre-test established the compatibility with the autoclaving procedure and subsequent water-tightness by immersion into a water-filled bucket. The water-permeable membranes allowed only a slow water entry into the module interior. The membrane-modules were equipped with sintered steel filters (with a slightly smaller diameter than those used in previously deployed modules as the ones presented in Chapter 2 of this thesis; from ⌀106/100 × 250 mm to ⌀102/96 × 248 mm) to make sure that the membrane remains intact during the module assembly. Between 15 and 20 mL of glue was applied to all modules regardless of the presence of a membrane to create similar conditions for the case that the glue could be degraded by the microorganisms. The used glue was a resin commercially available as ARALDITE® Rapid (Huntsman Advanced Materials, Huntsman International LLC, The Woodlands, Texas, U.S.A.).

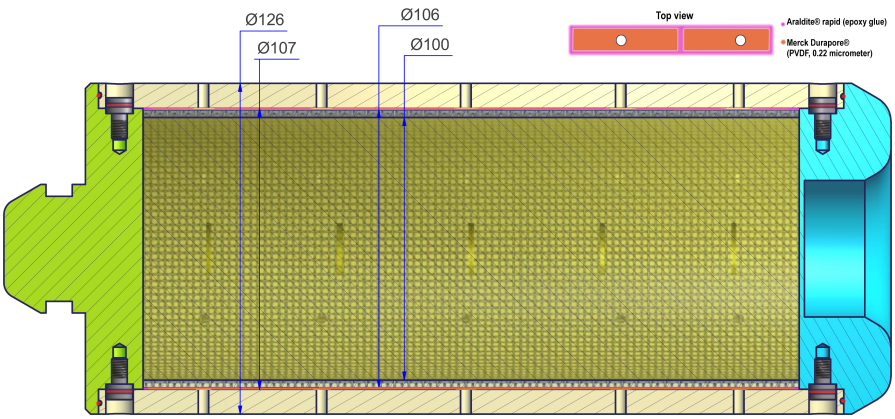

Figure 3.3 – Strips of Durapore® membrane were glued to the inside of some modules, covering the water entrance holes. At the module lid, bottom and around the screws holding them, rubber O-rings were added to achieve water-tightness.

3.2.4 Cultivation of bacteria

A microbial community was added to several modules to mimic the anaerobic bentonite microbiome with special emphasis on sulfate-reducing bacteria. The community was obtained within an anoxic glovebox by amending one laboratory spatula-spoon of MX-80 Wyoming bentonite (Nagra powder-pellet batch) to each of three anoxic bottles containing 100 mL Postgate's Medium B for SRB. The 3 bottles were incubated at 37°C in an anoxic glovebox for 20 days. After this pre-culture, three bottles, each containing 500 mL Postgate's Medium B for SRB, were amended with either 10 or 5 mL from the pre-culture bottles (depending on how well they grew), and incubated as previously. After 15 days of incubation, growth was observed in all bottles and a black precipitate was evident to the naked eye. Two liters of fresh Postgate's medium B was prepared and amended with 5 ml of culture from the darkest of the three intermediate incubation bottles.

After a growth period of 10 days, the SRB were harvested and 500 mL of culture was transferred into clean centrifuge flasks disinfected with 70% ethanol. A pellet of microorganisms was obtained by centrifugation at 5,000xg at 4°C for 30 minutes. Under a laminar flow hood, the microbial pellet was resuspended in 1x sterile, anoxic PBS and stored overnight in 50mL sterile Falcon tubes at 4°C. Prior to addition to the bentonite in the test modules, a second centrifugation was performed at 5,000xg at 4°C for 20 min and the pellet resuspended 1x sterile, anoxic PBS. Cells in the resuspended SRB pellet were enumerated by MPN number determination post-deployment. The used MPN method was identical to the one described in Chapter 2 of this thesis. Due to the high cell density in the culture (both vegetative cells and spores), the MPN method provided a rather big range for the SRB cell number, as shown in Table 3.1 and below in the Results section.

The addition of the bacteria was done in a drop-wise manner, assuming that 1 drop=50 µL. A dilution of SRB was prepared for each layer (as some vary in the mass of bentonite) such that four drops of the correct cell density could be added to the respective layer. Four drops were added to each quadrant of the circular layer of the cylinder approximately in the middle of each quadrant.

3.2.5 Module deployment, retrieval

After assembly, the modules were transferred to the antechamber of an MBraun LABstar glovebox (M. Braun Inertgas-Systeme GmbH, Garching, Germany) anoxic glovebox in which six cycles of vacuum and nitrogen (changing slowly the pressures to not disrupt the added membrane) were applied. The modules remained in the glovebox for a duration that varied between 22 hours (M23) and three days (M19). Within the glovebox, sterile (autoclaved), anoxic artificial Opalinus Clay rock porewater was used for a ten-day pre-saturation of the modules, the composition of the artificial porewater was based on (Pearson et al., 2003). The pre-saturated modules were then sealed within two layers of a thick Mylar® foil and transported to the URL 'Mont Terri' for immediate deployment. The placement of the modules

was performed under constant argon gas flow to the borehole to maintain anoxic conditions. After closing the borehole by placing back the borehole packer, the borehole was pressurized with 10 bar of argon gas.

After 1 year of deployment, Figure 3.1, four modules (M19, M21, M22, and M23) were retrieved. Immediately upon retrieval, the module surface and water exchange holes were sampled with forensic swabs (Sarstedt, Nümbrecht, Germany) for subsequent DNA analysis. The modules were then placed in sterile autoclaved transport flasks, two liters of borehole water added to the flask, and the gas phase replaced with Ar gas filtered through a 0.5 µm filter. Module disassembly and bentonite sampling started two weeks later.

3.2.6 Porewater chemistry, DNA analysis

The chemical analysis of the porewater, DNA extraction from borehole porewater, DNA extraction from bulk and coupon bentonite, DNA extraction from swab samples and the 16S rRNA gene V4 region amplification of the borehole porewater were performed identically to the methods presented in Chapter 2 of this thesis.

3.2.7 Bentonite sampling, microbial cultivation, DNA extraction from bentonite and DNA sequencing

The sampling of the modules was identical to the presented one in Chapter 2 of this thesis except for the bentonite obtained for cultivation and DNA analysis. Cutting tools such as a commercial cheese knife (Victorinox AG, Ibach, Switzerland) and do-it-yourself store available spatula were cleaned with a 3% bleach solution, rinsed with sterile, DNA-free (80-minutes autoclaved) MilliQ water and vacuum-dried within a glovebox antechamber, shortly before utilisation. Sterile, DNA-free (80-minutes autoclaved) cleanroom-grade swipes (Spec-Wipe® 7, VWR International LLC, Avantor Inc., Radnor, Pennsylvania, U.S.A.) were used for the cleaning of cutting tools and to protect them by covering them within the glovebox and during the vacuum drying. Inside the glovebox, the workplace was covered in these cleanroom-grade swipes to minimize potential contamination. Instead of slicing the bentonite cylinder perpendicularly to the cylinder axis (i.e., parallel to the basis plane) like in previous phases, the following dissection was performed. First, the middle part of the bentonite cylinder (containing copper balls) was removed, followed by the sampling of the upper and lower parts of the bentonite cylinder. The top and bottom parts of the cylinder were cut lengthwise, parallel to the central cylinder axis, but at a safe distance from the coupons, obtaining two lengthwise cuts for each half-cylinder. The four subsamples obtained were carefully placed in sterile sampling bags, double-sealed in argon-filled Mylar® bags and stored at 4°C until dissection. Unlike for previous phases, the separation between the interior or exterior of the bentonite was not performed.

The DNA sequence analysis was improved relative to previous IC-A microbiome characteriza-

tions as presented in Chapter 2 of this thesis by choosing a longer fragment of the 16S rRNA gene, which includes the V3 and V4 region rather than the V4 region only. Therefore, the DNA-based microbiome data are presented at the genus rather than the family level. Comparisons with the previous phases are still possible (and were performed) at the family level. The 16S rRNA gene-library was sequenced on an Illumina MiSeq (Illumina Inc., San Diego, California, U.S.A.) platform by the team at the Lausanne Genomics Technologies Facility (University of Lausanne, Switzerland), applying 10 pM of the 16S-library with a 15% Phi-X spike in a paired-end 300bp mode.

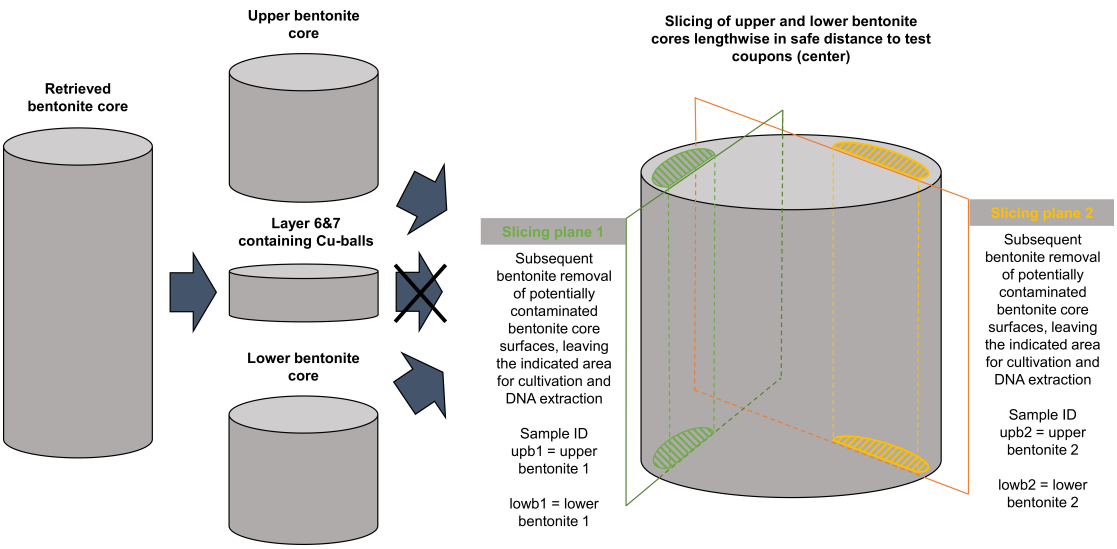

Figure 3.4 – Bentonite core sampling procedure within gloveboxes. Four bulk bentonite samples for cultivation and DNA extraction were obtained from each bentonite core.

3.2.8 Oxygen desorption and specific surface area

Oyxgen bound to bentonite, sealed within nitrogen-gas filled serum bottles was analysed by using the following gas chromatography system: GC-450 (Varian, Middelburg, The Netherlands) equipped with a molecular sieve column (CP81071: 1.5m*1/8” ultimetal molsieve 13 9 80-100 mesh). Oxygen was detected by a thermal conductivity detector.

BET analysis were performed by Lionel Sofia of the service department of the Laboratory of Construction Materials (LCM) at EPFL, Lausanne, Switzerland. Bentonite samples were sieved for particles smaller than one millimeter and dried in an oven for two hours at 200°Celsius. A TriStar II Plus system (Micromeritics Instrument Corporation, Norcross, Georgia, USA) was used to determine the specific surface area.

3.3 Results & Discussion

3.3.1 Porewater chemistry

Analysis of the borehole water indicated low levels of dissolved sulfide and reduced iron(II), indicative of potential precipitation reactions within the borehole and consistent with findings from previous phases, Table 3.2. The presence of acetate at 0.2 mM may be indicative of acetogenic metabolism within the borehole. Alternatively, acetate may originate from the surrounding Opalinus Clay host rock (Courdouan et al., 2007). This analyte was not considered at earlier timepoints.

3.3.2 Porewater microorganisms

The porewater microbiome evolution can be seen in the heatmap, Figure 3.5. The borehole water sample obtained at the retrieval of the phase 4 modules, in July 2019, confirmed the observed stabilization of the borehole community observed from 2017 to 2018. This is evidenced by the more diverse community and the stable contribution of SRB to the community. The dominant operational taxonomical units (OTUs) continue to belong to the family Pseudomoadaceae, along with large contributions from Peptococcaceae and Desulfobulbaceae.

3.3.3 Humidity, free swelling and increased bioavailable electron donors in irradiated bentonite

Humidity, free swelling, irradiation Visual inspection of the irradiated bentonite revealed that larger aggregates of MX-80 had disappeared after the exposure to gamma rays. Also, the grey color was of a lighter shade. Thus, we suspected the desiccation of bentonite during irradiation. Indeed, 50 kGy of irradiation decreased the relative water content from 9.844±0.029% to 6.441±0.028% (n=6 each). Measurements also showed that irradiation increased the normalized free-swelling capacity of bentonite, i.e., the total volume after swelling per gram dry bentonite, from 14.2±1.2 mL to 15.3±1.5 mL. Hence, all bentonite used (in sterile and non-sterile modules) was first irradiated to ensure comparability across treatments. The observed decrease in the humidity may be indicative of radiolysis of water, a process also expected in the near-field of high-level waste and spent fuel (Barr & Allen, 1959; Gournis et al., 2000). Gas adsorption by smectite clay is documented (for H_2 (Edge et al., 2014), CH_4 and CO_2 (Grekov et al., 2020)) and recently also for O_2 (Giroud et al., 2018) and reported within Chapter 2 of this thesis; thus, the evolution of hydrogen from water radiolysis may also result in its adsorption by bentonite. In addition, several irradiation-induced changes to bentonite mineralogy have been documented (Gournis et al., 2000). It is also possible that high molecular-weight organic carbon present in bentonite (Maanoja et al., 2020), may be transformed to lower-molecular weight organic compounds upon irradiation.

Table 3.2 – Borehole BIC-A1 (Opalinus Clay rock porewater) chemical analysis of five time-points.

Component	January 2013 (Bagnoud, de Bruijn, et al., 2016)	September 2014	July 2017	July 2018	July 2019	Unit
Fe(II)	1.3	76.3 (Smart et al., 2017)	0.3	31.6	0.01	µM
H_2S	7.4		<0.1	<0.1	<0.1	µM
Co	<10		<50	<500	<500	µg L-1
Cu	13		<50	<500	<500	µg L-1
Sr	60.657		18.387	26.467	25.25	mg L-1
Ni	<10		69.3	<500	<500	µg L-1
Mn	53		125.9	<500	<500	µg L-1
Cr	31		<50	<500	<500	µg L-1
Zn	<10		<50	<500	<500	µg L-1
Al	<10		<50	<500	<500	µg L-1
Na^+	313.6	267.1	257.9	258.7	271.2	mM
NH_4^+	0.3		4.6	0.9	0.8	mM
Mg^{2+}	15.0	3.0	13.0	9.8	6.9	mM
K^+	1.9	9.0	3.8	3.4	3.3	mM
Ca^{2+}	18.8	15.3	12.3	13.4	15.9	mM
F^-	0.1		0.03	<0.005	<0.005	mM
Cl^-	290.3	226.5	264.6	274.8	281.1	mM
NO_2^-	<0.005		<0.005	<0.005	<0.005	mM
SO_4^{2-}	15.6	23.3	21.8	22.5	18.5	mM
Br^-	0.5		<0.005	<0.005	<0.005	mM
NO_3^-	<0.005		0.16	0.09	<0.005	mM
PO_4^{3-}	<0.005		0.04	<0.005	<0.005	mM
Acetate					0.2	mM
pH	8.2		8.30	8.45	9.23	
EH	-88	-88	-271.8	-230.1	-307.7	mV
DOC			39.75	18.72	40.59	mg/L
DIC			22.97	24.24	17.02	mg/L

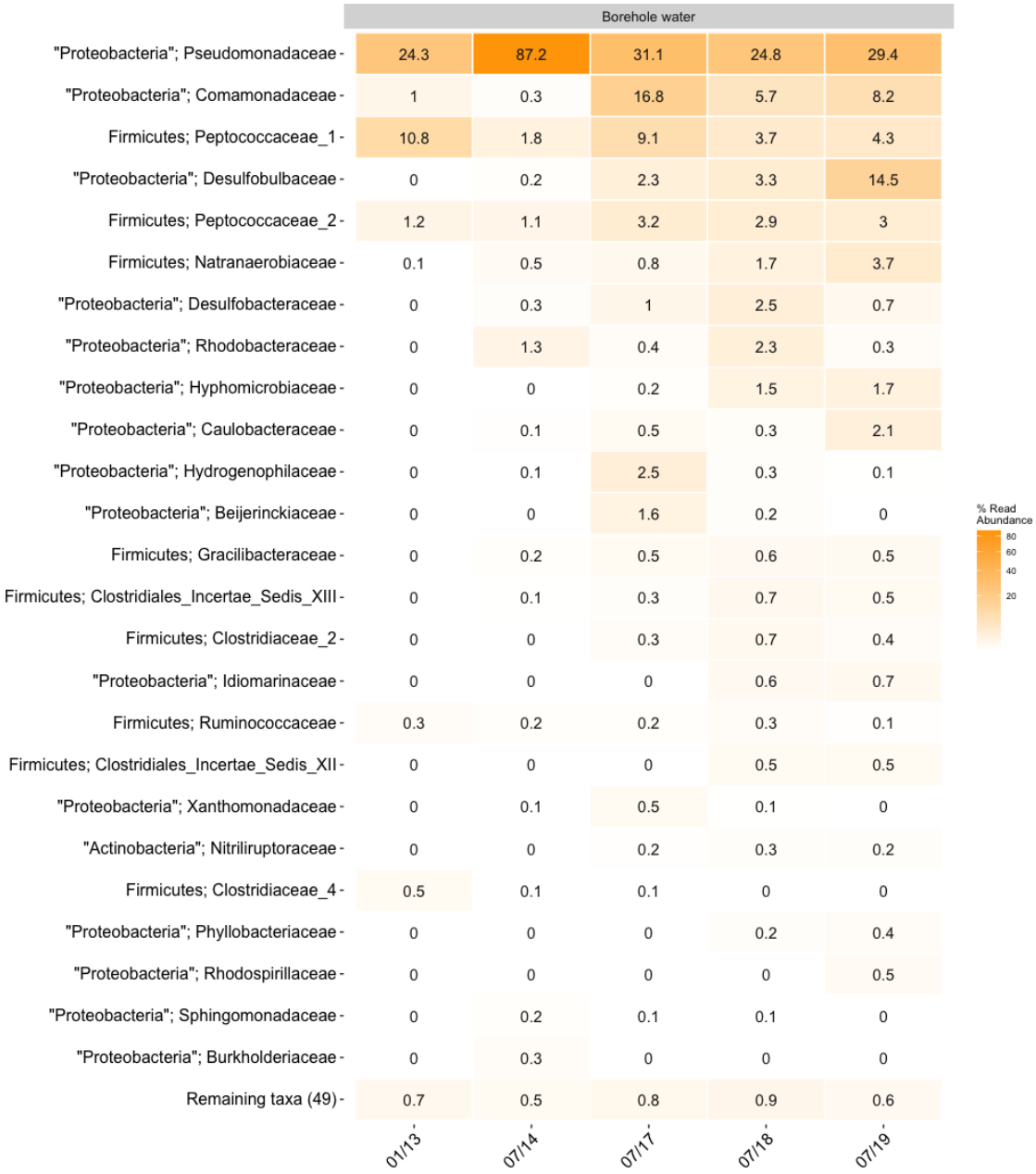

Figure 3.5 – BIC-A1 borehole water community based on the 16S rRNA gene V4 region. The y-axis shows the 25 most abundant OTUs of those shared amongst all samples at the phylum and family levels. The x-axis represents the time of collection of each sample. Only known taxonomic affiliations are shown. 'Remaining taxa' represent known taxa that are present at a lower abundance than the top 25.

Increased bioavailability of electron donors We speculate that upon saturation with Opalinus Clay borehole porewater, a fraction of the hydrogen and low-molecular weight organics may have leached out and thus acted as electron donors for borehole water microorganisms

at the bentonite cylinder and sintered steel filter interface. This hypothesis is put forth due to the accumulation of a black coating on the bentonite cylinder after only one year of deployment, Figure 3.6, when, in a previous one-year deployment of unirradiated bentonite, only a few black spots were observed on the bentonite surface, see Chapter 2. Thus, we suggest that additional electron donors are available to increase the rate of microbial activity at the bentonite surface to result in its accelerated discoloration. Areas at the weld of the sintered steel filter were covered with a particularly thick coating with what is presumed to be iron sulfide, Figure 3.6. This was confirmed by scanning electron microscopy (SEM) coupled with energy dispersive x-ray spectroscopy (EDS), which revealed hotspots of Fe and S, corresponding to FeS (perhaps mackinawite, Figure 3.7, Table 3.5) and FeS_2 (perhaps pyrite, Figure 3.9, Table 3.7) mineral grains, similar to previous reports (Maanoja et al., 2020; Pedersen et al., 2017). However, the variations in color in broad swaths of the bentonite surface observed with the naked eye do not appear to be exclusively related to the iron and sulfur content as only slight increases in the sulfur signal were detected by EDS in bentonite regions of darker color compared with areas of native color, Table 3.7. Thus, these findings suggest that the dark coloration on the bentonite surface is not due exclusively to iron sulfide production but that the formation of these minerals is part of the processes underway.

3.3.4 Deployed bentonite water content and dry-densities

Water content and dry-density Irradiated bentonite exhibited greater variability in both water content and dry density as compared to the equivalent unirradiated bentonite deployed under the same conditions, as presented in Chapter 2. The deployed bentonite water content of all four modules (n=32) averaged 25.7±0.17%. In contrast, non-sterile bentonite deployed for 1 year in the same borehole exhibited an average of 25.5 ±0.05 (n=6) . The average observed dry density of the sterilized bentonite of all four modules (n=31) was measured to be 1.49 g/cm^3 (standard deviation of 0.16 g/cm^3), Table 3.3, while for the equivalent unirradiated bentonite system (n=6) is reported with an average of 1.50 g/cm^3 (standard deviation of 0.07 g/cm^3).

The higher variability in water content and dry density of the irradiated bentonite may be related to variable and spatially heterogeneous changes in the mineralogy due to heterogeneous irradiation (Gournis et al., 2000).

3.3.5 Oxygen availability and specific surface area

Three 300g aliquots of irradiated bentonite were sealed in gas-tight glass bottles and flushed with nitrogen and stored in dark at room temperature. The gas phase was analyzed every 24h using a gas chromatograph. At each sampling, the removed volume of gas was replaced with nitrogen. No further flushing of the gasphase was performed. After the experiment, BET analysis was performed to estimate the specific surface area of three bentonite samples The results are shown in Table 3.4.

Table 3.3 – Bulk bentonite water content (relative to the wet mass) and achieved dry density after deployment of all four modules M19, M21-23. All four modules were designed for a target dry-density of 1.45 g/cm^3.

Module	water content$_{wet}$ [%]			dry density [g/cm^3]		
	number of observations	Avg.	std. dev.	number of observations	avg.	std. dev.
M19	8	25.65	0.95	8	1.464	0.15
M21	8	26.39	0.71	8	1.471	0.10
M22	8	25.25	0.46	7	1.478	0.12
M23	8	25.45	0.32	8	1.546	0.24
overall	**32**	**25.7**	**0.78**	**31**	**1.490**	**0.17**

Table 3.4 – BET analysis and maximum observed O_2 concentration in a bentonite-gas desorption experiment. Values for non-irradiated bentonite (denoted as avg. bentonite) are presented in Chapter 2

Sample	BET surface area	max O_2 (vol.% of gasphase) [after x days]
1 (irradiated)	31.15 m^2/g	0.091 [10d]
2 (irradiated)	33.73 m^2/g	0.094 [9d]
3 (irradiated)	31.14 m^2/g	0.077 [10d]
avg irradiated bentonite	32.01 m^2/g (n=3)	0.087 [9.7d] (n=3)
avg bentonite	31.18 m^2/g (n=3)	0.190 [8.3d] (n=7)

Figure 3.6 – Module M23 during bentonite cylinder sampling within an argon gas-filled glovebox. Dark precipitates on the bentonite surface indicate extensive microbial activity after one year of deployment within the BIC-A1 borehole. The sintered steel filter welds are clearly seen due to increased precipitation of a black material on both the bentonite core and the sintered steel filter (arrows), suggesting that corrosion may have taken place at the weld. Scanning electron microscopy and energy dispersive spectroscopy (EDS) was performed from the indicated area, results shown in Figures 3.7, 3.8, and 3.9.

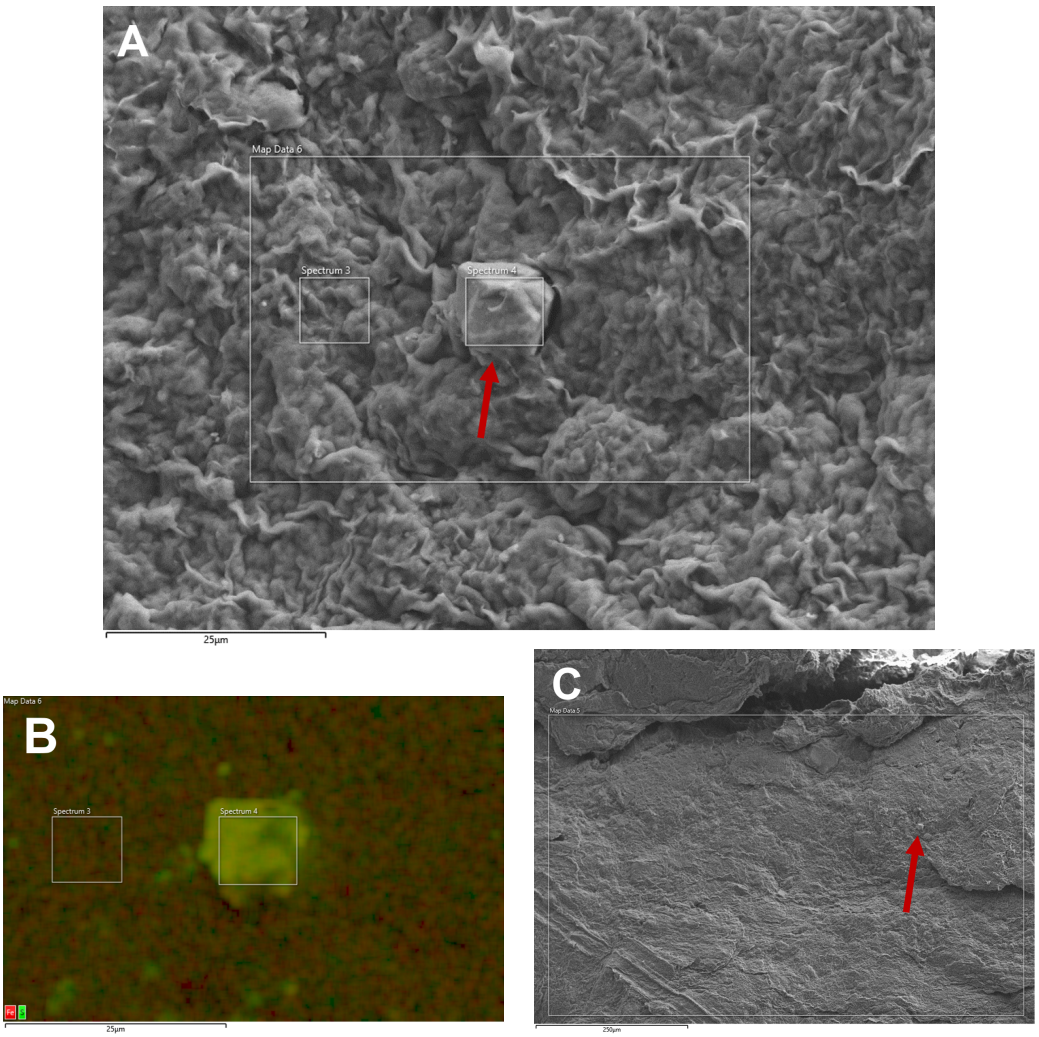

Figure 3.7 – Scanning electron microscopy (SEM) and energy dispersive spectroscopy (EDS) of the M23 cylinder surface opposite the sintered steel filter weld, see Figure 3.6. (A) & (C) SEM images, red arrow indicates an observed precipitate in the overview image (C) and a close-up (A) of the feature, and (B) energy dispersive spectroscopy (EDS) derived overlay map, showing iron (red) and sulfur (green), resulting in yellow for iron-sulfur signals. Observed precipitate is presumably mackinawite (FeS), see Table 3.5.

Table 3.5 – Elemental composition of bentonite and iron-sulfide precipitate identified on the bentonite surface of M23, shown in Figure 3.7. Results derived from energy dispersive spectroscopy (EDS) of bentonite and iron-sulfide precipitate, which has a Fe:S ratio of 1:1.3 thus presumably mackinawite (FeS).

Spectrum Label	Spectrum Map 5 (C) (bentonite, 390'025 µm^2) [at. weight %]	Spectrum 3 (A) (bentonite close to grain, 62 µm^2) [at. weight %]	Spectrum 4 (A) (grain, 62 µm^2) [at. weight %]
O	67.1	53.56	27.74
Na	1.7	1.99	0.96
Mg	1.4	1.70	0.70
Al	8.3	11.51	4.37
Si	20.3	28.46	10.91
P	0.00	0.00	0.02
S	**0.2**	**0.13**	**28.21**
Cl	0.1	0.18	
K	0.1	0.22	0.08
Ca	0.3	0.50	0.30
V	0.00	0.01	0.02
Cr	0.00	0.00	0.00
Mn	0.00	0.00	0.13
Fe	**0.60**	**1.72**	**21.07**
Co	0.00	0.00	0.00
Ni	0.00	0.00	5.48
Cu	0.00	0.00	0.00
Zn	0.00	0.00	0.00
Total	100.0	100.00	100.00

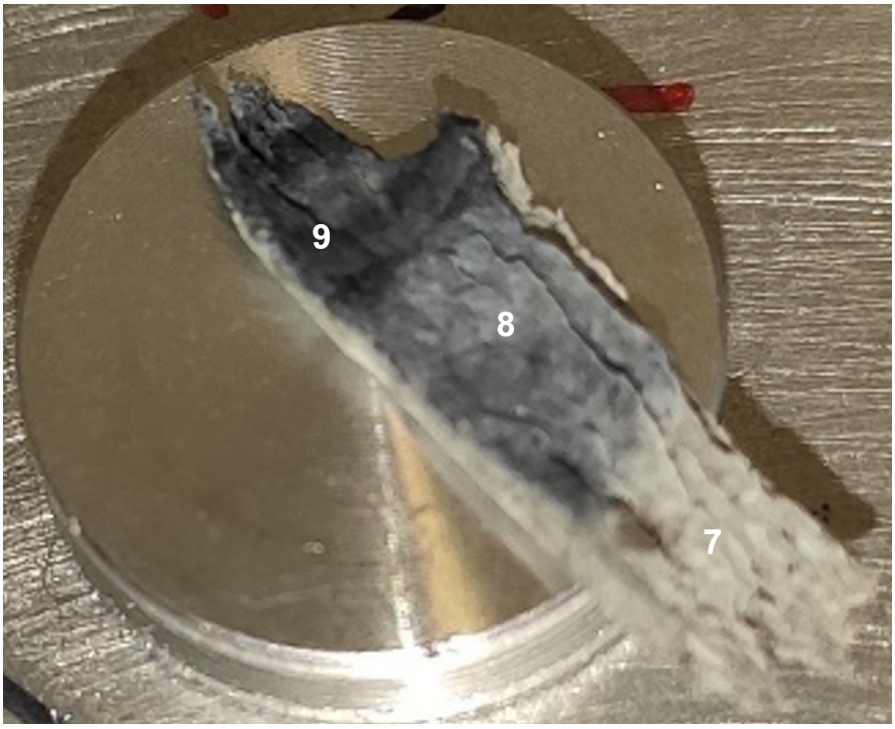

Figure 3.8 – Second SEM-EDS bentonite core surface sample of M23 collected near the sintered steel filter weld, see Figure 3.6. Three distinctive parts were analyzed: a clear black coloration on the bentonite opposite of the weld (spot 9) and a less obvious dark color several millimeters away (dark shade of grey, spot 8). Just below the core surface, at about 1mm depth, the native light shade of grey of bentonite is observed (spot 7). The elemental composition of the selected areas are presented in Table 3.6 and an iron sulfide precipitate within the black colored bentonite (spot 9) is shown in Figure 3.9

Table 3.6 – Elemental composition of the bentonite core surface of module M23, opposite of the sintered steel filter weld. EDS was used to determine elemental variations of the three different bentonite colorations as indicated in Figure 3.8.

Spectrum Label	**Spectrum 7 (light shade of grey bentonite, 87,500 µm^2) [at. weight %]**	**Spectrum 8 (dark shade of grey bentonite, 1,062,500 µm^2) [at. weight %]**	**Spectrum 9 (black colorized bentonite, 289,520 µm^2) [at. weight %]**
O	64.27	64.38	64.43
Na	1.60	1.73	1.52
Mg	1.44	1.36	1.35
Al	8.86	8.87	8.40
Si	22.50	22.50	23.10
P	0.00	0.00	0.00
S	**0.09**	**0.25**	**0.22**
Cl	0.14	0.15	0.13
K	0.12	0.17	0.18
Ca	0.45	0.45	0.33
Ti	0.03	-	-
V	0.00	0.00	0.00
Cr	0.00	0.02	0.01
Mn	0.00	0.03	0.00
Fe	**0.49**	**0.07**	**0.32**
Co	0.00	0.00	0.00
Ni	0.00	0.00	0.00
Cu	0.00	0.00	0.00
Zn	0.00	0.01	0.00

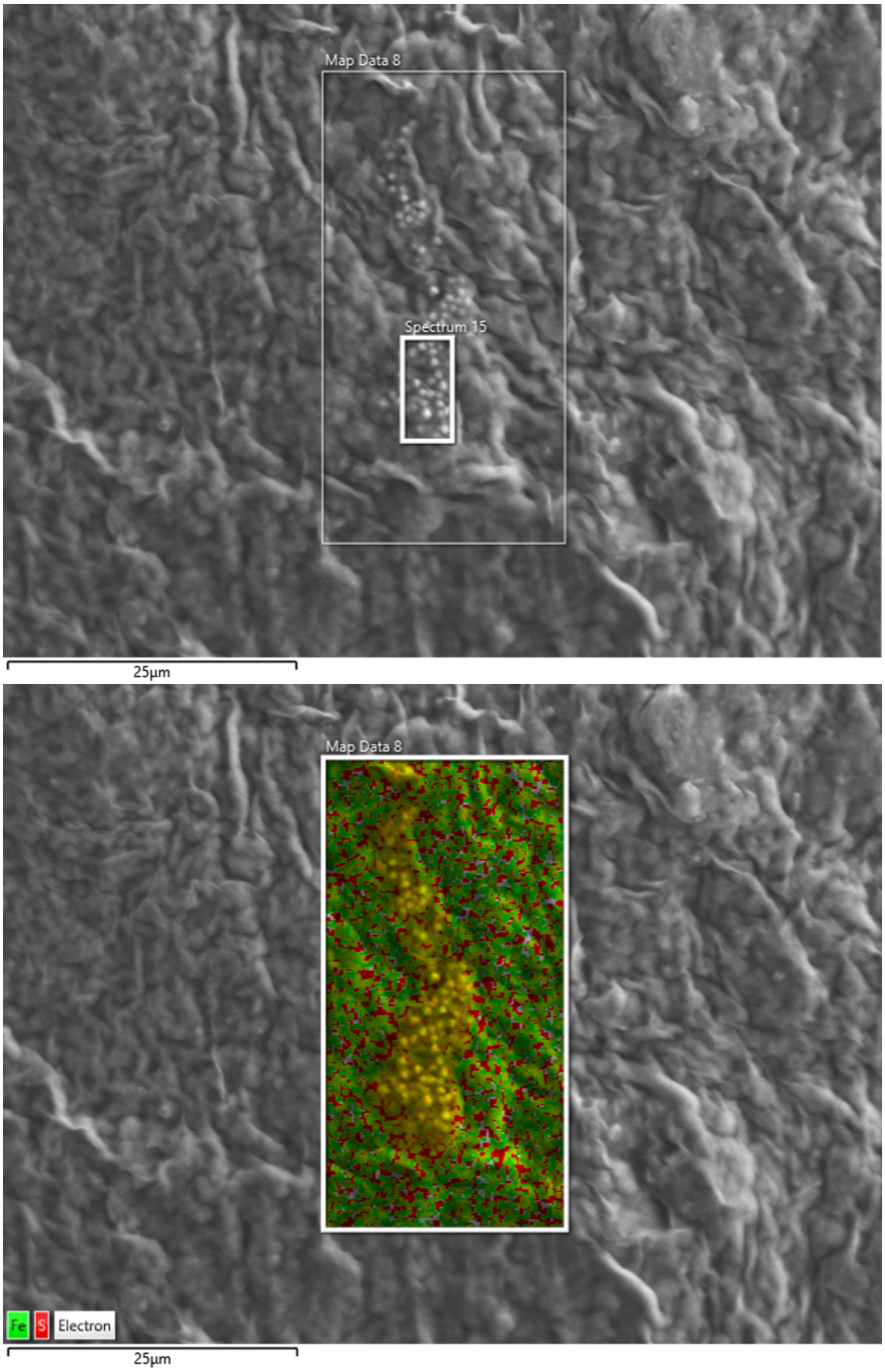

Figure 3.9 – SEM imaging of black coloration on the bentonite core surface opposite of the sintered filter weld in M23, as indicated in Figure 9, spot 9. EDS analysis and mapping revealed the indicated area with accumulated iron (green) and sulfur (red) resulting in yellow for iron sulfides, the corresponding elemental composition is presented in Table 3.7 and indicates pyrite as mineral form of the iron sulfide precipitate.

Table 3.7 – Elemental composition of EDS recorded areas as indicated in Figure 3.9. The brighter, higher density spots observed are enriched in iron and sulfur, with a Fe:S ratio of 1:2, thus presumably in form of pyrite minerals, FeS_2.

Spectrum Label	Map 8 Spectrum, 500 µm^2) [at. weight %]	Spectrum 15, 47 µm^2) [at. weight %]
O	60.16	44.91
Na	1.47	0.77
Mg	1.47	0.88
Al	8.72	4.80
Si	22.96	13.32
P	0.01	
S	**2.94**	**23.38**
Cl	0.14	
K	0.17	
Ca	0.40	
V	0.00	
Cr	0.00	
Mn	0.04	
Fe	**1.53**	**11.94**
Co	0.00	
Ni	0.00	
Cu	0.00	
Zn	0.00	
Total	100.00	100

3.3.6 Cultivation results

Cultivation of aerobic and anaerobic heterotrophs and sulfate-reducing bacteria from the irradiation-sterilized bentonite did not yield any evidence for viable organisms. In contrast, bulk bentonite from the deployed modules evidenced some growth. There was large variability in the number of organisms ranging from 0 to 22,965 colony- forming units normalized per gram of bentonite (CFU/g), Figure 3.10. Despite the measures used in our experimental handling of the bentonite, we cannot completely exclude that these results are due to introduced microbial contamination during module assembly and pre-saturation, or during the sampling of the bulk bentonite within a glovebox. On the other hand, the obtained CFU/g values may also represent the range of potential colonization of Opalinus Clay rock porewater microorganisms into incompletely saturated bentonite. However, the rather large variation amongst individual modules points to an introduced contamination, e.g., when comparing the CFU/g numbers of M19 of 0 to 10 CFU/g with M22 of 0 to 22,965 CFU/g. A comparison of the modules with the distinct configurations (+/- membrane and +/- SRB amendment) did not show a specific pattern. In fact, analysis of the impact of the membrane on the number of cultivable aerobes, anaerobes or SRB shows that it is not statistically significant, Table 3.8. An analysis of variance (ANOVA) shows that amongst modules M19, M21, M22 and M23, the *p-value* for the ANOVA is >0.2 for all two tested variables and for all microbial groups except for the count of SRB when testing for their amendment, with a *p-value* of 0.065. Similarly, the amendment of SRB does not significantly impact the number of aerobes and anaerobes cultivated, Table 3.8. However, the difference in SRB counts between the modules that received SRB and those that didn't comes close to being significant with a *p-value* of 0.065.

Therefore, we can conclude that, while the experiments were designed to result in the segregation of the two pools of microorganisms, the actual experimental conditions were essentially identical for all four bentonite modules. None included bentonite microbiota and all included contact with the borehole porewater microbiota.

The reasons for the lack of impact of the membrane intended to keep the borehole microbiota away from the bentonite is that the membranes were ruptured immediately upon deployment due to the pressurization of the borehole gas phase with argon post-closure (10 bar). This was evidenced clearly at least for one module (M23) in which a visible tear in the membrane was observed. This was not as evident in the second membrane-equipped module (M22), but it can also be assumed to have been compromised. In addition, the O-rings installed to render the modules water-tight were only tested by submerging an assembled module rather than by applying the 10-bar overpressure applied to the borehole.

Table 3.8 – Analysis of Variance (ANOVA) table considering whether the SRB addition or the presence of the membrane or both are statistically significant as drivers of the observed variances in the number of viable (an)-aerobic heterotrophs and sulfate-reducing bacteria (SRB).

Module	Analysis	$p_{SRBaddition}$			$p_{membrane}$			$p_{interaction}$		
		aerobes	anaerobes	SRB	aerobes	anaerobes	SRB	aerobes	anaerobes	SRB
M19 no membrane										
M21 SRB added, no membrane	Two-factor ANOVA: SRB addition & membrane	0.2648	0.2143	0.0646	0.2634	0.2077	0.3278	0.2649	0.2073	0.3018
M22 + membrane										
M23 SRB added, + membrane										

Most surprisingly, the SRB-containing community that was amended to the sterile bentonite did not grow significantly, Table 3.8. Indeed, the observed number of SRB in the spiked irradiated bentonite is found to be very small compared to the actual number of SRB added. The spiked bentonite was expected to have received between $2.57 \cdot 10^3$ and $2.57 \cdot 10^5$ SRB per g of bentonite but the observed SRB in the deployed bentonite ranged from 56-185 SRB per gram bentonite. Thus, there was two to four orders of magnitude decrease in the number of viable SRB upon incubation. The viability of the used SRB dilution was proven by enumeration of the SRB population in Postgate's Medium B (after an additional 16h of storage at 4°C in oxic conditions).

In contrast to bulk bentonite, the surface of the bentonite cylinder, including the bentonite that remained associated with the top and bottom lid of the module upon disassembly exhibited abundant microbial counts, Table 3.9. Thus, as was shown in previously deployed modules, in the absence of an effective barrier for the borehole microorganisms (due to the failure of the membranes), the microbiome colonizes the bentonite surface effectively and results in the discoloration of the bentonite and the production of iron-sulfide minerals. Furthermore, the values of CFU/g of bentonite obtained for aerobes, anaerobes and the MPN/g for SRB from bentonite that came off with the lid, Table 3.9, were much higher than those reported for bulk bentonite, Figure 3.10. For instance, in M21, POI-7 bottom lid shows $1.88 \cdot 10^6$ CFU/g of aerobes while the bulk bentonite in the same module peaks at 858 CFU/g; M23, POI-1 black ring on lid top shows $1.73 \cdot 10^7$ CFU/g of aerobes while the bulk bentonite peaks at 38 CFU/g.

This discrepancy is attributable to the fact that the sintered steel filters used for this phase were shorter (248 mm) than those used for previous phases (250 mm). As a result, there was room for the bentonite to swell more at the top and the bottom of the bentonite cylinder than elsewhere. Thus, at those two locations, the achieved densities after saturation may be low enough for the porewater microorganisms to grow into the bentonite, Table 3.9.

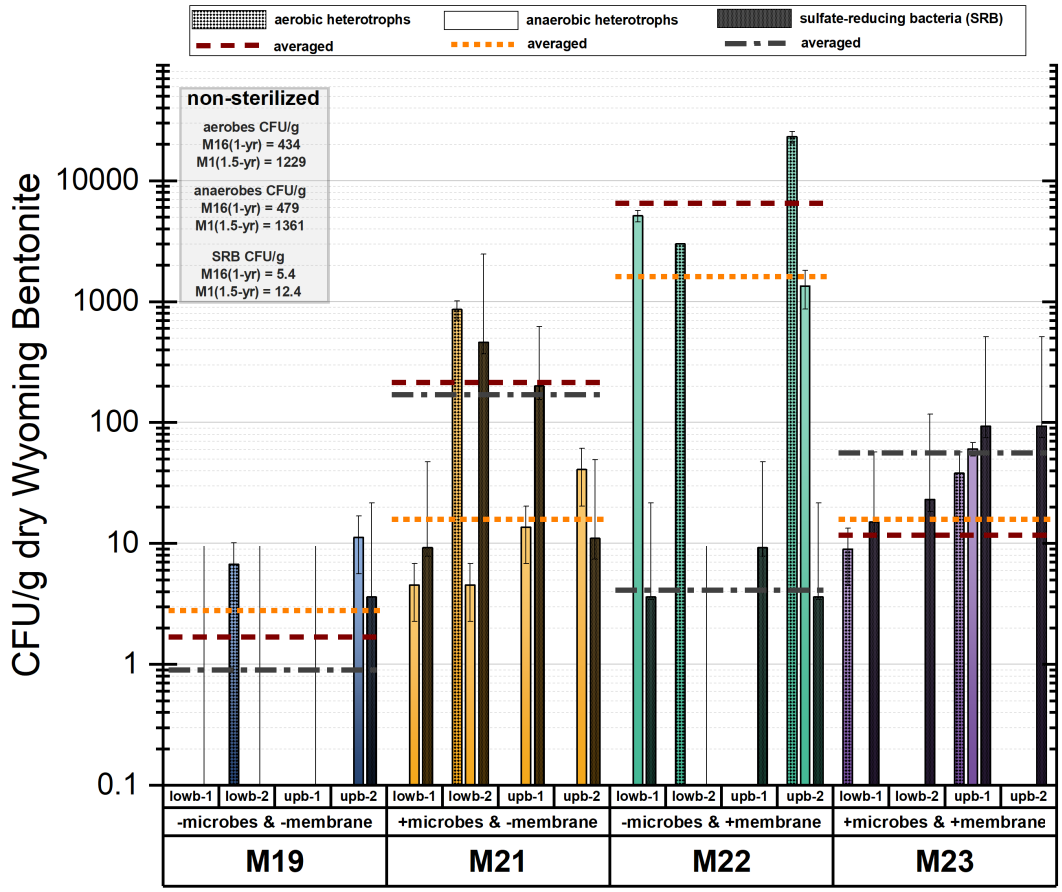

Figure 3.10 – Enumeration of heterotrophs and SRB in bulk bentonite. The four sampled bulk bentonite samples obtained per module are shown for aerobic and anaerobic heterotrophs and sulfate-reducing bacteria. Dotted/dashed/dash-dotted lines indicate their respective average for the modules. Inset indicates average CFU/g observed for non-sterilized pellet-powder bentonite for comparison: M16, presented in Chapter 2, features a similar deployment time but a different module assembly procedure; M1 (Smart et al., 2017), features a 50% longer deployment time but the same module assembly procedure.

Table 3.9 – Enumeration of (an)-aerobic heterotrophs and sulfate-reducing bacteria and 16S rRNA gene quantification copy-numbers of bentonite sampled from points-of-interest (POI) located at the interface between the bentonite cylinder and the sintered steel filter (core surface) or the stainless-steel module (top lid or bottom lid, i.e., bentonite that remained associated with the bottom lid of the module). The sample amount was not sufficient for cultivation for 'black ring on top lid' for M19, M21, M22 and for 'bentonite on bottom lid' for M19, M22, M23. For these samples, DNA extraction was given the priority over cultivation. 16S rRNA quantification results are presented in gene copies per gram bentonite or indicated as 'bdl' when below detection limit. The sample M22 POI-9 'bentonite cylinder core surface (black)' was too small to perform SRB enumeration but sufficient for the enumeration of (an)-aerobic heterotrophs.

Sample Type	Sample ID	Module number	Membrane	Location	Aerobes (CFU/g) st.-dev	Anaerobes (CFU/g) st.-dev	SRB (MPN/g) high-low confidence	16S rRNA gene quantification
bentonite on top lid	POI-2 lid top	M19	none	Interface of module and bentonite at the lid, visually indistinguishable from bulk bentonite	0	0	<3 {9.5-0}	bdl
	POI-6 lid top	M21			22.6 {11.3}	0 {0}	43 {180-9}	bdl
	POI-2 lid top	M22	yes		44.6 {22.3}	0 {0}	n.d.	bdl
	POI-2 lid top	M23			$1.26 \cdot 10^4$ {33.5}	$3.51 \cdot 10^3$ {190}	240 {1000-42}	bdl
black ring on top lid	POI-1	M23	yes	Interface of bentonite cylinder and steel filter and module lid, clear black coloration and higher degree of saturation with water, i.e. bentonite that was not as confined	$1.73 \cdot 10^7$ $\{7.3 \cdot 10^5\}$	$5.07 \cdot 10^5$ $\{7.4 \cdot 10^4\}$	$2.40 \cdot 10^4$ $\{1 \cdot 10^5 - 4200\}$	$7.92 \cdot 10^8$ copies/g
bentonite on bottom lid	POI-5 lid bottom	M19	none	Interface of module and bentonite at the base, visually indistinguishable from bulk bentonite	not performed	not performed	not performed	$3.82 \cdot 10^8$ copies/g
	POI-7 lid bottom	M21			$1.88 \cdot 10^6$ $\{6.9 \cdot 10^4\}$	$5.61 \cdot 10^4$ $\{5.7 \cdot 10^3\}$	$4.60 \cdot 10^4$ $\{2 \cdot 10^5 - 9000\}$	6.25 · 109 copies/g
	POI-4 lid bottom	M22	yes		not performed	not performed	not performed	bdl
	POI-3 lid bottom	M23			not performed	not performed	not performed	bdl
bentonite cylinder core surface (black)	POI-3	M23	yes	Interface of bentonite cylinder and steel filter, thin black precipitates covering the entire cylinder surface	$1.89 \cdot 10^5$ $\{7.2 \cdot 10^3\}$	$5.81 \cdot 10^3$ $\{6.43 \cdot 10^{-13}\}$	$3.6 \cdot 10^3$ {9400-870}	$2.80 \cdot 10^8$ copies/g
	POI-4	M19	none		$3.41 \cdot 10^5$ {0}	$8.70 \cdot 10^4$ $\{7.6 \cdot 10^3\}$	750 {2000-170}	$1.44 \cdot 10^4$ copies/g
	POI-9	M22	yes		$3.42 \cdot 10^5$ $\{6.4 \cdot 10^4\}$	$3.88 \cdot 10^4$ $\{5.1 \cdot 10^3\}$	n.d.	$1.01 \cdot 10^8$ copies/g

3.3.7 DNA sequencing results

The V3-V4 region of the 16S rRNA gene was amplified and sequenced for bulk bentonite samples, bentonite close to the metallic test coupons, bentonite core surfaces in contact with the sintered steel filter, bentonite obtained from the top lid and the bottom of the core, borehole water, the microbiome spike, as well as controls. Four negative controls (representing non-template controls), were obtained and only one of the four (indicated as '-ve ctrl' in Figure 3.11) included amplifiable DNA. The resulting sequences were mostly classified as *Pelomonas* and *Escherichia/Shigella*, Figure 3.11. It should be noted that while DNA from this single negative control could be amplified and sequenced, it was found to have only 558 16S rRNA gene copies per µL, compared with 10^6-10^7 16S rRNA gene copies per µL for swab samples and 10^3-10^4 16S rRNA gene copies per µL for cut black spot samples obtained from the bentonite core surface, Table 3.11 in this Chapter appendix. Thus, the amplifiable DNA was present but at very low abundance, as expected for such a control.

Additionally, experimental controls were also obtained and corresponded to control samples obtained from the glovebox and from the DNA extraction kits (and are indicated as 'Glovebox' and 'Kitome' in Figure 3.11). Those samples included for the DNA-extraction kits 'Kitome': *Pelomonas*, *Rothia, Escherichia/Shigella*, *Propionibacterium*, *Kocuria*, *Streptococcus* and *Massilia*. It was already reported that the DNA extraction kit used (formerly MoBio, now DNeasy PowerSoil Kit, Qiagen NV, Venlo, The Netherlands) contains contaminant DNA belonging to *Rothia*, *Escherichia/Shigella*, *Propionibacterium*, *Massilia* and *Streptococcus* and similar DNA-extraction kits were reported with contaminant *Pelomonas* and *Kocuria* (Glassing et al., 2016; Salter et al., 2014). The 'Glovebox' wipe controls showed contributions of *Pseudomonas*, *Pelomonas*, *Desemzia*, *Desulforosporosinus*, *Propionibacterium*, *Arthobacter*, *Fusibacter*, *Kocuria*, *Ralstonia*, *Streptococcous*, *Methylobacterium*, *Tepidimonas*, *Massilia*, *Blastococcus* and several other known taxa within 'Remaining taxa'. *Pseudomonas* and *Desulforosporosinus* from glovebox wipe controls is most likely a signature from borehole water spilled onto the base of the anoxic chamber during sampling, Figure 3.11. *Desemzia* and *Tepidmonas*, however, are only observed in glovebox samples and thus might be a contaminant source from that particular glovebox, Figure 3.11. *Arthrobacter*, *Fusibacter*, *Ralstonia*, *Stenotrophomonas* and *Streptophyta* are found in the glovebox and in bulk bentonite and coupon bentonite samples, however, we consider these as contamination originating from the glovebox, except for *Stenotrophomonas* as discussed further below.

Only two out of 16 bulk bentonite samples (M21 upper bentonite sample 1, M22 upper bentonite sample 2) yielded successfully amplifiable DNA that was quantified to represent $3.02 \cdot 10^4$ and $6.88 \cdot 10^4$ 16S rRNA gene copies per gram bentonite, respectively. This indicates that the biomass within the bentonite was very low because the lower limit of detection was 403 16S rRNA gene copies. Thus, we can conclude that no microbial growth is apparent in the bulk bentonite and the two successful amplifications can be attributed to introduced contaminations. Indeed, the microbiome composition of the two bulk bentonite samples show contributions of OTUs found in the control samples and the negative controls: *Pseudomonas*,

Pelomonas, and *Escherichia/Shigella* are found both in the two bulk bentonite and in 'Kitome', 'Glovebox' and '-ve controls' with the source of *Pseudomonas* being most likely the spilled borehole water and from handing the modules within the glovebox. Given the established very low/absent microbiome within bulk bentonite, it is very likely that even a small contamination with *Pseudomonas* results in a strong signal, as observe here. For one bulk bentonite sample, we also see contributions of *Arthrobacter*, *Ralstonia*, *Nocardioides*, *Paracoccus* all of which are also observed in control swabs of the glovebox. Considering the fact that only 2 out of 16 samples provided amplifiable DNA and that only one and not both bulk bentonite sample are showing these contributions, points to contamination as the source of the microbial signal rather than actual microbial colonization of the bulk bentonite.

In addition, two bentonite samples obtained close to a copper coupon of M21 and M23 (M21/M23couponEDC labeled in Figure 3.11) were observed with a quantifiable 16S rRNA gene copy number of $1.40 \cdot 10^5$ and $1.11 \cdot 10^5$ per gram bentonite. Considering that the metallic test coupons were only exposed to 70% ethanol briefly and no 70%-ethanol-wiping was performed, it is certainly possible that the coupons have introduced some cells. The major OTUs contributing to the microbiome of the two bentonites close to the test coupon show *Pelomonas*, *Arthrobacter*, *Ralstonia*, *Nocarioides*, *Brevundimonas*, *Paracoccus*, *Psychrobacter*, *Stenotrophomonas*, *Streptophyta* and several other OTU in 'Remaining taxa' , Figure 3.11. Here again, we see many of the OTUs found in negative controls such as *Pelomonas*, but also the OTUs already discussed from control wipes of the glovebox such as *Ralstonia*. Additionally, to be considered a trustworthy signal, we argue that we would expect more than two out of eight coupon bentonite samples to show meaningful amplification. Furthermore, the two successful amplifications did not show the same taxa apart from *Stenotrophomonas* (7.8 and 3.2% for 'M21couponEDC' and 'M23couponEDC' respectively) and *Nocardioides* (2.3 and 0.1% for 'M21couponEDC' and 'M23couponEDC' respectively). A member of the genus *Stenotrophomonas* is being reported as an indigenous microbe isolated from bentonites (Sánchez-Castro et al., 2017), however the detection of this genus in the coupon bentonite samples only and not in the irradiated bulk bentonite samples points to the possibility that this OTU was introduced with the test coupon which were prepared in the same laboratory as the bentonite used for this experiment. Similarly, the observation of *Nocardioides* within one bulk bentonite (at 16.5%) and the two coupon bentonites (at 2.3 and 0.1%) but the absence of other typical bentonite microorganisms points to contamination as the source of this signal, or to the detection of "relic" DNA adsorbed and stabilized by the bentonite clay. It is readily observable from a comparison between the microbiome of unsterilized Wyoming bentonite of the IC-A experiment (previous phases, Chapter 2 of this thesis) and irradiation-sterilized Wyoming bentonite (phase 4, Figure 3.13) that most of the OTUs frequently observed in untreated bentonite are absent in irradiated bentonite despite a 1-year deployment, Table 3.10. The only exceptions are Nocardiodaceae, (to which *Nocardioides* belongs) and Xanthomonadaceae (to which *Stenotrophomonas* belongs).

Lastly, we observe that for the 'Spike' (SRB-culture added to the bentonite of modules M21 and M23), the major OTUs are *Desulfosporosinus* and *Clostridium sensu stricto*. These are

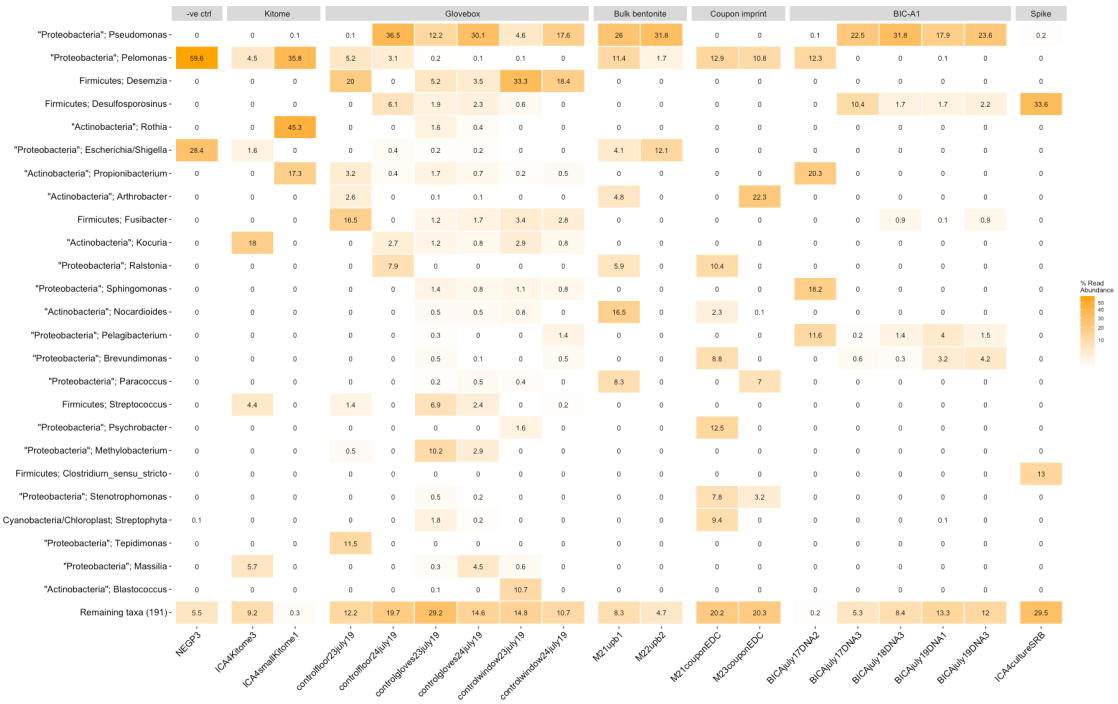

Figure 3.11 – Microbial community based on the 16S rRNA gene V3V4 region obtained for two bulk and two coupon bentonite samples which were successfully amplified and quantified. The y-axis shows the 25 most abundant OTUs of those shared amongst all samples at the phylum and genus levels. Only known taxonomic affiliations are shown. The bottom x-axis represents the sample-ID and the top x-axis the sample type/location. 'Remaining taxa' represent known taxa that are present at a lower abundance than the top 25.

not observed within the bulk bentonite nor the coupon bentonite of M21 nor M23. This observation bolsters the cultivation-based observation that there is no growth of SRB within sterilized bentonite.

Figure 3.12 represents the spatially-resolved distribution of microorganism of samples which are successfully amplified and their 16S rRNA gene copy numbers quantified. Of the four bottom lid bentonite samples (bentonite that remained associated with the bottom lid of the module), only one sample could be used for both DNA extraction and cultivation and exhibited high cultivation counts, Table 3.9. DNA-based analysis shows that the bottom lid bentonite microbiome shares *Pseudomonas* and *Desulfosporosinus* with the borehole microbiome (two out of four observations, M19 and M21). This is in contrast to the results for the abovementioned bulk and coupon bentonite, for which DNA was amplifiable for only two out of sixteen samples and whose microbiome is distinct from that of the bottom lid bentonite, Figure 3.12 'bentonite' category. Moving outwards, away from the bentonite core, are samples in contact with the borehole porewater. These include 'Core surface' category samples, Figure 3.12, obtained from the bentonite core surface and filter sample ('Filter' category in Figure 3.12) from the sintered steel filter. The bentonite cylinder surface and the sintered steel filter exhibit

almost identical microbial communities, similar to but not identical to that of the borehole water. This represents a microbiome at the interface between bulk bentonite and the borehole water. It consists mainly of *Pseudomonas* and smaller contributions of *Desulfosporosinus* and Acidobacteria group Gp7. Further away from the bentonite, towards the borehole environment ('Module' category in Figure 3.12) is the steel module surface, both the inside where epoxy glue was used as well as the outside and the water exchange holes. These environments are colonized by borehole water microorganisms similar to the bentonite core surface and filter. Finally, samples obtained from the module transport flasks ('Tr. Flask' category in Figure 3.12). Clean transport flasks were autoclaved before use but DNA could still be amplified, showing signatures of *Pseudomonas*, *Desulfosporosinus* and several OTUs identified as contaminants, e.g., *Escherichia/Shigella* and *Propionibacterium*. However, because the flasks were autoclaved for 80 mins, we suggest that no viable flask microorganisms are present during the transport and that the DNA sampled prior to transport represents relic DNA. The flasks were filled with approximately 2 liters of borehole water after module transfer to avoid bentonite desiccation during the 2 weeks of transit. Swabs of the inner surface of the flasks were obtained after the transport and evidenced a community dominated by *Pseudomonas* and *Fusibacter*. This suggests that growth of *Pseudomonas* and *Fusibacter* took place during the transport.

As discussed above, the top and bottom lid samples exhibited more abundant biomass than bulk and coupon bentonite from the middle of the bentonite cylinder, Table 3.9. In particular, two out of four samples from the bottom lid bentonites were successfully amplified and quantified, showing higher gene copy numbers than observed from the other two bentonite locations (bulk and coupon bentonite): 'M19POI-5' exhibits $3.82 \cdot 10^8$ 16S rRNA gene copies per g bentonite while 'M21POI-7' shows even higher numbers at $6.25 \cdot 10^9$ gene copies per g bentonite, Table 3.9. These two modules, M19 and M21, were not equipped with membranes, whereas modules M22 and M23 were and the DNA extracted from their respective bottom bentonite samples remained below the limit of detection (403 copies per g bentonite). In Figure 3.12, it can be readily observed that the bottom bentonite microbiome is in good agreement with the transport flask microbiome after the transport to the United Kingdom, with the only difference being the lower contribution of *Fusibacter* within the bottom of the bentonite cylinder. We hypothesize that during the transport of the modules, perturbations of the bentonite cylinder at the bottom lid occurred. Due to the shortened sintered steel filters, the bentonite is expected to have had a lower dry density at the extremities of the cylinder. The decrease in density and jostling during the transport enabled borehole water microorganisms abundant in the 2 liters of borehole water added to the transport canisters, to colonize that region of the bentonite cylinder. The reason why only the bottom of the cylinder exhibited this colonization is due to the fact that the module was only about ½ submerged. The absence of any quantifiable 16S rRNA genes in modules M22 and M23 indicates that the membrane system was working well in this case and that the tears/failures of the membrane were located on the top end of the modules. In fact, the membrane tear observed at M23 was located at the top most water entrance hole.

Hence, we hypothesize that the three borehole microbial genera *Pseudomonas*, *Fusibacter* and

Desulfosporosinus were able to colonize the sterilized bentonite at the lower density bottom lid bentonite (M19 and M21 exclusively) during module transport.

At the bentonite cylinder surface, which interfaces with the sintered steel filter and showed dark colorations for all four modules, we observe the dominance of Pseudomonas, with contributions from *Desulfosporosinus*, *Acholeplasma*, *Acidobacteria* group Gp7 and *Desulfitibacter*. All of the above are commonly observed at the bentonite cylinder surface and all of them are also part of the borehole water. In direct contact with the bentonite core surface, within the sintered steel filter, we observe a similar microbiome as already discussed above. The module surface at the inside, where the ARALDITE® Rapid glue was applied, shows higher abundance of *Fusibacter*, *Desulfosporosinus* and *Pseudomonas*, as well as increased relative counts of *Desulfitibacter* and *Acetobacterium*.

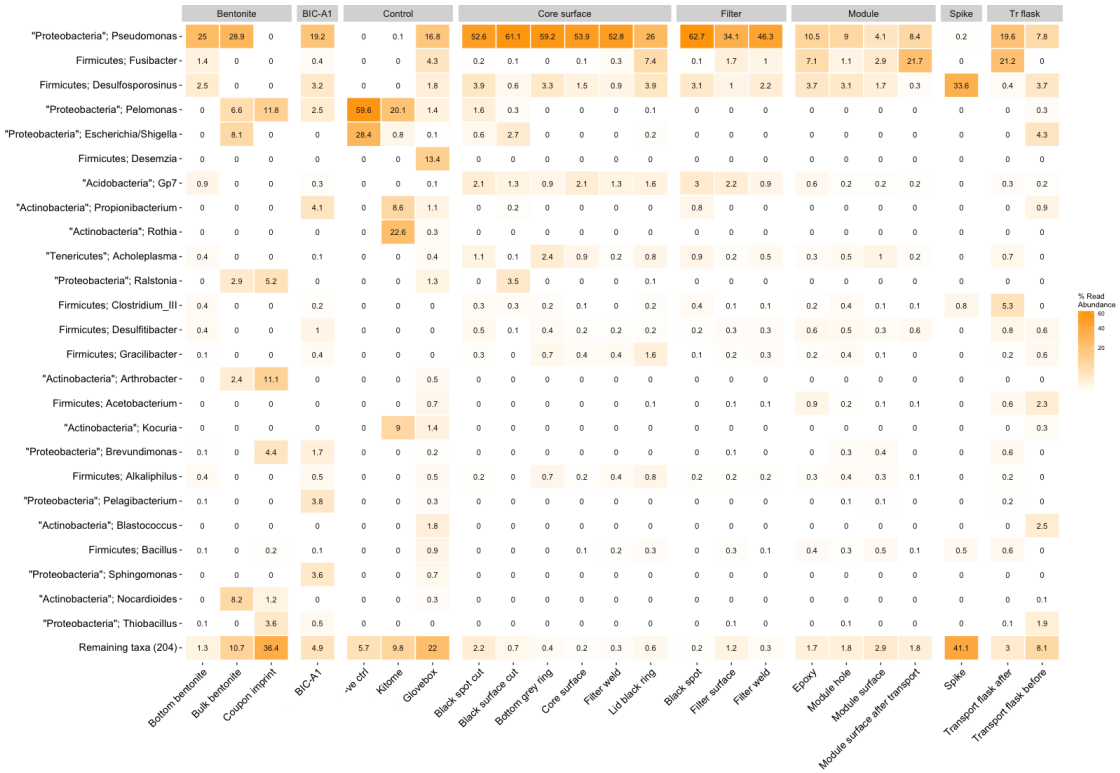

Figure 3.12 – Sampling location-resolved heatmap obtained from all four modules at the phylum and genus level of known taxa (in rel. % abundance) from high and medium confidence based on 16S rRNA gene V3V4 amplicon sequencing (but separated in sampling locations as 'Bentonite', 'Core surface', 'Filter', 'Module', 'Tr flask'), the borehole porewater community 'BIC-A', control samples (containing one successful amplification of a negative control, control wipes of the 'Glovebox' and negative controls of the used extraction kits 'Kitome'), the SRB 'Spike' and the transport flasks ('Tr flask').

	Bentonite		Control		
	Bulk bentonite	Coupon imprint	-ve ctrl	Kitome	Glovebox
"Proteobacteria"; Pseudomonadaceae	28.9	0	0	1.5	16.8
"Proteobacteria"; Comamonadaceae	6.6	14	60.6	20.5	2
"Actinobacteria"; Micrococcaceae	2.5	11.1	0	31.8	2.9
Firmicutes; Carnobacteriaceae	0	0	0	0	13.5
"Proteobacteria"; Rhodobacteraceae	4.2	3.5	0.4	25.5	1.4
"Proteobacteria"; Enterobacteriaceae	8.1	0	28.5	0.8	0.3
"Actinobacteria"; Propionibacteriaceae	2.3	0	0	8.6	1.2
"Proteobacteria"; Oxalobacteraceae	0	7.8	0	2.8	1
"Proteobacteria"; Desulfobacteraceae	0	0	0	0	4.4
Firmicutes; Clostridiales_Incertae_Sedis_XII	0	0	0	0	4.3
"Proteobacteria"; Burkholderiaceae	2.9	5.2	0	0	1.4
"Proteobacteria"; Desulfobulbaceae	0	0	0	0	3.8
"Actinobacteria"; Nocardioidaceae	8.2	1.2	0	0	0.3
"Proteobacteria"; Moraxellaceae	0	6.3	0	0	0.8
"Proteobacteria"; Xanthomonadaceae	0	7.5	0	0	0.2
Firmicutes; Streptococcaceae	0	0	0	2.2	1.9
Firmicutes; Peptococcaceae_2	0	0	0	0	2.3
"Proteobacteria"; Methylobacteriaceae	0	0	0	0	2.3
Cyanobacteria/Chloroplast; Chloroplast	0	4.7	0.4	0	0.5
"Proteobacteria"; Burkholderiales_incertae_sedis	0	0	0	0	1.9
"Proteobacteria"; Sphingomonadaceae	0	0	0	0	1.9
Firmicutes; Peptococcaceae_1	0	0	0	0	1.9
"Actinobacteria"; Geodermatophilaceae	0	0	0	0	1.8
"Proteobacteria"; Caulobacteraceae	0	4.4	0	0	0.3
Firmicutes; Staphylococcaceae	0	0	0	1.4	1.1
"Actinobacteria"; Mycobacteriaceae	0	4.2	0	0	0.1
"Actinobacteria"; Dermabacteraceae	0	0	0	0	1.4
"Actinobacteria"; Micromonosporaceae	3.8	0	0	0	0
"Proteobacteria"; Hydrogenophilaceae	0	3.6	0	0	0
"Actinobacteria"; Pseudonocardiaceae	0	2.2	0	0	0.4
"Actinobacteria"; Microbacteriaceae	0	1.4	0	0	0.6
Firmicutes; Bacillaceae_1	0	0.2	0	0	0.9
Firmicutes; Peptostreptococcaceae	2.5	0	0	0	0
Firmicutes; Lachnospiraceae	0	0	0	0	0.8
"Proteobacteria"; Acetobacteraceae	1.4	0	0	0	0.4
Firmicutes; Planococcaceae	0	0	0	0	0.8
"Actinobacteria"; Streptomycetaceae	1.6	0	0	0	0.2
Firmicutes; Eubacteriaceae	0	0	0	0	0.8
"Actinobacteria"; Nakamurellaceae	0	0	0	0	0.7
"Actinobacteria"; Rubrobacteraceae	0	1.9	0	0	0
"Bacteroidetes"; Cytophagaceae	0	1	0	0	0.3
"Proteobacteria"; Neisseriaceae	0	0	0	0	0.6
"Proteobacteria"; Vibrionaceae	0	0	0	1.6	0
"Actinobacteria"; Acidimicrobiaceae	0	1.5	0	0	0
Firmicutes; Natranaerobiaceae	0	0	0	0	0.5
"Proteobacteria"; Geobacteraceae	0	0	0	0	0.5
Firmicutes; Clostridiaceae_2	0	0	0	0	0.5
"Chloroflexi"; Anaerolineaceae	0	0	0.2	0	0.4
"Proteobacteria"; Hyphomicrobiaceae	0	0	0	0	0.4
"Proteobacteria"; Rhodospirillaceae	0	0	0	0	0.4
Remaining taxa (78)	0	0.5	3.1	0.2	5.7

% Read Abundance
60
50
40
30
20
10

Figure 3.13 *(previous page)* – Bulk (M21, M22) and coupon bentonite microbiome on family level for comparison with previous IC-A phases, see Table 3.10. The observation of Comamonadaceae, Micrococcaceae, Rhodobacteraceae, Enterobacteriaceae and Propionibacteriaceae can be attributed to contaminations as these families are also observed in the negative control (-ve ctrl) and in the used kitome. This leaves for the bulk bentonite Pseudomonadaceae, Nocardioidacae, Burkholderiacae, Micromonosporacaeae and Peptrostreptococcaceae as the dominant OTU. Bentonite adjacent to coupons share with the bulk OTU the signature of Nocardioidaceae and Burkholderiaceae but has in contrast to the bulk bentonite also contributions of Caulobacteraceae, Xantohomonadaceae, Moraxellaceae, Chloroplast-associated DNA, Mycobacteriaceae and Pseudonocardiaceae. It is possible that these microorganisms were introduced with the coupon itself as the coupon was only briefly dipped in 70% ethanol and no other sterilization/disinfection was performed to prohibit interference with the corrosion assessment (not part of this thesis).

Table 3.10 – Bentonite microbiome comparison between Nagra powder/pellets undeployed, deployed for one year (M16), or irradiation-sterilized and deployed for 1 year (M21, M22). The maximum % abundance found in either bulk or in coupon bentonite is shown, for irradiation-sterilized bentonite, only M21 and M22 resulted in trustworthy microbiome signals. $_X$ family dominated by aerobes. [a] also observed in -ve control (no template PCR control). [b] high abundance also observed in Kitome (DNA-extraction kit negative control) or Glovebox.

OTU (family)	**% abundance in undeployed Nagra pellets**	**% abundance in M16 (1-yr non-sterile)**	**% abundance M21, M22 (1-yr sterile)**
$_X$Streptomycetaceae	22.2	7.2	1.6 [b]
$_X$Pseudonocardiaceae	5.2	2.0	2.2 [b]
$_X$Nocardiopsaceae	6.0	2.2	8.2 [b]
$_X$Xanthomonadaceae	3.9	6.6	7.5 [b]
$_X$Sphingomonadaceae	31.5	21.8	0.0 [b]
$_X$Alcaligenaceae	0.5	5.1	0.0
Burkholderiaceae	0.04	4.5	5.2 [b]
(Order: Burkholderiales)	0.04	0.2	0 [b]
Enterobacteriaceae	2.1	11.2	8.1 [a,b]
Micrococcaceae	4.5	2.9	11.1 [b]

3.4 Conclusion

3.4.1 Porewater

Within the last three timepoints (2017, 2018 and 2019), the composition of the BIC-A borehole microbiome is shown to fluctuate less than observed for previous timepoints (2013, 2014, and 2017). We assume that the microbiome is supported by organic matter leaching out of the bentonite core and is degraded by fermenting bacteria, producing low-molecular weight organics used by sulfate-reducing bacteria, as previously shown (Bagnoud, de Bruijn, et al., 2016; Maanoja et al., 2020). However, an interesting development could be observed from the 16S rRNA gene V3V4 region sequencing results (only available for 2017, 2018 and 2019 timepoints): the emergence of the genera *Desulfitibacter* (Nielsen et al., 2006), (abundance 3.3% in 2019, 0% in 2017, data not shown) and *Dethiobacter* (Melton et al., 2017), (abundance 0.5% in 2018 and 2019, 0.2% in 2017, data not shown). These are microorganisms that reduce or disproportionate intermediate S valence states. Thus, their increased abundance might point to the presence of oxidation states of sulfur other than sulfate (+6) and sulfide (-2). However, in a reducing environment such as this borehole, an oxidative force must be present to form intermediate sulfur species. A possible source may be the reported trapped oxygen within Wyoming bentonite (Giroud et al., 2018) and Chapter 2 of this thesis. Within the experimental modules, sulfate-reducing bacteria colonize the sintered steel filter, obtaining electron donors from organics (and molecular hydrogen in case of gamma-irradiated bentonite) leached out of the bentonite cylinder and sulfate from the Opalinus Clay rock porewater. The bentonite cylinder itself represents an anoxic-oxic interface with abundant oxygen inside the bulk bentonite (potentially further elevated due to gamma-irradiation) and the sintered steel filter offers a large surface area and iron source such that iron-sulfide minerals precipitate on the bentonite cylinder, Figure 3.6, Figure 3.7, Table 3.5. At this interface, oxidative sulfur processes may take place and thus provide the oxidative driving force for sulfur-cycling.

3.4.2 Bentonite

Even though we took many precautions during the module assembly and disassembly, the enumeration results of heterotrophs suggest that some bacterial contamination must have happened, Figure 3.10. This is almost unavoidable but is usually masked by the native microbial community. However, in this case, due to the sterilization of bentonite, any contamination is amplified. This is indicated by the variability in the observed numbers of colony forming units, as discussed above, Subsection 3.3.6. More striking though, is the absence of the high numbers of SRB added in the spiked modules M21 and M23, which received $2.57 \cdot 10^3$ - $2.57 \cdot 10^5$ SRB per g sterile bentonite but resulted in only 56-184.5 SRB/g bentonite after one year of deployment. This indicates that the conditions within bentonite are not suitable for the growth and survival of SRB, even though the SRB were cultivated from the exact same batch of bentonite pre-sterilization. We suspect that the presence of oxygen trapped within bentonite can be attributed as the major inhibitory effect for SRB (Giroud et al., 2018) and Chapter 2.

The SRB spike culture was amended to bentonite under oxic conditions in form of vegetative cells, rather than as resilient endospores like they occur in Wyoming bentonite. However, enumeration of SRB in the spike culture was performed after that short oxygen exposure, thus it cannot be the reason for the very low numbers of SRB in the bentonite post-deployment. Therefore, it is more likely that the vegetative SRB cells from the spike culture were not able to grow within the bentonite nor were they able to form endospores to retain viability over the one-year deployment time.

16S rRNA gene V3V4 region sequencing delivered trustworthy results only for two out of sixteen bulk bentonite and two out of eight coupon bentonite samples. Within the two subsets, a wide variation of observed taxonomies is reported (DNA sequencing results, Figure 3.11). The observed correspondence between microbiomes in sterile bentonite and the negative controls and the kitome and glovebox control swabs ('-ve control', 'Kitome', 'Glovebox') indicates very low biomass. Indeed, for nearly all bulk bentonite and coupon imprint bentonite samples, no quantification of 16S rRNA genes was successful and the amplification had to be carried out up to 40 PCR-cycles. Therefore, any contamination, whether it is bacterial cells or gDNA added during the assembly, deployment, retrieval, disassembly, sampling and gDNA extraction, will have a disproportionately strong signal in the otherwise sterile bentonite samples. Furthermore, it might be possible that portions of the observed DNA fingerprints of bacterial families similar to non-sterile, undeployed and deployed bentonite, Table 3.10, are remains of DNA fragments within the sterile bentonite, due to the stabilization of DNA through interaction with clay (Greaves & Wilson, 1969; Slon et al., 2017). An indication for this is that there are bulk bentonite samples for which there is quantifiable gDNA (labelled lowb and upb in Table 3.11 in this Chapter appendix) but no 16S rRNA genes could be quantified in most cases, whereas the opposite is the norm (due to PCR amplification). Here, we speculate that gDNA fragments remained on the clay but these were too damaged by the irradiation for 16S rRNA gene amplification. Combining the observations, we conclude that no microbial growth was observed in the sterile bentonite of all four modules and that SRB are efficiently inhibited by bioavailable oxygen.

Gamma irradiation resulted not only in the sterilization of bentonite but presumably also in an enhanced bioavailability of electron donors, perhaps molecular hydrogen and low-molecular weight organics, allowing enhanced surface colonization of the bentonite as compared to previously deployed, unirradiated bentonite. This is evidenced by the dark coloration of the bentonite cylinder surface and its colonization. We observed that during irradiation of the bentonite within closed glass bottles, the humidity decreased, thus we suspect radiolysis of the interlayer water and generation of hydrogen, which could be bound to the clay surface (Edge et al., 2014). Upon the partial saturation of the bentonite and the accompanying structural changes, the hydrogen diffused towards the bentonite-borehole water interface, providing an excellent electron donor for the borehole water communities. Similarly, organic carbon within bentonite may not have been fully oxidized during the irradiation and, instead, resulted in the production of low-molecular organics, potentially providing the microorganisms with a good carbon and electron source. These processes may also be expected for spent fuel and

high-level waste that emit radiation and therefore may change the chemical composition of the surrounding bentonite.

Furthermore, from the observed microbiome at bottom lid bentonite, Table 3.9, it appears that some borehole water bacteria are capable to colonize the bentonite and thrive off the organic matter in bentonite, when the bentonite dry density is artificially decreased due to the absence of sintered filter at those locations. In this context, the dominant genus *Pseudomonas*, a genus of facultatively anaerobic bacteria, may be suitable to colonize the oxic environment of the bulk bentonite as long as there is enough space, i.e., when the bentonite is disturbed in terms of cracks/low density anomalies. Other Opalinus Clay rock microorganisms may follow as soon as the bentonite-associated oxygen is used up, such as the observed SRB genus *Desulfurosporosinus*. Heterogenous swelling of powder/pellet bentonite may prove beneficial for the colonization, however, a dedicated experimental setup would be necessary to investigate these interactions.

Chapter 3 - Appendix

Table 3.11 – DNA sample list of module samples, n=123, concentration of extracted genomic DNA (gDNA) and number of copies of 16S rRNA genes from bacteria/archaea are shown per µL for swab sample and per g bentonite for bentonite from bulk and core samples. When both gDNA concentration and 16S rRNA genes could be quantified, the reliability/trustworthiness of the obtained 16S rRNA gene sequences is labelled with a high confidence level; if only 16S rRNA genes could be quantified but no gDNA (bdl=below detection limit), the label is medium confidence; if neither of both could be quantified, the number of microorganisms in the sample was so low that 16S rRNA gene sequencing should not trusted, and the samples was labelled as assigned low confidence.

Module	Sample Type	Sample ID	gDNA quantification [ng/μL]	16S rRNA gene quantification successful	16S rRNA gene sequencing confidence	16S rRNA copy #/g bentonite	16S rRNA copy #/μL gDNA extracted
M19 no added microorganisms no membrane	bentonite adjacent to coupons	M19coupon BM	bdl	no	low	-	-
		M19coupon EDC	0.0164	no	low	-	-
	bulk bentonite	M19lowb1	0.017	no	low	-	-
		M19lowb2	0.0168	no	low	-	-
		M19upb1	bdl	no	low	-	-
		M19upb2	bdl	no	low	-	-
	top bentonite	M19POI2	bdl	no	low	-	-
	bottom bentonite	M19POI5	0.1984	yes	high	$3.82 \cdot 10^8$	$4.53 \cdot 10^6$
M21 added microorganisms no membrane	bentonite adjacent to coupons	M21coupon BM	0.0348	no	low	-	-
		M21coupon EDC	0.01	yes	high	$1.40 \cdot 10^5$	$7.14 \cdot 10^2$
	bulk bentonite	M21lowb1	bdl	no	low	-	-
		M21lowb2	0.0448	no	low	-	-
		M21upb1	0.0142	yes	high	$3.02 \cdot 10^4$	$1.56 \cdot 10^3$
		M21upb2	bdl	no	low	-	-
	top bentonite	M21POI6	bdl	no	low	-	-
	bottom bentonite	M21POI7	2.74	yes	high	$6.25 \cdot 10^9$	$3.21 \cdot 10^7$
M22 no added microorganisms with Membrane	bentonite adjacent to coupons	M22coupon BM	0.0488	no	low	-	-
		M22coupon EDC	0.0154	no	low	-	-
	bulk bentonite	M22lowb1	0.0362	no	low	-	-
		M22lowb2	0.0382	no	low	-	-
		M22upb1	0.0138	no	low	-	-
		M22upb2	0.0224	yes	high	6.88E+04	7.71E+02
	top bentonite	M22POI2	bdl	no	low	-	-
	bottom bentonite	M22POI4	bdl	no	low	-	-

Module	Sample Type	Sample ID	gDNA quantification [ng/μL]	16S rRNA gene quantification successful	16S rRNA gene sequencing confidence	16S rRNA copy #/g bentonite	16S rRNA copy #/μL gDNA extracted
M23 added microorganisms with Membrane	bentonite adjacent to coupons	M23coupon BM	bdl	no	low	-	-
		M23coupon EDC	0.0168	yes	high	$1.11 \cdot 10^5$	$6.18 \cdot 10^2$
	bulk bentonite	M23lowb1	0.0438	no	low	-	-
		M23lowb2	0.0222	no	low	-	-
		M23upb1	bdl	no	low	-	-
		M23upb2	0.0378	no	low	-	-
	top bentonite	M23POI2	bdl	no	low	-	-
	bottom bentonite	M23POI3	bdl	no	low	-	-
Control of equipment and reagents	glovebox swab controls	controlfloor 23july19	bdl	yes	medium	-	$8.61 \cdot 10^2$
		controlfloor 24july19	bdl	yes	medium	-	$2.12 \cdot 10^3$
		controlgloves 23july19	bdl	yes	medium	-	$3.89 \cdot 10^4$
		controlgloves 24july19	bdl	yes	medium	-	$2.32 \cdot 10^4$
	module control	ICA4grease	bdl	no	low	-	-
	DNA extraction kitome	ICA4small Kitome1	bdl	yes	medium	-	$5.09 \cdot 10^2$
		ICA4small Kitome2	bdl	no	low	-	-
		ICA4Kitome3 maxikit	bdl	yes	medium	-	1.94E+03
16S V3V4 amplification control	-ve ctrl	NEGP1	-	no	-	-	-
		NEGP2	-	no	-	-	-
		NEGP3	-	yes	medium	-	-
		NEGP4	-	no	-	-	-
M19 no added microorganisms no membrane	module swab of glue	M19epoxy1	0.204	yes	high	-	$3.85 \cdot 10^6$
		M19epoxy2	0.112	yes	high	-	$1.52 \cdot 10^6$
	black ring at lid, inside	M19FPOI1cut	0.1414	yes	high	-	$1.78 \cdot 10^6$
	filter weld	M19FPOI1swab	0.1034	yes	high	-	$2.02 \cdot 10^6$
	filter surface	M19FPOI3	0.0456	yes	high	-	$8.01 \cdot 10^5$
	module holes	M19H1	0.1134	yes	high	-	$2.15 \cdot 10^6$
		M19H2	0.646	yes	high	-	$5.43 \cdot 10^5$
	black ring at top lid, inside swab	M19POI1	bdl	yes	medium	-	$6.96 \cdot 10^4$
	core surface	M19POI3	0.095	yes	high	-	$1.32 \cdot 10^6$
	core black surface cut	M19POI4	0.0174	yes	high	$1.44 \cdot 10^4$	$1.57 \cdot 10^4$
	black ring at top lid, inside cult	M19POI6	0.043	yes	high	-	$4.93 \cdot 10^5$
	module surface, outside	M19S1	0.936	yes	high	-	$6.25 \cdot 10^6$

Module	Sample Type	Sample ID	gDNA quantification [ng/μL]	16S rRNA gene quantification successful	16S rRNA gene sequencing confidence	16S rRNA copy #/g bentonite	16S rRNA copy #/μL gDNA extracted
M19 no added microorganisms no membrane	module surface after transport	M19S1after	0.062	yes	high	-	$1.03 \cdot 10^6$
	module surface, outside	M19S2	0.536	yes	high	-	$7.68 \cdot 10^6$
	transport flask after	M19Ta1	0.0214	yes	high	-	$2.52 \cdot 10^5$
	transport flask before	M19Tb1	0.0104	yes	high	-	$1.14 \cdot 10^4$
		M19Tb2	bdl	yes	medium	-	$7.70 \cdot 10^2$
M21 added microorganisms no membrane	core surface at filter weld	M21POI5	0.0726	yes	high	-	$1.71 \cdot 10^6$
	filter surface	M21FPOI2	bdl	yes	medium	-	$2.17 \cdot 10^5$
	core surface	M21POI2	0.0468	yes	high	-	$1.08 \cdot 10^6$
	filter weld	M21FPOI5	0.0362	yes	high	-	9.54E+05
	module swab of glue	M21epoxy1	0.384	yes	high	-	$5.24 \cdot 10^6$
		M21epoxy2	0.264	yes	high	-	$2.81 \cdot 10^6$
	black ring at top lid, inside	M21lidPOI1	0.0326	yes	high	-	$8.48 \cdot 10^5$
	filter surface, outside	M21Foutside	0.1282	yes	high	-	$1.69 \cdot 10^6$
	core surface black spot	M21POI3	bdl	no	low	-	-
	core black surface cut	M21POI4	bdl	yes	medium	-	$7.97 \cdot 10^3$
	core black surface cut	M21POI42	bdl	yes	medium	-	$1.18 \cdot 10^4$
	module holes	M21H1	0.1306	yes	high	-	$1.57 \cdot 10^6$
		M21H2	0.0528	yes	high	-	$7.25 \cdot 10^5$
	module surface, outside	M21S1	0.214	yes	high	-	$4.65 \cdot 10^5$
		M21S2	0.0198	yes	high	-	$3.65 \cdot 10^5$
	module surface after transport	M21S1after	0.0296	yes	high	-	$9.61 \cdot 10^5$
	transport flask after	M21Ta1	bdl	yes	medium	-	$2.08 \cdot 10^5$
	transport flask before	M21Tb1	bdl	yes	medium	-	$4.57 \cdot 10^2$
		M21Tb2	bdl	yes	medium	-	$4.42 \cdot 10^2$
M22 no added microorganisms with Membrane	module swab of glue	M22epoxy1	0.296	yes	high	-	$4.50 \cdot 10^6$
		M22epoxy2	0.214	yes	high	-	$3.71 \cdot 10^6$
		M22epoxy3	0.308	yes	high	-	$5.47 \cdot 10^6$
	black ring at top lid, inside	M22FPOI1	0.318	yes	high	-	$2.92 \cdot 10^6$
	filter weld	M22FPOI2	0.044	yes	high	-	$1.39 \cdot 10^6$

Module	Sample Type	Sample ID	gDNA quantification [ng/μL]	16S rRNA gene quantification successful	16S rRNA gene sequencing confidence	16S rRNA copy #/g bentonite	16S rRNA copy #/μL gDNA extracted
M22 no added microorganisms with Membrane	filter surface black spot	M22FPOI6BS	bdl	yes	medium	-	$7.59 \cdot 10^4$
		M22FPOI7BS	bdl	yes	high	-	$1.66 \cdot 10^4$
		M22FPOI8BS	0.0168	yes	high	-	$6.16 \cdot 10^4$
	module holes	M22H1	0.878	yes	high	-	$9.90 \cdot 10^6$
		M22H2	bdl	yes	medium	-	$5.84 \cdot 10^6$
	black ring at top lid, inside	M22POI1cult	0.0946	yes	high	$2.43 \cdot 10^8$	$1.57 \cdot 10^5$
		M22POI1cut	0.0124	no	low	-	-
	black ring at top lid, inside swab	M22POI1swab	0.0314	yes	high	-	$1.46 \cdot 10^6$
	grey ring at bottom lid	M22POI3	0.1012	yes	high	-	$1.96 \cdot 10^6$
	core surface	M22POI5	0.0538	yes	high	-	$1.27 \cdot 10^6$
	core surface black spot swab	M22POI6	bdl	no	low	-	-
	core surface black spot cut	M22POI6BS	bdl	yes	medium	-	$3.04 \cdot 10^4$
	core surface black spot swab	M22POI7	bdl	no	low	-	-
	core surface black spot cut	M22POI7BS	0.0112	yes	high	$2.51 \cdot 10^7$	$2.92 \cdot 10^3$
	core surface black spot swab	M22POI8	bdl	no	low	-	-
	core surface black spot cut	M22POI8BS	bdl	yes	medium	-	$3.15 \cdot 10^4$
	core black surface cut	M22POI9	0.0168	yes	high	$1.01 \cdot 10^8$	$8.26 \cdot 10^4$
	module surface, outside	M22S1	0.428	yes	high	-	$7.49 \cdot 10^6$
		M22S2	bdl	yes	medium	-	$3.26 \cdot 10^6$
	module surface after transport	M22Safter	0.0466	yes	high	-	$5.15 \cdot 10^5$
	transport flask after	M22Ta1	0.014	yes	high	-	$2.33 \cdot 10^5$
	transport flask before	M22Tb1	bdl	no	low	-	-
		M22Tb2	bdl	no	low	-	-
M23 added microorganisms with Membrane	module swab of glue	M23epoxy1	1.578	yes	high		$1.69 \cdot 10^7$
		M23epoxy2	0.522	yes	high		$4.06 \cdot 10^6$
	black ring at top lid, inside	M23FPOI1	0.1656	yes	high		$2.09 \cdot 10^6$
	filter weld	M23FPOI2	0.0476	yes	high		$9.40 \cdot 10^5$
	module holes	M23H1	0.204	yes	high		$2.52 \cdot 10^6$
		M23H2	bdl	yes	medium		$6.59 \cdot 10^6$

Module	Sample Type	Sample ID	gDNA quantification [ng/μL]	16S rRNA gene quantification successful	16S rRNA gene sequencing confidence	16S rRNA copy #/g bentonite	16S rRNA copy #/μL gDNA extracted
M23 added microorganisms with Membrane	black ring at top lid, inside swab	M23POI1	0.24	yes	high	$7.92 \cdot 10^8$	$2.96 \cdot 10^6$
	core black surface swab	M23POIswab	bdl	yes	low		-
	core black surface cut	M23POI3cut	0.0728	yes	high	$2.80 \cdot 10^8$	$1.93 \cdot 10^6$
	module surface, outside	M23S1	0.191	yes	high		$4.07 \cdot 10^6$
		M23S2	0.0856	yes	high		$1.35 \cdot 10^6$
	module surface after transport	M23Safter	0.1004	yes	high		$2.69 \cdot 10^6$
	transport flask after	M23Ta1	0.0294	yes	high		$5.45 \cdot 10^5$
	transport flask before	M23Tb1	bdl	no	low		-
		M23Tb2	bdl	yes	medium		$1.17 \cdot 10^3$

Heatmaps of DNA sequencing results including low confidence amplifications and positive control (Zymo Microbial Community standard).

	-ve ctrl	+ve ctrl	Control	M19	M21	M22	M23	Spike	Water
Firmicutes; Desulfosporosinus	0	0	1.5	5.4	3.6	7.5	6.1	44	8.5
"Proteobacteria"; Escherichia/Shigella	20.4	16.5	0.5	1.1	6.1	7.6	7.2	0	0.7
"Proteobacteria"; Pelomonas	43.7	0	19.9	3.3	5.1	7.9	7.6	0	3.5
Firmicutes; Fusibacter	3.3	0	3.6	12.1	9.2	8.8	9.8	0	0.6
Firmicutes; Clostridium_III	0	0	0	0.3	0.5	1.2	1.1	1.1	0.5
"Actinobacteria"; Mycobacterium	0	0	0.1	0	1	1.1	1.3	0	0
"Proteobacteria"; Brevundimonas	0	0	0.2	0.2	1.1	1	0.5	0	3.5
"Actinobacteria"; Nocardioides	0	0	0.2	0.1	1	1.5	0	0	0
Firmicutes; Streptococcus	0	0	2.5	0	0	1.4	0	0	0
"Proteobacteria"; Acinetobacter	0	0	0.4	0	0	1.1	0	0	0
"Tenericutes"; Acholeplasma	0	0	0.3	1.3	0.5	1.8	1.8	0	0.1
"Proteobacteria"; Ralstonia	0	0	1	2.3	0.7	1.2	0.9	0	0
Firmicutes; Gracilibacter	0	0	0	0.6	0.4	0.6	2	0	1.8
Firmicutes; Desulfitibacter	0	0	0	0.8	1.1	0.6	1.7	0	1.6
Firmicutes; Acetobacterium	0	0	0.6	1.2	0.4	0.3	1.8	0	0
"Bacteroidetes"; Hymenobacter	0	0	0.1	0	0.1	0	1.4	0	0
"Bacteroidetes"; Dyadobacter	0	0	0	0	0	0	1.5	0	0
"Proteobacteria"; Neisseria	0	0	0.4	0	0	0	1.3	0	0
"Actinobacteria"; Arthrobacter	0	0	0.4	0	1.7	0.7	2.4	0	0
"Proteobacteria"; Tepidimonas	0	0	1.6	0	0	0.4	0	0	0
"Proteobacteria"; Devosia	0	0	0.1	0.1	0.3	0.1	0.3	0	1
"Proteobacteria"; Paracoccus	0	0	0.2	0	0.4	0.4	0.8	0	0
"Euryarchaeota"; Methanolobus	0	0	0.1	0.3	0.4	0.3	0.5	0	0
"Proteobacteria"; Moraxella	0	0	0	0.6	0	0.6	0.6	0	0
Cyanobacteria/Chloroplast; Streptophyta	0	0	0.3	1.1	0.4	0	0	0	0
"Proteobacteria"; Geobacter	0	0	0.4	1.1	0	0	0	0	0
"Proteobacteria"; Thiobacillus	0	0	0	1.2	0.1	0.1	0.6	0	1
Microgenomates; Microgenomates_genera_incertae_sedis	6.8	0	0.1	0	0	0	0	0	0.3
"Proteobacteria"; Pelagibacterium	0	0	0.3	0.1	0.2	0.1	0.1	0	5.1
Firmicutes; Dethiobacter	0	0	0.1	0.4	1.2	0.4	0.7	0	0.5
Firmicutes; Alkaliphilus	0	0	0.5	1.1	0.8	0.3	0.7	0	0.8
"Deinococcus-Thermus"; Deinococcus	0	0	0	0	1.2	0	0	0	0
"Actinobacteria"; Pseudonocardia	0	0	0.1	0.2	1.5	0.2	0.4	0	0.1
"Actinobacteria"; Blastococcus	0	0	1.4	0	1.2	0	0	0	0
"Actinobacteria"; Rothia	0	0	4.9	0	0	0	0	0	0
"Actinobacteria"; Kocuria	0	0	5.3	0.2	0	0.5	0	0	0
"Proteobacteria"; Acidovorax	0	0	0.1	2.8	0	0	0	0	0
"Actinobacteria"; Corynebacterium	4.2	0	0.3	3.7	0	0.8	0	0	0.2
"Proteobacteria"; Sphingomonas	0	0	0.6	0	0	1.2	0	0	12.1
"Actinobacteria"; Nitriliruptor	0	0	0	0.2	0.3	2.9	0.3	0	3.8
Firmicutes; Listeria	0	11.4	0	0	0	0.1	0	0	0
Firmicutes; Enterococcus	0	7.7	0	0	0	0	0	0.3	0
Firmicutes; Staphylococcus	0	11.5	1.5	0	0.6	1	0	0	0
Firmicutes; Bacillus	1.7	16.2	0.8	1	0.7	0.3	0.5	0.7	0.1
Firmicutes; Lactobacillus	1.7	26.9	0	0	0	0	0	0	0
Firmicutes; Desemzia	0	0	11.8	0	0	0	0	0	0
"Actinobacteria"; Propionibacterium	8.4	0	8.3	1.8	6.6	0.4	0.8	0	5.8
"Proteobacteria"; Bradyrhizobium	0	0	0	4.9	0.3	2.4	6.6	0	0.2
"Acidobacteria"; Gp7	0	0	0.1	1.1	1.7	1.6	4.8	0	0.4
"Proteobacteria"; Pseudomonas	1.7	9.7	14.8	47.2	44.5	39.3	29.5	0.3	39.8
Remaining taxa (181)	8.1	0	14.5	2	4.9	2.3	4.3	53.6	7.8

-ve ctrl, +ve ctrl, Control, no added Microbes no Membrane, added Microbes no Membrane, no added Microbes with Membrane, added Microbes with Membrane, Spike, Borehole water

% Read Abundance: 40, 30, 20, 10

Figure 3.14 – Module heatmap of the percent contribution of each OTUs (at the phylum and genus level) to the overall community. The data were obtained from 16S rRNA gene V3V4 amplicon sequencing. Here, including low-confidence sequencing results. The columns from left to right showing the various types of samples and on the y-axis each row represents the relative abundance of a given OTU. The positive control is an equimolar mix of eight bacteria[I] (12.5% each) that allows the validation of the method. The results show that only Lactobacillus is overrepresented in this control, and this is likely due to the mis-assignment of Salmonella to Lactobacillus.

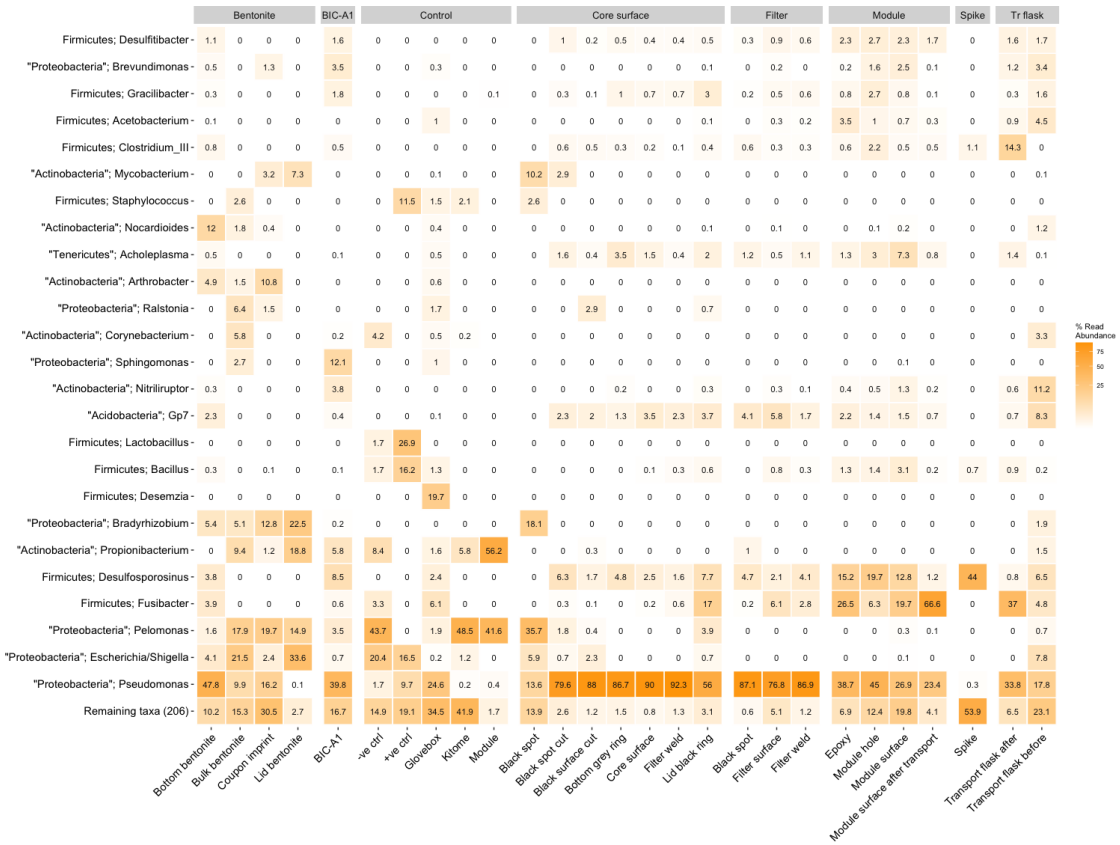

Figure 3.15 – Sampling location-resolved heatmap of OTUs at the phylum and genus level from 16S rRNA gene V3V4 amplicon sequencing of all four modules, the borehole porewater community, control samples, the SRB spike and the transport flasks (Tr flask). Here, including low-confidence sequencing results.

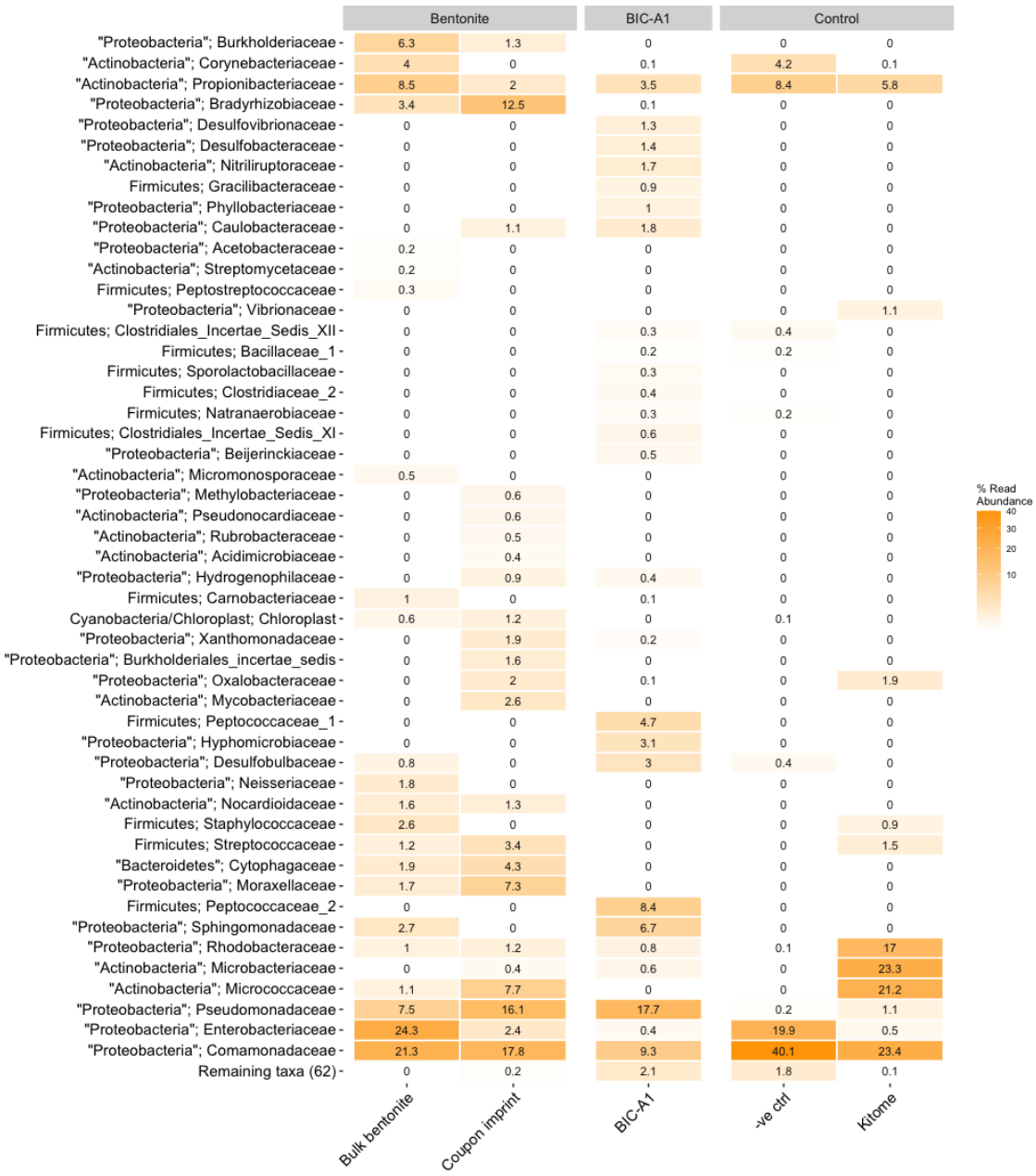

Figure 3.16 – Bulk and coupon imprint bentonite microbiome, OTU taxa on family level to enable comparison with previous IC-A experimental phases. Here, including low-confidence sequencing results

4 Harnessing the H_2-oxidizing microbial community in the Swiss radioactive waste repository

Niels Burzan

Environmental Microbiology Laboratory (EML), Ecole Polytechnique Fédérale de Lausanne (EFPL), Switzerland

Experimental work performed by the student with occasional help during sampling by Manon Frutschi and Aislinn Ann Boylan. MIP analysis were performed by Franco Zunino, IC and ICP-MS analysis of water samples were performed by Karine Vernez Thomas and Sylvain Coudret, EPFL, Lausanne, Switzerland. 16S rRNA gene-library sequencing was performed by the team of the Lausanne Genomics Technologies Facility (University of Lausanne, Switzerland). Fe microXRF and XAS data were acquired by Sharon Bone and Sam Webb, SLAC, SSRL, Menlo Park, CA, U.S.A. S microXRF and XAS data were acquired with help from Konstantin Ignatyev, DLS, Harwell, U.K. The content of this chapter is under preparation for submission as a manuscript to Frontiers in Microbiology, Section Terrestrial Microbiology with contributions by the following co-authors in addition to the student: Rizlan Bernier-Latmani, Oliver X. Leupin, Aislinn Boylan, Manon Frutschi, Simiao Wang, Konstantin Ignatyev, Sam Webb, Sharon Bone.

Abstract

The activity of subsurface microorganisms, if well characterized, can be harnessed for the benefit of engineering projects. The Swiss radioactive waste repository design aims to take advantage of the presence and activity of microbial life in the deep subsurface. After closure, anaerobic steel corrosion of waste and waste canisters in low- and intermediate-waste repositories will lead to a build-up of hydrogen gas. This accumulation should be avoided to preclude any damage to the structural integrity of host rock. Strategies to mitigate the risks arising from pressure build-up are under investigation. The access and operation tunnels provide an opportunity to create conditions favorable for the microbially-mediated removal of excess gas. Here, we consider the possibility of promoting the activity of sulfate-reducing microorganisms and methanogens in order to oxidize dissolved hydrogen and, by mass-transfer, consume

gaseous H_2. Four bioreactors containing a 80/20% (w/w) mixture of quartz and Wyoming bentonite were supplied with naturally sulfate-rich Opalinus Clay rock porewater and with hydrogen gas during 73, 78, and 102 days. Within 14 days, sulfate-reducers, e.g., *Desulfovibrio*, were active in areas where the sulfate-rich porewater and hydrogen mixed. Additionally, starting at day 28, methane was detected in the gas phase, suggesting the activity of methanogens, e.g., *Methanosarcina*. Other bacterial groups belonging to *Pseudomonas*, *Sunxiuqinia*, and *Symbiobacter* were commonly found. Sulfate reduction led to a consumption of H_2 and the production of sulfide, a corrosive agent. However, we observed the potential formation of polysulfides and elemental sulfur, which would suggest the depletion of reactive iron due to the high abundance of hydrogen sulfide. In contrast, methane does not impact corrosion and is favorable in the context of a radioactive waste repository. Thus, promoting the growth of microorganisms, at the appropriate location such as the access or operation tunnels, can contribute to the long-term safety of a radioactive waste repository.

4.1 Introduction

Nuclear waste repositories are an engineered solution to the societal problem of the disposal of nuclear waste. They are engineered facilities in the deep subsurface that are designed to house nuclear waste until it decays and its potential negative impact on the biosphere is removed. A low-level repository consists of the following components, based on (O. Leupin et al., 2016):

- The waste matrix, conditioned for a slow degradation, Figure 1.8a
- Waste container that are assembled within disposal containers, Figure 1.8b
- Caverns holding the disposal containers are backfilled with a cement mortar that is a suitable interface to the host rock
- Storage caverns within a suitable host rock, the Opalinus Clay rock formation. The final cavern size depends on the mechanical properties of the chosen host rock site and the overburden of the formation, i.e., the depth, Figures 1.7b and 1.7a.
- Access and operational tunnels connecting the storage caverns with the surface, theses also need to be backfilled with a suitable material, Figure 1.6

However, there are still a few questions that are being resolved, particularly with respect to the role of microorganisms in nuclear waste disposal. One such questions is the accumulation of H_2 gas. More specifically, upon closure of the repository, iron (from carbon steel) and other metallic elements within the waste and waste packages such as zirconium, aluminium, copper, lead, zinc and magnesium are expected to react with porewater and undergo anoxic corrosion, resulting in the evolution of di-hydrogen gas (Diomidis et al., 2016). The creation of a gas phase which displaces the porewater will impact the structural integrity of the subsurface. Therefore,

ways to mitigate the gas-related changes in the host-rock stress regime are necessary to ensure the long-term safety case of a low-level radioactive waste repository in Swiss Opalinus rock. In addition to the aforementioned source, there are also sinks for H_2, which are primarily microbial, Figure 4.1 (Diomidis et al., 2016; O. Leupin et al., 2016).

4.1.1 Microbial gas sink

The main microbial processes expected to remove hydrogen gas are sulfate reduction and methanogenesis. The equation for sulfate reduction for example can be written as:

$$6\,H_2 + HCO_3^-(aq.) + SO_4^{2-}(aq.) + 2\,H^+(aq.) \rightarrow CH_2O(biomass) + HS^-(aq.) + 6\,H_2O \tag{4.1}$$

Or without biomass formation, written as:

$$4\,H_2 + SO_4^{2-}(aq.) + H^+(aq.) \rightarrow HS^-(aq.) + 4\,H_2O \tag{4.2}$$

Methanogenesis uses four moles of hydrogen gas and results in one mole of methane gas, thus also helps to lower the amount of gas within a repository:

$$4\,H_2 + CO_2 \rightarrow CH_4 + 2\,H_2O \tag{4.3}$$

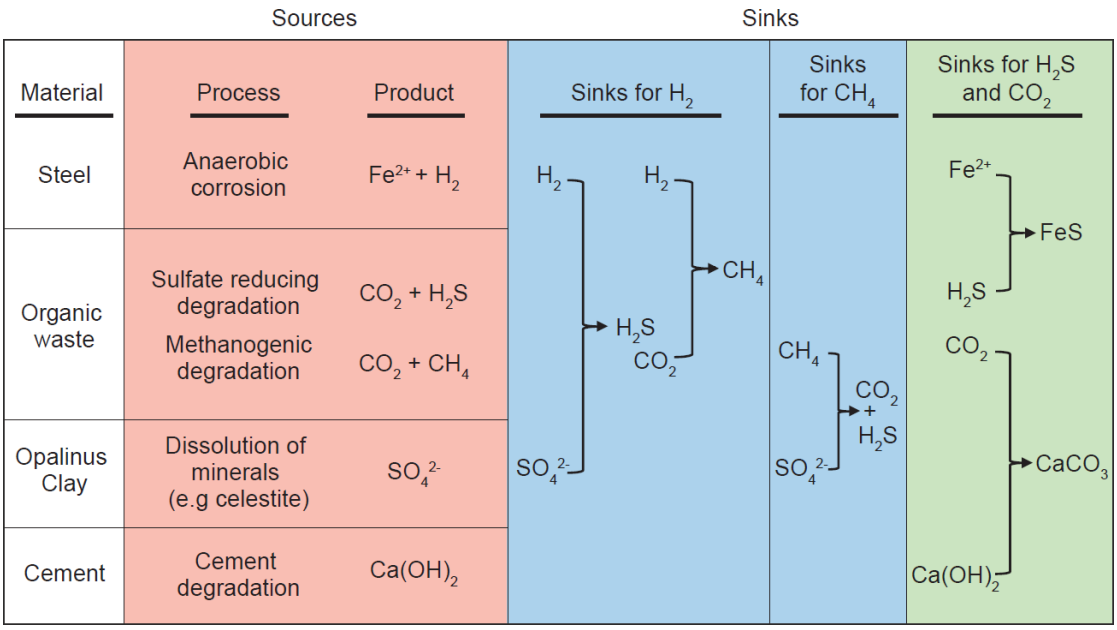

Figure 4.1 – Gas sources (red) and gas sinks within a low-level waste repository identified by Nagra, figure from (Diomidis et al., 2016). In blue are microbial and in green abiotic/chemical gas sinks shown.

The main questions are:

1. Can sulfate-reduction and methanogenesis occur within the repository?
2. What are the requirements to facilitate their activity such that their metabolic potential can be taken into account for the overall gas balance?

The first question will be answered with the experimental work presented in the chapter. The second question, a conceptual microbial gas sink is envisioned for for a Swiss low-level waste repository.

4.1.2 Testing a potential operational tunnel backfill

The proposed engineered mitigation for H_2 build-up is to establish a section of the depository in which there is net consumption of H_2. The operational tunnels represent a candidate for that section. Can the backfill in these tunnels be tailored in such a way that it enables the consumption of the high amount of gas evolving from the low-level waste caverns? As indicated above, each cavern (containing the waste) is connected to the operational tunnel via branch tunnels, Figure 4.2. The operational tunnel (indicated in purple) could include microbial activity and remain approximately 100 meters away from the waste caverns. Based on a conservative complete waste degradation/corrosion (Diomidis et al., 2016), estimate a base case scenario (based on MIRAM14) in which from the day of emplacement until about 1,000 years after about 6 moles of H_2 are produced per meter of length of the cavern per year. From 1,000 to 100,000 years (the end of the safety assessment time frame), the gas-production rate is declining. In the following assumptions, we consider only the maximum, initial hydrogen-production rate. Assuming caverns of approximately 200 meters length (reference length (O. Leupin et al., 2016)), about 3.29 moles of H_2 per day and per cavern are expected. Considering a hypothetical biofilm capable of consuming 0.2 moles H_2 per day and per cubic meter, approximately 16.45 m^3 of (idealized) biofilm are necessary for each cavern to consume the entire gas production of one cavern per day. To put this in perspective, the biofilm would occupy a porous space of $\approx$ 0.92 times the volume of a gray whale (*Eschrichtius robustus*) (WolframAlpha, 2020a). In total 9 of these caverns (reference design) are expected, thus 148.05 m^3 of active biofilm-occupied porespace would be necessary. As indicated by (Diomidis et al., 2016), the base case is a rather conservative assumption and the real rate of hydrogen evolution will be lower and the volumes of gas, due to the temperature and pressure conditions within a repository, lower.

Thus, if this maximum rate of production of H_2 is considered, the spacing between caverns and the porosity of the back-fill needs to be chosen such that 148.05 m^3 of pore space remains accessible for microorganisms for growth. Their growth requires Opalinus Clay rock porewater and hydrogen gas from anoxic corrosion and the pore space mentioned above. Thus, the requirement for space for microbial activity as well as the high-pressure environment of a subsurface engineered gas transport system with approximately 600 meter overburden, both

need to be taken into account when choosing the material and mixture of a operational tunnel back-fill.

In this experiment, we chose a 80% (w) quartz sand and 20% (w) bentonite mixture as the porous back-fill because of its previous characterization as a potential plug and back-fill material for the Swiss low-level waste repository (Manca et al., 2015; Manca, 2015, 2016).

A modular *in-situ* test system containing an 80/20% (w/w) sand-bentonite matrix, saturated with natural Opalinus Clay porewater, and stimulated with the injection of molecular hydrogen was employed to investigate the adequacy of the concept. Here, we demonstrate the feasibility of a microbial gas sink made up by naturally-occurring microorganisms, consuming excess hydrogen gas and sulfate from the Opalinus Clay rock and Wyoming bentonite. The system produced hydrogen sulfide and methane. If this were implemented in the operational tunnel, the sulfide would be produced at a safe distance to the radioactive waste. Thus, we argue that a 80/20% (w/w) sand-bentonite back-fill of the operational and service galleries may improve the overall long-term safety of a deep geological repository in Swiss Opalinus Clay rock formations.

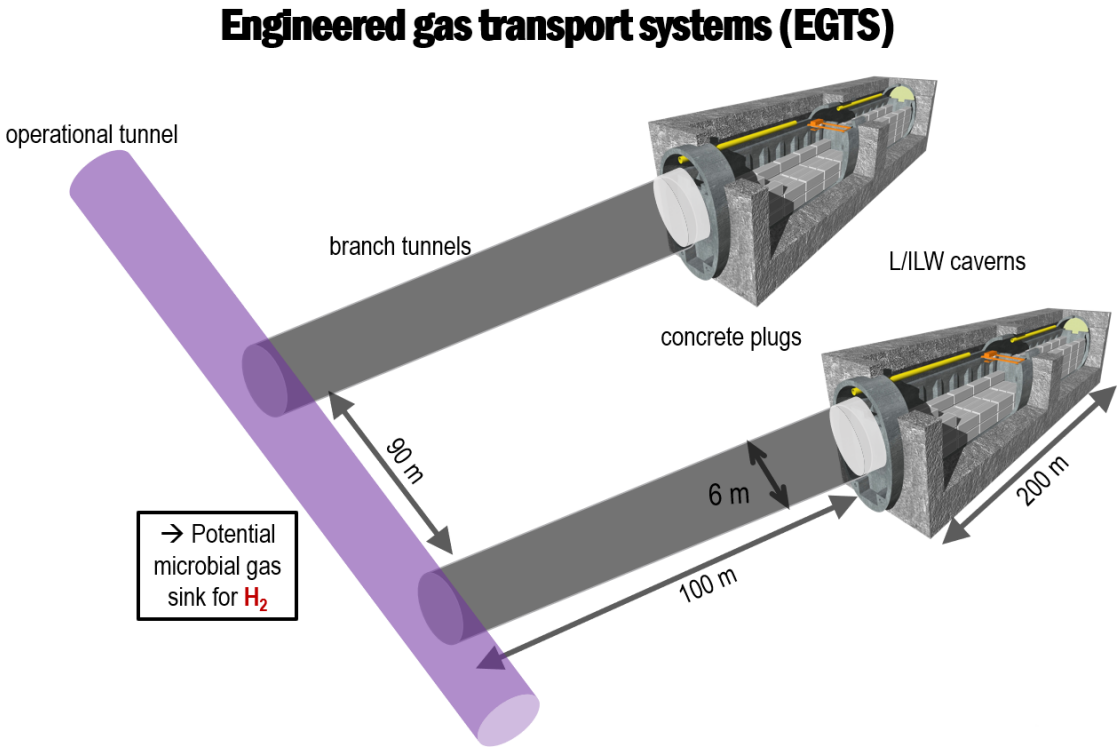

Figure 4.2 – Schematic of a potential microbial gas sink within the backfilled operational tunnels (purple), gallery dimensions approximated, based on (Diomidis et al., 2016), cavern illustration from (**leupin_research_2017**).

4.2 Experiment, Materials & Methods

The experiment consists of the application of hydrogen gas to porous medium in order to simulate its production from anaerobic steel corrosion, radiolysis of water, and from the degradation of the organic waste in the context of a low- and intermediate-level waste repository. The presence of H_2, an efficient electron donor for microbial metabolism, enabled the stimulation of microbial growth and provided insight into the potential influence of the biosphere on low- and intermediate-level waste repositories. The aims included:

- (i) testing a potential material which could be used as service and construction tunnel back-fill and simultaneously provide enough pore space for microbial activity. The rationale for enabling microbial activity is to exploit their beneficial impact while avoiding the adverse effects of their metabolism. The benefit would be the consumption of the excess hydrogen gas;
- (ii) determining the *in-situ* hydrogen consumption rate of the naturally-forming biofilms under repository-relevant conditions. The relevance of hydrogen as the main electron donor for microbial life is illustrated by the high amount expected to evolve Figure 1.9.

4.2.1 Drilling of BMA-A1

A dedicated borehole (BMA-A1) was drilled in early May 2015 to a depth of 16.3 meters with an 47° inclination into the ceiling of the gallery of the Underground Rock Laboratory (URL) 'Mont Terri', Switzerland, Figure 4.3a. The borehole is located at the main fault, at the transition from shaly to the sandy facies (the latter starting at a depth of 12 meters, thus within the interval). Because of the inclination, the borehole is oriented perpendicularly to the bedding of the Opalinus Clay rock. To prevent contamination, all drill rods were cleaned and disinfected with 70% (v/v) ethanol, Figure 4.3b. During handling, emphasis was put on keeping the rods as clean as possible, e.g., by usage of 70% (v/v) ethanol-treated nitrile gloves. The borehole was sealed with an inflatable packer. The packer systems offers two water sampling possibilities via polyamide tubing/lines (Q1 and Q2) and a pressure measuring line (P1), Figure 4.4. The packer seal created a 6.5-meter long interval with a diameter of 10.1 cm , with a maximum capacity of of 52.08 liters. It included a wet spot of the Opalinus Clay rock at the 13.75 m mark, situated near the middle of the interval. After borehole drilling and packer insertion, the borehole and the sampling lines were flushed and pressurized with sterile argon gas to restore anaerobic conditions and thus minimize the disturbance to the microbial community.

4.2.2 *In-situ* equipment and modifications

All bioreactor experiments were carried out within the URL 'Mont Terri' under controlled conditions. Special emphasis was given to a) the avoidance of any contamination of the native, natural Opalinus Clay rock porewater microbiome and b) the delivery of the porewater

from the borehole to the bioreactors with neither disturbance of the microbiome nor the chemical composition. Therefore, the design was made for a strict 'one-way flow' policy for the porewater and experiments had to be conducted in such a way that the gas-phase within the borehole remained above atmospheric pressure. Second, in a continuous operation mode of the experiment, the slow flow of borehole porewater through polyamide lines towards the experimental system might allow the diffusion of oxygen into the water within the lines, thus influencing the chemical conditions and the microbiome. Thus, a stainless steel isolation was put into place for all water-containing polyamide lines before the experiment and flushed several times with argon gas and maintained at an over-pressure of 2.5-3.5 bars. The space between the ceiling of the gallery of the URL 'Mont Terri' and the packer of BMA-A1 was isolated with a flange and constantly flushed with a controlled argon gas flow (50 mL argon gas at standard conditions per hour).

4.2.3 Anoxic chamber equipment

Within the URL 'Mont Terri', a nitrogen gas-filled glovebox (UniLab Plus, M. Braun Inertgas-Systeme GmbH, Garchingen, Germany) was used as the experimental platform. Figure 4.5 shows the layout of the experimental system. The glovebox hosts the four bioreactors and several electrodes, sensors and controllers and maintains a well-controlled anoxic environment. Opalinus Clay rock porewater from the borehole BMA-A1 (upper left in Figure 4.5) was anoxically transported to the MBraun anoxic chamber (N_2 atmosphere, green). Four bioreactors were placed within the MBraun anoxic chamber and supplied with porewater from the borehole at a constant elevated pressure, regulated with a pressure controller (PC, EL-PRESS, Bronkhorst High-Tech BV, Ruurlo, The Netherlands). The water flow was driven by the hydraulic gradient from the ≈ 20-meter water column down to near atmospheric pressure within the glovebox (pressure gradient). Hydrogen gas was supplied from a computer controlled hydrogen-grade syringe pump (500D Syringe Pump, Teledyne ISCO Inc., Lincoln, Nebraska, U.S.A.), operated via a purpose-built system (Solexperts AG, Moenchaltdorf, Switzerland). Precise volumes of pure hydrogen gas were applied once a day to each bioreactor, whereas porewater could flow continuously. The flow-through of each bioreactor was measured by four CMOS-based flow-recorders (FR, SLI-0430, Sensirion AG, Staefa, Switzerland). The outflow water was divided with a 4-position 2-flow-valve (EUTA-VLSC4MWE2HC, VICI AG International, Schenkon, Switzerland) such that the outflow of a single bioreactor could be investigated using a electric conductivity indicator (ECI, Conducell 4USF Arc 120, Hamilton Bonaduz AG, Switzerland), a pH probe (PHI, Heito, Chauvin Arnoux, Asnieres-Sur-Seine, France), a dissolved hydrogen sulphide sensor (H2SI, Heito, Chauvin Arnoux, Asnieres-Sur-Seine, France) and a redox potential probe (EHI, Polilyte Plus, Hamilton Bonaduz AG, Switzerland). The low end of the pressure gradient was realized by collecting the outflow water within a Tedlar® bag, placed onto a scale (KB 60.2, Mettler Toledo, Columbus, Ohio, United States).

4.2.4 Bioreactor experimental setup

Four bioreactors, designed as shown in Figure 4.6, were used for the experiment. Each has dimensions of 12 x 10 cm (inner height x inner diameter) and the design can withstand swelling pressures in the mega-pascal range, thus the design can be used for tests with up to 100% bentonite content. Sulfate-rich porewater was supplied by two titanium inlets at the bottom whereas hydrogen gas was provided via a long titanium tube into the middle of the bioreactor. The matrix simulating the potential back-fill material (sand-bentonite, 80/20% w/w) is the core located in the middle, sandwiched between a lower and an upper coarse sand (quartz) layer. It is not in direct contact with the stainless steel cylinder but held in place by a inner cylinder made out of Plexiglas, including a top and a bottom. Two different sizes of commercial, kiln-dried quartz sand were used, both supplied by Carlo Bernasconi AG, Bern, Switzerland. The grains were naturally rounded and used as delivered without any further treatment. The lower and upper bioreactor layer was made of coarse sand with 1.5-2.2 mm grain size. To produce the sand-bentonite matrix, kiln-dried quartz sand with 0.1-0.6 mm grain size was used. For both grain-sizes, the chemical composition is given in 4.1. Wyoming bentonite MX-80 was provided by Nagra from their remaining stock of the Full Scale emplacement (FE) experiment (Müller et al., 2017). It is a well-characterized bentonite used in repository research, e.g. (Karnland & AB, 2010), and its mineral composition is given in Table 4.2 based on the technical report of the Swedish Nuclear Fuel and Waste Management Co (SKB AB) and Clay Technology AB (Karnland et al., 2006). Using a 70% ethanol-disinfected porcelain mortar and pestle, all large bentonite aggregates were ground manually until no aggregates larger than 0.6 mm could be observed. The mixing of 0.1-0.6mm sand and the ground Wyoming bentonite was performed similar to the method described by (Chen et al., 2019): Sand and bentonite were poured in corresponding weight ratios to obtain a 80/20% (w/w) mix onto a large sheet of plastic-reinforced paper. Lifting the paper at one corner and folding it diagonally towards the opposite corner, releasing and repeating this folding with the next corner clockwise. This was repeated 10 times and resulted in a homogeneous mixture that was poured into the bioreactor. All bioreactor parts, the stainless steel, Plexiglas, tubing, connections, were disinfected shortly before assembly. All tubes were amended with fine mesh commercial organza to preclude the movement of sand or bentonite particles into the tubes. Pretests showed that this synthetic fiber, made out of 50% polyester and 50% polyamide was stable under the experimental conditions and was obtained from Stoffe.de, fabfab GmbH, Schenefeld, Germany. The bioreactor filling was was started from the top with the top lid containing the hydrogen delivery tube being located at the bottom. The filling procedure thus started by pouring the top coarse sand layer until approximately 1.5 cm height, followed by 850 g of homogeneous sand-bentonite mix (80/20% w/w) and another approximately 1.5 cm of the lower coarse sand layer. The bottom lid was then put into place and the bioreactors carefully inverted. No shaking or other compacting method was applied to the bioreactor filling. The modules were then transferred by car to the URL 'Mont Terri' and placed within the anoxic chamber. Anoxic conditions were created by passing each bioreactor through an antechamber, applying 3 cycles of high vacuum followed by 1 bar of nitrogen. Once set in the

anoxic chamber and connected to the borehole porewater flow system, each bioreactor was flooded with porewater. The four bioreactors were installed with intervals of one week. After 5 to 30 days of saturation, depending on the installation date, the bioreactors started receiving continuous porewater flow from borehole BMA-A1, controlled via the pressure controllers.

Two different set-ups for the bioreactor experiment, called MA-A1.x[I] were chosen:

- Serial set-up: Bioreactors MA-A1.1 and 1.2 were connected such that 1.1 received borehole porewater as its inflow while 1.2 received the outflow of 1.1 as its inflow. The rationale for this set-up was to provide to 1.2 water with a distinct chemical and microbial composition. The inflow water for 1.2 was depleted in sulfate and enriched in sulfide and hydrogen, representative of an aged repository back-fill when sulfate is depleted but the anoxic corrosion of steel continues.
- Parallel setup: Bioreactors MA-A1.3 and 1.4 were both connected to the borehole water as their inflow and with separate outflow paths. Under ideal conditions, both would have received the same volume of borehole water at the same rate and developed very similar microbiomes.
- Negative control: MA-A1.NC was intended as an abiotic control. Sterilized (γ-irradiated) Wyoming bentonite from the IC-A experiment was mixed with sterile quartz sand (autoclaved for 80 minutes) to obtain an 80/20% (w/w) mixture, filled into an exact same sized Plexiglas cylinder. Anoxic conditions were established by placing MA-A1.NC within a nitrogen-gas filled glovebox, and saturating it with sterile (80-minutes autoclaved) artificial porewater, resembling the composition of Opalinus Clay porewater (Pearson et al., 2003). No flow-through system was setup, only up to 5 mL of artificial porewater was added daily to compensate for evaporation losses within the dry atmosphere of the glovebox. After 30 days, the negative control was sampled for DNA extraction, elemental mapping and speciation of iron and sulfur.

Table 4.1 – Commercial quartz sand chemical composition, as provided by the suppliers documentation.

Substance	**Weight**
SiO_2	98.70%
Al_2O_3	0.60%
$K_2O + Na_2O$	0.45%
$CaO + MgO$	0.05%
TiO_2	0.04%
Fe_2O_3	0.02%
loss on ignition	0.25%

[I] MA-A1.x stands for microbial activity experiment A, 1st iteration, x stands for the individual bioreactor number, NC stands for negative control, i.e., a sterile sand-bentonite mixture devoid of microbial activity

Table 4.2 – Wyoming bentonite MX-80 mineralogical composition, based on Siroquant determinations by (Karnland et al., 2006)

Mineral phase	Weight
Montmorillonite	83.50%
Illite	0.70%
Anatase	0.20%
Calcite	0.20%
Cristobalite	0.40%
Goethite	0.20%
Gypsum	0.90%
Hematite	0.10%
Lepidocrocite	0.70%
Magnetite	0.10%
Microcline	0.80%
Muscovite	2.80%
Orthoclase	0.70%
Plagioclase	2.90%
Pyrite	0.60%
Quartz	2.80%
Tridymite	1.90%

(a) Positioning of the drilling rods on the inclined drilling rig.

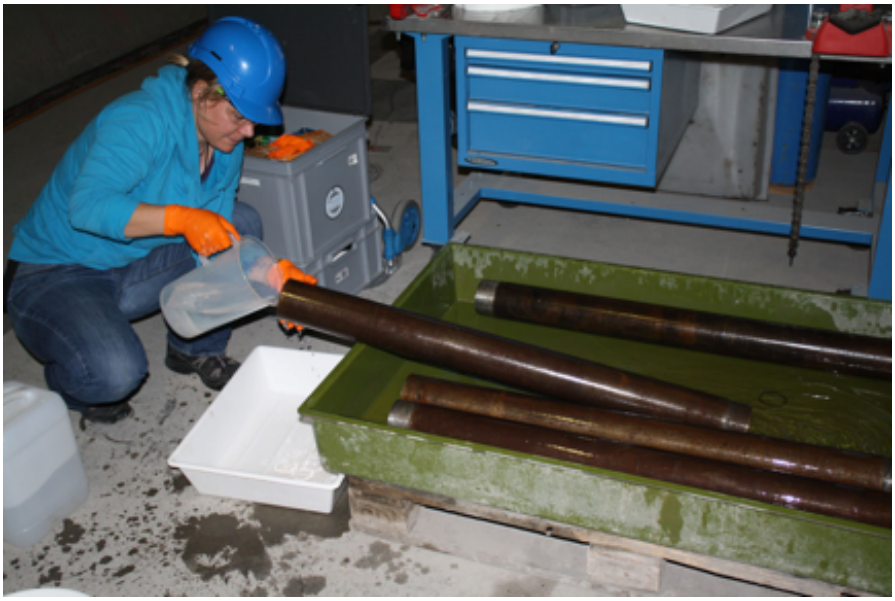

(b) Drilling rods were cleaned with 70% (v/v) ethanol in order to minimize potential influences on the evolving microbial community within the borehole. Pictures from M. Frutschi with permission.

Figure 4.3 – Borehole BMA-A1 drilling, May 2015.

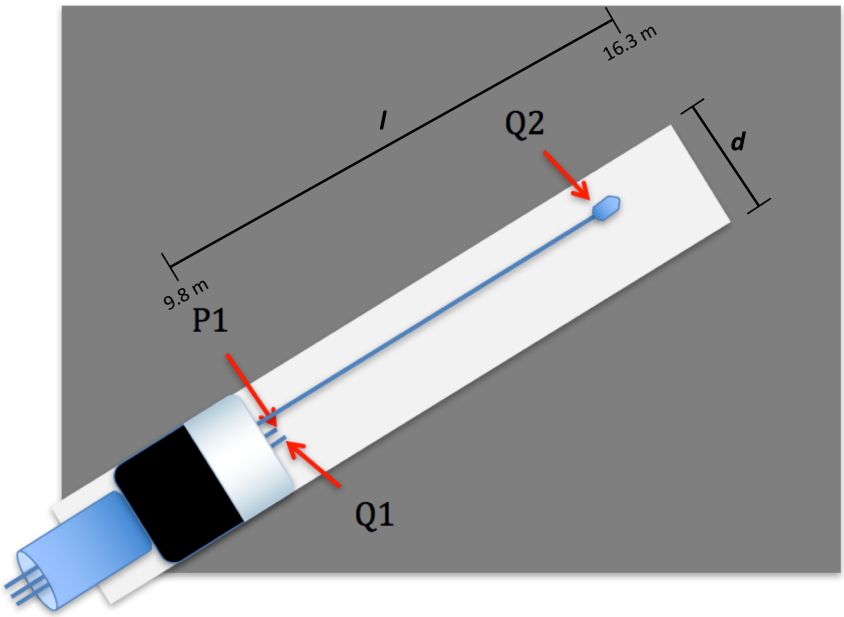

Figure 4.4 – Schematic representation of the 43° inclined borehole and packer. Two sampling lines Q1 and Q2 allow collection of porewater, P1 is used to measure the pressure within the borehole. Dimensions: l = 6.5 m, d = 0.101 m, 52.08 L total volume. The interval starts after the packer ends at the 9.8 m mark and ends at 16.3 m. At the 12 m mark, the transition from shaley to sandy facies occurs. At 13.75 m, a wet spot was observed during drilling. Graphic from M. Frutschi with permission.

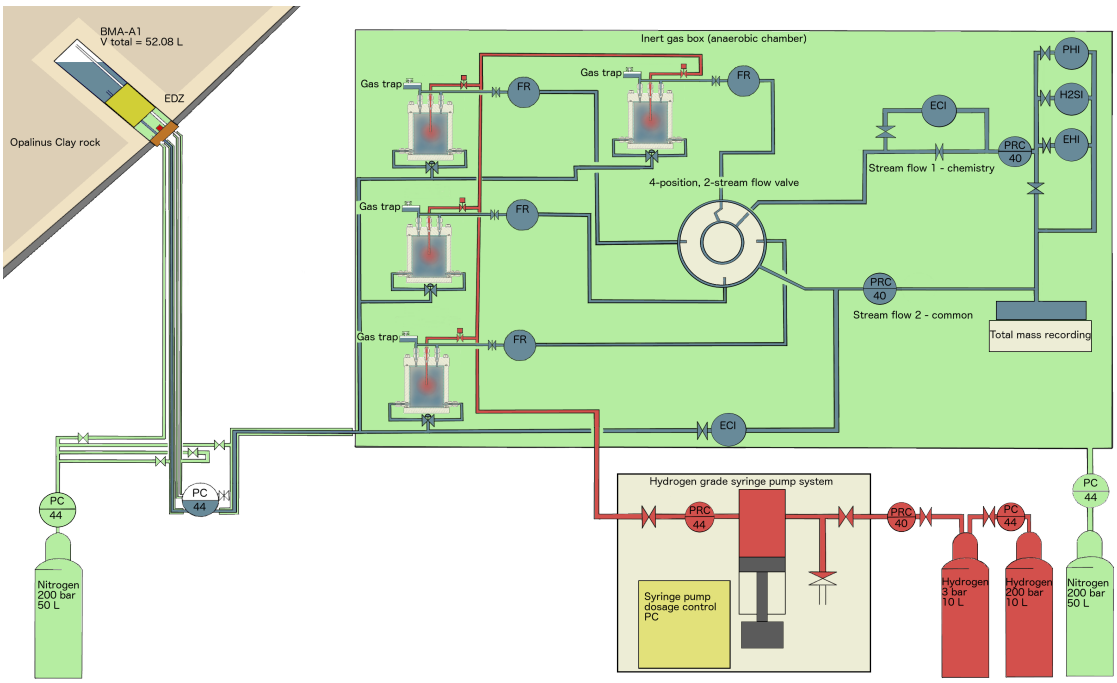

Figure 4.5 – Experimental setup of the MA-A1.x experiment, described in Section 4.2, Experiment, Materials & Methods.

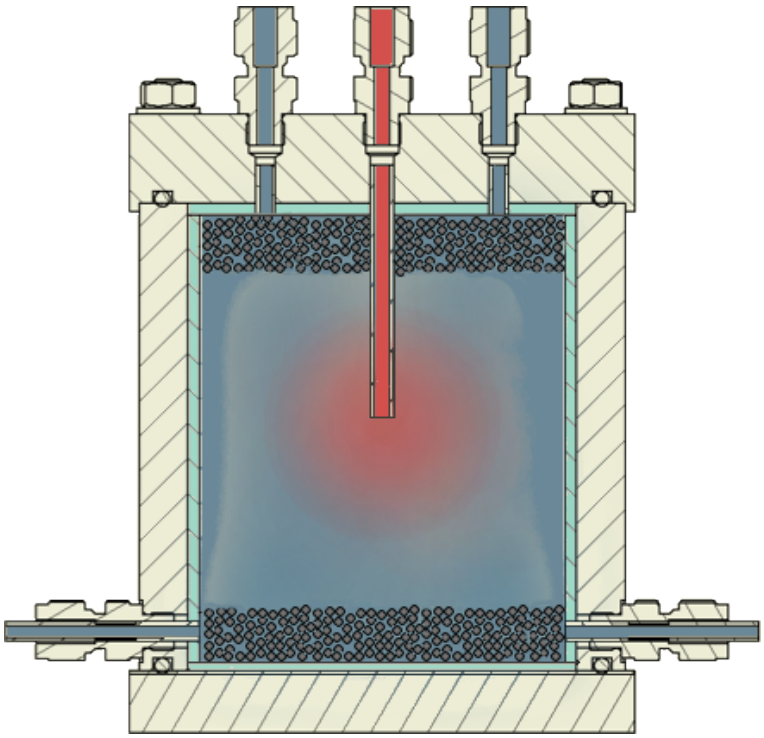

Figure 4.6 – A stainless steel bioreactor (beige), equipped with an inner Plexiglas cylinder (turquoise) filled with a 80/20% (w/w dry mass) mixture of sand-bentonite mixture and with a layer of coarse sand at the top and bottom layers. The sand and the sand-bentonite mixture are saturated with Opalinus Clay porewater from the BMA-A1 borehole (blue) through two water inlets at the bottom. Daily pulses of hydrogen gas were applied to the middle (red) via a titanium tube directly to the center of the sand-bentonite core. Water outlets on the top enabled the porewater to follow a controlled pressure gradient. The dark blue area indicates the expected preferential water flow path along the contact surface or edge of the Plexiglas cylinder.

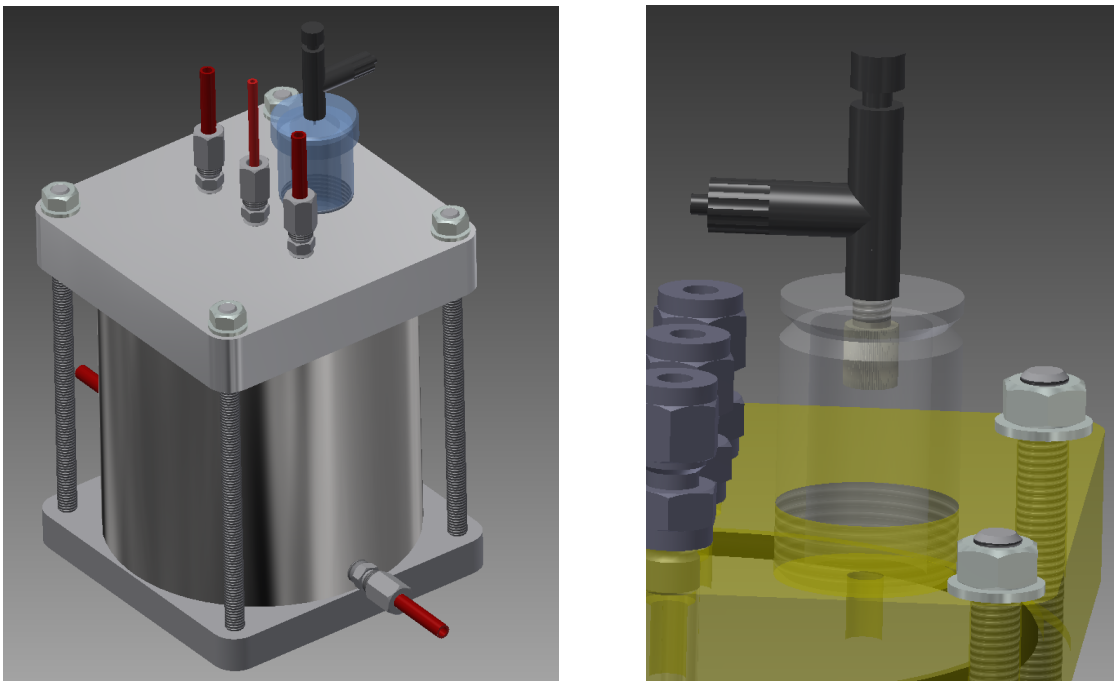

(a) (b)

Figure 4.7 – 3D-rendering of (a) a stainless steel bioreactor, equipped with two water inlets and outlets, a hydrogen-delivery tube and a gas-trap within the top-lid of the cylinder. The (b) gas-trap is equipped with an HPLC-sampling valve with Luer-Lock connection for syringe-needles, thus the sampling into gas-tight serum bottles can be performed.

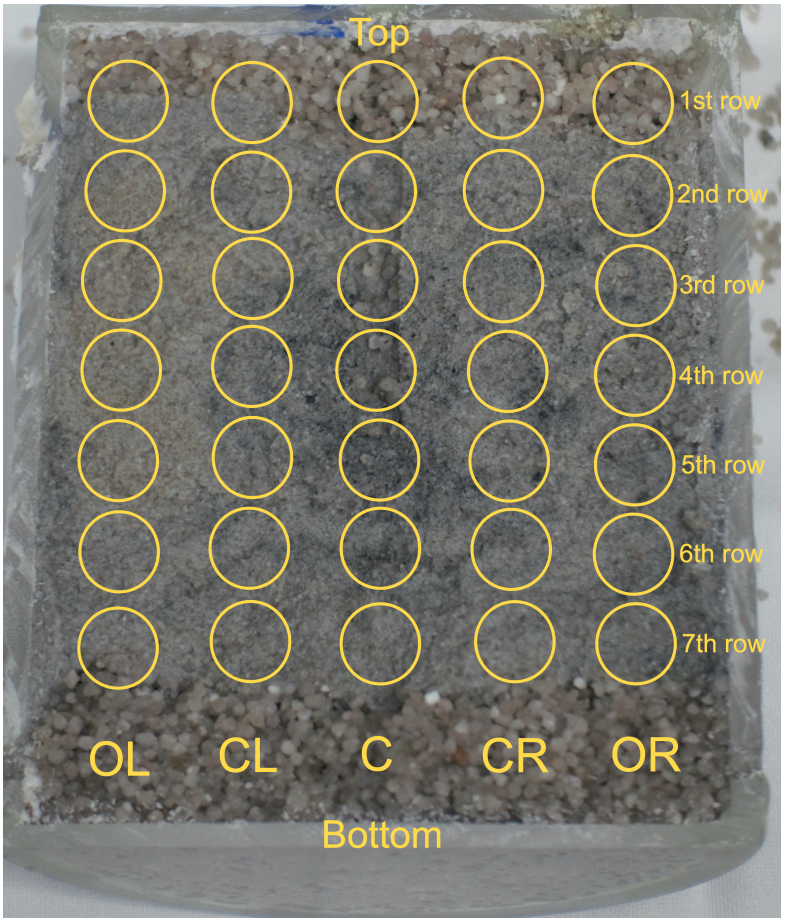

Figure 4.8 – Example of the sampling performed for DNA extraction. Within an anoxic chamber, the Plexiglas cylinder was cut open lengthwise and two halves were exposed: Five lines (outer left [OL], center left [CL], center [C], center right [CR] outer right [OR]), representing different radial locations were sampled at seven heights, numbered from 1st row (top) to 7th row (bottom). For each spot a new scalpel blade was used and the substrate was stored in DNA-free cryotubes at -20°C until DNA extraction.

4.2.5 Analytical methods

Bioreactor gas phase and porewater sampling Once per week, all valves connecting the individual bioreactors to the porewater flow system were closed to avoid any potential back-flow during the sampling. First, a sterile 50 mL serum bottle filled with filtered nitrogen gas (1bar) was attached to the gas trap and allowed to equilibrate with the elevated pressure of the respective bioreactor until water was observed. Second, at the two outflow connections, a 0.2 μm sterile syringe filter was installed and up to 7 milliliters of bioreactor outflow was collected. The outflow of gas and water were purely driven by the pressure difference between the interior of the bioreactor and the glovebox atmosphere (+10 mbar relative to the gallery atmosphere).

Gas phase analysis The gas phase was qualitatively analysed for the presence of methane gas using the following gas chromatography system: GC-450 (Varian, Middelburg, The Netherlands) equipped with a molecular sieve column (CP81071: 1.5m*1/8" ultimetal molsieve 13 9 80-100 mesh). Methane was detected by a flame ionization detector.

Porewater analysis The filtered porewater was aliquoted and conditioned for subsequent chemical analysis of sulfide, iron(II), using a UV-2501PC spectrometer (Shimadzu, Kyoto, Japan). Sulfide was analyzed using the (Cline, 1969) method and iron(II) using the ferrozine assay (Stookey, 1970). At the Central Environmental Laboratory (CEL) at the Environmental Engineering Institute (IIE), EPFL, Lausanne, Switzerland, ion chromatography (IC) and inductively coupled plasma mass spectrometry (ICP-MS) were performed by Karine Vernez Thomas and Sylvain Coudret. Major anions and cations were detected and quantified by Ion Chromatography: An IonPac® CS12A-5µm cation-exchange column (Thermo Fisher Scientific Inc., Waltham, Massachusetts, U.S.A.) and eluent 20 mM methanesulfonic acid were used for major cations, whereas an IonPac® AS18-4µm anion-exchange column (Thermo Fisher Scientific Inc., Waltham, Massachusetts, U.S.A.) with a gradient eluent KOH (from 0.0 to 30 mM) was used for major anions. Trace metals Al, Co, Cr, Cu, Fe, Mn, Mo, Ni, Si, Sr, Zn, were measured using inductively coupled plasma mass spectrometry (ICP-MS), on an Agilent 8900 Triple Quadrupole (Agilent Technologies Inc., Santa Clara, U.S.A.), with all samples prepared in dilutions with 0.1 M HNO_3 (final concentration, ultra-pure grade, MilliporeSigma, Merck KGaA, Darmstadt, Germany).

Borehole BMA-A1 sampling Borehole porewater was sampled for chemical analysis in a manner similar to that from bioreactors. The microbial community of the porewater was investigated by DNA extraction and amplification of the V3-V4 region of the 16S rRNA gene. 200 ml of borehole porewater were directly filtered using a sterile, DNA-free (80 min-autoclaving), 0.2 μm polycarbonate filter membrane (Isopore Membrane hydrophilic polycarbonate, Merck Millipore, Darmstadt, Germany) in a vacuum filter-tower setup (Nalgene® Nunc International,

Rochester, New York, USA). The biomass retained on the filter were preserved in LifeGuard Soil Preservation solution (Qiagen NV, Venlo, The Netherlands), stored at -20°C until subjected to a modified phenol-chlorophorm-isoamylalcohol DNA extraction protocol, originally based on (Bagnoud, Chourey, et al., 2016). Modifications applied were described by (Bell et al., 2018). Additionally, the polycarbonate filter remained in the test tubes until the addition of phenol because this treatment resulted in its solubilization, which increased the DNA yield. A second change applied concerns the DNA cleanup which was performed with synthetic linearized polyacrylamide (GenElute™-LPA, MilliporeSigma, Merck KGaA, Darmstadt, Germany) rather than naturally sourced glycogen from mussels. Subsequent DNA analysis steps are similar to the bioreactor samples as described below.

Bioreactor disassembly After the experiment, the bioreactors were retrieved from the URL 'Mont Terri', packed in argon gas-filled Mylar® bags and transferred to the laboratory at EPFL. Within a similar nitrogen gas-filled MBraun anoxic chamber as the one used in the URL 'Mont Terri', the bioreactors were disassembled and the sand-bentonite core contained within the Plexiglas cylinder was extracted. Sterile, DNA-free (autoclaved for 80-minute) cleanroom-grade wipes (Spec-Wipe® 7, VWR International LLC, Avantor Inc., Radnor, Pennsylvania, U.S.A.) were used to handle the Plexiglas core. A Dremel®3000 tool was used to cut the Plexiglas lengthwise open (DREMEL Europe Bosch Power Tools B.V., Breda, The Netherlands). After cutting, the core was placed on the DNA-free cleanroom-grade wipes on its side and the two halves came apart on their own within 2 minutes. The left half was used for immediate DNA sampling (as described above, Figure 4.8), while the right half was used for sample collection for subsequent synchrotron-based X-ray fluorescence imaging and X-ray absorption spectroscopy. The remaining sample of the left half was embedded in a resin for subsequent broad X-ray fluorescence imaging, as described below.

Mercury intrusion porosimetry About 30g of the right half of selected bioreactors was analysed with mercury intrusion porosimetry at the Laboratory of Construction Materials (LCM) at EPFL, Lausanne, Switzerland.

16S rRNA gene amplification, analysis methods DNA from the coarse sand and the sand-bentonite were isolated based on the protocol by (Engel et al., 2018; Engel, Coyotzi, Vachon, et al., 2019), which is a slightly modified protocol of the DNeasy® PowerSoil® Kit (QIAGEN NV, Venlo, The Netherlands). Substrate (0.2 g) was transferred to the kit-provided PowerBead® tubes in a sterile laminar flow hood with flame-sterilized spatulas. The mass was recorded and the sampled briefly vortexed. After addition of the kit-provided solution C1, the samples were briefly vortexed and incubated for 10 minutes at 70°C. Homogenization was carried out with a Precellys 24 homogenizer (Bertin Technologies SAS, Montigny-le-Bretonneux, France), for 45 seconds at 6'000 rpm. The remaining steps were carried out as indicated by the manufacturer except for the elution of the extracted DNA: 65 µL of the kit-provided elution

buffer C6 were applied to the center of the DNA binding membrane of a MB Spin Column. After centrifugation for 1 min at 8'000 g, the DNA was collected in a 2mL Soreson™ Dolphin tube and stored at -20°C until DNA analysis. All DNA was quantified using the Qubit® ds-DNA HS Assay Kit (Thermo Fisher Scientific Inc., Waltham, Massachusetts, U.S.A.) according to the manufacturer's protocol. The fluorescence signal was measured with a Qubit® 2.0 Fluorometer (Thermo Fisher Scientific Inc., Waltham, Massachusetts, U.S.A.). Amplification of the 16S rRNA gene was performed with a modified protocol of the Quick-16S NGS Library Prep Kit (Zymo Research Corp., Irvine, California, U.S.A.). The utilization of SYBR Green fluorescence signals during the PCR amplification limits the generation of chimeric DNA amplicons, thus greatly improving the control over the amplification process. The Kit provides primers for the V3-V4 region of the 16S rRNA gene that cover both bacteria and archaea. Additionally, we took advantage of the fluorescence signal to perform a semi-quantitative assessment of the 16S rRNA gene copy number. It is semi-quantitative because of two major limitations: i) no amplification replicates instead of the usual triplicates were performed and ii) employing a standard curve method, using a pGEM-T plasmid (Promega Corp. Madison, Wisconsin, U.S.A.) containing a *E. coli* 16S rRNA gene copy as a standard. The latter is known to perform poorly for the quantification of environmental microbial communities (Brankatschk et al., 2012). Nevertheless, qPCR provided insight into the relative quantities of 16S rRNA genes, and thus improved the robustness of the DNA sequencing interpretation. The 6-point standard curve was performed from 10^7 copies per μL, down to 100 copies per μL in ten-fold dilution steps. Together with a positive control (Zymo Microbial Community Standard®) and a negative control, each 96-well plate of the Quick-16S NGS Library Prep Kit could be used to amplify 88 samples. The amplification was carried out on a LightCycler® 96 Instrument (F. Hoffmann-La Roche AG, Basel, Switzerland) using LightCycler® 480 Multiwell plates (96-well, white, F. Hoffmann-La Roche AG, Basel, Switzerland). For this system, the fluorescence threshold was determined at 0.404, which indicates the onset of an exponential increase of the fluorescence signal based on the amplification of a targeted DNA sequence. The amplification, barcoding and 16S-library generation was carried out as suggested from Zymo Research Corp. PCR efficiencies were calculated using LinRegPCR (Ruijter et al., 2009), and the 16S rRNA gene copy number for the samples on each plate were calculated based on the standard curve method with the standard-values obtained on the same plate (Brankatschk et al., 2012). The 16S rRNA gene-library was sequenced on an Illumina MiSeq (Illumina Inc., San Diego, California, U.S.A.) platform by the team at the Lausanne Genomics Technologies Facility (University of Lausanne, Switzerland), applying 10 pM of the 16S-library with a 15% Phi-X spike in a paired-end 300bp mode. The processing of raw reads was carried out as recommended in the USEARCH v 11 manual: Raw sequencing reads were preprocessed (merging, quality filtering) with USEARCH (Edgar, 2010), version 11, allowing a maximum of 10 bases difference between the paired-end reads. Operational taxonomic units (OTUs) were assigned with UPARSE (Edgar, 2013), and chimeras were removed utilizing UNOISE2 (Edgar, 2016c). Taxonomies of OTUs were assigned using SINTAX (Edgar, 2016b), based on the published and curated 16S RDP database version 16, training set (2016) (Edgar, 2016a), release 11. The high-quality reads were imported to ampvis2 (Andersen et al., 2018), which was used to analyze and visualize

the sequence data in heatmaps at the genus level. Heatmaps represent the normalized (% relative) abundance of the top 25 OTUs (shared throughout all bioreactor samples). Unknown taxonomic affiliations were filtered out and all other OTUs that do not correspond to the top 25 were combined into 'remaining taxa'. Spatial maps of selected top OTUs and boxplots of 16S rRNA gene semi-quantification were generated using Origin Pro, Version Number 2020b (OriginLab Corporation, Northampton, Massachusetts, U.S.A.)

X-ray fluorescence (XRF) spectroscopy Subsequent to the DNA sample collection from the left bioreactor halves, the remaining core was dried in vaccuum for 24h within a MBraun antechamber. EPO-TEK 301-2 resin (JP Kummer Semiconductor Technology GmbH, Augsburg, Germany) was applied to embed the dried half of the bioreactor core. At least 10 cycles of soft-vacuum and ambient pressure cycles were applied to remove trapped nitrogen gas bubbles. After a low-temperature curing for 48 hours, a longitudinal cut was performed, approximately 1.5 cm below the plane used for DNA sampling, using a diamond wire saw (MURG 394, WELL Diamond Wire Saws SA, Le Locle, Switzerland). X-ray fluorescence spectroscopy maps of sodium, silicon, phosphorus, potassium, sulfur, calcium, titanium, vanadium, chromium, manganese, iron and nickel (all K-edge) were obtained at the Crystal Growth Facility, Institute of Physics (iPHYS) at EPFL, Switzerland, with an EDAX Orbis PC Micro EDXRF analyzer system (AMETEK Inc., Berwyn, Pennsylvania, U.S.A.), equipped with a Rh micro-focus X-ray tube at 45kV acceleration and 1mA current and an Apollo XRF-ML50 Silicon Drift Detector. A 25 μm titanium foil filter was applied to reduce the background signal in the energy range of the sulfur K-edge and the spectra were recorded for 10 seconds at each spot. Detail maps had a scanning step size of 30 μm. Boxplots and maps of iron, calcium and sulfur fluorescence signals (representing atom-percent values for each element) were generated using Origin Pro, Version Number 2020b (OriginLab Corporation, Northampton, Massachusetts, U.S.A.) and converted into grey-scale pictures. The overlay images of calcium-sulfur and iron-sulfur were generated with Fiji (Schindelin et al., 2012).

Synchrotron (SR) micro X-ray fluorescence (SR-microXRF), Fe K-edge and S K-edge micro X-ray absorption spectroscopy (microXAS) Sand-bentonite samples of about 3 cm length and 1.5 cm width were obtained from the right half of each bioreactor. The samples were chosen based on visually observable features such as dark coloration and/or red/brownish halos. These samples were placed into custom-built sample holders and dried in a vacuum within an MBraun antechamber for 12 hours. Subsequently, within the glovebox, EPO-TEK 301-2 resin (JP Kummer Semiconductor Technology GmbH, Augsburg, Germany) was applied to embed the sand-bentonite matrix. A minimum of 6 soft-vacuum and ambient pressure cycles were applied to remove trapped nitrogen gas bubbles. After 48h of a low-temperature curing, the embedded sample surfaces were gradually exposed by rough removal of excess resin using a Dremel®3000 tool (DREMEL Europe Bosch Power Tools B.V., Breda, The Netherlands). Fine wet grinding using silicon carbide grinding paper of three grit grades (Struers Inc., Cleveland, Ohio, U.S.A.) and ethanol, analytical reagent grade (Thermo Fisher Scientific Inc., Waltham,

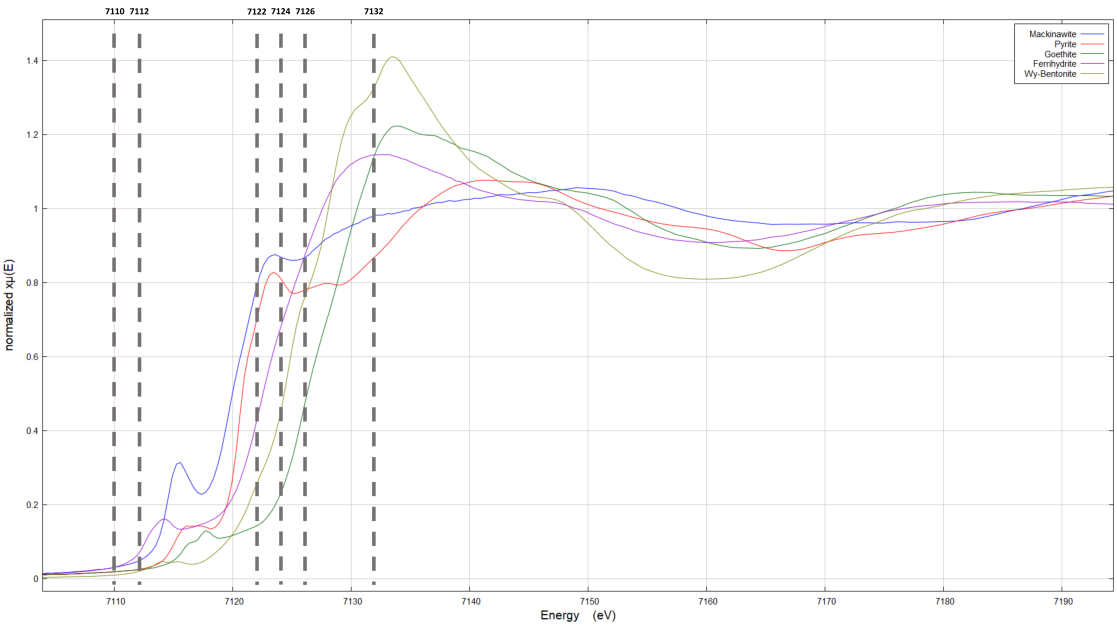

Figure 4.9 – XAS spectra of standards used for 6-point energy XAS fitting of iron speciation maps. The following standard are shown: mackinawite (blue), pyrite (red), goethite (green), ferrihydrite (purple), Wyoming bentonite octahedral iron(III) (khaki).

Massachusetts, U.S.A) was performed by hand until a even and shiny sample plane was achieved. The prepared samples were sealed within a nitrogen atmosphere by packing in three layers of Mylar® and shipped to the respective synchrotron research facilities.

Synchrotron (SR) X-ray micro XRF imagining and Fe K-edge XAS data were collected at the beamline (BL) 2-3 of the Stanford Synchrotron Radiation Lightsource (SSRL) at the Stanford Linear Accelerator Laboratory (SLAC) (Menlo Park, California, U.S.A.). Fe-XAS data were recorded in the energy range of 6,927 eV to 7,520 eV. The obtained microXRF images were additionally probed with X-rays at six distinct wavelengths to create a Fe-speciation map of the same image. The following wavelengths were chosen for Fe-speciation (in eV), see Figure 4.9: 7,110, 7,112, 7,122, 7,124, 7,126, 7,132. Micro XRF and Fe speciation imagining data were visualised and fitted using Sam's Microprobe Analysis Toolkit (SMAK) (Webb, 2011). The fit images of mackinawite and pyrite were combined using Fiji (Schindelin et al., 2012) and are presented as 'iron-sulfide'. SR-microXRF imagining and S K-edge microXAS was performed at BL I-18 at the Diamond Light Source (DLS) (Didcot, Oxfordshire, U.K.) using the Data Analysis WorkbeNch (DAWN) (Basham et al., 2015). The S microXAS data were recorded in the energy range of 2,400 eV to 2,600 eV.

Both Fe and S XAS data were analyzed using Athena (Ravel & Newville, 2005).

4.3 Results & Discussion

4.3.1 Borehole BMA-A1

The borehole BMA-A1 was first sampled in March 2017. The modification that precluded oxygen diffusion into the water during transit from the borehole to the anoxic chamber was put into place starting in October 2017. A good indication of the adequacy of this measure was the decrease in redox potential from 31.10.2017 onward, see Table 4.3. In addition, the borehole microbiome was characterized with an established porewater filter method. The microbiome mainly consists of OTUs related to the genera *Pseudomonas*, *Desulfosporosinus*, *Limnobacter*, *Gracilibacter*, *Phenylobacterium*, 4.10, but also OTUs less well decipherable at the genus level but belonging to the Paenibacillaceae, Peptococcaceae families and to the Clostridiales and Burkholderiales order, Figure 4.50 on page 186 in this Chapter's Appendix. After installation of the modification to ensure that oxygen diffusion into porewater during transit was excluded, there is high confidence that strictly anoxic conditions were maintained and that anaerobic organisms could thrive.

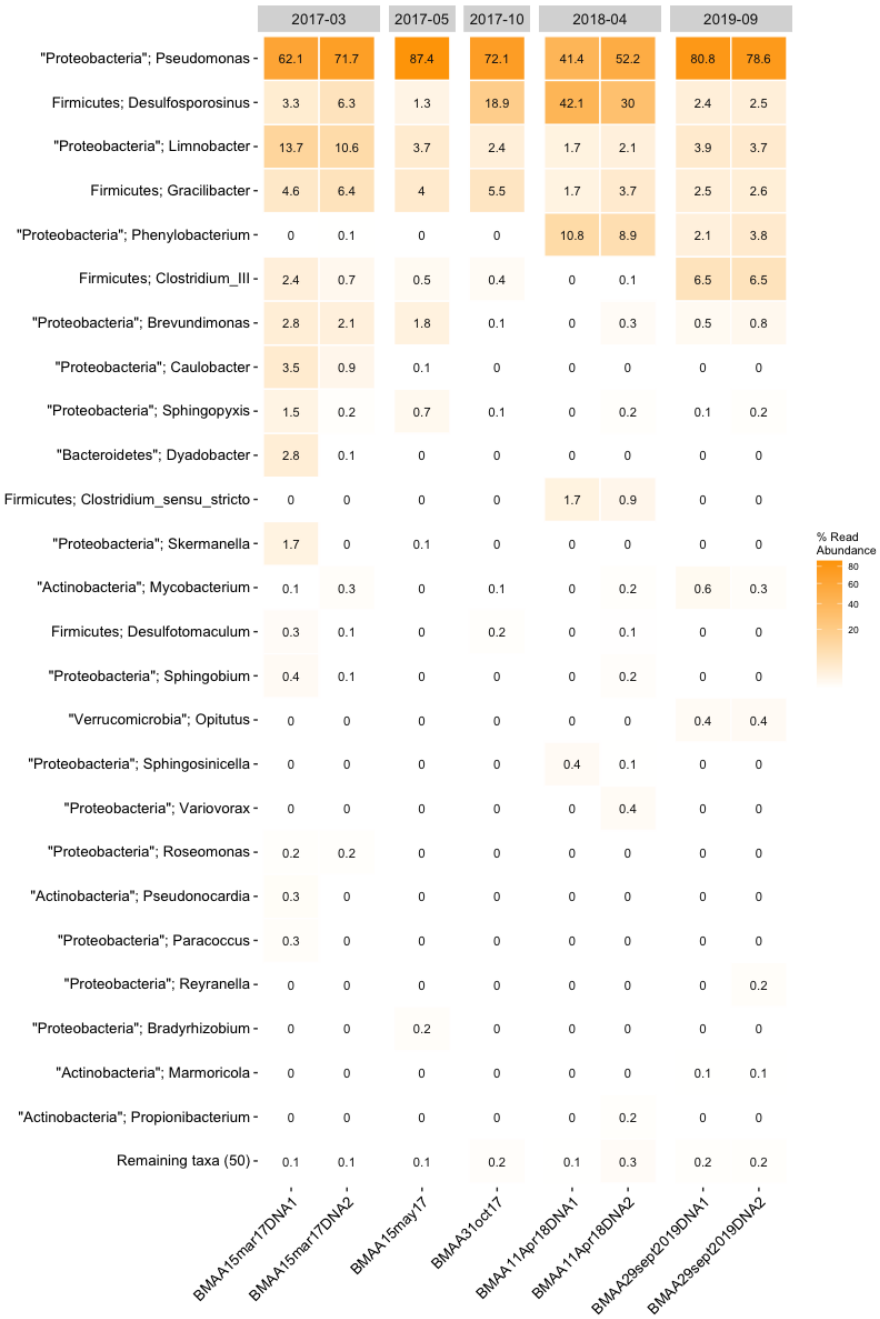

Figure 4.10 – Heatmap of 16S rRNA gene sequences obtained from filtered borehole porewater microorganisms within the borehole BMA-A1 that served as natural water source for the *in-situ* MA-A1.x experiment. The 25 most abundant OTUs with known taxonomic affiliation at the genus level are shown and the 'remaining taxa' category contains know taxa not in the top 25. Only genera with at least 0.1% relative abundance were considered. A heatmap including unknown taxonomic affiliation on genus level can be found in this chapter's appendix, Figure 4.50 on page 186.

Table 4.3 – Porewater chemistry of BMA-A1 from 2017 until 2019.

	15.03.2017	**15.05.2017**	**31.10.2017**	**11.04.2018**	**24.09.2019**	**average**
Eh [mV]	-267.9	-261.6	-316.6	-366.5	-332.5	-309.0
pH	6.4	7.3	8.0	7.1	7.2	7.2
DOC [mg/L]	6.80	9.71	7.01	4.76	19.44	9.54
DIC [mg/L]	63.95	112.85	58.87	54.60	47.35	67.52
Na^+ [mM]	198.400	198.567	152.754	187.955	217.696	191.074
NH_4^+ [mM]	1.619	5.866	-	2.262	0.552	2.575
K^+ [mM]	1.835	1.298	1.642	1.572	1.440	1.557
Mg^{2+} [mM]	13.989	13.937	13.875	13.788	15.063	14.130
Ca^{2+} [mM]	12.357	12.391	12.575	12.469	11.990	12.356
F^- [mM]	-	-	-	-	-	-
Cl^- [mM]	242.891	245.678	241.992	231.202	245.316	241.416
NO_2^- [mM]	-	-	-	0.304	-	0.304
SO_4^{2-} [mM]	15.659	15.226	14.897	14.682	14.042	14.901
NO_3^{2-} [mM]	-	0.559	-	1.560	-	1.060
PO_4^{3-} [mM]	0.302	-	0.003	-	-	0.153
Al [mM]	-	-	-	-	-	-
Co [mM]	-	-	-	-	-	-
Cr [mM]	-	-	-	-	-	-
Cu [mM]	-	-	-	-	-	-
Fe [mM]	-	0.007	-	-	0.029	0.018
Mn [mM]	-	0.002	-	-	-	0.002
Ni [mM]	-	-	-	-	0.002	0.002
Si [mM]	-	0.063	0.101	0.109	-	0.091
Sr [mM]	-	0.186	0.395	0.382	0.192	0.289
Zn [mM]	-	-	-	-	0.012	0.012

4.3.2 Porosity of sand-bentonite mixtures

The porosity of the sand-bentonite matrix is an important parameter for the realisation of a prospective microbial gas sink located within the service galleries. Mercury intrusion porosimetry (MIP) was employed on four vacuum dried bioreactor samples: two containing dried biofilms (MA-A1.1 and 1.2), one control without biofilm (MA-A1.NC), and one pre-test sand-bentonite matrix that was not previously saturated (MA-A0.x). Figure 4.11 shows the respective MIP curves for the four samples. Two definitions of macro-pores were used to determine the porosity. Within soil science, macro-pores are defined as pores larger than 75 μm= 75′000 nm (of America, 2020), see Table 2 therein. As can be observed in the saturated sand-bentonite samples (a, b, c) compared to the unsaturated sample (d), the bentonite has swollen enough to close off the original macro-pores larger than 75 μm (d, 7.17 % porosity) and maintained some of this even after drying. After saturation (a, b, c), the macropores larger than 75 μm can barely be observed, even though measurements were obtained within that size-region (a,b,c, 0% - 1.66% porosity). In chemistry, based on IUPAC recommendations, macropores are defined as larger than 50 nm (Rouquerol et al., 1994). According to this definition, for saturated sand-bentonite mixtures of 80/20% (w/w), the porosity is between 29.8% and 36.8%. An unsaturated mixture shows 19.6% porosity for pores larger than 50 nm.

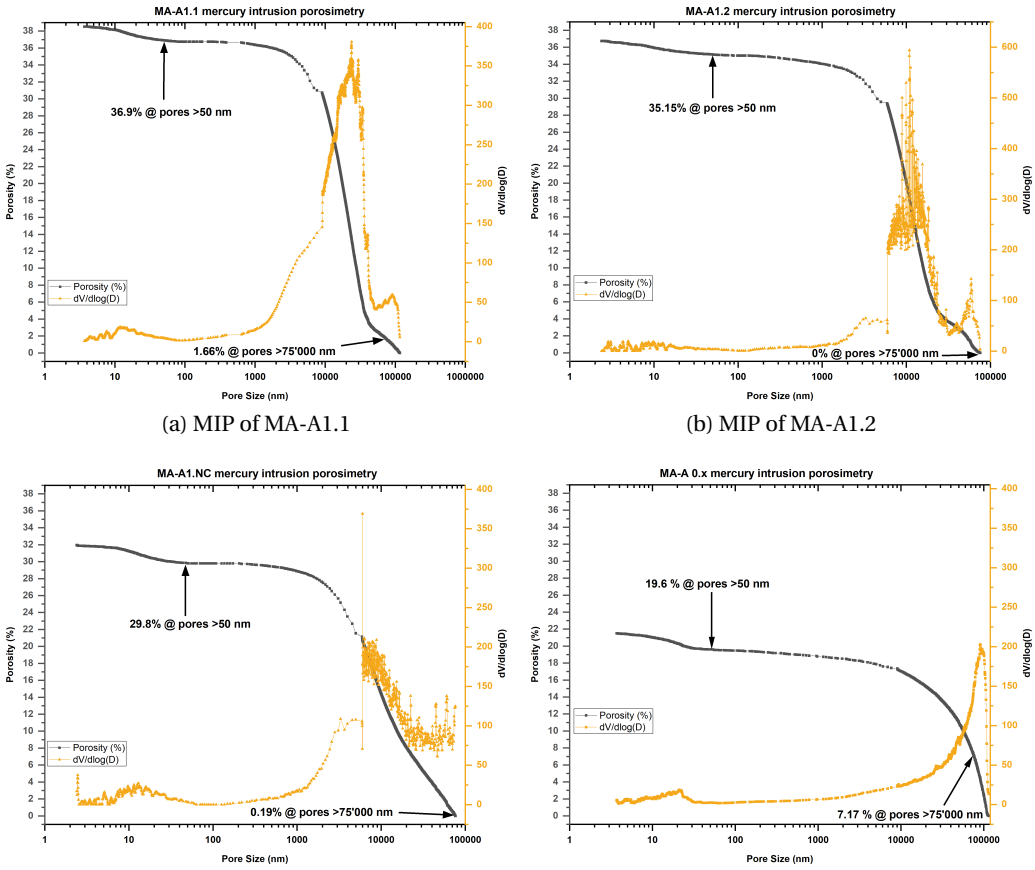

(a) MIP of MA-A1.1

(b) MIP of MA-A1.2

(c) MIP of MA-A1.NC

(d) MIP of MA-A0.x

Figure 4.11 – Mercury intrusion porosimetry of four sand-bentonite mixtures, for pores larger than 75 μm ranging from 0% (MA-A1.2, deployed bioreactor) to 7.17% macro-pores (MA-A0.x, pre-test), for pore larger than 50 nm ranging from 19.9% (MA-A0.x, pre-test) to 36.9% (MA-A1.1, deployed bioreactor)

4.3.3 Chemical analysis of bioreactor efflux

Each week during the hydrogen injection phase of the bioreactor experiment, porewater outflow was sampled and analysed. Cations show a slightly increased concentration of sodium (approx. +25 mM) and potassium (+0.4 mM) and a slightly decreased concentration of magnesium (approx. -5 to -10 mM) and calcium (approx. -4 mM) for all bioreactors as compared to the inflow borehole water BMA-A1 (at top of each of the stack-plots in Figure 4.13) over the course of the experiment. Trace metals and dissolved ferrous iron are plotted in Figure 4.14. The stainless steel cylinder appear to have leached molybdenumm, nickel and iron. This leaching must have occurred during the saturation phase, when no porewater was flowing and no hydrogen was applied. Dissolved ferrous iron was quickly consumed and stayed below the limits of detection throughout the experiment from about the second week of hydrogen application. Most likely, the reaction with dissolved hydrogen sulfide consumed dissolved iron(II), as indicated in equation 4.4 on page 143. The evolution of dissolved sulfide and sulfate is shown in Figure 4.15. As evident from both plots, sulfate-reduction was ongoing within the bioreactors. Coinciding with the depletion of dissolved ferrous iron is the appearance of dissolved sulfide from the second week onward within the bioreactor outflow. Sulfate is shown to be slightly increased in the bioreactor outflow at the start of the experiment (approx. +9 mM for MA-A1.2, 1.3 and 1.4, approx +4 mM for MA-A1.1). The dissolution of gypsum found in bentonite is the most likely reason for this (Maanoja et al., 2020). Due to the high amount of steel within the experimental system, the evolution of sulfide could not be used as indicator of the hydrogen oxidation rate of the developing biofilm. Instead, the sulfate reduction rate was used for a linear regression model for the overall sulfate reduction rate, as indicated by a red, decreasing linear (zeroth order) fits in the plots of Figure 4.15b. The calculated reduction rates for each bioreactor were:

- for MA-A1.1: $R^{red}_{SO_4^{2-}} = 0.222 \frac{\mu M}{day\, cm^3}$
- for MA-A1.2: $R^{red}_{SO_4^{2-}} = 0.275 \frac{\mu M}{day\, cm^3}$
- for MA-A1.3: $R^{red}_{SO_4^{2-}} = 0.234 \frac{\mu M}{day\, cm^3}$
- for MA-A1.4: $R^{red}_{SO_4^{2-}} = 0.274 \frac{\mu M}{day\, cm^3}$
- **on average:** $\mathbf{R^{red}_{SO_4^{2-}} = 0.251 \frac{\mu M}{day\, cm^3} \pm 0.024 \frac{\mu M}{day\, cm^3}} (SD)$

The rate is close to the reported sulfate reduction rate of $R^{red}_{SO_4^{2-}} = 0.14 - 0.2 \frac{\mu M}{day\, cm^3}$ (Bagnoud, Leupin, et al., 2016), for a similar Opalinus Clay rock derived microbial community but within a porewater-filled borehole.

Based on equation 4.2 on page 113, each mole of sulfate reduced requires four moles of dihydrogen to be oxidized. Based on previous work by (Bagnoud, Leupin, et al., 2016) however, the stoichiometry of sulfate reduction was observed to be closer to 8.5 moles of dihydrogen

per mole of sulfate reduced. This can be attributed to other reduction reactions coupled with hydrogen oxidation and H_2losses. Using both a 4-to-1 and a 8.5-to-1 ratio, the hydrogen oxidation rate based on the observed rate of sulfate reduction across all four bioreactors can be determined from (4:1)

$$R_{H_2}^{ox} = 1.004 \frac{\mu M}{day\, cm^3} = 1.004 \frac{M}{day\, m^3}$$

to (8.5:1)

$$R_{H_2}^{ox} = 2.125 \frac{\mu M}{day\, cm^3} = 2.125 \frac{M}{day\, m^3}$$

Which is 5 to 10 times higher than the H_2 oxidation capacity of the hypothetical biofilm mentioned in the introduction, section 4.1.

Here however, the reported rate of sulfate-reduction can be viewed as a conservative, bottom range due to three important restrictions. First, the sulfate-reducing biofilm within the bioreactor was not fully developed yet as evident by the remaining sulfate within the outflow water after more than 100 days of daily hydrogen injections. Given the condition that hydrogen is not limited, the sulfate availability will become the limiting factor. A fully grown biofilm in sand-bentonite may show faster sulfate reduction than reported here. Second, the non-uniform flow of borehole porewater through the bioreactors may have influenced the observed sulfate reduction rate. Locally, within the sand-bentonite matrix, sulfate-depleted conditions may have prevailed during the experiment but are not captured because of the inaccessibility of that pore space. Furthermore, the hydrogen oxidation rate appears underestimated on the per volume of bioreactor matrix because of these sulfate-depleted regions. Third, as shown below in subsection 4.3.7 (16S rRNA gene analysis of biofilm), the hydrogen-oxidizing community within the sand-bentonite matrix is not exclusively composed of sulfate-reducing bacteria, but also of methanogens, even though a considerable amount of sulfate is detected in the bioreactor outflow. Thus, the actual hydrogen oxidation rate is likely to be higher as it cannot be exclusively modelled based on the rate of sulfate-reduction.

4.3.4 Bioreactor porewater, hydrogen and methane

Borehole porewater Both bioreactor set-ups, the serial (MA-A1.1 and 1.2) and parallel (MA-A 1.3 and 1.4) ones, resulted in non-uniform porewater flow as evident from the recorded flow rates, Figure 4.12. Liquids exhibit flow preferentially along the path of lowest resistance. This means that the two bioreactors placed in series received less water. From Figure 4.12, it can be readily observed that the majority of borehole water applied to the reactors went through MA-A1.4 (most of the times) or MA-A1.3, and that MA-A1.1 and 1.2 (placed in series) received much less water (see Table 4.4 for the total amounts of water). Thus, a low flow rate was recorded for MA-A1.1 and 1.2 (placed in series). However, each week after sampling, about 7-10 milliliters of BMA-A1 porewater was flushed into MA-A1.1 due to pressure equilibration.

After sampling the outflow of MA-A1.2, the sampled volume got replaced by MA-A1.1 outflow, however that bioreactor outflow contained by then a mixture of bioreactor porewater and fresh BMA-A1 borehole porewater.

During the first 10 days of experiment, the two-path flow setup had to be disconnected because the pressure controller of the sensor-equipped flow-path was blocked and had to be sent for repair. Bioreactor MA-A1.3 (red line in Figure 4.12) indicates this by the very low recorded flow rate compared to MA-A1.4. Therefore, all three bioreactor outflow were connected to a common tube precluding the possibility to monitor the evolution of the outflow chemistry of each reactor in real-time.

Hydrogen gas was applied daily to each bioreactor, Table 4.4 with the aim to avoid the formation of a gas phase. The rationale to avoid a gas phase is because of the possibility that it might escape directly into the gas trap or the water outlets without stimulating microbial growth within the sand-bentonite matrix.

Only a few gas samples could be obtained during the weekly bioreactor sampling. Nevertheless, the analysis showed that methane was detected starting after 28 days of daily hydrogen injections in MA-A1.2 Bioreactors MA-A1.3 and 1.4 showed only one occurrence of methane in the gas phase each, while MA-A1.1 showed five occurrences, albeit the experimental run-time was also longer for the latter bioreactor.

Table 4.4 – Borehole porewater supply and applied daily hydrogen to 4 bioreactors of the MA-A1.x experiment.

Bioreactor	**Setup**	**Total porewater [mL]**	**Porewater duration [days]**	**Total H_2 [mmol]**	**Daily H_2, duration [days]**	**Amount of H_2 $\left[\frac{mM}{day}\right]$**			
						average	**median**	**min**	**max**
MA-A1.1	Series	330.9	108	49.098	102	0.477	0.475	0	1.431
MA-A1.2				43.009		0.418	0.368	0	1.442
MA-A1.3	Parallel	732.7	73	32.606	73	0.466	0.450	0	1.150
MA-A1.4		1180.4	79	33.07	78	0.435	0.384	0	1.250

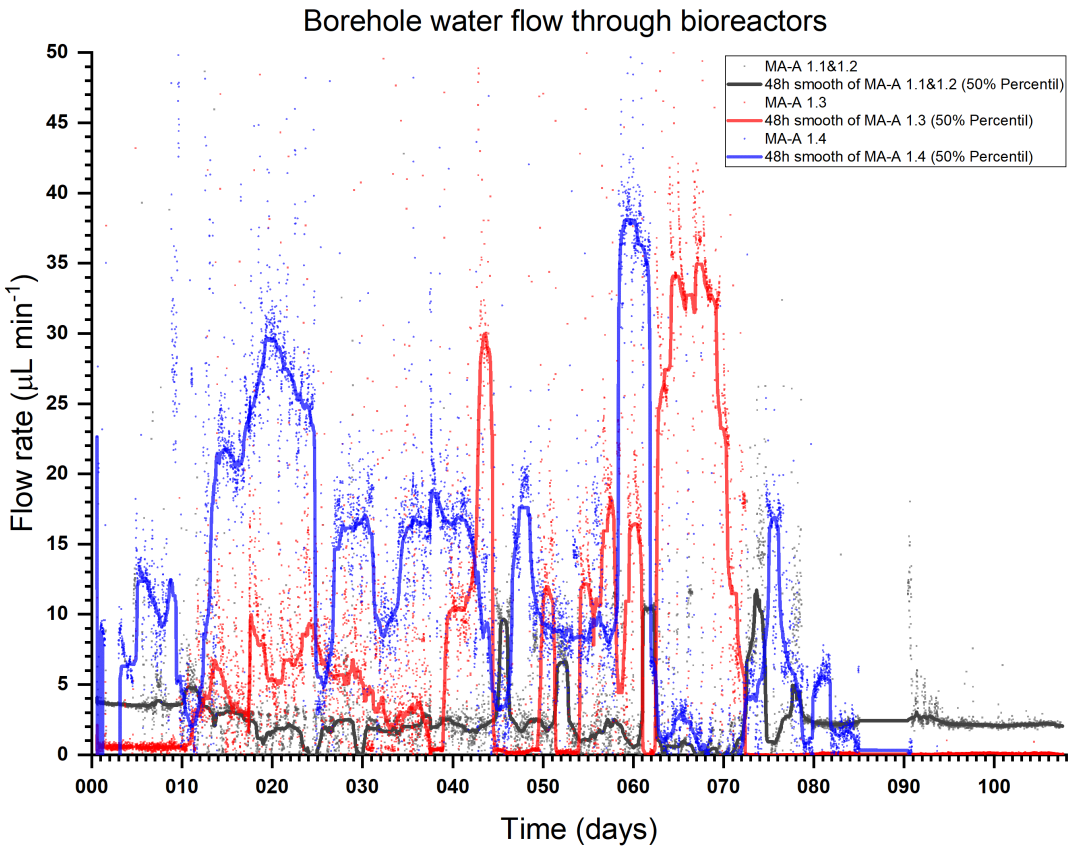

Figure 4.12 – Flow rates through each bioreactor individually (MA-A1.3, 1.4) or the bioreactor assembly (MA-A1.1 and 1.2). Lines represent moving averages of 48h using a cutoff at the 50% percentile.

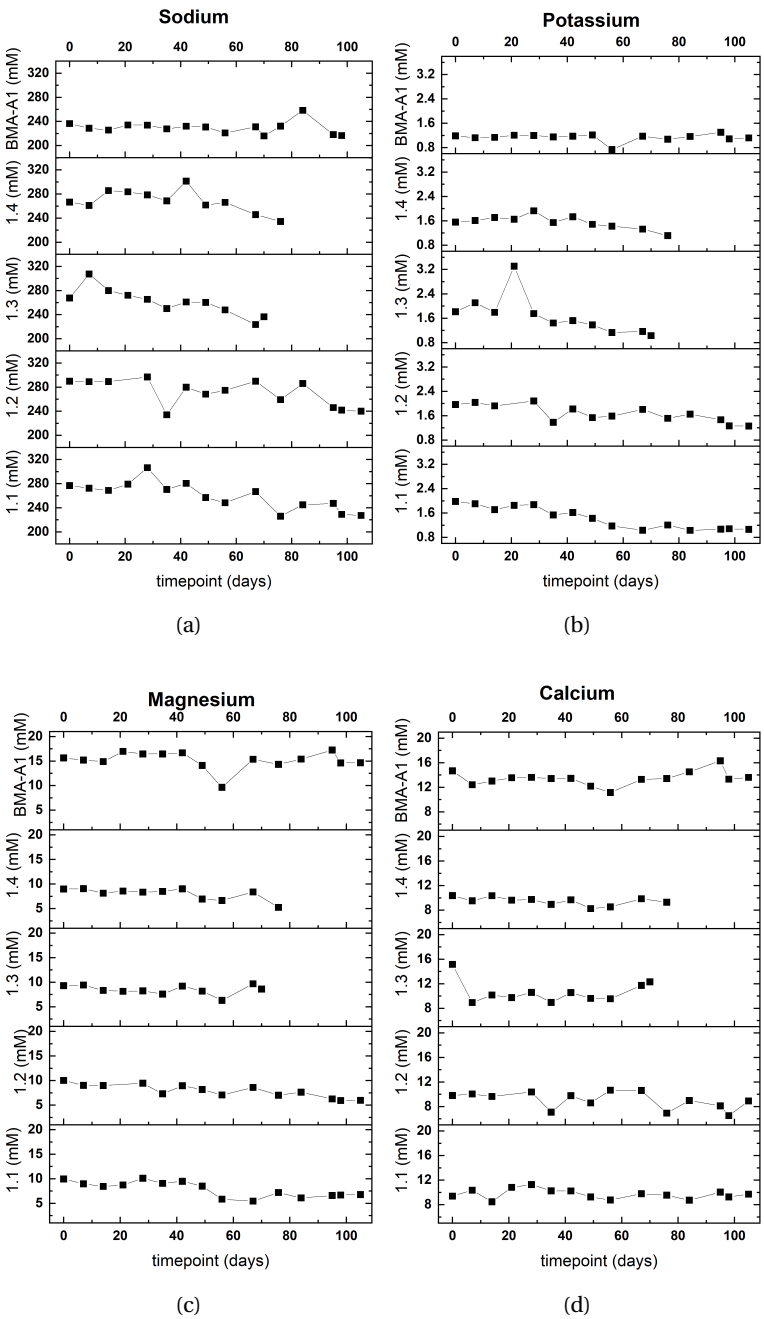

Figure 4.13 – Cations found in the effluent porewater of each bioreactor during the hydrogen inject phase.

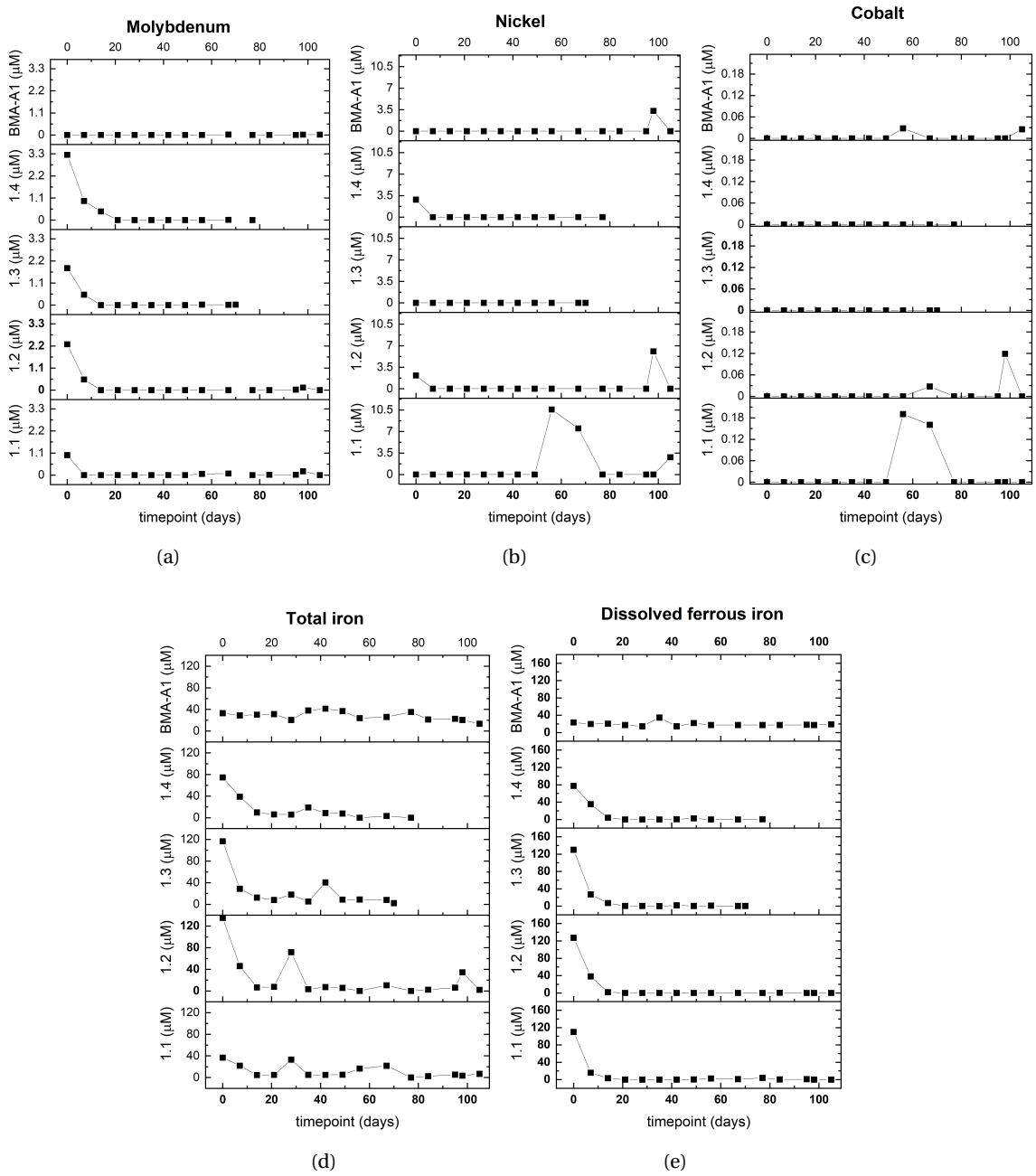

Figure 4.14 – Trace elements found in the effluent porewater of each bioreactor during the hydrogen inject phase.

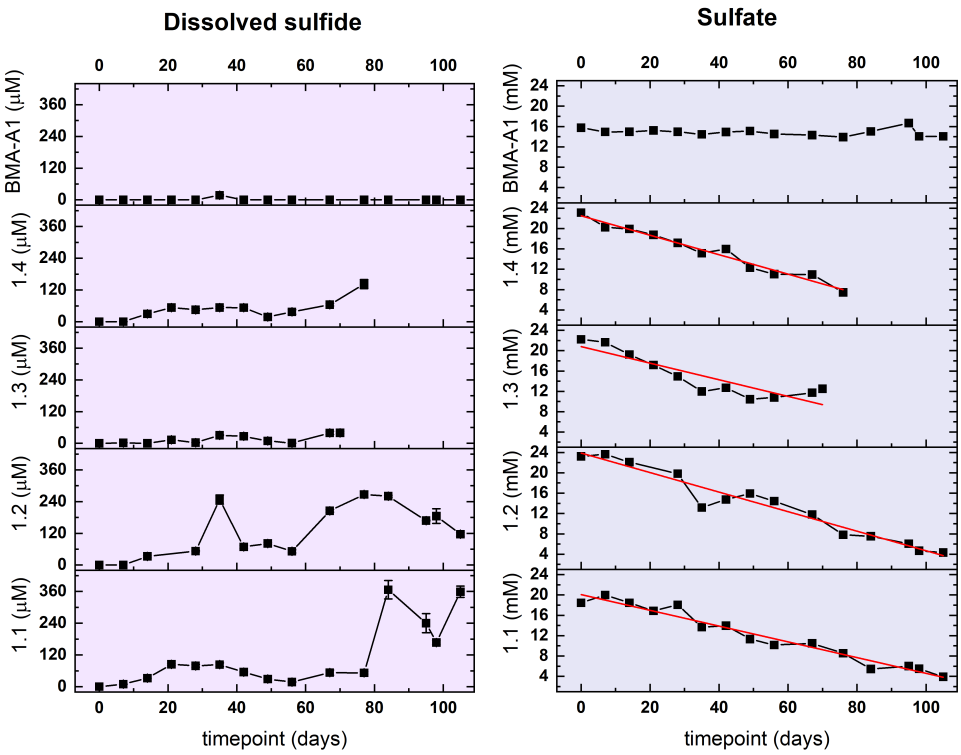

(a) (b)

Figure 4.15 – Dissolved sulfide and sulfate evolution in the effluent porewater of each bioreactor during the hydrogen inject phase. Red lines indicate the sulfate reduction linear regressions used to obtain the rate of sulfate reduction in this experiment.

4.3.5 Tabletop XRF

Elemental mapping of the resin-embedded bioreactor halves was performed with an emphasis on sulfur accumulation because the only sulfur-bearing minerals in the starting material are gypsum (0.9% weight) and pyrite (0.6% weight) in bentonite. The sulfide produced was expected to react with ferrous iron, creating iron sulfide phases such as mackinawite and pyrite, or, in the absence of iron, polysulfides and elemental sulfur. The Opalinus Clay rock porewater provides about 20 μM of ferrous iron, however, no ferrous iron could be detected in the outflow after 2 weeks of experiment, Figure 4.14e, thus biogenic hydrogen sulfide is thought to have scavenged all ferrous iron:

$$Fe^{2+}(_{aq.}) + HS^{-}(_{aq.}) \rightarrow FeS + H^{+}(_{aq.}) \tag{4.4}$$

However, the biogenic hydrogen sulfide might also have reacted with the structural ferric iron in montmorillonite (MM), the main mineral component of bentonite, under the formation of elemental sulfur, as shown by (Pedersen et al., 2017):

$$Fe^{3+}(_{MM}) + HS^{-}(_{aq.}) \rightarrow Fe^{2+}(_{MM}) + S^{0}(_{MM}) + H^{+}(_{aq.}) \tag{4.5}$$

Following this, reaction 4.4 takes place immediately within the bentonite phase due to the omnipresent HS^{-}, resulting in the formation of amorphous FeS and mackinawite:

$$Fe^{2+}(_{MM}) + HS^{-}(_{aq.}) \rightarrow FeS(_{MM}) + H^{+}(_{aq.})$$

However, iron sulfides are shown to react further in the presence of abundant hydrogen sulfide, resulting in the formation of pyrite (Drobner et al., 1990; Rickard, 1997). Thus, within the bentonite phases, one expects:

$$FeS(_{MM}) + HS^{-}(_{aq.}) \rightarrow FeS_2(_{MM}) + H^{+}(_{aq.}) \tag{4.6}$$

In addition, the dissolution of gypsum (from bentonite) is another source of sulfur in this system, as shown for Wyoming bentonite by (Maanoja et al., 2020). In the reaction cascade considering sulfur from gypsum as well, the oxidation states of sulfur decrease from +6 (gypsum) to -2 (hydrogen sulfide, iron sulfide [amorphous and as mackinawite]), then increases to -1 (pyrite) and stabilizes at 0 (elemental sulfur and polysulfides). Based on this tendency of an apparent stabilization towards a neutral oxidation state of sulfur the formation of polysulfides coupled with pyrite dissolution is proposed:

$$FeS_2(_{MM}) + \mathbf{n}HS^{-}(_{aq.}) \rightarrow S^{2-}_{\mathbf{n}} + Fe^{2+}(_{aq.}) \tag{4.7}$$

Observations of sulfur accumulation in broad overview XRF scans of embedded bioreactor halves guided the selection of areas for detailed maps with a 30 μm step size. These areas are indicated by red boxes in Figures 4.18, 4.21, 4.28 and 4.40. For each the detailed map, overlay images of the calcium and sulfur or the iron and sulfur signals were produced, Figures 4.19,

4.22, 4.23, 4.24, 4.29, 4.30 and 4.41. In all detailed maps, sulfur appears associated with the bentonite phase, as indicated by its association with calcium and iron. The empty space in between bentonite regions corresponds to the silicon (quartz) signal, thus represents the sand grains. Undeployed Wyoming bentonite contains sulfur-bearing minerals in form of gypsum, $CaSO_4 \cdot 2H_2O$, and as pyrite FeS_2, at low concentrations (0.9% and 0.6% weight, respectively (Karnland et al., 2006)). The presence of these minerals served as a starting point to assess the reactions facilitated by hydrogen sulfide produced by sulfate-reducing bacteria. The negative control and all bioreactors except MA-A1.4 were analysed with detailed maps. The overlay images were analysed in the following way: First, major sulfur spots were identified by visual comparison of the size and intensity of the yellow sulfur signal, e.g., for the negative control, see Figure 4.41. In this example, nine major sulfur spots were identified and their elemental composition (in % atom weight) was recorded. Based on the calcium:sulfur and the iron:sulfur ratio, a potential mineral phase was assigned. The observations revealed the following trends:

- gypsum dissolution is observed in all detailed XRF maps. The largest number of gypsum observations were obtained for the control sand-bentonite sample MA-A1.NC, while the fewest were obtained for bioreactor MA-A1.2. The following trend in deployment time and relative state of reduction in the system was surmised: (30 d) MA-A1.NC > (73 d) MA-A1.3 > (108 d) MA-A1.1 = MA-A1.2
- Fe:S ratios of 1:1 and 1:2 were observed in all the deployed bioreactors with the notable observation that bioreactor MA-A1.2 had almost exclusively ratios of Fe:S larger than 1:2.2 compared with MA-A1.1 and 1.3 which also exhibited ratios between 1:1 and 1:2.
- sulfur and/or polysulfide was often observed at MA-A1.2 associated with iron as evidenced by high sulfur atomic weight % (up to 48.1 % at.) and low calcium (0.5% at. at that same spot), see Figure 4.22. This suggests that gypsum is absent and excess sulfur relative to iron precludes the exclusive presence of iron sulfide minerals.
- The accumulation of iron sulfides appear localized within bentonite at calcium spots. However, the longer deployment time and the low sulfate / high sulfide conditions of MA-A1.2 have led to the almost complete dissolution of gypsum as evidenced by the lack of sulfur at calcium spots as shown in Figures 4.22, 4.23 and 4.24.

Figure 4.16 summarizes the observation that calcium is replaced by reactive iron at sulfur spots for the biotic bioreactor systems. The known pools of iron are: Ferrous iron from the porewater, which reacts rapidly, iron oxides in the form of lepidocrocite (0.7% weight in Wyoming bentonite), and some goethite (0.2% weight) and hematite (0.1% weight). But, the majority of iron in bentonite is present as structural iron(III) in montmorillonite (85.9%) (Karnland et al., 2006). Iron from both montmorillonite as well as goethite and hematite is known to react rather slowly with sulfide as compared to ferrous iron and lepidocrocite (Canfield, 1989). Here, due to large amount of sulfide produced in the system, and the depletion of (easily accessible) reactive iron, the formation of polysulfide may be facilitated in

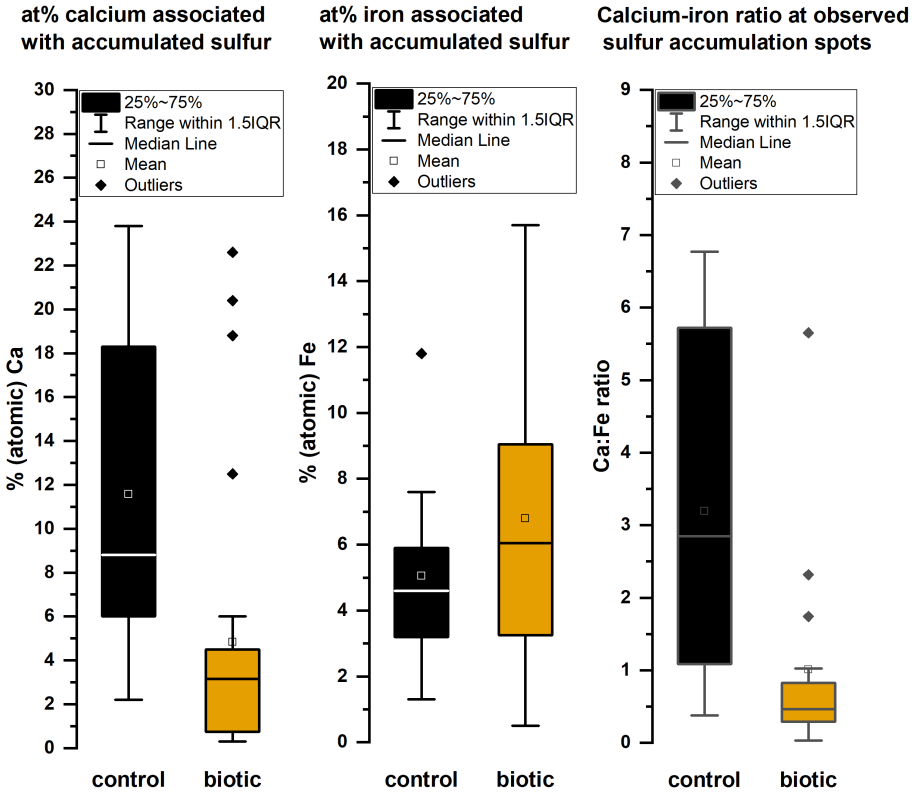

(a) (b) (c)

Figure 4.16 – Sulfide produced by sulfate-reducing bacteria and an increasing scarcity of sulfate in certain conditions led at sulfur-rich spots to the transformation of gypsum (a) to (b) iron sulfide minerals and ultimately to polysulfides and elemental sulfur. Plot (c) summarizes that for sulfur spots, the ratio between calcium and iron shifts towards iron for biotic reactor conditions.

reaction with pyrite, as shown in equation 4.7. Bioreactor MA-A1.2, which received sulfate-depleted and sulfide-enriched porewater, showed the highest sulfur signals which could not be explained exclusively by iron sulfide formation.

4.3.6 Synchrotron (SR) X-ray XRF maps, iron and sulfur XAS

Small samples of the sand-bentonite matrix from bioreactors MA-A1.2, 1.3 and 1.4 and 1.NC (negative control) were analysed using bright, coherent synchrotron X-ray radiation. microXRF images of iron and sulfur were produced to identify spots with iron sulfide or sulfur accumulation. Iron speciation analysis was performed on each pixel of the maps and on several spots outside the mapped area.

Iron speciation Figure 4.25 on page 157 shows the microXRF-mapped area of a sample from MA-A1.2 and the corresponding iron and sulfur K-edge maps. The dark area on the left of the area-of-interest, Figure 4.25a, shows the accumulation of sulfur, Figure 4.25b, and iron, Figure 4.25c. Figure 4.26 on page 158 shows the fitted iron speciation for the same area, evidencing the presence of montmorillonite iron (III), Figure 4.26a, Goethite, FeOOH, Figure 4.26c, was fitted almost throughout the entire bentonite phase as a small contribution. A bright spot made up by iron sulfides, Figure 4.26d, is observed on the left of the map. Low contribution could be fitted to ferrihydrite (Fe(III)oxide-hydroxide), Figure 4.26b. The round, dark-blue shapes between the iron signal represent quartz sand grains.

Figure 4.31 on page 162 shows the microXRF-mapped area of a MA-A1.3 sample, Figure 4.31a, and the corresponding sulfur, Figure 4.31b, and iron K-edge maps, Figure 4.31c. In contrast to the aforementioned MA-A1.2 sample, the intense black coloration observed here neither has a sulfur K-edge nor an iron K-edge signal. Only a single bright spot can be observed at the iron K-edge. Maps fitting the iron phases, Figure 4.32 on page 163, appear to attribute the signal to bentonite iron(III), Figure 4.32a, and goethite on the left part of the mapped area, Figure 4.32c, but no iron sulfide could be observed, Figure 4.32d. The high intensity point-signal observed in the iron K-edge is also observed in the ferrihydrite, Figure 4.32b, and iron sulfide fit, Figure 4.32d, however, this point should be neglected as it also has a high fit error, Figure 4.32e. The apparent discrepancy between the dark coloration of MA-A1.2 (above) and 1.3 (here) may be related to the embedding procedure with a visually transparent resin, thus the dark area is visible but the surface is not exposed. Indicative for this is the very low sulfur K-edge signal but the stronger iron K-edge signal, Figure 4.31, where for the latter the quartz-grains can be clearly distinguished. Reason for this might be the lower penetration depth of the incident beam (7keV for iron but only 2.5keV for sulfur) and the lower energies of the resulting fluorescence signals of sulfur, lowering the total detectable counts. However, the absence of a clear iron sulfide signal like observed for MA-A1.2 is pointing towards another reason than an iron sulfide accumulation for the intense black coloration.

Figure 4.35 on page 166 shows the first of two microXRF-mapped areas of a MA-A1.4 sample and the corresponding iron, and sulfur K-edge maps. Here again, we aimed at determining the iron speciation of the dark coloration and the nearby area. Both sulfur, Figure 4.35b, and iron K-edge, Figure 4.35c, confirm the potential presence of iron sulfide minerals in the dark area in the visual picture, Figure 4.35a. Iron speciation maps are presented in Figure 4.36 on page 167 and evidence the bentonite-iron(III) between sand grains, Figure 4.36a. The location of the dark area on the top right can be adequately fitted with bentonite iron, Figure 4.36a surrounding goethite iron, Figure 4.36c. Iron sulfide is only observed in a discrete spot in the top-right, Figure 4.36d. The second iron sulfide spot in the lower-left quadrant of the map, is also shown as high-error prone based on the fit error, Figure 4.36e.

Another small area of MA-A1.4 was mapped as presented in Figure 4.37 on page 168 as a visual picture and the corresponding iron and sulfur K-edge maps. A strong sulfur K-edge signal is observed as elongated spot on the upper corner of the mapped area, Figure 4.37b.

Several iron spots are observed in the iron K-edge map, Figure 4.37c, at the same location as the aforementioned sulfur spot, but also at six other locations approximately within the upper-right quadrant of the map. Iron speciation fits, Figure 4.38 on page 169, show that the strong sulfur signal is associated with iron sulfide, Figure 4.38d. No obvious iron(III) signal from bentonite, Figure 4.38a, or ferrihydrite, Figure 4.38b, can be observed at this spot, confirming the formation of an iron sulfide phase. However a strong goethite-fitted signal is observed in close proximity to the iron sulfide, Figure 4.38c.

In conclusion, the microXRF and iron-speciation mapping of the selected three bioreactors resulted in:

- Proof of iron sulfide formation within the bentonite phase, driven by HS^- interacting with free Fe^{2+} and the limited pool of reactive iron (0.70% weight of lepidocrocite within the initial bentonite), followed by iron(III) in the octahedral layers of montmorillonite.
- An alternative possible explanation for the intense black coloration identified within the sand-bentonite matrix may be the formation of iron-species other than the fitted ones.
- Low concentration of goethite throughout the bentonite matrix may be reason for the observed brown-yellowish halo across the sand-bentonite core.
- An additional indication of polysulfide and/or elemental sulfur formation as some sulfur K-edge signals could not be explained by the formation of iron sulfide. Gypsum could be ruled out as the potential source of the sulfur K-edge signal due to the absence of calcium signal at the investigated sulfur accumulations (data not shown).

With the three selected samples for iron-speciation mapping we primarily aimed to identify the nature of the dark coloration. However the secondary goal was to identify the nature of the brown-yellowish halo, apparent to the naked eye where there is no dark-grey or even black coloration, as can be observed in Figures 4.17, 4.20, 4.27, and 4.34. From the limited observations made, the only possible explanation is a low background of goethite, as can be observed in Figures 4.26c, 4.32c, 4.36c and 4.38c. Further Fe-speciation studies including standards for hematite, magnetite and lepidocrocite in addition to the here used ferrihydrite and goethite would be needed to answer the origin of the brown-yellowish halo conclusively.

Full XANES spectra were obtained at iron hotspots other than the ones mapped in the microXRF. The spectra were fitted as linear combination fits of iron-standards, Table 4.5. The results indicate that iron(II) from sulfide minerals (such as mackinawite and pyrite) is often associated with iron(III) from bentonite. Only once were goethite and ferrihydrite obtained as fitting parameters. This finding suggests that the majority of iron from iron oxides has reacted with sulfide to produce iron sulfide. Bentonite iron also reacts with sulfide but the process is slower and the pool of iron much larger. Two example linear combination fits, used to classify the iron-speciation of the selected points can be found in this Chapter's Appendix, Figure 4.51 on page 187.

Table 4.5 – Fe-XAS were recorded for iron spots outside of the microXRF mapped area.

Sample	Scan ID	Spot mineral assignment (LCF)	Major mineral
MA-A1.2-2	4	Bentonite/Goethite	Bentonite
	2	Bentonite/Mackinawite	
	7	Bentonite/Mackinawite	
	8	Bentonite/Mackinawite	
	3	Bentonite/Pyrite	
	5	Pyrite	Pyrite
	6	Pyrite/Bentonite	
MA-A1.3-4	20	Bentonite	Bentonite
	19	Bentonite/Pyrite	
	25	Bentonite/Mackinawite	
	21	Pyrite/Bentonite	Pyrite
	22	bad spectrum	
	23	bad spectrum	
	24	bad spectrum	
MA-A1.4-5	16	Goethide/Bentonite	Goethite
	17	Bentonite/Pyrite	Bentonite
	10	Bentonite/Pyrite	
	13	Bentonite/Pyrite	
	15	Bentonite/Ferrihydrite/Mackinawite	
	18	Bentonite/Mackinawite	
	11	Pyrite/Bentonite	Pyrite
	9	Mackinawite/Pyrite/Bentonite	Mackinawite
	12	Mackinawite/Bentonite	
	14	Mackinawite/Pyrite	

Sulfur speciation A similar set of embedded samples obtained from the sand-bentonite matrix was analysed for sulfur speciation, based on microXRF scans (for the systems with ongoing sulfate-reduction, see Figure 4.33 on page 164 and for the control experiment, see Figure 4.42 on page 173). The results, Table 4.6, confirm the dissolution of gypsum, which was commonly found in the control MA-A1.NC but almost not at all in samples from bioreactor MA-A1.3. Instead, most sulfur signals can be attributed to iron sulfide mineral phases, Table 4.6. In two observations, the LCF indicates sulfur as the main S-species, which can be interpreted as the onset of polysulfide formation. Two example linear combination fits, used to classify the sulfur speciation at the selected spots are in the Chapter's Appendix, Figure 4.52 on page 188.

Table 4.6 – Sulfur-XAS recorded for the control MA-A1.NC and bioreactor MA-A1.3, sulfur-speciation linear combination fitting (LCF) guided for the mineral assignment. MA-A1.NC POI1: Visual dark coloration with two sulfur spots around silicon and iron accumulation. POI2: A band of sulfur at the interface with silicon. POI4: Sulfur close to silicon grain. MA-A1.3: POI1: Visual dark spot, no silicon signal but high iron and sulfur signals within bentonite phase. POI2: Similar conditions as POI1. Images of the investigated area for MA-A1.3 can be found in Figure 4.33 on page 164 and for MA-A1.NC in Figure 4.42 on page 173

Sample	POI ID	Spot ID	Spot mineral assignment	Major mineral
MA-A1.NC	1	1	Bentonite/Sulfur/Pyrite	Bentonite
		2	Bentonite	
	2	1	Bentonite	
		3	Bentonite/Sulfur	
		2	Sulfate/Bentonite/Sulfur	Gypsum
	4	1	Sulfate/Bentonite	
		2	Bentonite	Bentonite
		3	Bentonite	
MA-A1.3	1	1	Pyrite/Mackinawite	Pyrite
		2	Pyrite/Mackinawite	
		5	Pyrite/Mackinawite	
		6	Pyrite/Mackinawite	
		7	Pyrite/Mackinawite	
		3	Sulfur/Mackinawite/Bentonite	Potentially polysulfides
		4	Sulfur/Mackinawite/Bentonite	
	2	1	Pyrite/Mackinawite	Pyrite
		2	Pyrite/Mackinawite	
		4	Pyrite/Mackinawite	
		5	Pyrite/Mackinawite	
		6	Pyrite/Mackinawite	
		3	Bentonite/Mackinawite/Pyrite	Bentonite

Figure 4.17 – Left half of Bioreactor MA-A1.1, before sampling for DNA extraction. The bentonite appears darker in the middle and at the edges close to the Plexiglas cylinder, the left part of the cylinder appears also slightly brown-yellowish.

Figure 4.18 – Left half of Bioreactor MA-A1.1, after sampling for DNA extraction and embedding. This cut is several centimeters below the middle cutting-plane presented in Figure 4.17. Vacuum-dried and embedded in EPO-TEK 301-2 resin, diamond band-saw cutting to obtain an even surface. The red box indicates the area of interest for detailed elemental mapping.

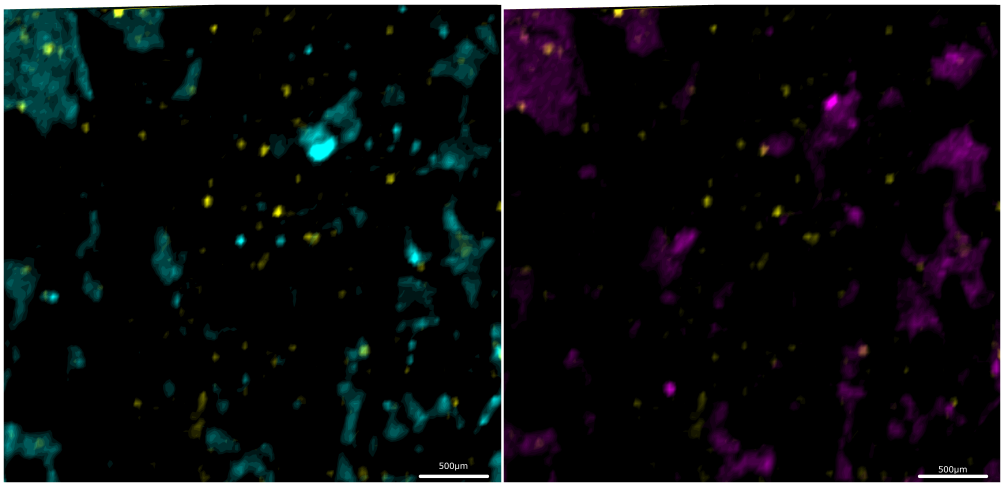

(a) MA-A1.1 gypsum (green) map (b) MA-A1.1 iron sulfide (red) map

Figure 4.19 – Spatial distribution of chosen elements within the small area of bioreactor MA-A1.1, indicated as red box in Figure 4.18. (a) Calcium (cyan) and sulfur (yellow), addition of these two colors results in green which is indicative for gypsum. (b) Iron (magenta) and sulfur (yellow), resulting in red which is indicative for iron sulfides.

.

Figure 4.20 – Left half of Bioreactor MA-A1.2, before sampling for DNA extraction. The bentonite appears darker in the middle and at the bottom of the Plexiglas cylinder, the left part of the cylinder appears also slightly brown-yellowish. The curvature of the darker area at the bottom part of the cylinder aligns with the expected flow pattern of the sulfide-rich (and sulfate-poor) effluent of bioreactor MA-A1.1 which served as influx for this bioreactor MA-A1.2.

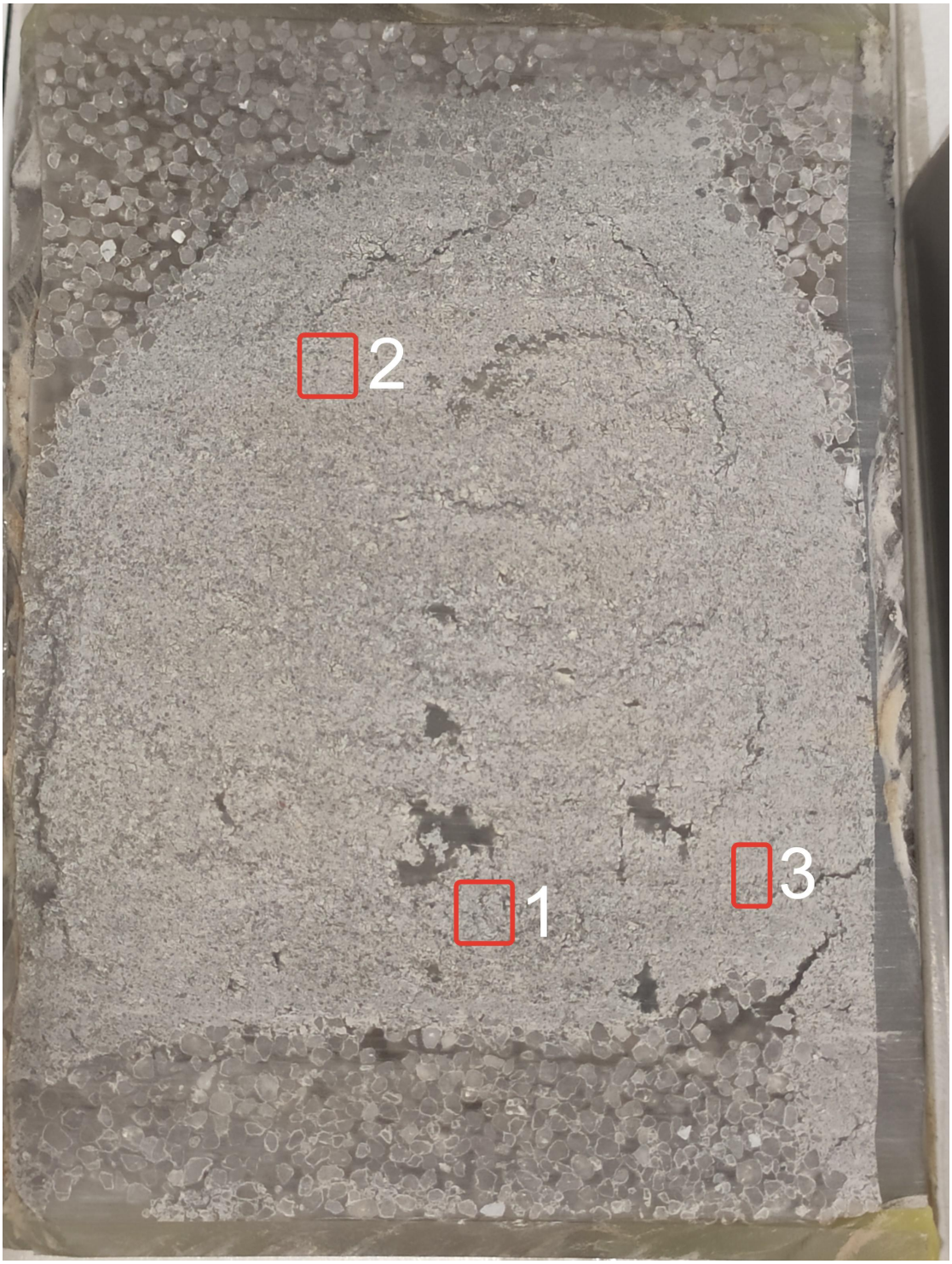

Figure 4.21 – Left half of Bioreactor MA-A1.2, after sampling for DNA extraction and embedding. This cut is several centimeters below the middle cutting-plane presented in Figure 4.20. Vacuum-dried and embedded in EPO-TEK 301-2 resin, diamond band-saw cutting to obtain an even surface. The red boxes indicate the three areas of interest for detailed elemental mapping.

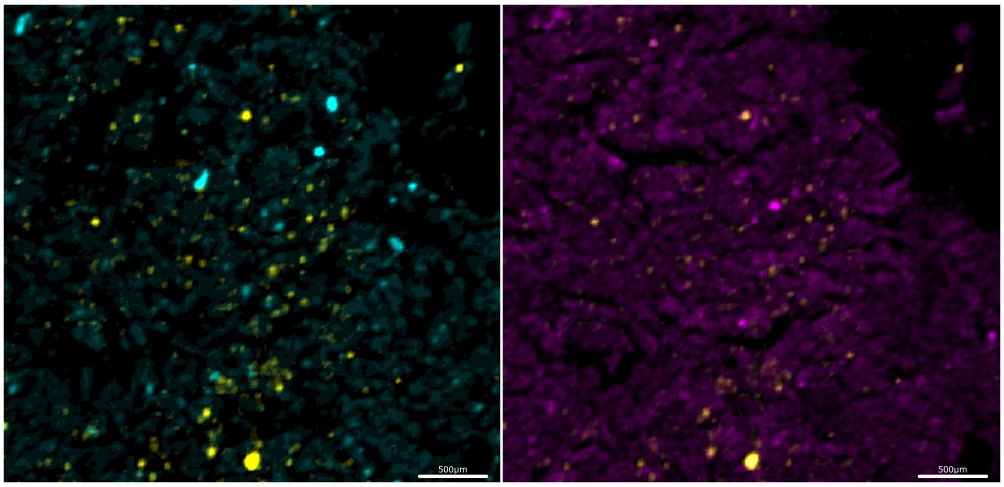

(a) MA-A1.2 gypsum (green) map 1 (b) MA-A1.2 iron sulfide (red) map 1

Figure 4.22 – Spatial distribution of chosen elements within the small area of bioreactor MA-A1.2, indicated as red box (1) in Figure 4.21. (a) Calcium (cyan) and sulfur (yellow), addition of these two colors results in green which is indicative for gypsum. (b) Iron (magenta) and sulfur (yellow), resulting in red which is indicative for iron sulfides.

.

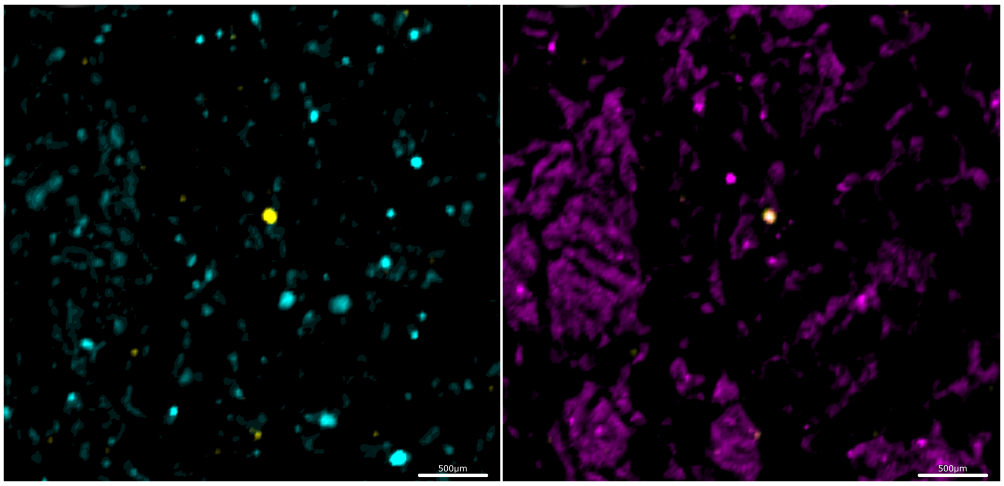

(a) MA-A1.2 gypsum (green) map 2 (b) MA-A1.2 iron sulfide (red) map 2

Figure 4.23 – Spatial distribution of chosen elements within the small area of bioreactor MA-A1.2, indicated as red box (2) in Figure 4.21. (a) Calcium (cyan) and sulfur (yellow), addition of these two colors results in green which is indicative for gypsum. (b) Iron (magenta) and sulfur (yellow), resulting in red which is indicative for iron sulfides.

.

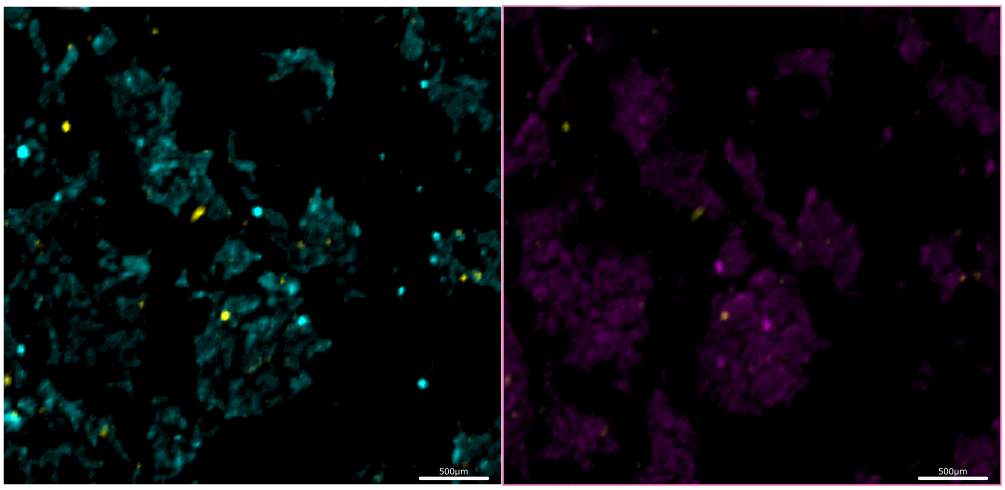

(a) MA-A1.2 gypsum (green) map 3 (b) MA-A1.2 iron sulfide (red) map 3

Figure 4.24 – Spatial distribution of chosen elements within the small area of bioreactor MA-A1.2, indicated as red box (3) in Figure 4.21. (a) Calcium (cyan) and sulfur (yellow), addition of these two colors results in green which is indicative for gypsum. (b) Iron (magenta) and sulfur (yellow), resulting in red which is indicative for iron sulfides.

.

(a) Embedded MA-A1.2 sample for microXRF and Fe-XAS mapping. Indicated area approx. 1 cm long.

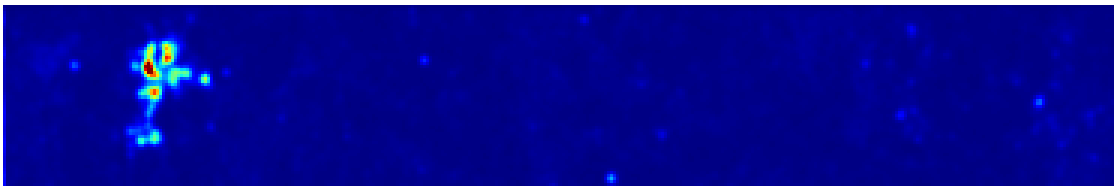

(b) Sulfur K-edge map

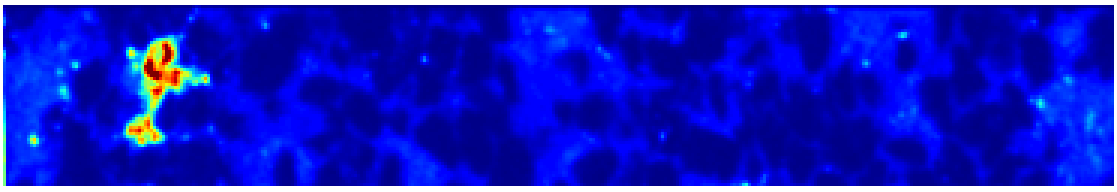

(c) Iron K-edge map

Figure 4.25 – Maps of sulfur (b) and iron (c) obtained from the indicated area in (a, orange) at SSRL BL2-3.

.

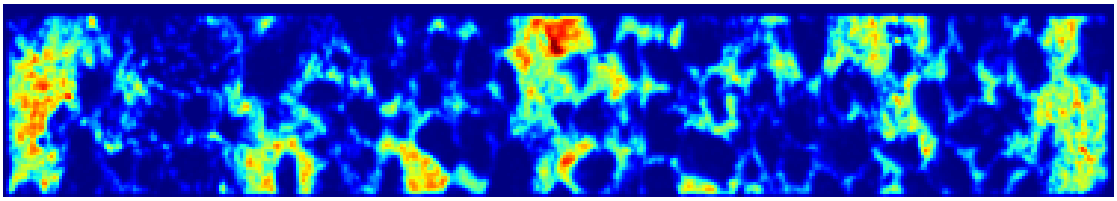

(a) Wyoming bentonite fit

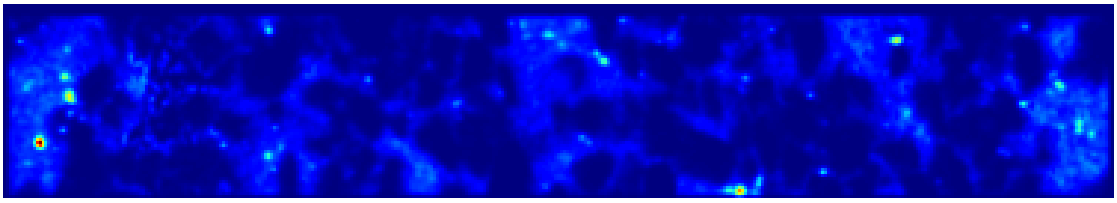

(b) Ferrihydrite fit

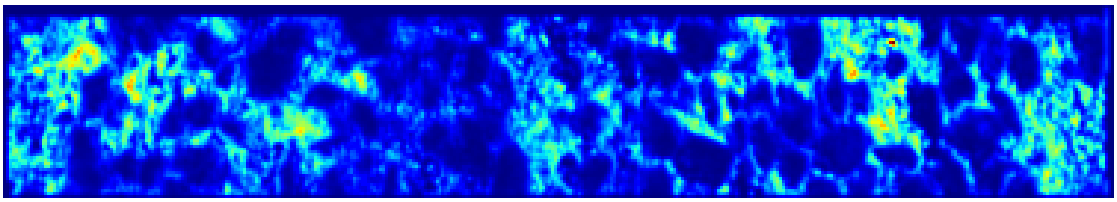

(c) Goethite fit

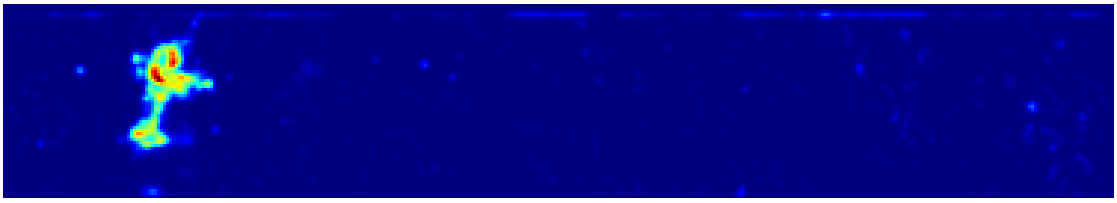

(d) Iron sulfide fit

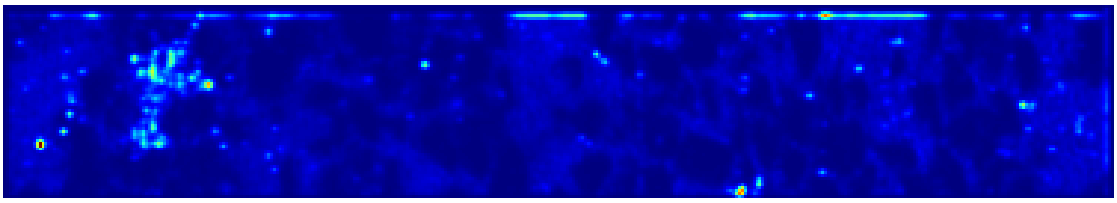

(e) Fit error

Figure 4.26 – MA-A1.2 Fe-XAS mapping. Mapped area approx. 1 cm long.

.

Figure 4.27 – Left half of Bioreactor MA-A1.3, before sampling for DNA extraction. The bentonite appears darker at the bottom part and closer to the Plexiglas. Two black spots can be spotted at the lower middle and the upper middle-right part, of which the lower one was selected for Fe microXRF and Fe microXAS analysis, Figure 4.31

Figure 4.28 – Left half of Bioreactor MA-A1.3, after sampling for DNA extraction and embedding. This cut is several centimeters below the middle cutting-plane presented in Figure 4.27. Vacuum-dried and embedded in EPO-TEK 301-2 resin, diamond band-saw cutting to obtain an even surface. The red boxes indicate the two areas of interest for detailed elemental mapping.

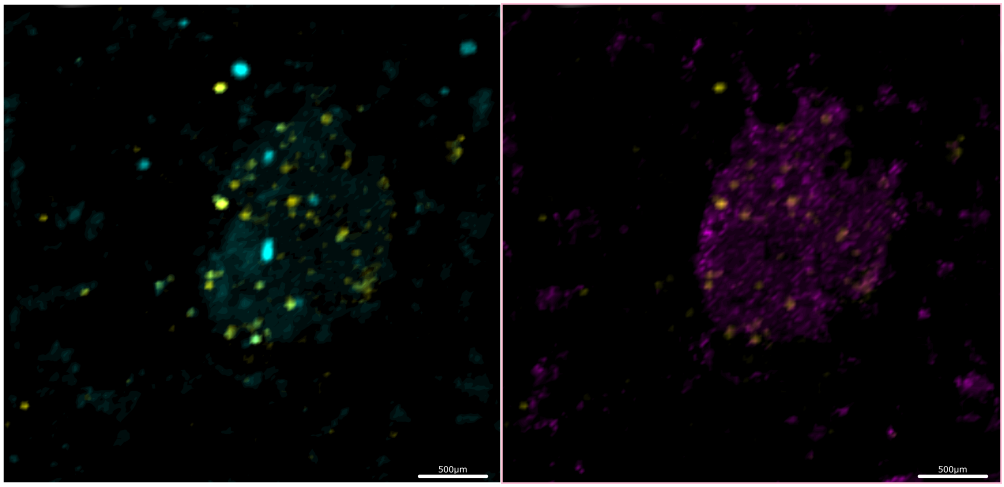

(a) MA-A1.3 gypsum (green) map 1 (b) MA-A1.3 iron sulfide (red) map

Figure 4.29 – Spatial distribution of chosen elements within the small area of bioreactor MA-A1.3, indicated as red box (1) in Figure 4.28. (a) Calcium (cyan) and sulfur (yellow), addition of these two colors results in green which is indicative for gypsum. (b) Iron (magenta) and sulfur (yellow), resulting in red which is indicative for iron sulfides.

.

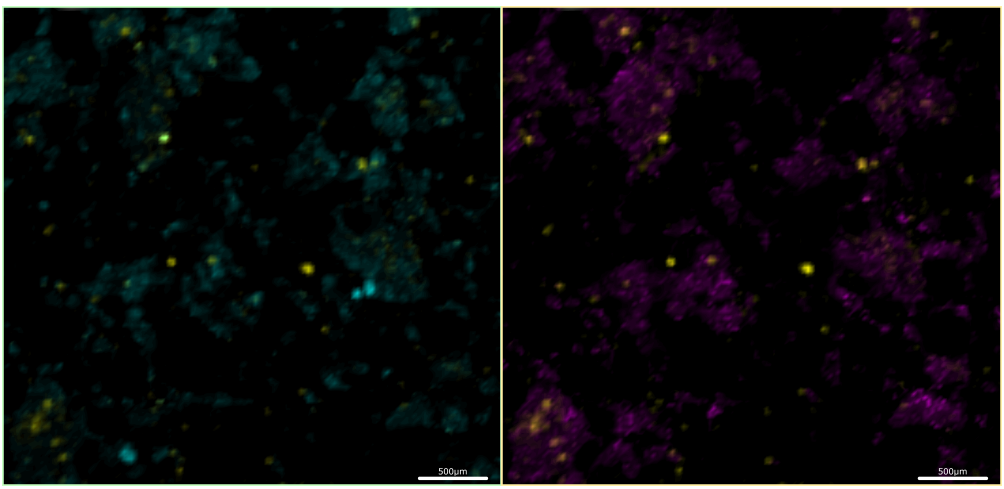

(a) MA-A1.3 gypsum (green) map 2 (b) MA-A1.3 iron sulfide (red) map

Figure 4.30 – Spatial distribution of chosen elements within the small area of bioreactor MA-A1.3, indicated as red box (2) in Figure 4.28. (a) Calcium (cyan) and sulfur (yellow), addition of these two colors results in green which is indicative for gypsum. (b) Iron (magenta) and sulfur (yellow), resulting in red which is indicative for iron sulfides.

.

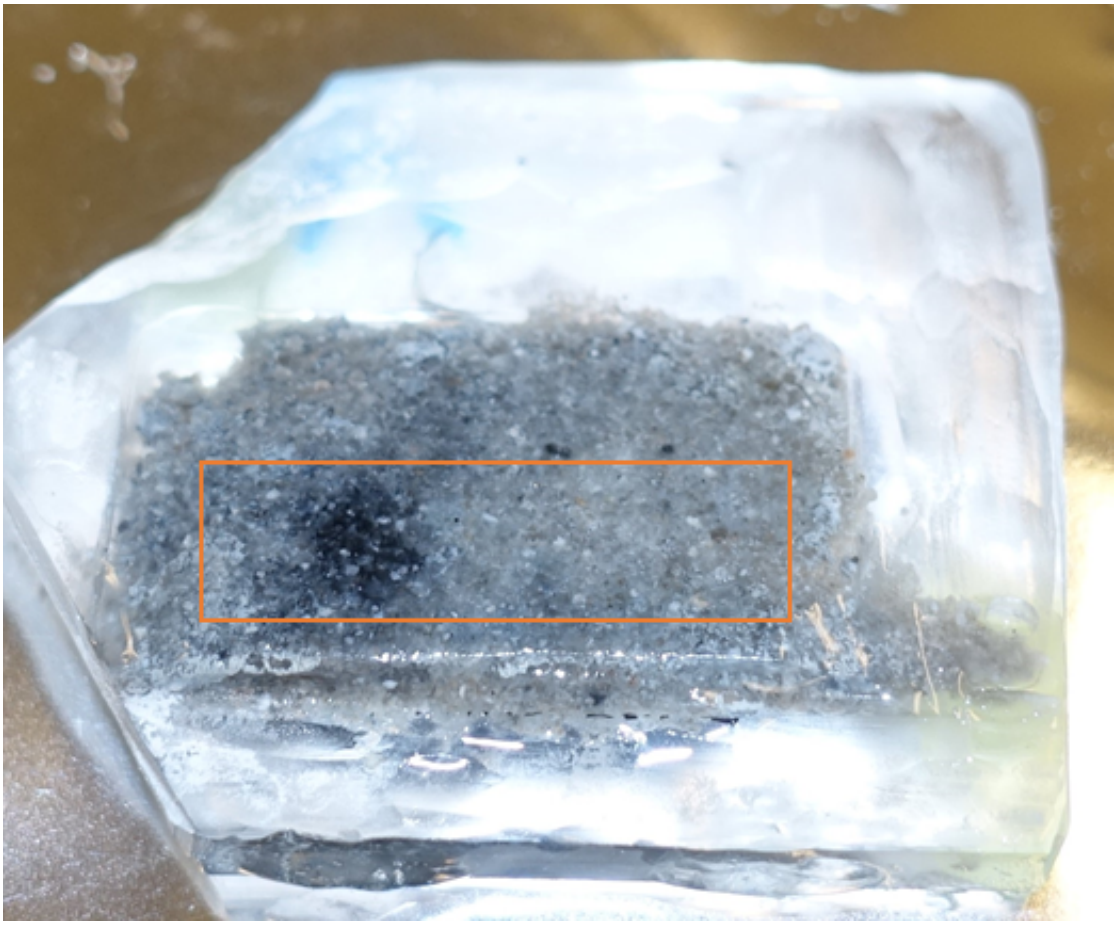

(a) Embedded MA-A1.3 sample for microXRF and Fe-XAS mapping. Indicated area approx. 1 cm long.

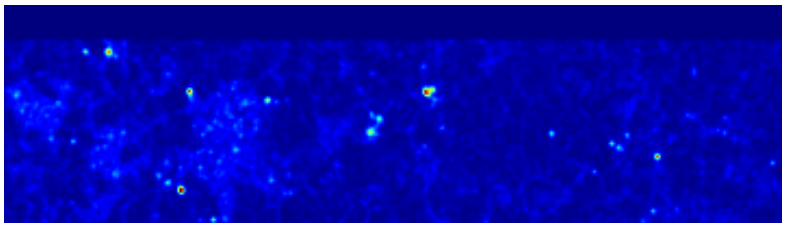

(b) Sulfur K-edge map

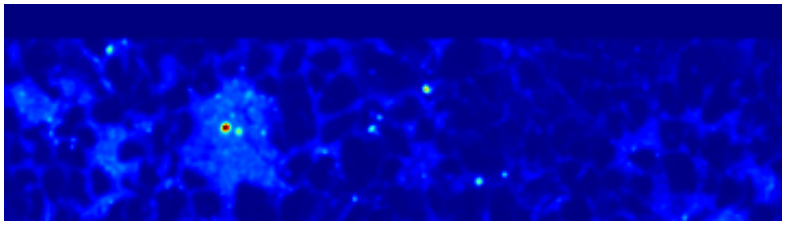

(c) Iron K-edge map

Figure 4.31 – Maps of sulfur (b) and iron (c) obtained from the indicated area in (a, orange) at SSRL BL2-3.

.

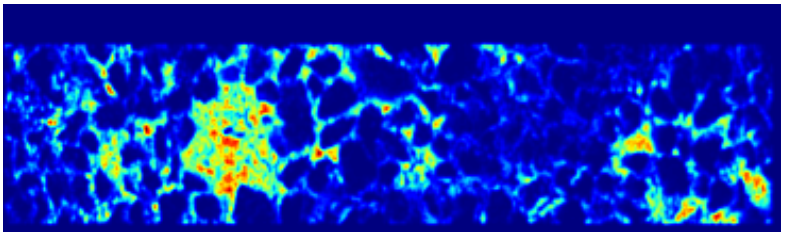

(a) Wyoming bentonite fit

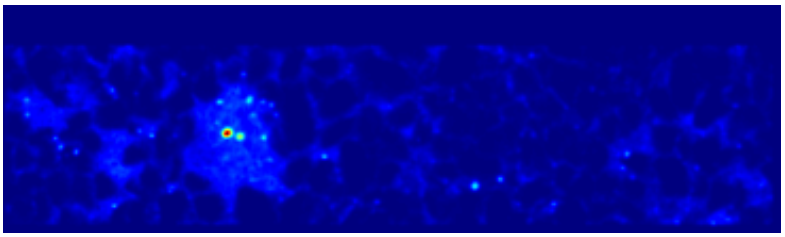

(b) Ferrihydrite fit

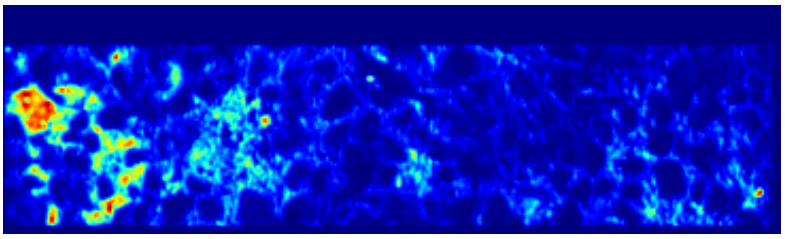

(c) Goethite fit

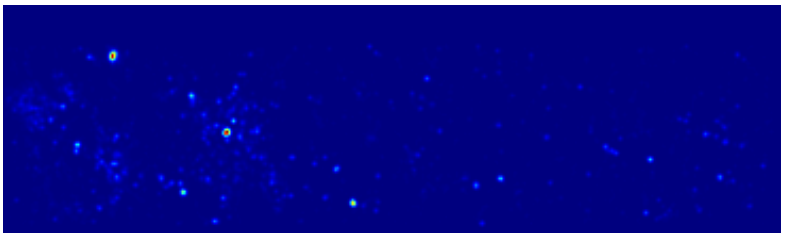

(d) Iron sulfide fit

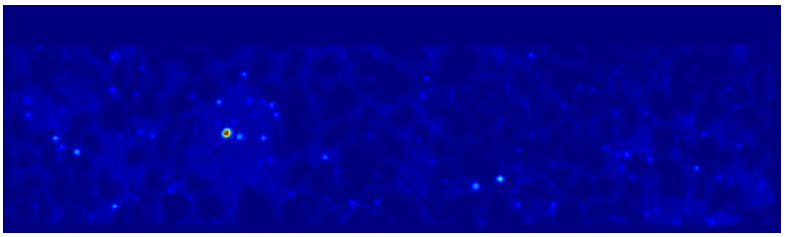

(e) Fit error

Figure 4.32 – MA-A1.3 Fe-XAS mapping. Mapped area approx. 1 cm long.

.

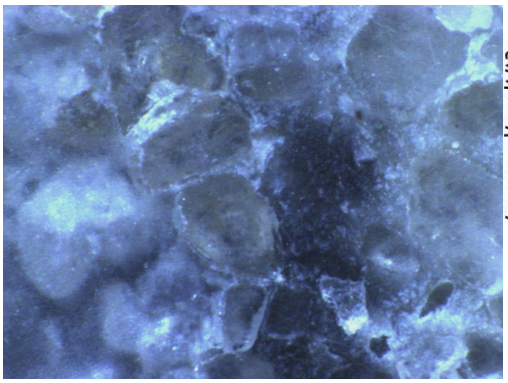

(a) Optical image of POI 1

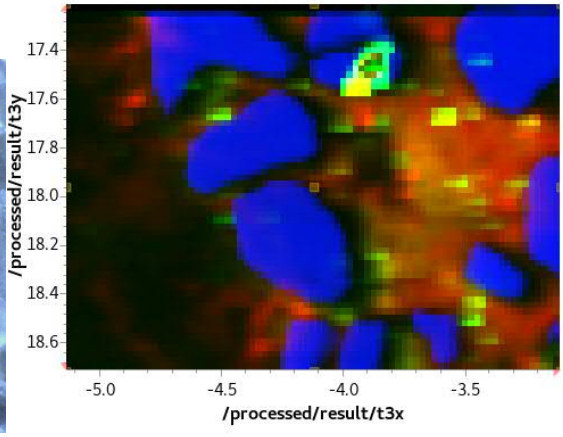

(b) Tricolour microXRF image of POI 1

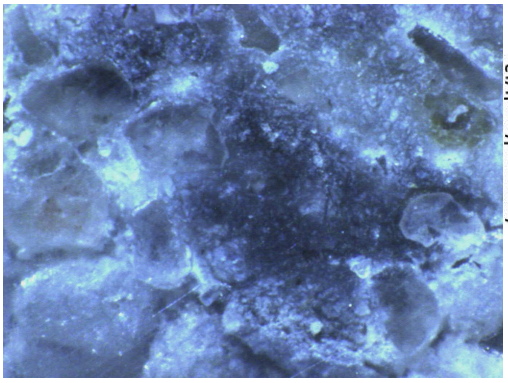

(c) Optical image of POI 2

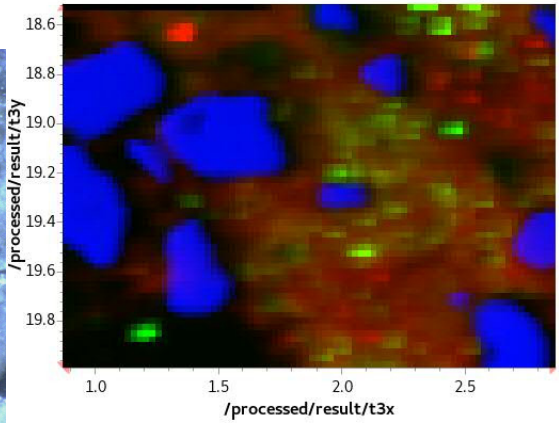

(d) Tricolour microXRF image of POI 2

Figure 4.33 – microXRF maps of MA-A1.3 obtained at DLS I-18, (a, c) optical image of POI 1 and 2 respectively, (b, d) tricolour plots thereof showing iron (red), sulfur (green) and silicon (blue). A dust contamination in (b) can be seen as bright green spot on top of a sand grain (blue), no sulfur XAS measurements were taken from such dust contamination.

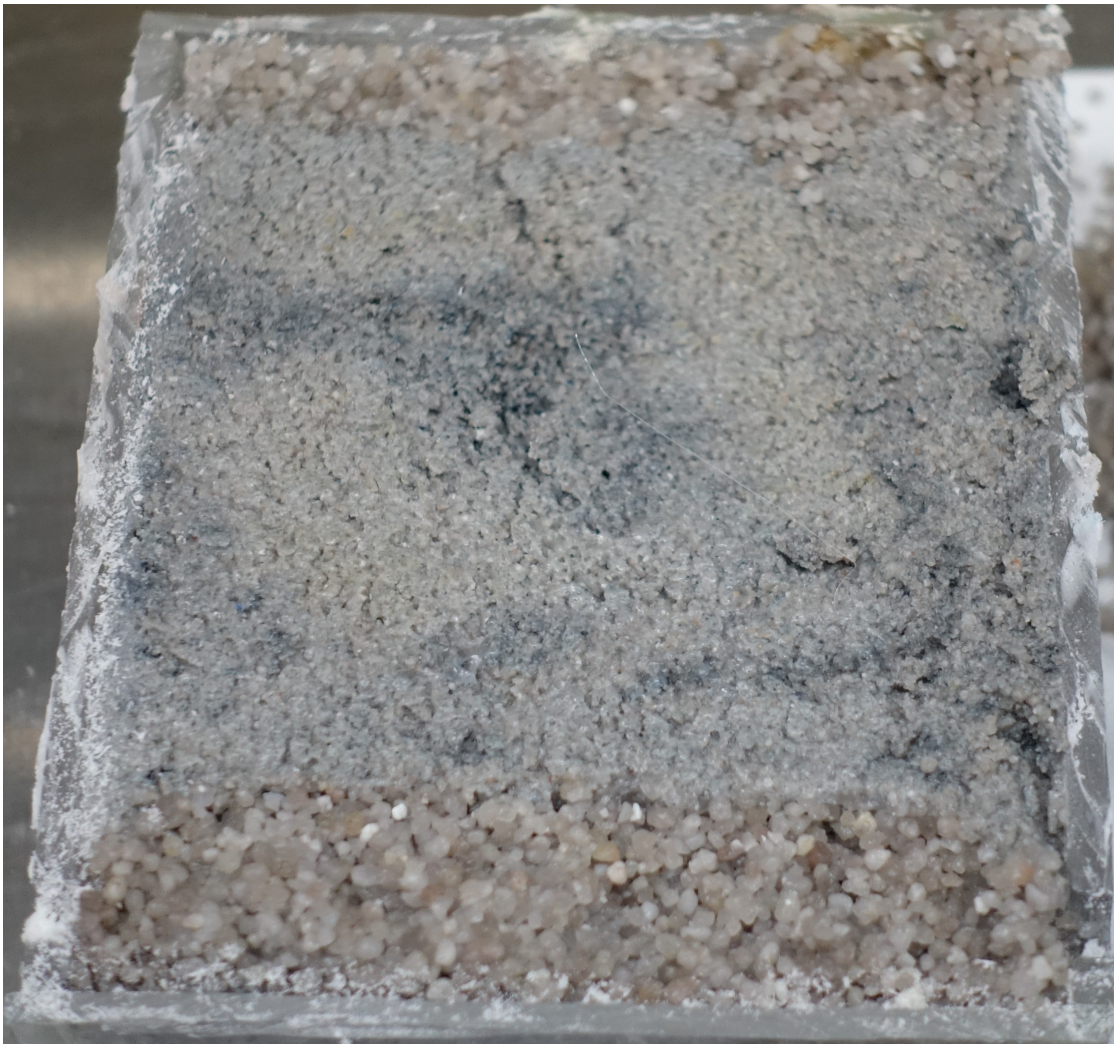

Figure 4.34 – Left half of the bioreactor MA-A1.4, before sampling for DNA extraction. Similar patterns of dark colouration at the middle and the edges are observed. XRF overview observations showed similar results as for the other three bioreactors, thus no further detailed elemental mapping was performed for MA-A1.4.

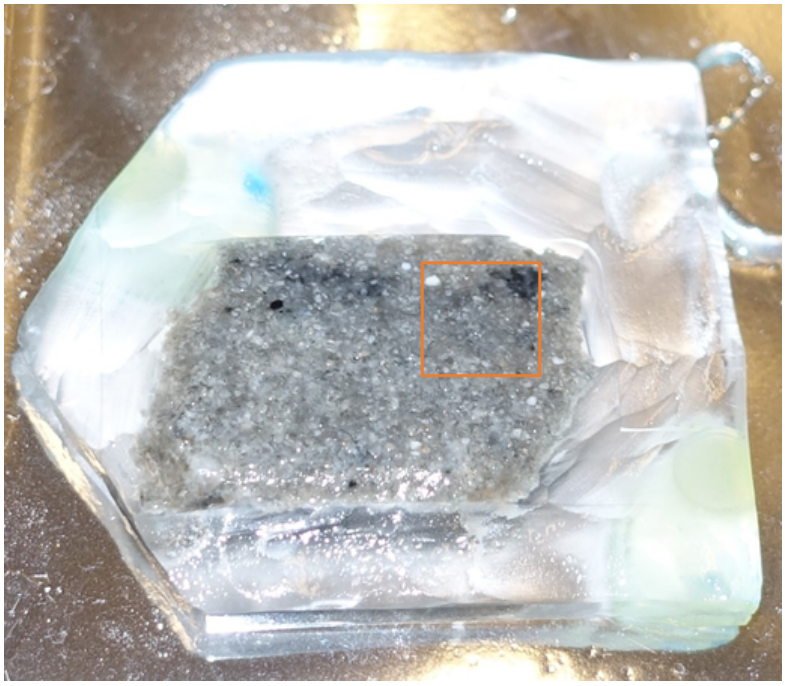

(a) Embedded MA-A1.4 sample for microXRF and Fe-XAS mapping. Indicated area approx. 0.3 cm long.

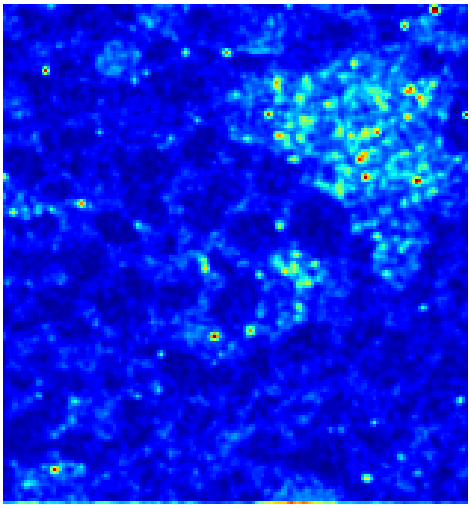

(b) Sulfur K-edge map

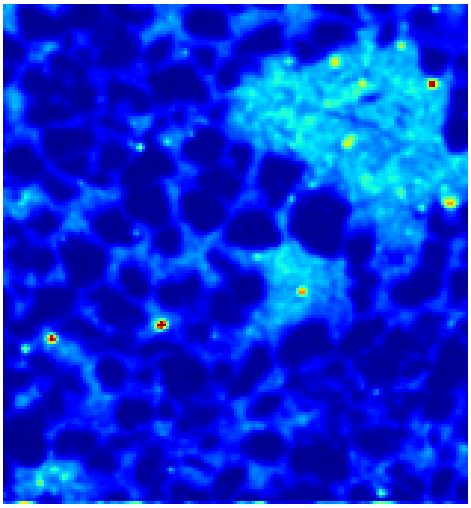

(c) Iron K-edge map

Figure 4.35 – Maps of sulfur (b) and iron (c) obtained from the indicated area in (a, orange) at SSRL BL2-3.

.

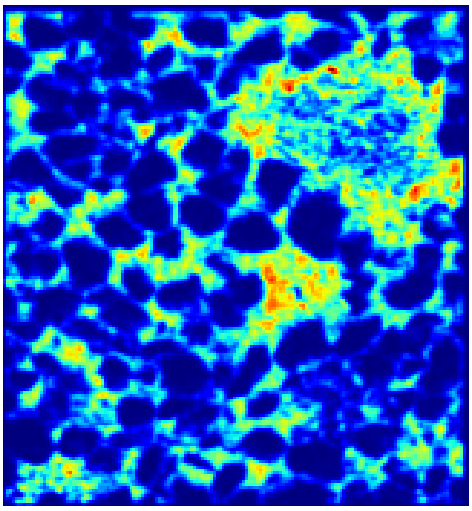

(a) Wyoming bentonite fit

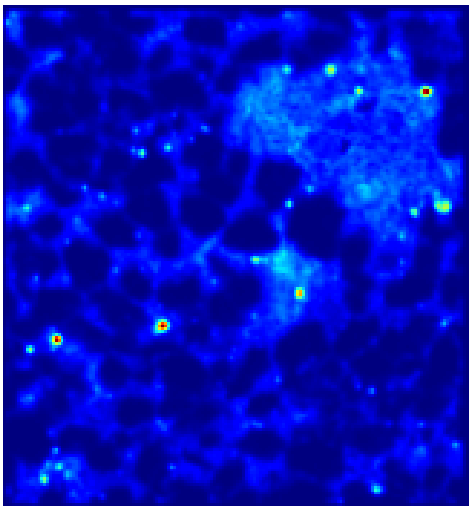

(b) Ferrihydrite fit

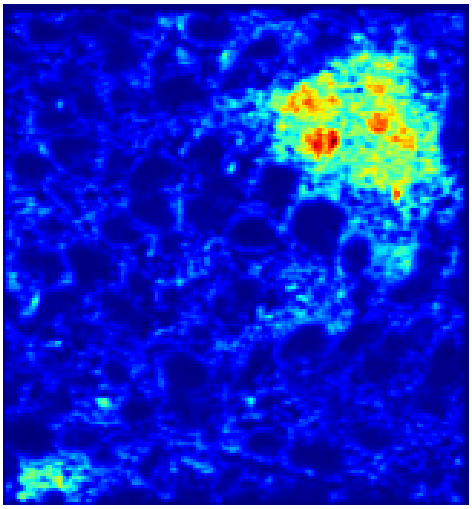

(c) Goethite fit

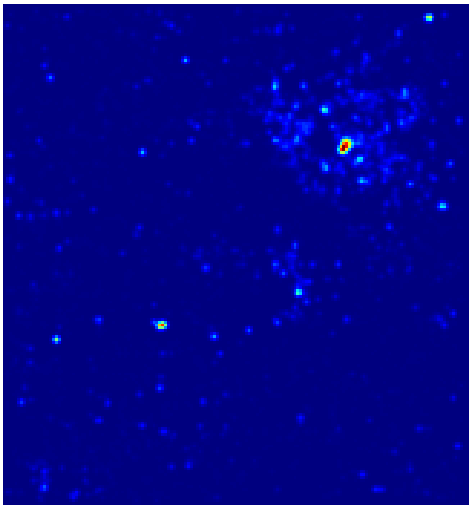

(d) Iron sulfide fit

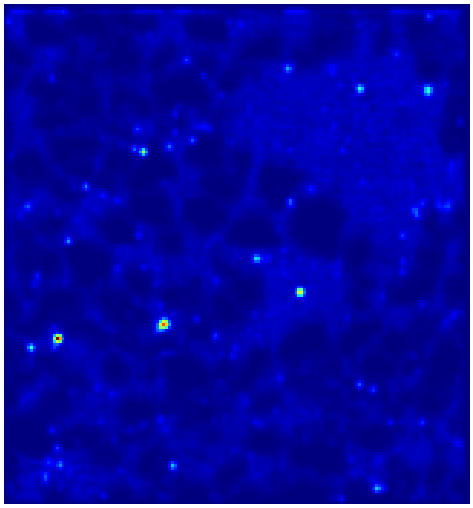

(e) Fit error

Figure 4.36 – MA-A1.4 Fe-XAS mapping. Mapped area approx. 0.3 cm long.

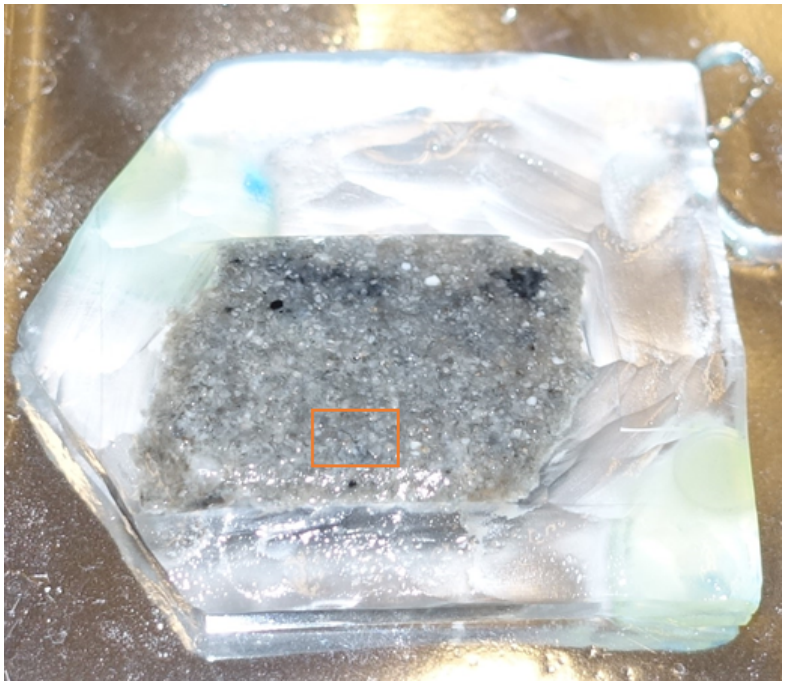

(a) Embedded MA-A1.4 sample for microXRF and Fe-XAS mapping. Second area of interest, indicated area approx. 0.15 cm long.

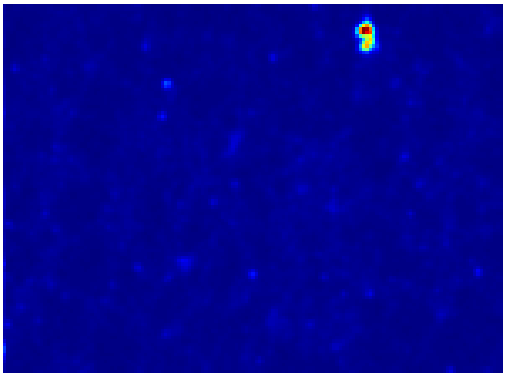

(b) Sulfur K-edge map

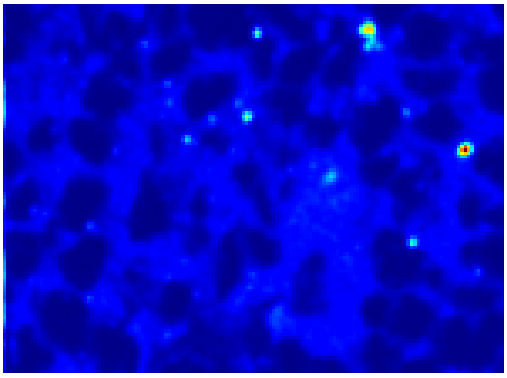

(c) Iron K-edge map

Figure 4.37 – Maps of sulfur (b) and iron (c) obtained from the indicated area in (a, orange) at SSRL BL2-3.

.

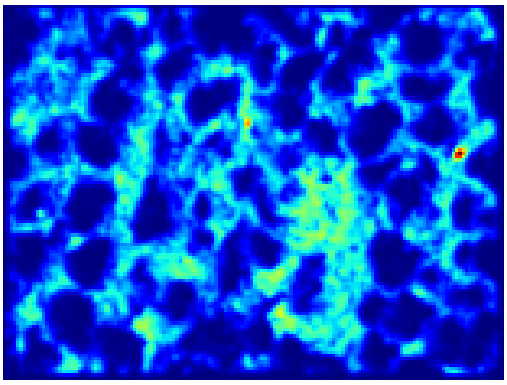

(a) Wyoming bentonite fit

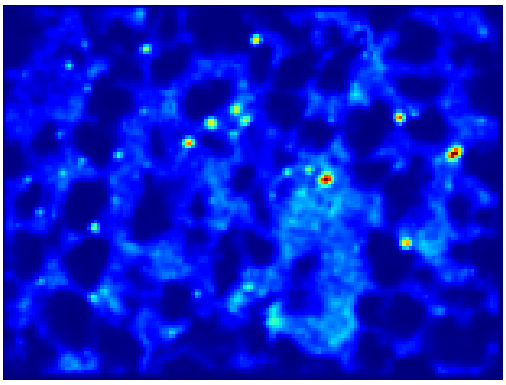

(b) Ferrihydrite fit

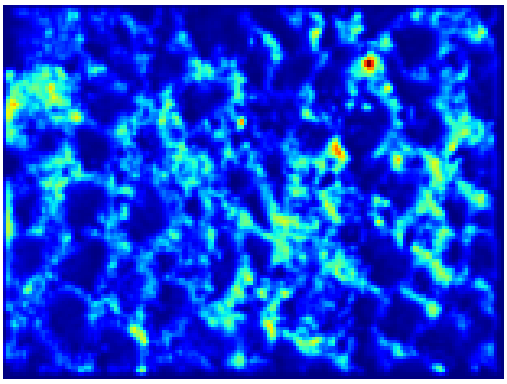

(c) Goethite fit

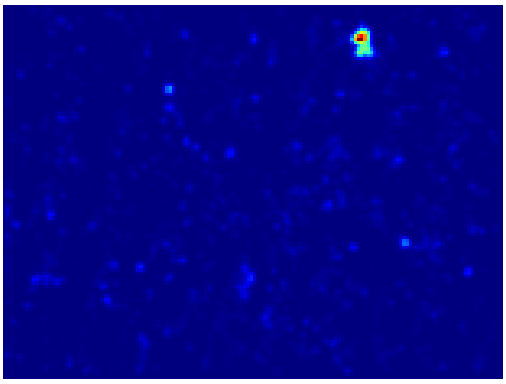

(d) Iron sulfide fit

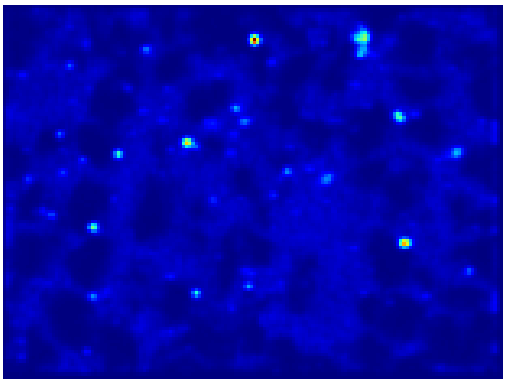

(e) Fit error

Figure 4.38 – MA-A1.4 Fe-XAS mapping. Second area of interest, mapped area approx. 0.15 cm long.

.

Figure 4.39 – Left half of the control MA-A1.NC, before sampling for DNA extraction. No special features are observed.

Figure 4.40 – Left half of Bioreactor MA-A1.3, after sampling for DNA extraction and embedding. This cut is several centimeters below the middle cutting-plane presented in Figure 4.39. Vacuum-dried and embedded in EPO-TEK 301-2 resin, diamond band-saw cutting to obtain an even surface.

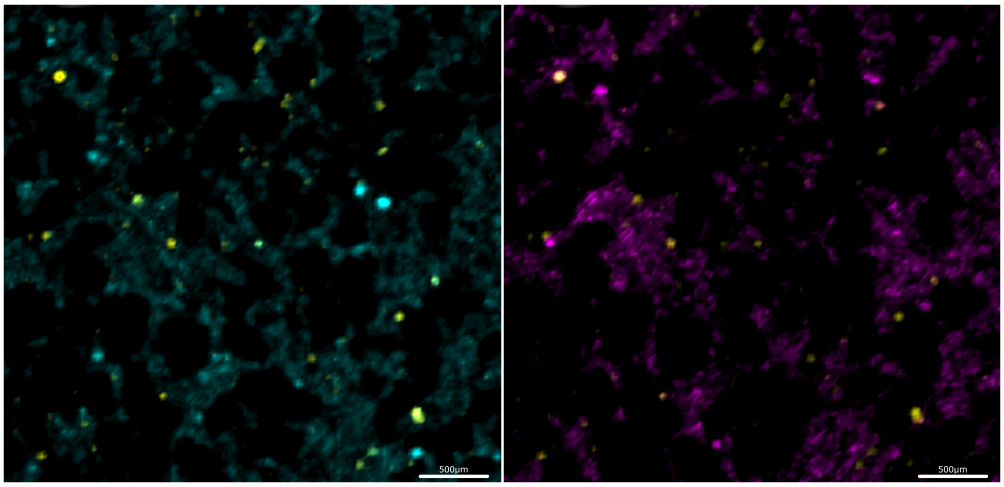

(a) MA-A1.NC gypsum (green) map (b) MA-A1.NC iron sulfide (red) map

Figure 4.41 – Spatial distribution of chosen elements within a small area of bioreactor MA-A1.NC. (a) Calcium (cyan) and sulfur (yellow), addition of these two colors results in green which is indicative for gypsum. (b) Iron (magenta) and sulfur (yellow), resulting in red which is indicative for iron sulfides.

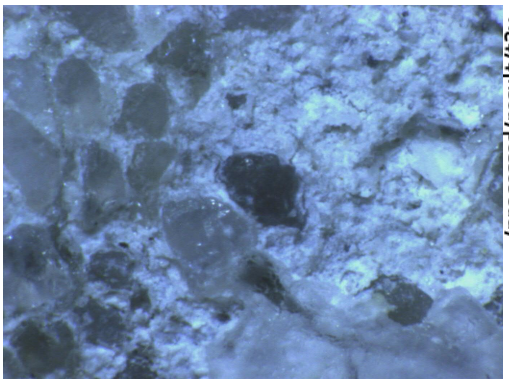

(a) Optical image of POI 1

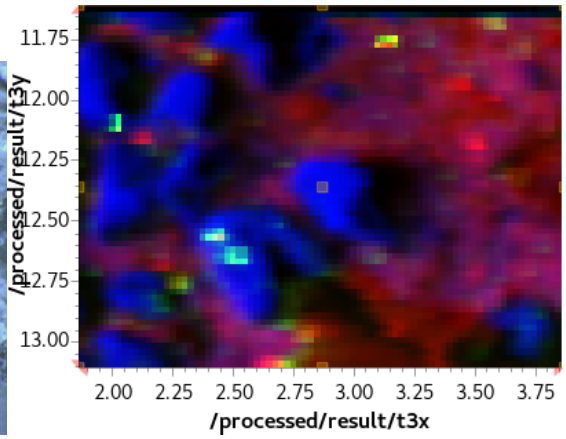

(b) Tricolour microXRF image of POI 1

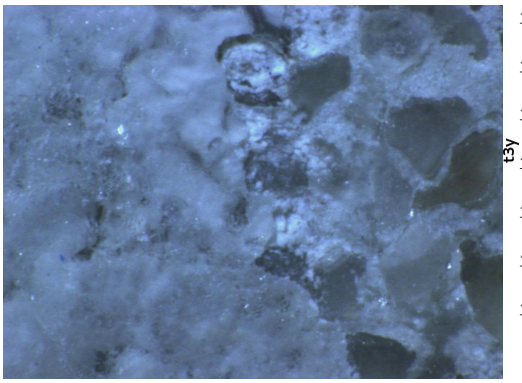

(c) Optical image of POI 2

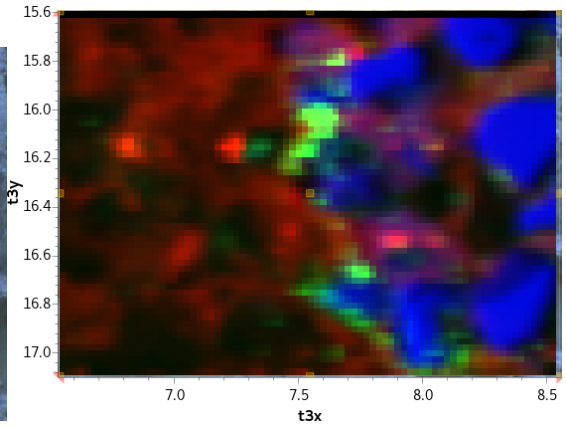

(d) Tricolour microXRF image of POI 2

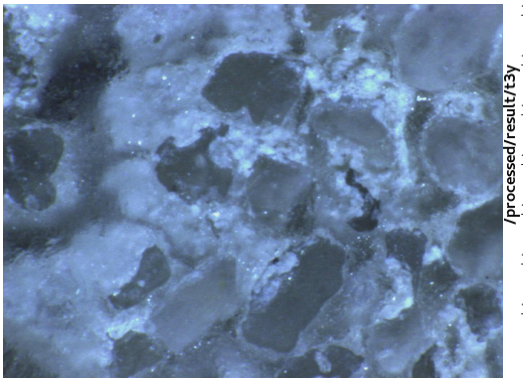

(e) Optical image of POI 4

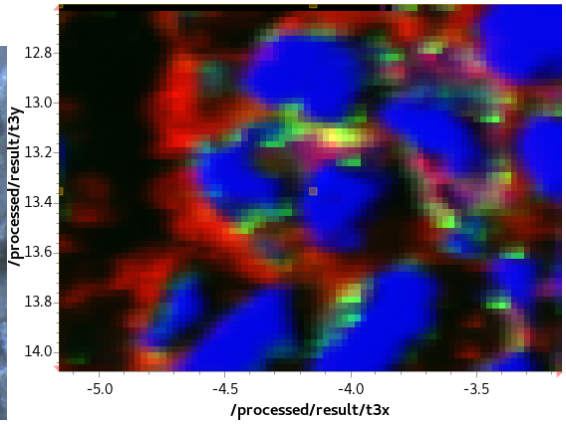

(f) Tricolour microXRF image of POI 4

Figure 4.42 – microXRF maps of MA-A1.NC obtained at DLS I-18, (a, c, e) optical images of POI 1, 2 and 4 respectively, (b, d, f) tricolour plots thereof showing iron (red), sulfur (green) and silicon (blue).

4.3.7 16S rRNA gene analysis of biofilm

The experimental set-up aimed to establish a link between the evolving microbiome and the two driving factors: (i) hydrogen availability, acting as the preferred electron donor and (ii) the porewater availability, providing the preferred electron acceptor for this system, sulfate. We hypothesized that in the middle of the bioreactor, close to the hydrogen outlet, the availability of H_2 will be high and bioavailable sulfate will be rapidly depleted due to the activity of sulfate-reducing bacteria. Sulfate-rich porewater enters the bioreactor from below and migrates the fastest along the inner wall of the Plexiglas cylinder. This conceptual view led to the expectation that a spatial separation of the evolving microbial community will develop, with a high contribution of SRB to the overall biomass in the specific area where high hydrogen and sulfate availability co-occur. Several other factors need to be considered: the daily supply of H_2-gas may, in some cases, create a gas bubble which could easily escape the sand-bentonite matrix upwards along the titanium tube and accumulate in either the coarse sand layer above or further up, into the gas trap. Furthermore, the flow rate of porewater from borehole BMA-A1 was not uniform throughout the experimental time-frame nor equal for each bioreactor, as shown in Figure 4.12. High flow rates occurred often for MA-A1.4 and to a lesser extent for MA-A1.3, whereas the serially-assembled MA-A1.1 and MA-A1.2 received the lowest amount of water (and thus sulfate). As a result, the supply of sulfate-rich porewater was unsteady over the entire time and further distortions were introduced at the weekly bioreactor outflow water sampling.

Five DNA extraction attempts from the negative control MA-A1.NC failed as no gDNA was found nor could the 16S rRNA gene be amplified. Thus, MA-A1.NC could be used as a control without sulfate-reducing bacteria influence.

4.3.8 16S rRNA gene copy number semi-quantitative results

Figures 4.43 and 4.44 show results obtained from 16S rRNA gene quantification. However, because only one observation of the 16S rRNA gene copy number was obtained for each sample point, based on a standard curve method as described in Section 4.2.5 (Analytical methods), the results are only semi-quantitative. Figure 4.43 evidences the biomass distribution across the cut sand-bentonite cores, Figure 4.8 on page 125 indicates the position labels. When comparing 16S rRNA gene copy numbers from the initial sand and bentonite and the reactors post-experiment, it is clear that growth has taken place within all four bioreactors Figure 4.43. The observed 16S rRNA gene copy numbers in the deployed sand-bentonite reactors are about two orders of magnitudes greater than those for the t=0 samples. For MA-A1.1 and MA-A1.4, we can also observe a tendency for higher 16S rRNA gene copy number at the center compared to the outer lanes. This effect can not be observed for MA-A1.3 and MA-A1.2, for the latter most likely because of the rather distorted top coarse sand layer. The biomass distribution from the top to the bottom of the cylinder is shown in Figure 4.44. The tendency of higher biomass at the center (4th row, i.e., at the vertical halfway point of the cylinder) is observed

for MA-A1.1 and MA-A1.4. Notable is also the sudden drop of biomass at the second lowest row (6th row) in bioreactor MA-A1.2. We speculate that the effluent of MA-A1.1 contained a relatively high microbial biomass that colonised the lower coarse sand layer, perhaps using dissolved hydrogen from the top of MA-A1.1 (from which the effluent is obtained) or dissolved organics, e.g., low-molecular weight organic acids. However, this colonisation appears less successful within the sand-bentonite matrix, as indicated by the sudden drop of 16S rRNA gene copies per gram substrate in that row (6th row).

4.3.9 Spatial distribution of major OTUs within the sand-bentonites matrix

Maps of the total number of 16S rRNA gene copies per gram substrate (coarse sand or sand-bentonite) and the relative abundance of the top five OTUs found across all four bioreactors are represented in Figures 4.45–4.48. The absolute number of 16S rRNA gene copies per gram substrate serves as an indicator of the accumulated biomass within the bioreactor. For each bioreactor, the topmost and the lowermost centimeter represents the boundary between coarse sand and the sand-bentonite matrix, except for bioreactor MA-A1.2 which has a distorted layering, Figure 4.20. For some sampled sites, no gDNA quantification could be performed, thus no consistent back-calculation to per gram substrate could be performed. These areas are found in grey color in the Figures 4.45–4.48. However, 16S rRNA genes could often be amplified and annotated to known taxa without quantified 16S rRNA gene concentration per gram substrate. An example is the case of bioreactor 1.4, for which the top right area exhibits abundant DNA sequences belonging to the genera *Pseudomonas*, *Sunxiuqinia* and *Symbiobacter*, Figure 4.48. Throughout the four bioreactors, the color intensity scale of the top five OTUs is equalized. The relative abundances can be qualitatively compared within each bioreactor and amongst the bioreactors.

We consider the spatial distribution of the top 5 OTUs:

- *Desulfovibrio*: The highest relative contributions are observed at the bioreactors MA-A1.4 (up to 36.7%) and MA-A1.1 (up to 31.5%), showing a spatial preference for the center of the sand-bentonite matrix, close to the hydrogen supply tube, Figure 4.45b and 4.48b. For bioreactor MA-A1.3, Figure 4.47b, *Desulfovibrio* shows a less strong preference for the middle but is also observed in higher abundance at the top of the sampled area, i.e., at the top sand-bentonite which interfaces the coarse sand layer. A possible explanation for this observation is that excess hydrogen may have been present as a bubble in this area. Bioreactor MA-A1.2 shows a more diffuse localization of *Desulfovibrio* with the highest relative abundance at the top left of the sampled area. For this particular bioreactor, sulfate availability was limited. As a result, colonization was limited to the few areas with high enough sulfate and hydrogen supply to support growth. Higher flow rates of water are expected at the edges and the higher concentrations of hydrogen, due to the formation of gas bubbles, is expected at the top of the bioreactor. Thus the observation of the higher relative abundance of these sulfate-reducing bacteria at the

top of MA-A1.2 is plausible. This genus appears to originate from the Opalinus Clay rock borehole BMA-A1 as there were 7 observations of 16S rRNA genes affiliated with *Desulfovibrio*, albeit at very low relative contributions.

- *Methanosarcina*: A methane signal was detected in the gas phase of all four bioreactors during the course of the experiment. The methane is expected to have been produced by *Methanosarcina*, a versatile methanogen capable of all three known methanogenic pathways (Madigan et al., 2017). It can use CO_2+H_2, methanol and methylamines, or acetate to produce CH_4. We observe this genus at highest relative abundance (33.1%) in bioreactor MA-A1.2, Figure 4.46c, localised at the top right, within a distorted coarse sand layer, Figure 4.20. Within the sand-bentonite matrix, in the middle, close to the outlet of the hydrogen tube and at the top layer, another colonization spot of *Methanosarcina* is observed. Compared with the total 16S rRNA gene copy number, Figure 4.46a, it is readily apparent that the high biomass in the upper right corner can be attributed to *Methanosarcina*. The MA-A1.1 and 1.2 serial assembly received the lowest total amount of water, 330.9 mL in total, and had the longest deployment time of 108 days. This resulted in a low total amount of sulfate and a long residence time for low-sulfate water as well as additional hydrogen gas supplied from bioreactor MA-A1.1. This combination of factors created good conditions for *Methanosarcina* to colonize the bioreactor, both the sand-bentonite as well as the coarse sand layer on top. The second highest relative abundance (28.1%) was observed for bioreactor MA-A1.1, Figure 4.45c, and was found near the center of the reactor, within the sand-bentonite matrix. Even though the sulfate supply was slightly higher than for bioreactor MA-A1.2, *Methanosarcina* could grow well compared to the remaining two bioreactors, likely due to the low overall amount of sulfate supplied. Bioreactor MA-A1.3, which was deployed for 73 days and received in total 732.7 mL porewater from borehole BMA-A1, shows lower *Methanosarcina* abundances (up to 20.2%) at the top of the sand-bentonite layer. The lowest relative abundance was observed for bioreactor MA-A1.4 (up to 7.4%) at the lower half of the sand-bentonite layer. This bioreactor received the highest total amount of water, 1,180.4 mL, and was deployed for 79 days. Thus we conclude that a high porewater supply, replenishing the bio-available sulfate, is inversely correlated with the activity and growth of *Methanosarcina*. The origin of this genus can only be restricted to two possible sources, at very low abundance in both cases: either the Opalinus Clay rock borehole BMA-A1 with two observations or the sand (the fine sand in the sand-bentonite matrix and the coarse sand at the top and bottom layers).

- *Pseudomonas*: In all four bioreactors, we observe a rather uniform presence of *Pseudomonas*, indicating that neither the availability of H_2 nor the porewater from borehole BMA-A1 is driving the colonization. *Pseudomonas* constitutes opportunistic, fermenting species and the occurrence of this genus is well documented in porewater-filled boreholes in Opalinus Clay rock of 'Mont Terri' (Bagnoud, de Bruijn, et al., 2016; Bleyen et al., 2017; O. X. Leupin et al., 2017).

- *Sunxiuqinia*: The highest relative abundance is observed for MA-A1.2 (up to 23.5%)

and MA-A1.4 (up to 23.3%) whereas the number are lower for the other two bioreactors (MA-A1.3 up to 16%, MA-A1.1 up to 10.1%). Spatially, this genus appears to be outcompeted by *Desulfovibrio*, because their abundance appears low where *Desulfovibrio* is highly abundant. Species within the genus have been reported in fresh and marine water systems. For instance, *Sunxiuqinia indica*, from a deep-water seafloor sediment, is described as a facultative anaerobe with the ability to live off of recalcitrant organics (Li et al., 2020). Other species of this genus are also described within deep sub-seafloor sediments, e.g. *Sunxiuqinia dokdonensis* by (Chang et al., 2013) and *Sunxiuqinia faeciviva* (Takai et al., 2013). Observations of this genus were made within the Opalinus Clay rock borehole at all sampled time-points between 2017 and 2019 (6 observations in total in very low abundance) but also within the sand (the fine sand in the sand-bentonite matrix and the coarse sand at the top and bottom layers, 5 observations) and in the used bentonite (4 observations) genes of this genus is found in very low abundances.

- *Symbiobacter*: All bioreactors are shown to harbor *Symbiobacter*, with MA-A1.1 being observed with the highest abundance (up to 17.6%) of this genus, MA-A1.2 (up to 13.5%), MA-A1.3 (up to 17.1%) and MA-A1.4 (up to 15.4%). No consistent spatial preference could be observed. This Candidatus genus is reported as an uncultured member of the Comamonadaceae family. The only species described thrives within a phototrophic consortium (Liu et al., 2013). The origin of this genus seems to be the sand and the bentonite used for the sand-bentonite matrix.

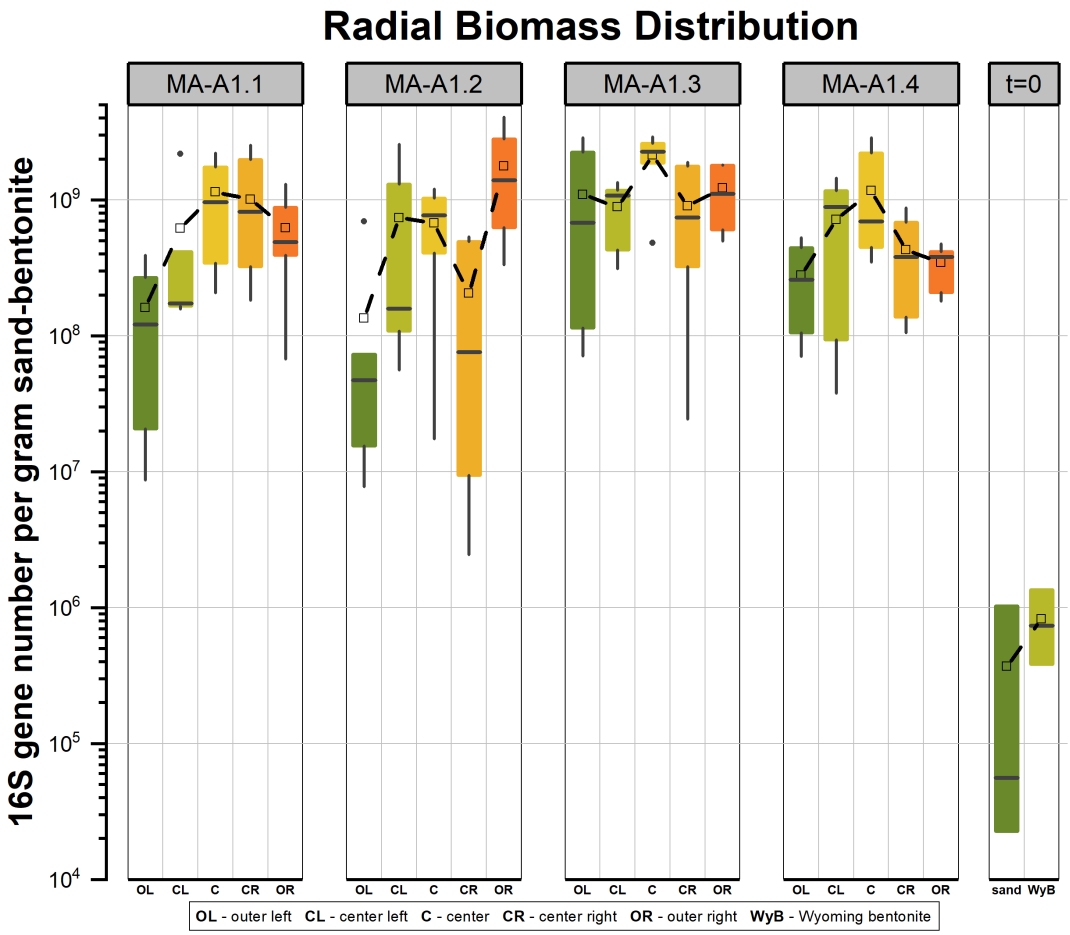

Figure 4.43 – Radial distribution of 16S rRNA gene copies per gram of substrate obtained from all bioreactors and the initial sand and bentonite used (t=0) as a function of the horizontal location of the vertical lane in the reactor. Boxplot features: 25th-75th percentile within boxes, whiskers represent 1.5 times the interquartile range (IQR), black line represents the median and the empty boxes the mean which is connected by a black dashed line, outliers are represented with black dots.

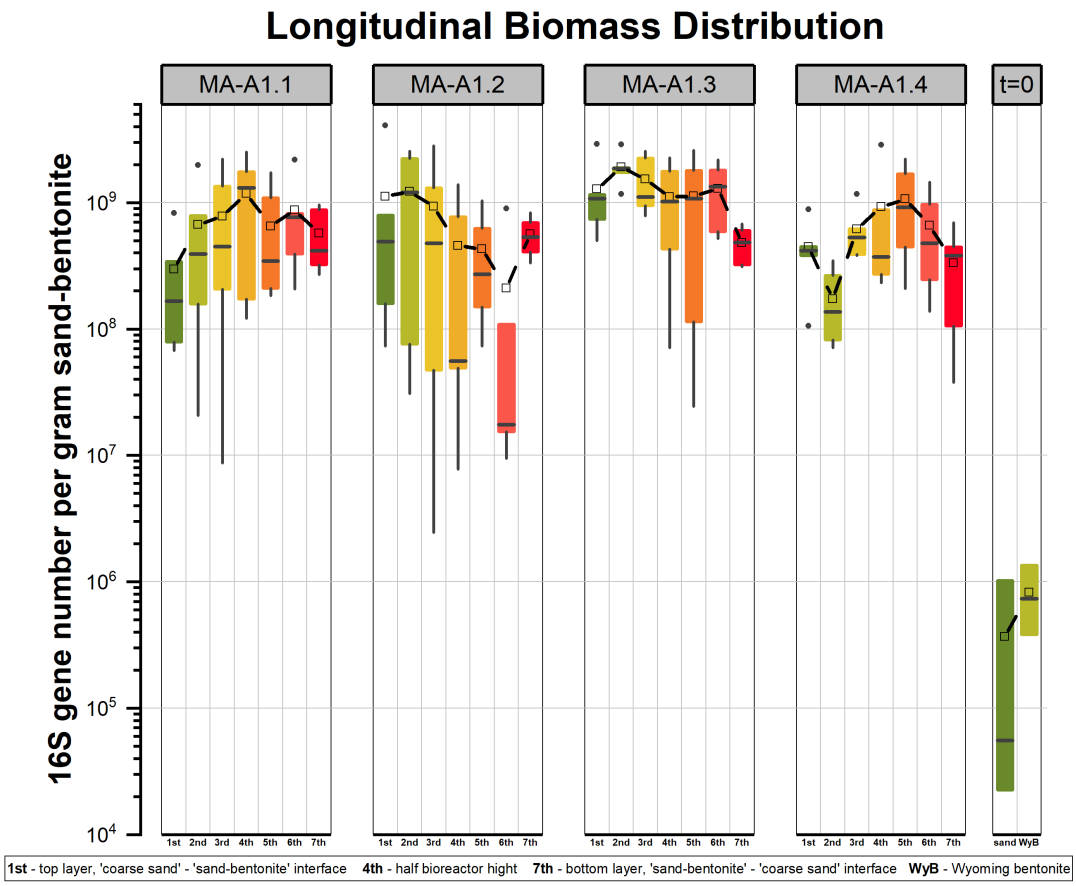

Figure 4.44 – Radial distribution of 16S rRNA gene copies per gram of substrate obtained from all bioreactors and the initial sand and bentonite used (t=0) as a function of the vertical location in the reactor. Boxplot features: 25th-75th percentile within boxes, whiskers represent 1.5 times the interquartile range (IQR), black line represents the median and the empty boxes the mean which is connected by a black dashed line, outliers are represented with black dots.

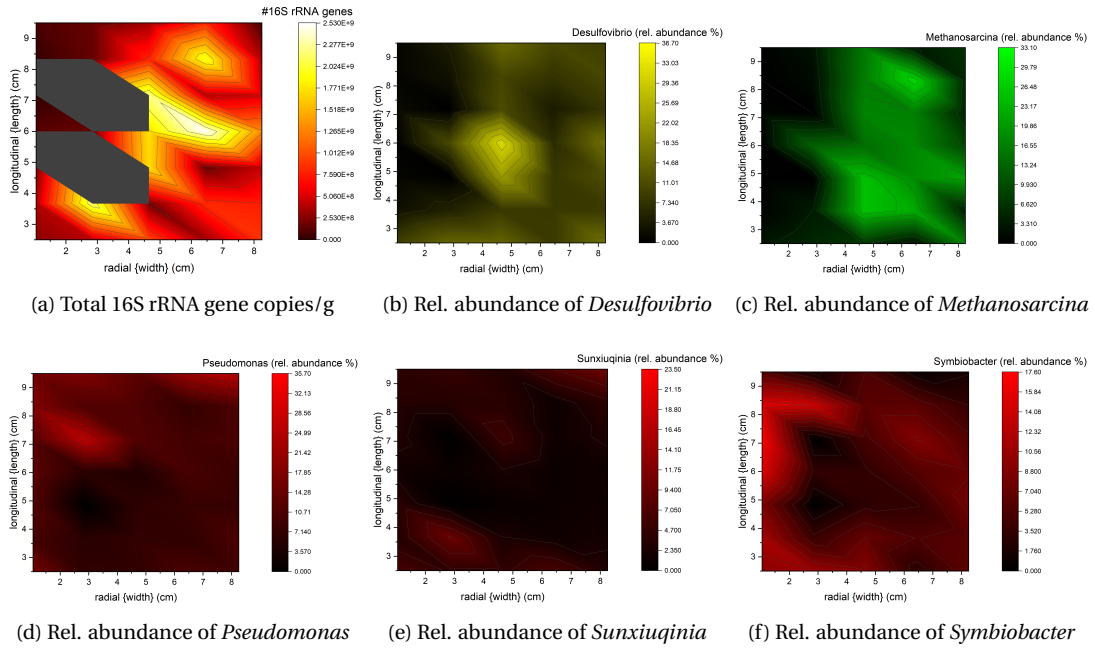

(a) Total 16S rRNA gene copies/g (b) Rel. abundance of *Desulfovibrio* (c) Rel. abundance of *Methanosarcina*

(d) Rel. abundance of *Pseudomonas* (e) Rel. abundance of *Sunxiuqinia* (f) Rel. abundance of *Symbiobacter*

Figure 4.45 – Spatial distribution of the top 5 OTU throughout the bioreactor MA-A1.1, in yellow a SRB, *Desulfovibrio*, in green a methanogenic archaea, *Methanosarcina* and in red, three (presumably) fermenting bacteria belonging to *Pseudomonas*, *Sunxiuqinia* and *Symbiobacter*.

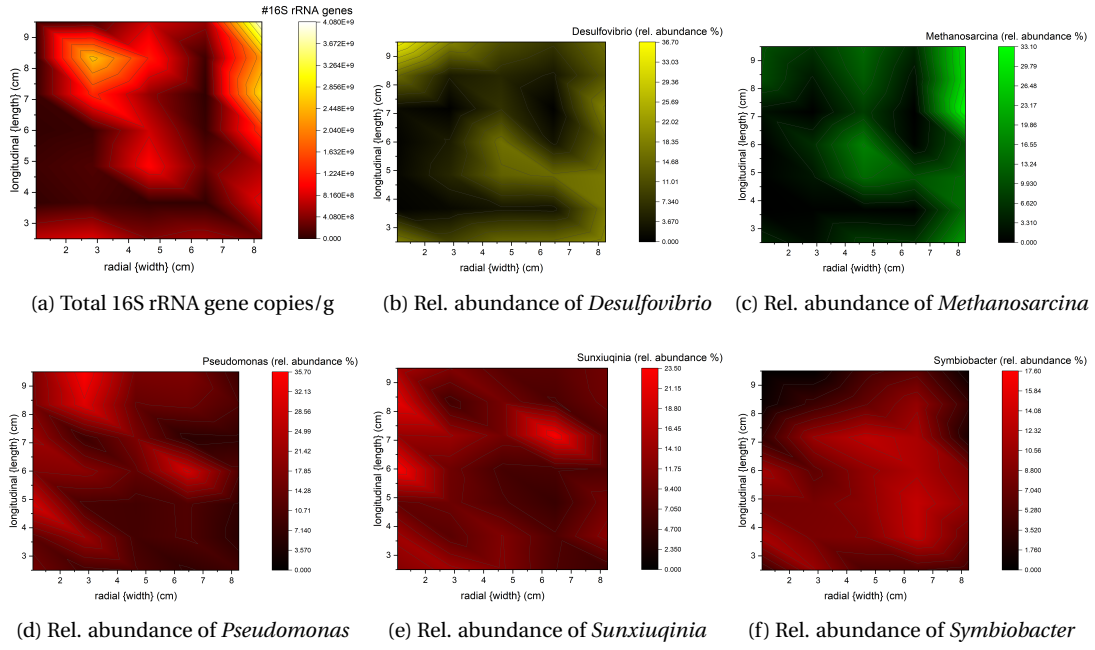

(a) Total 16S rRNA gene copies/g (b) Rel. abundance of *Desulfovibrio* (c) Rel. abundance of *Methanosarcina*

(d) Rel. abundance of *Pseudomonas* (e) Rel. abundance of *Sunxiuqinia* (f) Rel. abundance of *Symbiobacter*

Figure 4.46 – Spatial distribution of the top 5 OTU throughout the bioreactor MA-A1.2, in yellow a SRB, *Desulfovibrio*, in green a methanogenic archaea, *Methanosarcina* and in red, three (presumably) fermenting bacteria belonging to *Pseudomonas*, *Sunxiuqinia* and *Symbiobacter*.

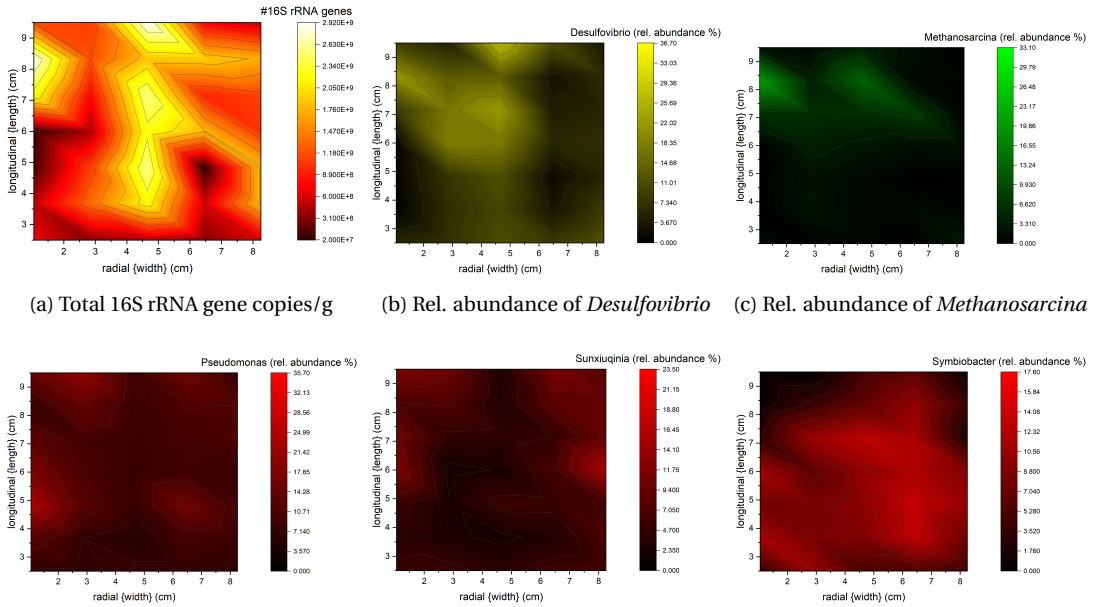

(a) Total 16S rRNA gene copies/g (b) Rel. abundance of *Desulfovibrio* (c) Rel. abundance of *Methanosarcina*

(d) Rel. abundance of *Pseudomonas* (e) Rel. abundance of *Sunxiuqinia* (f) Rel. abundance of *Symbiobacter*

Figure 4.47 – Spatial distribution of the top 5 OTU throughout the bioreactor MA-A1.3, in yellow a SRB, *Desulfovibrio*, in green a methanogenic archaea, *Methanosarcina* and in red, three (presumably) fermenting bacteria belonging to *Pseudomonas*, *Sunxiuqinia* and *Symbiobacter*.

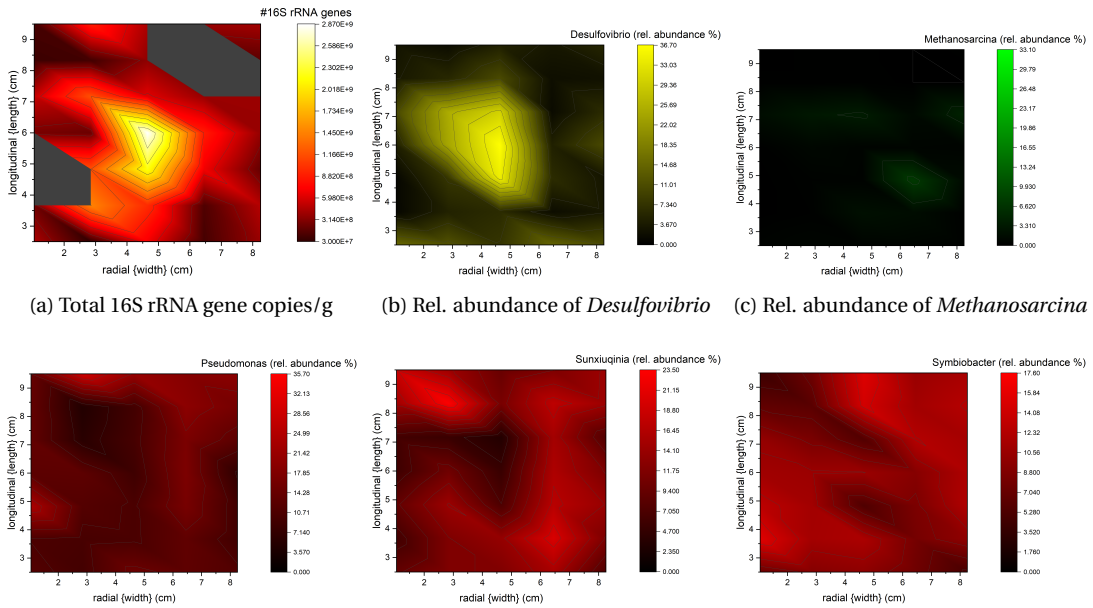

(a) Total 16S rRNA gene copies/g (b) Rel. abundance of *Desulfovibrio* (c) Rel. abundance of *Methanosarcina*

(d) Rel. abundance of *Pseudomonas* (e) Rel. abundance of *Sunxiuqinia* (f) Rel. abundance of *Symbiobacter*

Figure 4.48 – Spatial distribution of the top 5 OTU throughout the bioreactor MA-A1.4, in yellow a SRB, *Desulfovibrio*, in green a methanogenic archaea, *Methanosarcina* and in red, three (presumably) fermenting bacteria belonging to *Pseudomonas*, *Sunxiuqinia* and *Symbiobacter*.

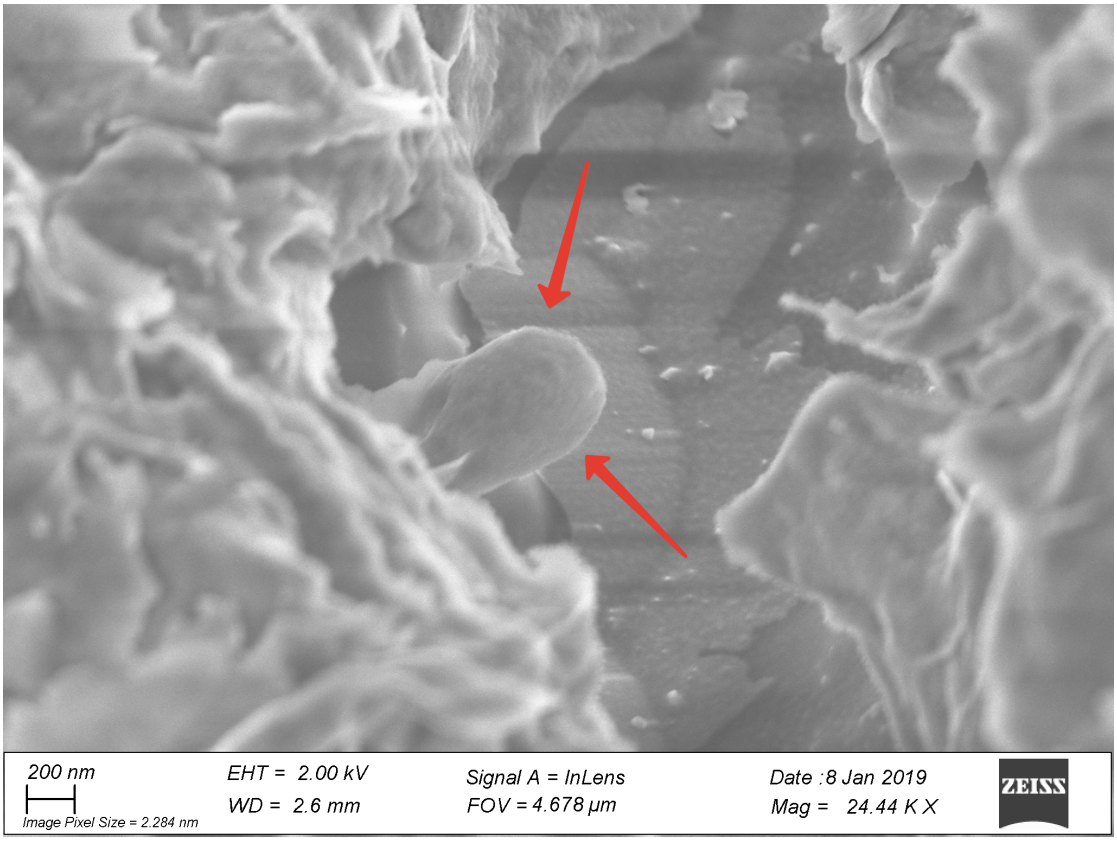

Figure 4.49 – Cryo-scanning electron microscopy of sand-bentonite close to the outlet of a hydrogen tube, obtained from a pre-test module with similar experimental conditions as for MA-A1.x. Red arrows indicate a bacterial cell found in a native, hydrated state within saturated bentonite.

4.3.10 Cryo-scanning electron microscopy imaging

Sand-bentonite obtained from a pre-test bioreactor module, similar to the MA-A1.x modules, was analyzed with cyro-scanning electron microscopy. The advantage of this technique is that due to the low operating temperatures (liquid nitrogen cooling), no sample preparation other than plunge-freezing is necessary. Small sample amounts freeze so fast, that the water remains in an amorphous state and ice crystals are not formed. Thus, the imaging enables the observation of native environments on the micro-scale. Figure 4.49 shows a rod-shaped bacterial cell in its native state, i.e., no desiccation or other imaging artefact can be observed. The cell appears to be associated with saturated bentonite.

4.4 Conclusion

4.4.1 Hydrogen-oxidizing biofilm in sand-bentonite matrix

The *in-situ* experiment presented here proves the ability of microorganisms to oxidize excess hydrogen within a repository-relevant context via sulfate reduction, Figure 4.15, and via methanogenesis, subsection 4.3.9. The main requirements for this microbial gas sink to play out its full potential are:

- Indigenous Opalinus Clay rock microorganisms and exogenous microorganisms from introduced materials
- A porous matrix as back-fill for the operational and service tunnels (the example presented here was a quartz sand - Wyoming bentonite matrix) that offers sufficient pore space for microorganisms to thrive and to develop as a hydrogen-oxidizing biofilm.
- Sulfate availability was identified as the main constraint for the hydrogen oxidation via sulfate reduction. Known sulfate sources are the Opalinus Clay rock porewater (dissolved sulfate), the Opalinus Clay rock (via the dissolution of gypsum ($CaSO_4$), celestine $SrSO_4$ and barite $BaSO_4$, see A9.4 in (Pearson et al., 2003)) and the gypsum ($CaSO_4$) fraction in Wyoming bentonite.

As was shown above, the microbial biofilm developed within 100 days primarily based on sulfate reduction and methanogenesis within both the sand-bentonite matrix as well as within the coarse sand layers at the top where high concentrations of hydrogen were available within a gas phase, subsection 4.3.9. Interestingly, the two bioreactors MA-A1.3 and 1.4, with conditions favorable to sulfate-reduction (due to a higher influx of sulfate-rich porewater, table 4.4 and figure 4.12) show nevertheless a considerable abundance of *Methanosarcina*. Local sulfate depletion while the hydrogen availability remains high is expected for a low- and intermediate-level repository. From the experiment it appears that there is no lag phase for the transition of the main metabolic regime from sulfate reduction to methanogenesis. Thus, microbial gas consumption will continue even in a low-sulfate environment, albeit less efficiently due to the production of CH_4. Because *Methanosarcina* appears to be indigenous to Opalinus Clay rock, it can be expected that this genus will colonise a prospective service gallery back-fill and produce methane once the anoxic corrosion produces enough hydrogen to reach the backfilled operational tunnels. This genus was so far not described for Opalinus Clay rock because it could not compete with the abundant sulfate-reducing bacteria and fermenters due to the high amounts of sulfate within the rock porewater and to the presence of recalcitrant organic matter electron donors. It appears that *Methanosarcina* is able to out-compete the other microorganisms once hydrogen, which is a readily available electron source, becomes abundant despite the presence of elevated sulfate concentrations.

The co-occurrence of sulfate reduction and methanogenesis did not allow the precise quantification of the rate of hydrogen oxidation for the SRB community. The rate of sulfate reduc-

tion observed was $R^{red}_{SO^{2-}_4} = 0.251\,\frac{\mu M}{day\,cm^3} \pm 0.024\,\frac{\mu M}{day\,cm^3}(SD)$ and thus the rate of hydrogen oxidation due to sulfate reduction (assuming H_2 is the sole electron donor) ranged from $R^{ox}_{H_2} = 1.004\,\frac{M}{day\,m^3}$ to $R^{ox}_{H_2} = 2.125\,\frac{M}{day\,m^3}$, as reported in subsection 4.3.3. This is likely a severe underestimate of the potential hydrogen oxidation rate of the system. One of the reasons for this underestimate is that H_2 consumption via methanogenesis was not considered in the calculation. Additionally, sampling the outflow provides a limited view of the processes in the porous medium. In particular, preferential flow paths associated with wall effects resulted in porewater only accessing a fraction of the pore space in the sand-bentonite matrix. Therefore, we conclude that the reported sulfate reduction rate is underestimated due to several experimental artefacts.

4.4.2 Iron sulfide, polysulfide and elemental sulfur formation

The observed reactions products of hydrogen sulfide within the bentonite phase of the sand-bentonite matrix confirm the assumption of iron-sulfide formation. The fate of sulfide produced by sulfate reduction was probed by X-ray based techniques which show that iron sulfide phases are produced. However, in addition, at the highest hydrogen sulfide load which is epitomized by bioreactor MA-A1.2, which received sulfide from the reactor placed in front of it, Figure 4.22, polysulfides and elemental sulfur were formed within the bentonite phase of the sand-bentonite matrix. This particular case corresponds to high hydrogen availability and the presence of elevated level of dissolved sulfide.

However, it remains unknown how polysulfides and elemental sulfur are formed. From the results presented in this work, no conclusive evidence is found for the postulated polysulfide formation from pyrite minerals, Equation 4.7 on page 143. Detailed XRF maps, Subsection 4.3.5, in particular Figures 4.22 and 4.23, show bright sulfur spots not localized with calcium nor iron and the initial observations from sulfur-XAS show that the most sulfur has reacted with iron but two out of thirteen sulfur-XAS were fitted with sulfur as the major chemical species, Table 4.6. Alternatively, polysulfide formation instead of elemental sulfur, Equation 4.5 on page 143, might happen directly through interaction of iron(III) from montmorillonite and sulfide, as proposed by Dr Paul Wersin of the University of Bern, Switzerland (personal communication). A detailed study of the reaction kinetics and the identification of the necessary conditions would be required.

Nevertheless, the observation of sulfur-species additional to iron sulfide phases can be viewed as a positive development in terms of a radioactive waste repository. This is because corrosive hydrogen sulfide species will be trapped within the engineered microbial gas sink, that is, the backfilled operational and service tunnels, rather than diffuse towards the metallic waste. An alternative explanation would be that sulfide- and sulfur-oxidizing microorganisms partly oxidize microbially-derived sulfide, generating a sulfur cycle within an aged operational backfill, potentially fueled by remaining H_2 from the anoxic waste degradation, by the methanogenic produced CH_4 and the accumulated biomass, similar to the observed sulfur-cycling in frac-

tured deep bedrock at Olkiluoto, Finland (Bell et al., 2020), but this would require a suitable electron acceptor to be present in an aged operational backfill.

Chapter 4 - Appendix

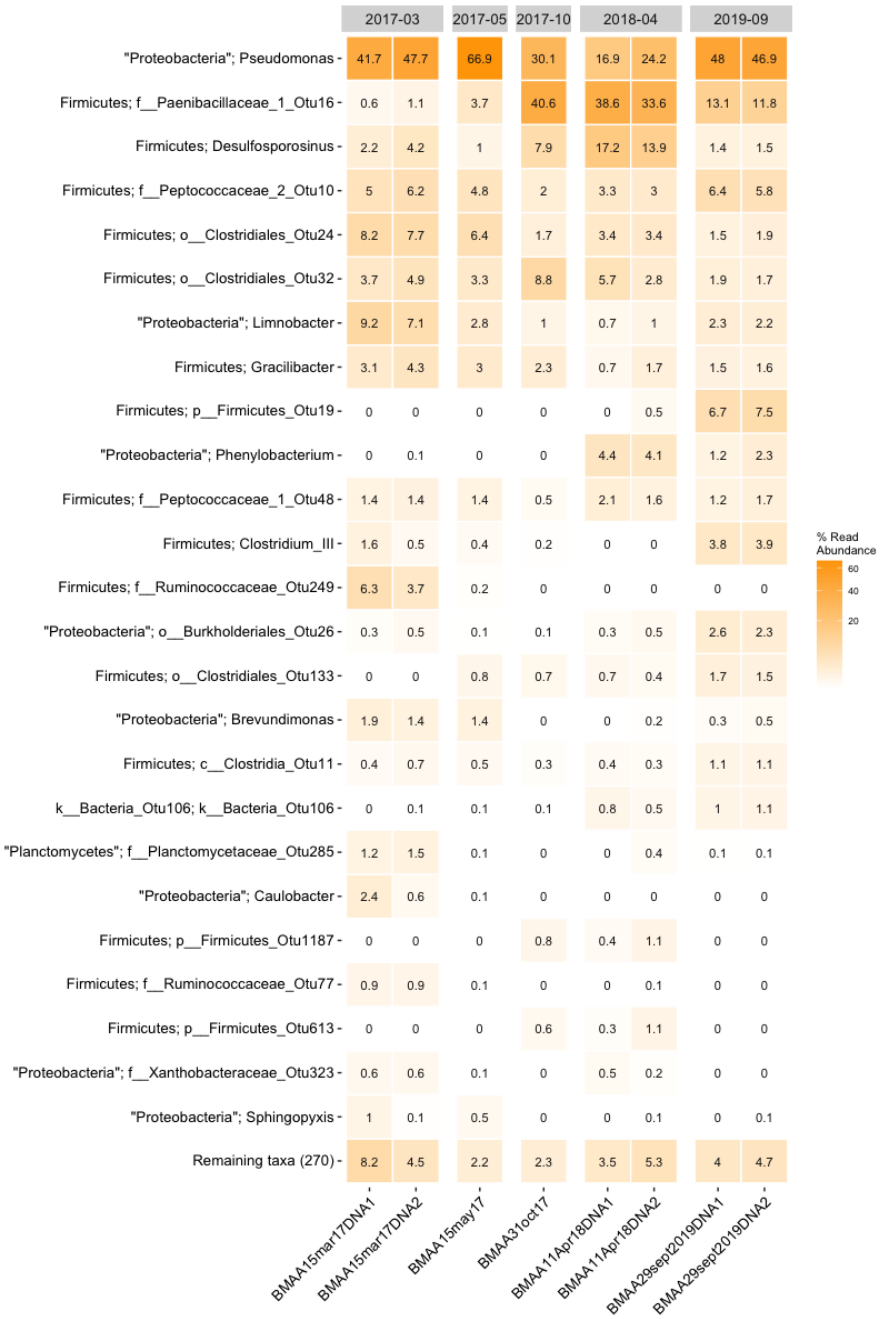

Figure 4.50 – Heatmap of 16S rRNA gene sequences obtained from filtered borehole porewater microorganisms within the borehole BMA-A1 that served as natural water source for the *in-situ* MA-A1.x experiment. Top 25 OTUs including unknown taxonomic affiliation on genus level are shown, 'remaining taxa' contains the taxa not in the top 25. Only genera with at least 0.1% relative abundance were considered.

```
LCF fit of MA_A_1_2_2_R1_MEXAS_004_001.txt as flattened mu(E)
from 7107.004395 to 7157.004395

Fit included 120 data points and 1 variables, and
approximately 37.528 measurements
Weights sum to 1: yes
Weights forced between 0 and 1: yes
Overall e0 shift used: no
Noise added to data: 0
R-factor = 0.0317006
Chi-square = 1.01502
Reduced chi-square = 0.0085296

.    standard              weight            e0
=========================================================
.   Goethite               0.053 (0.117)     0.000 (0.000)
.   Wy-Bentonite           0.947 (0.189)     0.000 (0.000)

.         sum ........... 1.000
```

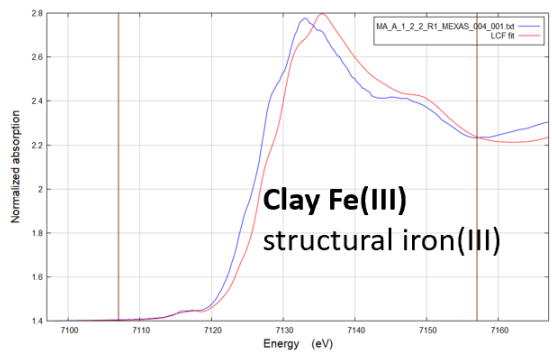

(a)

```
LCF fit of MA_A_1_4_5_R1b_MEXAS_014_001.txt as flattened
mu(E) from 7100.354492 to 7150.354492

Fit included 131 data points and 1 variables, and
approximately 37.528 measurements
Weights sum to 1: yes
Weights forced between 0 and 1: yes
Overall e0 shift used: no
Noise added to data: 0
R-factor = 0.0025062
Chi-square = 0.06214
Reduced chi-square = 0.0004743

.    standard              weight            e0
=========================================================
.   Mackinawite            0.623 (0.025)     0.000 (0.000)
.   Pyrite                 0.377 (0.138)     0.000 (0.000)

.         sum ........... 1.000
```

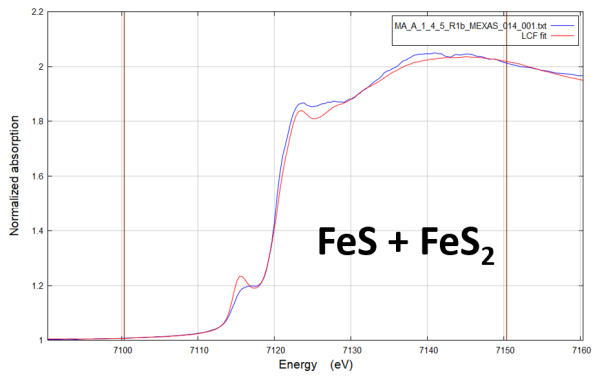

(b)

Figure 4.51 – Examples of linear combination fits of iron XAS. (a) Fe-XAS of MA-A1.2 bentonite-iron(III), (b) Fe-XAS of MA-A1.4 iron-sulfides.

```
LCF fit of 168127_maa13_POI_1_S_XANES_1.dat as flattened
mu(E) from 2460.9999 to 2500.9999

Fit included 79 data points and 1 variables, and
approximately 77.979 measurements
Weights sum to 1: yes
Weights forced between 0 and 1: yes
Overall e0 shift used: no
Noise added to data: 0
R-factor = 0.0137073
Chi-square = 0.19710
Reduced chi-square = 0.0024949

.    standard              weight            e0
=========================================================
.    Pyrite_Luca           0.653 (0.046)     0.000 (0.000)
.    FeS_Gosia             0.347 (0.017)     0.000 (0.000)

.          sum ........... 1.000
```

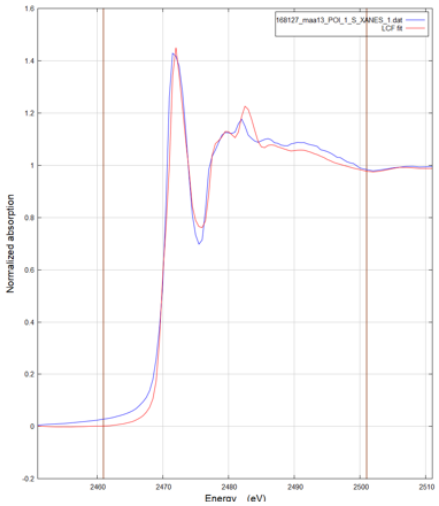

(a)

```
LCF fit of 168199_maa1nc_POI_4_S_XANES_1.dat as flattened
mu(E) from 2460.9999 to 2510.9999

Fit included 90 data points and 1 variables, and
approximately 97.474 measurements
Weights sum to 1: yes
Weights forced between 0 and 1: yes
Overall e0 shift used: no
Noise added to data: 0
R-factor = 0.1507906
Chi-square = 6.09907
Reduced chi-square = 0.0685289

.    standard              weight            e0
=========================================================
.    SO4                   0.852 (0.057)     0.000 (0.000)
.    WyBentonite           0.148 (0.077)     0.000 (0.000)

.          sum ........... 1.000
```

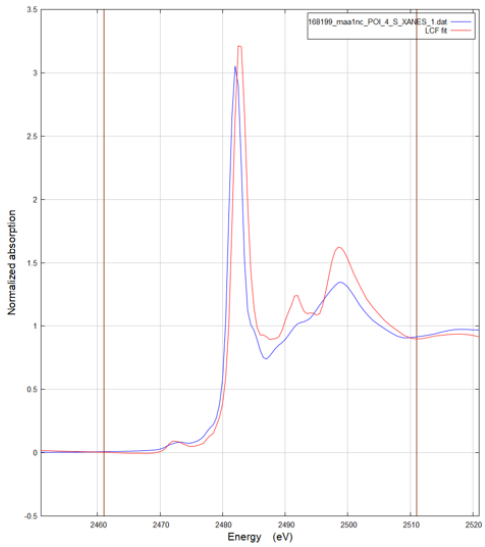

(b)

Figure 4.52 – Examples of linear combination fits of sulfur XAS. (a) S-XAS of MA-A1.3 iron-sulfides, (b) S-XAS of MA-A1.NC gypsum in bentonite.

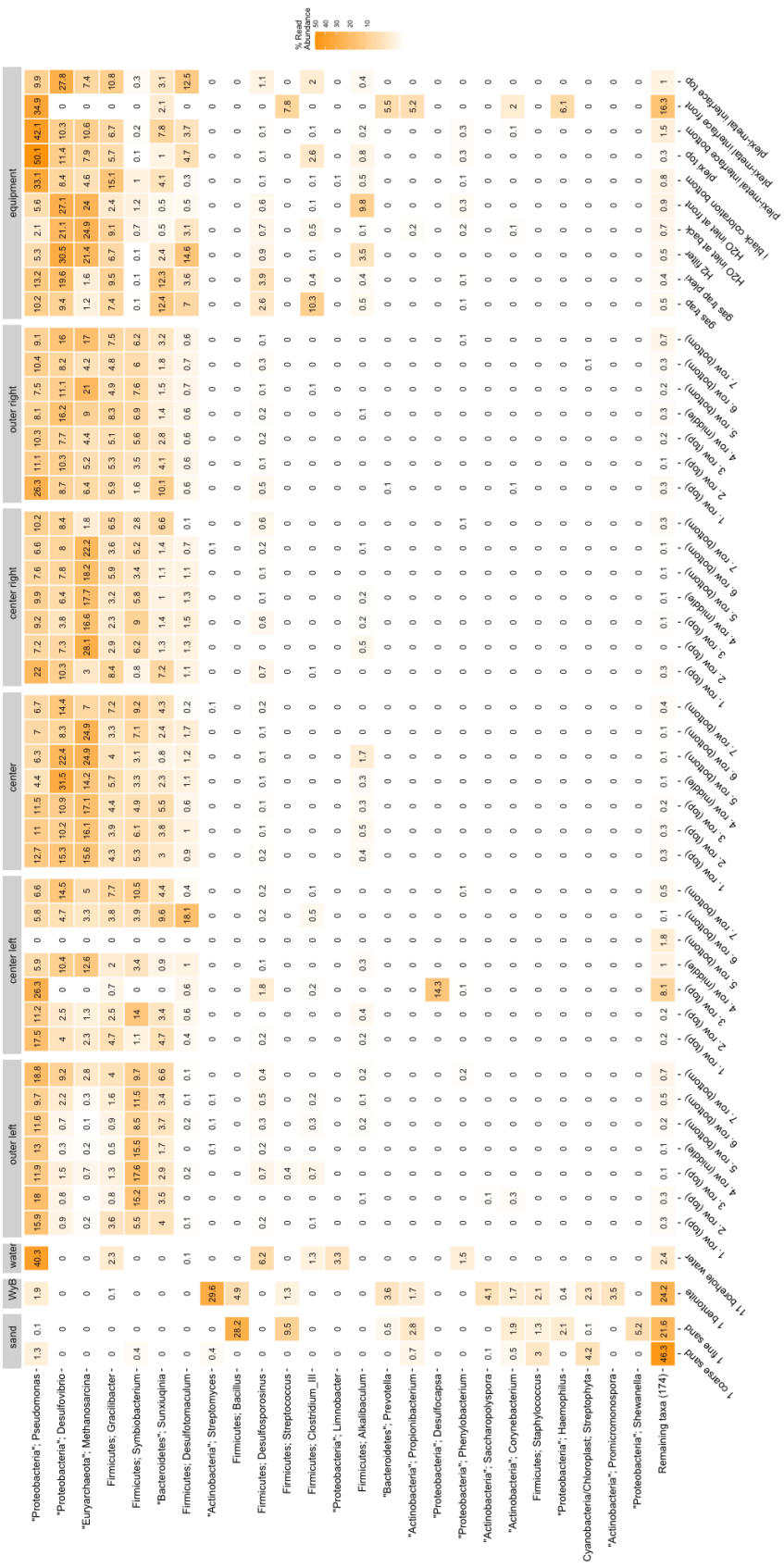

Figure 4.53 – Heatmap, based on 16S rRNA gene sequencing results, of known taxa for MA-A1.1. Top 25 OTUs are shown, remaining taxa combined in 'remaining taxa' and unknown taxonomic affiliations are excluded from the heatmap.

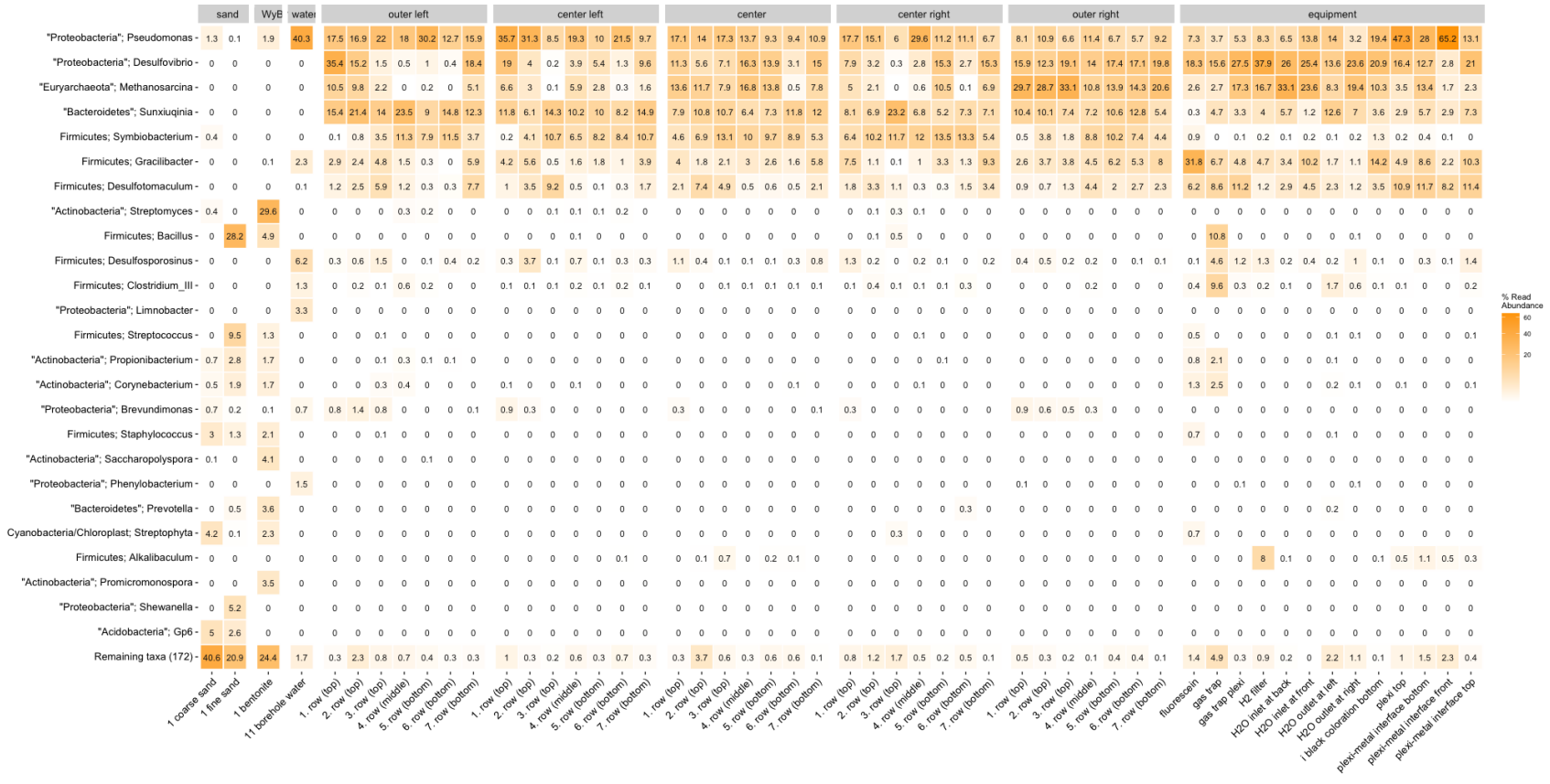

Figure 4.54 – Heatmap, based on 16S rRNA gene sequencing results, of known taxa for MA-A1.2. Top 25 OTUs are shown, remaining taxa combined in 'remaining taxa' and unknown taxonomic affiliations are excluded from the heatmap.

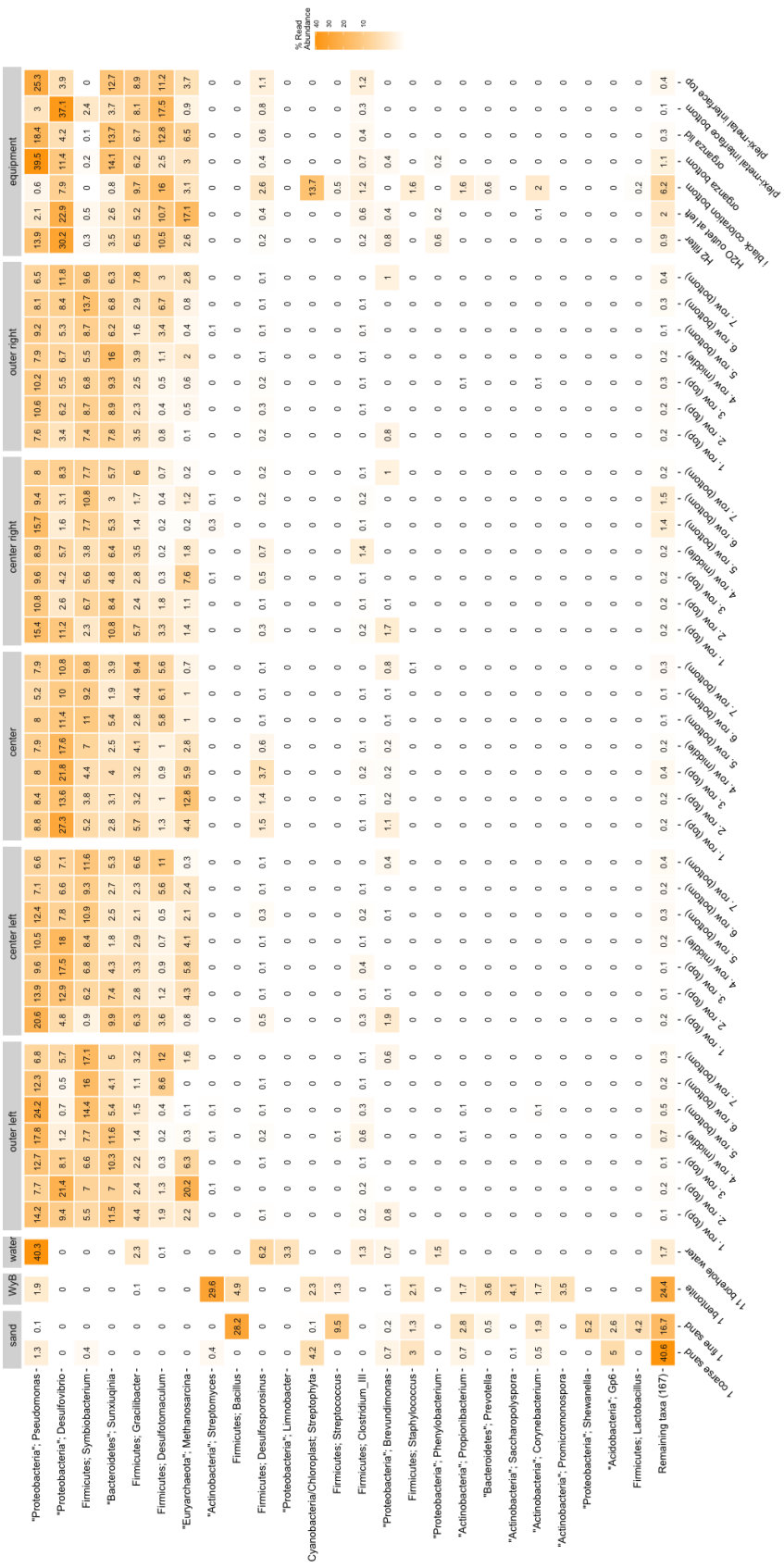

Figure 4.55 – Heatmap, based on 16S rRNA gene sequencing results, of known taxa for MA-A1.3. Top 25 OTUs are shown, remaining taxa combined in 'remaining taxa' and unknown taxonomic affiliations are excluded from the heatmap.

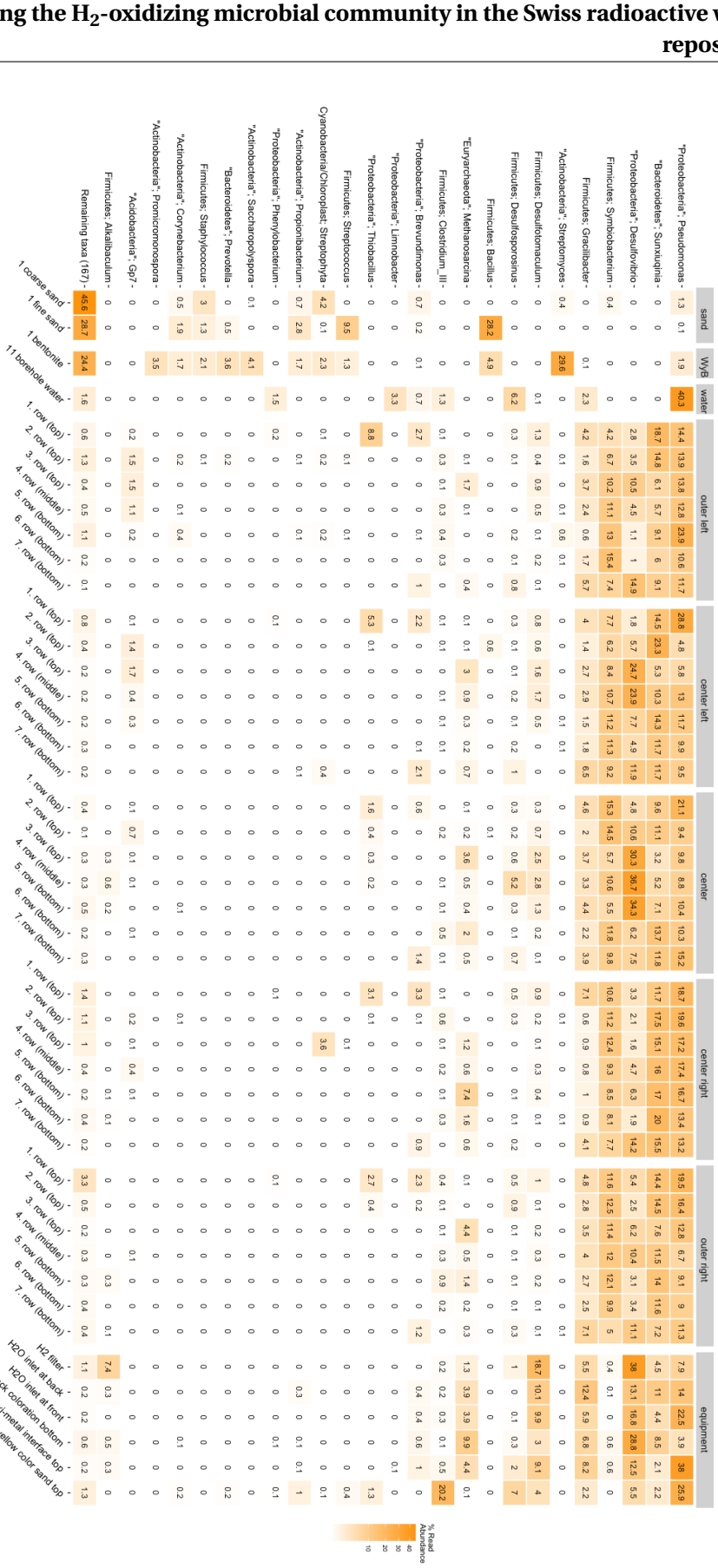

Figure 4.56 – Heatmap, based on 16S rRNA gene sequencing results, of known taxa for MA-A1.4. Top 25 OTUs are shown, remaining taxa combined in 'remaining taxa' and unknown taxonomic affiliations are excluded from the heatmap.

5 Conclusions

The timeline of the Swiss repository construction is presented to place this thesis into context of the practical application of the research performed. The main findings of the three projects are summarized and the remaining knowledge gaps outlined. Briefly, future research for the two experimental platforms used in this thesis is presented.

5.1 Conclusions

Decades of commercial nuclear fission, operated by both state and private actors, have left the following generations with the demanding task of safeguarding the biosphere for at least a hundred millennia to come. For Switzerland, which this thesis results concerns most, the final disposal planning is underway, with the following projected timeline (Nagra, 2020b):

- 2022: Scientific and technical site selection for a low- & intermediate-level and a spent fuel & high-level waste repository, or the selection of a combination-repository
- 2024: Submission of the general licence application (seeking construction approval)
- 2029: Federal Council decision, granting general licences for the construction of the repositories
- 2030: Approval of Federal Council decision by the Parliament
- 2031: National referendum, which is optional but very likely
- 2032 onward: Construction of the repositories and emplacement of radioactive waste, Figure 5.1a for low- and intermediate waste and Figure 5.1b for spent fuel and high-level waste.

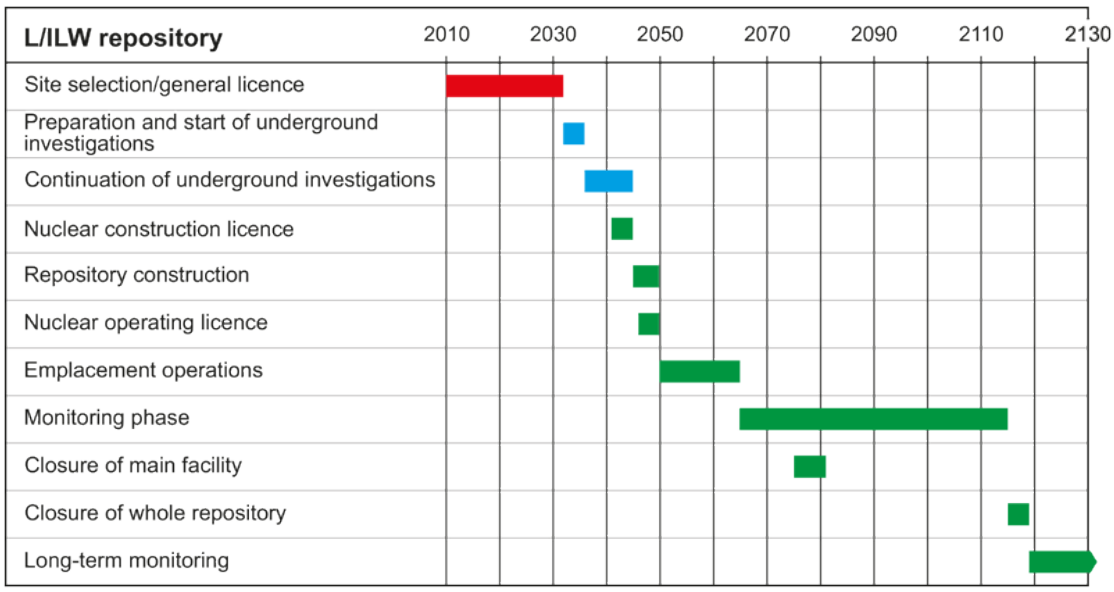

(a) Low- and intermediate-level waste repository timeline.

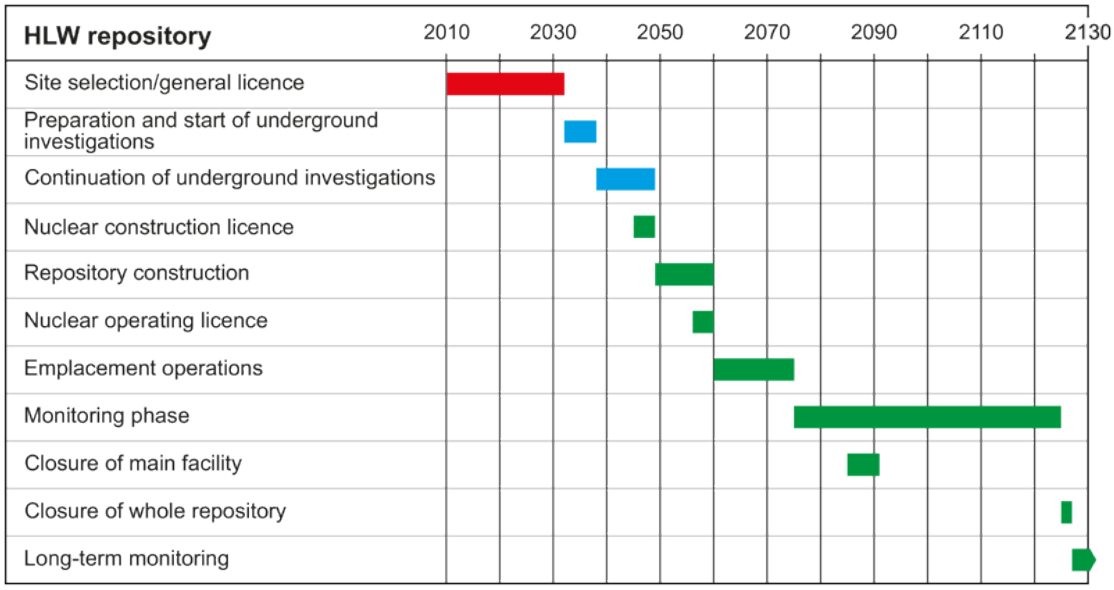

(b) Spent fuel and high-level waste repository timeline

Figure 5.1 – Expected timeline for the construction of a Swiss deep geological repository for the safe long-term storage of radioactive waste. Obtained from (Nagra, 2020b)

5.1.1 Spent fuel and high-level waste repository

The experimental work performed here shed light into the microbiome abundance and composition in Wyoming bentonite. It was not the first work on the microbiology of bentonite, but it is the first conducted under *in-situ* conditions within a porewater-filled borehole in Opalinus Clay rock. Therefore, it has practical relevance for the understanding and prediction

of the long-term repository evolution.

Chapter 2

The microbial characterization work performed alongside the *in-situ* corrosion assessment within the framework of the IC-A experiment resulted in the surprising observation of an aerobic heterotroph-dominated microbiome within bentonite. This aerobic-dominated microbiome appears to be growing in the initial time and, for the longest sampled time point (5.5-years), persistently viable. This observation was not expected for an anoxic environment. Anaerobic heterotrophs were found as well, but at lower numbers. A muted presence of sulfate-reducing bacteria was observed at very low viable numbers. Suppressing their activity is of outstanding importance due to their role in inducing corrosion of the spent fuel and high-level waste canisters. From our limited oxygen desorption tests of MX-80 Wyoming bentonite, it appears that trapped and adsorbed oxygen may be the reason for the observed microbiome composition and the inhibition of sulfate-reducing bacteria and other strict anaerobes. The growth and persistence of a bentonite microbiome through all tested dry-densities offers the possibility that any anomalies in the construction of the storage tunnels leading to a low-density bentonite back-fill, e.g., an undetected, jetcrete-concealed hollow space, may result in better conditions for microbial activity, although still on a very low level.

With the current experimental layout, it is questionable whether a true anoxic micro-environment will be reached within the bentonite filled modules. Our initial findings suggest that there is growth of facultative anaerobes and strict aerobes during the saturation of low-density bentonite (less than 1.55 g/cm^3) but not the growth of strict anaerobes and sulfate-reducing bacteria. On one hand, this can be viewed as a positive outcome because readily available electron donors are at least partially consumed during this initial growth. This means that this electron donors will not be available for anaerobic microorganisms such as sulfate-reducing bacteria once a reducing, anoxic bentonite micro-environment is establish. On the other hand, the observation of a longer-than-expected aerobic-dominated time leaves us with the experimental uncertainty about a delayed onset of sulfate-reducing bacteria, which may induce/enhance canister corrosion. The most favorable outcome would be that there is no pore space and no accessible nutrients left for the low number of viable sulfate-reducing bacteria we found, to thrive off of.

Chapter 3

Deciphering the sources of microbial activity in bentonite turned out to be an experimentally over-ambitious undertaking. In the experiment presented here, we aimed to observe the colonization and impact of microorganisms from the two different sources:

- i) A culture containing Wyoming bentonite-derived anaerobic, sulfate-reducing bacteria seeded into sterile Wyoming bentonite at a high cell density.

- ii) The anaerobic community of the Opalinus Clay rock porewater, potentially colonising the sterile Wyoming bentonite.

One of the prepared modules was designed to serve as an abiotic control, excluding both pools of microorganisms and allowing only the exchange of chemical substances with the surrounding borehole porewater. The borehole water was expected to effectively serve as an analogue to an active microbial population in the excavation disturbed zone, Figure 1.2 on page 7, interfacing with a bentonite back-fill, Figure 1.4 on page 11. This setup would have been used to evaluate the diffusive migration of dissolved hydrogen sulfide. This is for example the case when the pool of reactive iron(II) in Opalinus Clay rock (Boylan et al., 2019), is consumed but sulfate and hydrogen is still available. The diffusive migration of dissolved HS^- into a saturated Wyoming bentonite can be observed with the current system as well. However, the system also included microorganisms impacting the porewater chemistry at the bentonite cylinder surface because of their colonization of this surface, as described in Chapter 2 and 3.

However, the implemented membrane system and the addition of rubber o-rings to the top and bottom lids and screws holding them were not suitable for the high pressure applied to the borehole to maintain anoxic conditions (10 bar overpressure applied as argon gas phase on top of the porewater column equals a water depth of 100 meters).

Despite these shortcomings we were able to show two important outcomes for the repository safety:

- i) Wyoming bentonite inherently precludes the activity of sulfate-reducing bacteria during the saturation phase. This is critical for microbial growth because that is when significant microbial growth is observed. Presumably, it is because the pore space is large enough and the water activity high enough for microbial activity, Chapter 2.
- ii) The inability of the Opalinus Clay porewater microbiome to colonize 1.45 g/cm^3 (dry-density) Wyoming bentonite despite the absence of the indigenous microbiome.

However, for lower dry-densities, certain microorganisms of the Opalinus clay porewater could colonize the bentonite. As this was an experimental artefact (at the top and bottom lids), due to the usage of too short sintered steel filters, no confident conclusions can be drawn from this observation and a dedicated experiment would be necessary (see below).

5.1.2 Low- and intermediate-level waste repository

The research performed in this thesis can prove useful to decrease the uncertainty related the repository gas-balance, which is govern by gas-evolution rates due waste degradation and anoxic corrosion and gas-consumption rates due to geochemical reactions and, as shown in Chapter 4, biological activity.

Chapter 4

The experimental work performed prove the formation of a hydrogen-oxidizing biofilm within a prospective backfilled operational tunnel, using a porous sand-bentonite matrix (80/20% w/w), Opalinus Clay rock porewater and hydrogen gas. It is noteworthy that the observed biofilm has not fully grown after 102 days of hydrogen gas injection and porewater flow. However, already during these 102 days, we observed the transition from a metabolic regime dominated by sulfate-reduction to methanogenesis. Also for shorter experimental time frames (73 and 78 days) and higher availability of sulfate-rich porewater we observed co-occurring methanogenesis.

For the expected time-frames of high gas-evolution rate of up to 1,000 years after emplacement, the hydrogen-oxidation capacity observed for our experimental bioreactor modules appears suitable, as it is estimated between:

$$R_{H_2}^{ox} = 1.004 \frac{M}{day\, m^3}$$

and

$$R_{H_2}^{ox} = 2.125 \frac{M}{day\, m^3}$$

However, this can only be maintained as long as there is plentiful sulfate available for sulfate-reduction. The depletion of dissolved sulfate in the porewater is expected and the dissolution of sulfate-containing mineral phases in Opalinus Clay rock and Wyoming bentonite (if chosen as back-fill component) are also representing only a limited pool of sulfate. Therefore, we can conclude that initially, a biofilm dominated by sulfate-reducing bacteria will be able to consume all hydrogen evolving from the storage caverns of a low- and intermediate-level waste repository as long as there is enough sulfate available. The hydrogen-oxidation rate of a biofilm dominated by methanogens however needs to be determined to be able to calculate the gas-balance for the time when sulfate is diffusion-limited and finally depleted within the porous backfilled, operational tunnels.

The feasibility of a microbial gas sink can be proven with knowledge of the hydrogen-oxidation capacity of a biofilm that has fully transitioned from sulfate-reduction to a sulfate-depleted, methanogens dominated microbiome. Evaluating a hydrogen-mass balance of such a biofilm will allow to pin-point the hydrogen-gas consumption rate, applicable for the long term. The evolution of methane will still result in a net-decrease of overall gas pressure within the repository. Confirmation of the feasibility can be sought in updated gas-balance calculations similar as performed previously (O. Leupin et al., 2016). The realization of an adequately sized pore space with a tested back-fill material can then fulfil its design purpose, a gas sink, over the entire safety assessment period (i.e., 100,000 years). Based on the performed experiment, a quartz sand - Wyoming bentonite matrix appears suitable, but the exact mixture of the two components would need to be tailored according to the repository site selected. For the

biofilms, a interconnected porosity is the main factor as it allows access to nutrients and space for growth.

An assessment of the hydrogen-oxidation performance of other back-fill materials would be necessary if for example a backfill with crushed Opalinus Clay rock or Friedland Clay and quartz sand mixtures is considered over Wyoming bentonite (O. Leupin et al., 2016). Addition of gypsum could also be explored to prolong the times sulfate-reduction is active if it turns out that methanogenesis is not active (when using alternative back-fill materials) or proven too slow to influence the long-term gas balance. The modular MA-A experimental platform can be used for such tests, similar to the study performed and presented in Chapter 4.

5.2 Future research

5.2.1 IC-A experiment

Within the framework of the IC-A experiment (Chapter 2 and 3) the four follow-up experiments are proposed to tackle the outlined knowledge gaps:

1. Adsorbed oxygen removal prior to module assembly. A set of modules with 1.45 g/cm^3 MX-80 bentonite, deployed for 1-year. One module could be prepared similar to the first set of powder-pellet modules (M1, M4) in a completely oxic environment with no pretreatment of the bentonite (use as-delivered). Another module, however, should receive bentonite from exactly the same batch but allowed to degas the adsorbed oxygen within at least 100 days, similar to the (unintentionally) degassing of bentonite reported (Maanoja et al., 2020). Complete degassing could be confirmed by sealing 300 grams of degassed bentonite within gas-tight bottles for at least 10 days with subsequent analysis of the gas-phase in these bottles, similar to the reported approach in Chapter 2. For the degassed bentonite, one would expect a decrease in the contribution of aerobic heterotrophs and, consequently, a lower total heterotrophic viable community. A comparison between the cultivable microorganisms of the two bentonite treatments should prove a stark decrease of strict aerobes and a higher proportion of strict anaerobes among the cultivable anaerobic heterotrophs.

2. An analysis missing in the presented data in Chapter 2 is the identification of the cultivable microorganisms based on their 16S rRNA gene amplification. Only small fractions of the microbiome can be cultured, however the knowledge of which genera of aerobes, anaerobes and sulfate-reducing bacteria were cultivated would prove useful for the interpretation of 16S rRNA gene sequencing data from obtained bentonite samples. It also would underscore that the observed changes in relative abundances upon bentonite saturation are indeed related to microbial growth and not signatures of relic/adsorbed DNA.

3. Modules with sterile bentonite of 1.45 g/cm^3 dry-density, as presented in Chapter 3, but

without the membrane addition, could be prepared with a spike of aerobic heterotrophs, sourced in the non-sterile Wyoming bentonite. Growth of this spike community throughout the sterile bentonite during the saturation phase is expected. This would confirm the presence of bioavailable oxygen and uphold the conclusion of an oxygen-dependent sulfate-reducing bacteria inhibition during bentonite saturation.

4. Finally, a dedicated test of the inability of the Opalinus Clay porewater community to colonize sterile bentonite should be preformed by saturating the sterile bentonite modules with natural Opalinus Clay rock porewater. This would entail no presaturation in sterile, anoxic artificially porewater as was performed in Chapter 3. It may turn out that a certain opportunistic microorganisms are able to migrate with the porewater-front inside the bentonite. Additionally, a set of lower (1.25 g/cm^3) and higher (1.55g/cm^3) dry-density modules with sterile bentonite could be prepared to establish the threshold of colonization during saturation.

5.2.2 MA-A experiment

Hydrogen-oxidation rate of an aged biofilm in sand-bentonite Using the existing four bioreactor modules, an experiment simulating an aged sand-bentonite back-fill can be performed to determine the hydrogen-oxidation rate under increasing scarcity of sulfate. Precondition for such a test is a proven gas-phase sampling and gas-phase analysis with minor hydrogen-losses such that a hydrogen gas-balance can be established. As a set-up, a series of four bioreactors connected to each other is proposed. Doing so, only the first bioreactor receives Opalinus Clay rock porewater from BMA-A1 while the subsequent bioreactors receive the outflow from the respective bioreactor before. This will create a steep sulfate decrease across the four bioreactors, while hydrogen is applied to all four equally. While the first two are hypothesised to consume hydrogen efficiently via sulfate-reduction and methanogenesis, the other two are hypothesized to consume hydrogen mainly via methanogenesis. Additionally, by using a serial setup, the water flow-rate is equal for all bioreactors.

Hydrogen-oxidation rate of an aged biofilm in alternative backfill matrices The above mentioned setup and the performed biofilm characterizations as presented in Chapter 4, could also serve as a framework for the testing of alternative back-fill materials such as a quartz sand and crushed Opalinus Clay rock, or Friedland clay (O. Leupin et al., 2016).

Suggested bioreactor modifications Access to sample the pore space: Ceramic soil-rhizon samplers may offer a solution to mitigate the encountered problem of sampling only the easily accessible pore space. The insertion of ceramic soil-rhizon samplers enable the sampling of small volumes of the sand-bentonite matrix directly, but their placement into the used stainless-steel cylinder (2 cm thick walls) may prove difficult. Alternatively, ceramic soil-rhizon samplers could be a connected directly to the two efflux tubes at the top, Figure 4.6,

page 123, rending the flow-through pattern of the system when used as the only efflux path, but enabling the access to the sand-bentonite pore space. Such a modification would also lessen the amount of dark precipitates observed within the efflux lines during the experiment. We suspect that precipitates from the bioreactors but also salt-crystallization processes during the efflux residence times within the lines after the bioreactor, were responsible for the blockage of one of the Bronkhorst pressure controllers during the experiment. This resulted in the loss of the capacity to record the efflux chemistry evolution in real-time. Apart from the flow-sensors, none of the probes/sensors of the sensor array, Figure 4.5, page 122, could be used during the experiment reported in Chapter 4.

Redesign of the gastrap: The gas-trap in its current design, Figure 4.7, page 124, does not capture the gas-phase properly. During the course of the experiment, gas bubbles were observed to escape through the efflux water lines because there was no system implemented to capture the gases efficiently. Therefore, a quantification of the gas-phase composition could not be performed. Because of the relative high diffusivity of hydrogen in many substances we chose to manufacture most bioreactor parts out of stainless-steel, using a poly(ether ether ketone) (PEEK) sampling valve to be able to sample the gas-phase. However, due to that it was hard to evaluate the existence of a gas phase. Therefore, only when a gas-phase was present in the gas-trap, it could only indirectly be observed after the sampling, based on the pressure increase within the sample glass bottle. Any gas-bubbles at other parts of the bioreactor top-lid were not captured. Thus, a major improvement for the hydrogen-oxidation rate estimation would be an improved gas trap design, possibly by manufacturing a new gas-trap which also acts as water-efflux path instead of the two lines in the current layout (which could instead be used for a sand-bentonite matrix sampling as described above). Alternatively, the complete lid could be redesigned in terms of a flat dome with the gastrap-sampler right at the top of that dome.

Capturing the gas-phase daily, just before the injection of new hydrogen, would enable to establish a combined hydrogen-oxidation rate based on the mass-balance of hydrogen-gas injected and consumed via sulfate-reduction and methanogenesis, and account for losses and/or other hydrogen-oxidation processes. Using a similar experimental setup as presented here, the rate of methanogenesis could be estimated as well. This is of importance for the longer-term prediction of a low-level waste repository when the sulfate pool is depleted but hydrogen is still evolving from the anoxic corrosion processes.

Porewater flow sensors and pressure controllers: Suggestions for further iterations of this experiment include the placement of flow-sensors at the influx of each bioreactor, and the usage of new Swagelok-filters with adequate capacity for precipitates before each of the two Bronkhorst pressure controllers for every new experiment.

Bibliography

Andersen, K. S., Kirkegaard, R. H., Karst, S. M., & Albertsen, M. (2018). Ampvis2: an R package to analyse and visualise 16S rRNA amplicon data [Publisher: Cold Spring Harbor Laboratory Section: New Results]. *bioRxiv*, 299537. https://doi.org/10.1101/299537

Apprill, A., McNally, S., Parsons, R., & Weber, L. (2015). Minor revision to V4 region SSU rRNA 806R gene primer greatly increases detection of SAR11 bacterioplankton. *Aquatic Microbial Ecology*, *75*(2), 129–137. https://doi.org/10.3354/ame01753

Bagnoud, A. (2015). *Microbial metabolism in the deep subsurface* (Ph.D.). Ecole Polytechnique Federal de Lausanne EPFL. Retrieved March 22, 2017, from https://infoscience.epfl.ch/record/210436

Bagnoud, A., Chourey, K., Hettich, R. L., de Bruijn, I., Andersson, A. F., Leupin, O. X., Schwyn, B., & Bernier-Latmani, R. (2016). Reconstructing a hydrogen-driven microbial metabolic network in Opalinus Clay rock. *Nature Communications*, *7*. https://doi.org/10.1038/ncomms12770

Bagnoud, A., de Bruijn, I., Andersson, A. F., Diomidis, N., Leupin, O. X., Schwyn, B., & Bernier-Latmani, R. (2016). A minimalistic microbial food web in an excavated deep subsurface clay rock. *FEMS Microbiology Ecology*, *92*(1). https://doi.org/10.1093/femsec/fiv138

Bagnoud, A., Leupin, O., Schwyn, B., & Bernier-Latmani, R. (2016). Rates of microbial hydrogen oxidation and sulfate reduction in Opalinus Clay rock. *Applied Geochemistry*, *72*, 42–50. https://doi.org/10.1016/j.apgeochem.2016.06.011

Bar-On, Y. M., Phillips, R., & Milo, R. (2018). The biomass distribution on Earth. *Proceedings of the National Academy of Sciences of the United States of America*, *115*(25), 6506–6511. https://doi.org/10.1073/pnas.1711842115

Barr, N. F., & Allen, A. O. (1959). Hydrogen Atoms in the Radiolysis of Water. *The Journal of Physical Chemistry*, *63*(6), 928–931. https://doi.org/10.1021/j150576a037

Basham, M., Filik, J., Wharmby, M. T., Chang, P. C. Y., El Kassaby, B., Gerring, M., Aishima, J., Levik, K., Pulford, B. C. A., Sikharulidze, I., Sneddon, D., Webber, M., Dhesi, S. S., Maccherozzi, F., Svensson, O., Brockhauser, S., Náray, G., & Ashton, A. W. (2015). Data Analysis WorkbeNch (DAWN) [Number: 3 Publisher: International Union of Crystallography]. *Journal of Synchrotron Radiation*, *22*(3), 853–858. https://doi.org/10.1107/S1600577515002283

Bell, E. (2016). *Heat resistant thermophilic endospores in cold estuarine sediments* (Ph.D.). Newcastle University. Retrieved April 18, 2017, from http://hdl.handle.net/10443/3207

Bell, E., Lamminmäki, T., Alneberg, J., Andersson, A. F., Qian, C., Xiong, W., Hettich, R. L., Balmer, L., Frutschi, M., Sommer, G., & Bernier-Latmani, R. (2018). Biogeochemical Cycling by a Low-Diversity Microbial Community in Deep Groundwater [Publisher: Frontiers]. *Frontiers in Microbiology*, *9*. https://doi.org/10.3389/fmicb.2018.02129

Bell, E., Lamminmäki, T., Alneberg, J., Andersson, A. F., Qian, C., Xiong, W., Hettich, R. L., Frutschi, M., & Bernier-Latmani, R. (2020). Active sulfur cycling in the terrestrial deep subsurface [Number: 5 Publisher: Nature Publishing Group]. *The ISME Journal*, *14*(5), 1260–1272. https://doi.org/10.1038/s41396-020-0602-x

Bleyen, N., Smets, S., Small, J., Moors, H., Leys, N., Albrecht, A., Cannière, P. D., Schwyn, B., Wittebroodt, C., & Valcke, E. (2017). Impact of the electron donor on in situ microbial nitrate reduction in Opalinus Clay: results from the Mont Terri rock laboratory (Switzerland). *Swiss Journal of Geosciences*, 1–20. https://doi.org/10.1007/s00015-016-0256-x

Bossart, P., Meier, P. M., Moeri, A., Trick, T., & Mayor, J.-C. (2002). Geological and hydraulic characterisation of the excavation disturbed zone in the Opalinus Clay of the Mont Terri Rock Laboratory. *Engineering Geology*, *66*(1), 19–38. https://doi.org/10.1016/S0013-7952(01)00140-5

Boylan, A. A., Perez-Mon, C., Guillard, L., Burzan, N., Loreggian, L., Maisch, M., Kappler, A., Byrne, J. M., & Bernier-Latmani, R. (2019). H2-fuelled microbial metabolism in Opalinus Clay. *Applied Clay Science*, *174*, 69–76. https://doi.org/10.1016/j.clay.2019.03.020

Brankatschk, R., Bodenhausen, N., Zeyer, J., & Bürgmann, H. (2012). Simple Absolute Quantification Method Correcting for Quantitative PCR Efficiency Variations for Microbial Community Samples. *Applied and Environmental Microbiology*, *78*(12), 4481–4489. https://doi.org/10.1128/AEM.07878-11

Burzan, N., Frutschi, M., Rance, A., Reddy, B., Smart, N., Diomidis, N., & Bernier-Latmani, R. (2018). IC-A Experiment - in situ Iron Corrosion in Bentonite, Mont Terri Underground Research Laboratory: Microbial Analysis of Phase 2.

Burzan, N., Murad Lima, R., Frutschi, M., Diomidis, N., Janowczyk, A., & Bernier-Latmani, R. (2020). Temporal evolution of the microbial community associated with Wyoming bentonite MX-80 saturated with Opalinus clay rock porewater in situ. EPFL/NAGRA.

Canfield, D. E. (1989). Reactive iron in marine sediments. *Geochimica et Cosmochimica Acta*, *53*(3), 619–632. https://doi.org/10.1016/0016-7037(89)90005-7

Caporaso, J. G., Kuczynski, J., Stombaugh, J., Bittinger, K., Bushman, F. D., Costello, E. K., Fierer, N., Peña, A. G., Goodrich, J. K., Gordon, J. I., Huttley, G. A., Kelley, S. T., Knights, D., Koenig, J. E., Ley, R. E., Lozupone, C. A., McDonald, D., Muegge, B. D., Pirrung, M., ... Knight, R. (2010). QIIME allows analysis of high-throughput community sequencing data. *Nature Methods*, *7*(5), 335–336. https://doi.org/10.1038/nmeth.f.303

Černoušek, T., Shrestha, R., Kovářová, H., Špánek, R., Ševců, A., Sihelská, K., Kokinda, J., Stoulil, J., & Steinová, J. (2020). Microbially influenced corrosion of carbon steel in the presence of anaerobic sulphate-reducing bacteria [Publisher: Taylor & Francis _eprint: https://doi.org/10.1080/1478422X.2019.1700642]. *Corrosion Engineering, Science and Technology*, *55*(2), 127–137. https://doi.org/10.1080/1478422X.2019.1700642

Chang, D.-H., Lee, J.-B., Lee, G.-H., Rhee, M.-S., Lee, H., Bae, K. S., Park, D.-S., & Kim, B.-C. (2013). Sunxiuqinia dokdonensis sp. nov., isolated from deep sub-seafloor sediment. *Journal of Microbiology*, *51*(6), 741–746. https://doi.org/10.1007/s12275-013-3492-z

Chen, L., Larson, S. L., Ballard, J. H., Ma, Y., Zhang, Q., Li, J., Wu, L., Arslan, Z., & Han, F. X. (2019). Laboratory spiking process of soil with various uranium and other heavy metals. *MethodsX*, *6*, 734–739. https://doi.org/10.1016/j.mex.2019.03.026

Cline, J. D. (1969). Spectrophotometric Determination of Hydrogen Sulfide in Natural Waters1. *Limnology and Oceanography*, *14*(3), 454–458. https://doi.org/10.4319/lo.1969.14.3.0454

Cole, J. R., Wang, Q., Cardenas, E., Fish, J., Chai, B., Farris, R. J., Kulam-Syed-Mohideen, A. S., McGarrell, D. M., Marsh, T., Garrity, G. M., & Tiedje, J. M. (2009). The Ribosomal Database Project: improved alignments and new tools for rRNA analysis. *Nucleic Acids Research*, *37*(Database issue), D141–D145. https://doi.org/10.1093/nar/gkn879

Collins, L., & Watts, R. (2020). Equinor unveils plan for Europe's first blue hydrogen/CCS plant | Recharge [Section: transition]. Retrieved December 12, 2020, from https://www.rechargenews.com/transition/equinor-unveils-plan-for-europes-first-blue-hydrogen-ccs-plant/2-1-836408

core team, R. (2014). R: A language and environment for statistical computing. *Vienna, Austria*, R Foundation for Statistical Computing. Retrieved December 9, 2019, from http://www.r-project.org/

Courdouan, A., Christl, I., Meylan, S., Wersin, P., & Kretzschmar, R. (2007). Characterization of dissolved organic matter in anoxic rock extracts and in situ pore water of the Opalinus Clay. *Applied Geochemistry*, *22*(12), 2926–2939. https://doi.org/10.1016/j.apgeochem.2007.09.001

Curie, M. S. (1910). *Traite de radioactivite*. Paris, Gauthier. Retrieved April 10, 2017, from http://archive.org/details/traitderadioac01curi

Dadachova, E., Bryan, R. A., Huang, X., Moadel, T., Schweitzer, A. D., Aisen, P., Nosanchuk, J. D., & Casadevall, A. (2007). Ionizing Radiation Changes the Electronic Properties of Melanin and Enhances the Growth of Melanized Fungi. *PLOS ONE*, *2*(5), e457. https://doi.org/10.1371/journal.pone.0000457

Diomidis, N., Cloet, V., Leupin, O., Marschall, P., Poller, A., & Stein, M. (2016). Production, consumption and transport of gases in deep geological repositories according to the Swiss disposal concept - Technical Report 16-03. NAGRA.

Drobner, E., Huber, H., Wächtershäuser, G., Rose, D., & Stetter, K. O. (1990). Pyrite formation linked with hydrogen evolution under anaerobic conditions [Number: 6286 Publisher: Nature Publishing Group]. *Nature*, *346*(6286), 742–744. https://doi.org/10.1038/346742a0

Edgar, R. C. (2010). Search and clustering orders of magnitude faster than BLAST. *Bioinformatics*, *26*(19), 2460–2461. https://doi.org/10.1093/bioinformatics/btq461

Edgar, R. C. (2013). UPARSE: highly accurate OTU sequences from microbial amplicon reads. *Nature Methods*, *10*(10), 996–998. https://doi.org/10.1038/nmeth.2604

Edgar, R. C. (2016a). SINTAX: a simple non-Bayesian taxonomy classifier for 16S and ITS sequences. *bioRxiv*, 074161. https://doi.org/10.1101/074161

Edgar, R. C. (2016b). SINTAX: a simple non-Bayesian taxonomy classifier for 16S and ITS sequences. https://doi.org/10.1101/074161

Edgar, R. C. (2016c). UNOISE2: improved error-correction for Illumina 16S and ITS amplicon sequencing. *bioRxiv*, 081257. https://doi.org/10.1101/081257

Edge, J. S., Skipper, N. T., Fernandez-Alonso, F., Lovell, A., Srinivas, G., Bennington, S. M., Garcia Sakai, V., & Youngs, T. G. A. (2014). Structure and Dynamics of Molecular Hydrogen in the Interlayer Pores of a Swelling 2:1 Clay by Neutron Scattering [Publisher: American Chemical Society]. *The Journal of Physical Chemistry C*, *118*(44), 25740–25747. https://doi.org/10.1021/jp5082356

Energystock, G. (2020). The hydrogen project HyStock. Retrieved December 12, 2020, from https://www.energystock.com/about-energystock/the-hydrogen-project-hystock

Engel, K., Coyotzi, S., Slater, G., & Neufeld, J. D. (2018). Development of protocols for sampling and assessment of bentonite and environmental samples associated with in situ proof tests of engineered barrier systems - NWMO-TR-2018-04. NWMO - Nuclear Waste Managment Organisation.

Engel, K., Coyotzi, S., Vachon, M. A., McKelvie, J. R., & Neufeld, J. D. (2019). Validating DNA Extraction Protocols for Bentonite Clay. *mSphere*, *4*(5). https://doi.org/10.1128/mSphere.00334-19

Engel, K., Ford, S. E., Coyotzi, S., McKelvie, J., Diomidis, N., Slater, G., & Neufeld, J. D. (2019). Stability of Microbial Community Profiles Associated with Compacted Bentonite from the Grimsel Underground Research Laboratory [Publisher: American Society for Microbiology Journals Section: Research Article]. *mSphere*, *4*(6). https://doi.org/10.1128/mSphere.00601-19

Equinor. (2020). Carbon capture and storage in Equinor. Retrieved December 12, 2020, from https://www.equinor.com/en/what-we-do/carbon-capture-and-storage.html

Ewing, R. C., Whittleston, R. A., & Yardley, B. W. D. (2016). Geological Disposal of Nuclear Waste: a Primer. *Elements*, *12*(4), 233–237. https://doi.org/10.2113/gselements.12.4.233

Fox, P. M., Davis, J. A., Hay, M. B., Conrad, M. E., Campbell, K. M., Williams, K. H., & Long, P. E. (2012). Rate-limited U(VI) desorption during a small-scale tracer test in a heterogeneous uranium-contaminated aquifer. *Water Resources Research*, *48*(5). https://doi.org/https://doi.org/10.1029/2011WR011472

Fredrickson, J. K., & Balkwill, D. L. (2006). Geomicrobial Processes and Biodiversity in the Deep Terrestrial Subsurface. *Geomicrobiology Journal*, *23*(6), 345–356. https://doi.org/10.1080/01490450600875571

Frutschi, M., Rance, A., Reddy, B., Smart, N., Diomidis, N., & Bernier-Latmani, R. (2016). Microbiological Analysis of Samples from the IC-A Experiment (Iron corrosion in bentonite) at the Mont Terri Rock Laboratory - Final Report.

Gaucher, E. C., Fernández, A. M., & Waber, H. (2003). Annex 9: Rock and mineral characterization of the Opalinus Clay rock formation.

Gauthier-Lafaye, F. (1986). *Les gisements d'uranium du Gabon et les réacteurs d'Oklo. Modèle métallogénique de gîtes à fortes teneurs du Protérozoïque inférieur* (Vol. 78). Persée - Portail des revues scientifiques en SHS. Retrieved September 30, 2019, from https://www.persee.fr/doc/sgeol_0302-2684_1986_mon_78_1

Gauthier-Lafaye, F. (2002). 2 billion year old natural analogs for nuclear waste disposal: the natural nuclear fission reactors in Gabon (Africa). *Comptes Rendus Physique*, *3*(7), 839–849. https://doi.org/10.1016/S1631-0705(02)01351-8

Giroud, N., Tomonaga, Y., Wersin, P., Briggs, S., King, F., Vogt, T., & Diomidis, N. (2018). On the fate of oxygen in a spent fuel emplacement drift in Opalinus Clay. *Applied Geochemistry*, *97*, 270–278. https://doi.org/10.1016/j.apgeochem.2018.08.011

Glassing, A., Dowd, S. E., Galandiuk, S., Davis, B., & Chiodini, R. J. (2016). Inherent bacterial DNA contamination of extraction and sequencing reagents may affect interpretation of microbiota in low bacterial biomass samples. *Gut Pathogens*, *8*. https://doi.org/10.1186/s13099-016-0103-7

Gournis, D., Mantaka-Marketou, A. E., Karakassides, M. A., & Petridis, D. (2000). Effect of \gamma-irradiation on clays and organoclays: a Mössbauer and XRD study. *Physics and Chemistry of Minerals*, *27*(7), 514–521. https://doi.org/10.1007/s002690000089

Greaves, M. P., & Wilson, M. J. (1969). The adsorption of nucleic acids by montmorillonite. *Soil Biology and Biochemistry*, *1*(4), 317–323. https://doi.org/10.1016/0038-0717(69)90014-5

Gregory, S. P., Barnett, M. J., Field, L. P., & Milodowski, A. E. (2019). Subsurface Microbial Hydrogen Cycling: Natural Occurrence and Implications for Industry. *Microorganisms*, *7*(2). https://doi.org/10.3390/microorganisms7020053

Grekov, D. I., Suzuki-Muresan, T., Kalinichev, A. G., Pré, P., & Grambow, B. (2020). Thermodynamic data of adsorption reveal the entry of \ch{CH4} and \ch{CO2} in a smectite clay interlayer [Publisher: The Royal Society of Chemistry]. *Physical Chemistry Chemical Physics*, *22*(29), 16727–16733. https://doi.org/10.1039/D0CP02135K

Hamon, C. (2003). MPN - Most probable number method of counting viable bacteria - MIC.02 - AECL/EACL. AECL/EACL.

Hamon, C. (2006). Analysis of rock, soil and clay for microbes - MIC.05 - AECL/EACL. AECL/EACL.

Haynes, H. M. (, Pearce, C. I., Boothman, C., & Lloyd, J. R. (2018). Response of bentonite microbial communities to stresses relevant to geodisposal of radioactive waste. *Chemical Geology*, *501*. https://doi.org/10.1016/j.chemgeo.2018.10.004

Head, I. M., Jones, D. M., & Larter, S. R. (2003). Biological activity in the deep subsurface and the origin of heavy oil. *Nature*, *426*(6964), 344–352. https://doi.org/10.1038/nature02134

IAEA. (1995). The Principles of Radioactive Waste Management, In *Safety Fundamentals*. Vienna, International Atomic Energy Agency Vienna. www.nagra.ch/display.cfm/id/100227

IAEA. (2004). Environmental Contamination from Uranium Production Facilities and their Remediation [Publisher: International Atomic Energy Agency]. Retrieved December 12,

2020, from https://www.iaea.org/publications/7208/environmental-contamination-from-uranium-production-facilities-and-their-remediation

Inagaki, F., Hinrichs, K.-U., Kubo, Y., Bowles, M. W., Heuer, V. B., Hong, W.-L., Hoshino, T., Ijiri, A., Imachi, H., Ito, M., Kaneko, M., Lever, M. A., Lin, Y.-S., Methé, B. A., Morita, S., Morono, Y., Tanikawa, W., Bihan, M., Bowden, S. A., ... Yamada, Y. (2015). Exploring deep microbial life in coal-bearing sediment down to ~2.5 km below the ocean floor. *Science*, *349*(6246), 420–424. https://doi.org/10.1126/science.aaa6882

Jaeggi, D., Bossart, P., & Nussbaum, C. (2017). The Rock Mechanical Behavior of Opalinus Clay - 20 Years of Experience in the Mont Terri Rock Laboratory, In *Advances in Laboratory Testing and Modelling of Soils and Shales (ATMSS)*, Springer, Cham. https://doi.org/10.1007/978-3-319-52773-4_41

Jørgensen, B. B., & Boetius, A. (2007). Feast and famine — microbial life in the deep-sea bed [Number: 10 Publisher: Nature Publishing Group]. *Nature Reviews Microbiology*, *5*(10), 770–781. https://doi.org/10.1038/nrmicro1745

Jørgensen, B. B., & D'Hondt, S. (2006). A Starving Majority Deep Beneath the Seafloor. *Science*, *314*(5801), 932–934. https://doi.org/10.1126/science.1133796

Jørgensen, B. B., & Marshall, I. P. G. (2016). Slow Microbial Life in the Seabed. *Annual Review of Marine Science*, *8*, 5.1–5.22. https://doi.org/10.1146/annurev-marine-010814-015535

Karnland, O., & AB, C. T. (2010). Chemical and mineralogical characterization of the bentonite buffer for the acceptance control procedure in a KBS-3 repository SKB Technical Report 10-60. Swedish Nuclear Fuel; Waste Management Co.

Karnland, O., Olsson, S., & Nilsson, U. (2006). Mineralogy and sealing properties of various bentonites and smectite-rich clay materials. TR-06-30. SKB.

Kieft, T. L., Walters, C. C., Higgins, M. B., Mennito, A. S., Clewett, C. F. M., Heuer, V., Pullin, M. J., Hendrickson, S., van Heerden, E., Sherwood Lollar, B., Lau, M. C. Y., & Onstott, T. C. (2018). Dissolved organic matter compositions in 0.6 to 3.4km deep fracture waters, Kaapvaal Craton, South Africa. *Organic Geochemistry*, *118*, 116–131. https://doi.org/10.1016/j.orggeochem.2018.02.003

Leupin, O. X., Bernier-Latmani, R., Bagnoud, A., Moors, H., Leys, N., Wouters, K., & Stroes-Gascoyne, S. (2017). Fifteen years of microbiological investigation in Opalinus Clay at the Mont Terri rock laboratory (Switzerland). *Swiss Journal Of Geosciences*, *110*(1), 343–354. https://doi.org/10.1007/s00015-016-0255-y

Leupin, O., Zeyer, J., Cloet, V., Smith, P., Bernier-Latmani, R., Marschall, P., Papafotiou, A., Schwyn, B., & Stroes-Gascoyne, S. (2016). An assessment of the possible fate of gas generated in a repository for low- and intermediate-level waste - Technical Report 16-05. NAGRA.

Li, J., Qi, M., Lai, Q., Wang, G., & Shao, Z. (2020). Sunxiuqinia indica sp. nov., isolated from deep sea [Publisher: Microbiology Society,]. *International Journal of Systematic and Evolutionary Microbiology, 70*(7), 4186–4192. https://doi.org/10.1099/ijsem.0.004273

Lin, L.-H., Wang, P.-L., Rumble, D., Lippmann-Pipke, J., Boice, E., Pratt, L. M., Lollar, B. S., Brodie, E. L., Hazen, T. C., Andersen, G. L., DeSantis, T. Z., Moser, D. P., Kershaw, D., &

Onstott, T. C. (2006). Long-Term Sustainability of a High-Energy, Low-Diversity Crustal Biome. *Science*, *314*(5798), 479–482. https://doi.org/10.1126/science.1127376

Liu, Z., Müller, J., Li, T., Alvey, R. M., Vogl, K., Frigaard, N.-U., Rockwell, N. C., Boyd, E. S., Tomsho, L. P., Schuster, S. C., Henke, P., Rohde, M., Overmann, J., & Bryant, D. A. (2013). Genomic analysis reveals key aspects of prokaryotic symbiosis in the phototrophic consortium \textit{Chlorochromatium aggregatum}. *Genome Biology*, *14*(11), R127. https://doi.org/10.1186/gb-2013-14-11-r127

Lollar, G. S., Warr, O., Telling, J., Osburn, M. R., & Lollar, B. S. (2019). Follow the Water: Hydrogeochemical Constraints on Microbial Investigations 2.4 km Below Surface at the Kidd Creek Deep Fluid and Deep Life Observatory [Publisher: Taylor & Francis _eprint: https://doi.org/10.1080/01490451.2019.1641770]. *Geomicrobiology Journal*, *36*(10), 859–872. https://doi.org/10.1080/01490451.2019.1641770

Maanoja, S., Lakaniemi, A.-M., Lehtinen, L., Salminen, L., Auvinen, H., Kokko, M., Palmroth, M., Muuri, E., & Rintala, J. (2020). Compacted bentonite as a source of substrates for sulfate-reducing microorganisms in a simulated excavation-damaged zone of a spent nuclear fuel repository. *Applied Clay Science*, *196*, 105746. https://doi.org/10.1016/j.clay.2020.105746

Madigan, M. T., Bender, K. S., & Buckley, D. H. (2017). *BROCK BIOLOGY OF MICROORGANISM* (015 Edition). NY, NY, Pearson.

Magnabosco, C., Lin, L.-H., Dong, H., Bomberg, M., Ghiorse, W., Stan-Lotter, H., Pedersen, K., Kieft, T. L., van Heerden, E., & Onstott, T. C. (2018). The biomass and biodiversity of the continental subsurface [Number: 10 Publisher: Nature Publishing Group]. *Nature Geoscience*, *11*(10), 707–717. https://doi.org/10.1038/s41561-018-0221-6

Manca, D., Ferrari, A., & Laloui, L. (2015). Fabric evolution and the related swelling behaviour of a sand/bentonite mixture upon hydro-chemo-mechanical loadings. *Géotechnique*, *66*(1), 41–57. https://doi.org/10.1680/jgeot.15.P.073

Manca, D. (2015). Hydro-chemo-mechanical characterisation of sand/bentonite mixtures. https://doi.org/10.5075/epfl-thesis-6790,urn:nbn:ch:bel-epfl-thesis6790-4

Manca, D. (2016). Gas Transport and related Chemo-Hydro-Mechanical Response of Sand Bentonite Mixture - Technical Report 16-07. NAGRA.

Masson-Delmotte, V., Zhai, P., Pörtner, H.-O., Roberts, D., Skea, J., Shukla, P., Pirani, A., Moufouma-Okia, W., Péan, C., Pidcock, R., Connors, S., Matthews, J., Chen, Y., Zhou, X., Gomis, M., Lonnoy, E., Maycock, T., Tignor, M., & Waterfield, T. (2018). IPCC, 2018: Summary for Policymakers. In: Global Warming of 1.5°C. An IPCC Special Report on the impacts of global warming of 1.5°C above pre-industrial levels and related global greenhouse gas emission pathways, in the context of strengthening the global response to the threat of climate change, sustainable development, and efforts to eradicate poverty. IPCC. https://www.ipcc.ch/site/assets/uploads/sites/2/2019/05/SR15_SPM_version_report_LR.pdf

Mattimore, V., & Battista, J. R. (1996). Radioresistance of Deinococcus radiodurans: functions necessary to survive ionizing radiation are also necessary to survive prolonged desic-

cation. *Journal of Bacteriology*, *178*(3), 633–637. https://doi.org/10.1128/jb.178.3.633-637.1996

Mazurek, M., Hurford, A. J., & Leu, W. (2006). Unravelling the multi-stage burial history of the Swiss Molasse Basin: integration of apatite fission track, vitrinite reflectance and biomarker isomerisation analysis. *Basin Research*, *18*(1), 27–50. https://doi.org/10.1111/j.1365-2117.2006.00286.x

McMahon, S., & Parnell, J. (2014). Weighing the deep continental biosphere. *FEMS Microbiology Ecology*, *87*(1), 113–120. https://doi.org/10.1111/1574-6941.12196

McMahon, S., Parnell, J., & Blamey, N. J. (2016). Evidence for Seismogenic Hydrogen Gas, a Potential Microbial Energy Source on Earth and Mars. *Astrobiology*, *16*(9), 690–702. https://doi.org/10.1089/ast.2015.1405

McNamara, N. P., Black, H. I. J., Beresford, N. A., & Parekh, N. R. (2003). Effects of acute gamma irradiation on chemical, physical and biological properties of soils. *Applied Soil Ecology*, *24*(2), 117–132. https://doi.org/10.1016/S0929-1393(03)00073-8

Melton, E. D., Sorokin, D. Y., Overmars, L., Lapidus, A. L., Pillay, M., Ivanova, N., del Rio, T. G., Kyrpides, N. C., Woyke, T., & Muyzer, G. (2017). Draft genome sequence of Dethiobacter alkaliphilus strain AHT1T, a gram-positive sulfidogenic polyextremophile. *Standards in Genomic Sciences*, *12*(1), 57. https://doi.org/10.1186/s40793-017-0268-9

Merriam-Webster, D. (2020). Definition of SUBSURFACE. Retrieved December 12, 2020, from https://www.merriam-webster.com/dictionary/subsurface

Moran, U., Phillips, R., & Milo, R. (2010). SnapShot: key numbers in biology. *Cell*, *141*(7), 1262–1262.e1. https://doi.org/10.1016/j.cell.2010.06.019

Müller, H. R., Garitte, B., Vogt, T., Köhler, S., Sakaki, T., Weber, H., Spillmann, T., Hertrich, M., Becker, J. K., Giroud, N., Cloet, V., Diomidis, N., & Vietor, T. (2017). Implementation of the full-scale emplacement (FE) experiment at the Mont Terri rock laboratory. *Swiss Journal of Geosciences*, *110*(1), 287–306. https://doi.org/10.1007/s00015-016-0251-2

Nagra. (2002). Project Opalinus Clay - Safety Report - Demonstration of disposal feasibility for spent fuel, vitrified high-level waste and long-livedintermediate-level waste (Entsorgungsnachweis) - Technical Report 02-05. NAGRA.

Nagra. (2009). The Nagra Research, Development and Demonstration (RD&D) Plan for the Disposal of Radioactive Waste in Switzerland - Technischer Bericht 09-06. NAGRA.

Nagra. (2014a). Erlaeuterungen zur Verpackung radioaktiver Abfaelle im Endlagerbehaelter. - Technischer Arbeitsbericht NAB 14-104. NAGRA.

Nagra. (2014b). Modellhaftes Inventar fuer radioaktive Materialien MIRAM 2014 - Technischer Bericht 14-04. NAGRA.

Nagra. (2016). ENSI-Nachforderungen zum Indikator "tiefenlage im Hinblick auf bautechnische Machbarkeit"in SGT Etappe 2 - Zusammenfassende Darstellung der Zusatzdokumentation (Hauptbericht) NAB 16-41. NAGRA.

Nagra. (2020a). L\ILW Repository - Nagra. Retrieved December 14, 2020, from https://www.nagra.ch/en/repositoriesforlilw.htm#

Nagra. (2020b). Wo entsorgen. Retrieved December 14, 2020, from https://www.nagra.ch/de/woentsorgen.htm

Nielsen, M. B., Kjeldsen, K. U., & Ingvorsen, K. (2006). Desulfitibacter alkalitolerans gen. nov., sp. nov., an anaerobic, alkalitolerant, sulfite-reducing bacterium isolated from a district heating plant. *International Journal of Systematic and Evolutionary Microbiology*, *56*(Pt 12), 2831–2836. https://doi.org/10.1099/ijs.0.64356-0

Nixon, D. J., Reddy, B., Rance, A. P., & Smart, N. R. (2015). Preparation of Specimens for Mont Terri Corrosion Experiments. Amec Foster Wheeler Report D.000021/001.

Nixon, S. L., Cousins, C. R., & Cockell, C. S. (2013). Plausible microbial metabolisms on MarsMicrobial metabolisms on Mars. *Astronomy & Geophysics*, *54*(1), 1.13–1.16. https://doi.org/10.1093/astrogeo/ats034

Nutrition, C. f. F. S. a. A. (2019). BAM Appendix 2: Most Probable Number from Serial Dilutions. *FDA*. Retrieved October 16, 2019, from http://www.fda.gov/food/laboratory-methods-food/bam-appendix-2-most-probable-number-serial-dilutions

of America, S. S. S. (2020). Glossary of Soil Science Terms. Retrieved December 7, 2020, from https://www.soils.org/publications/soils-glossary/#

of Microorganisms and Cell Cultures, D. .-. G. C. (2018). Medium 63 - Postgate's Medium. https://www.dsmz.de/microorganisms/medium/pdf/DSMZ_Medium63.pdf

Parada, A. E., Needham, D. M., & Fuhrman, J. A. (2016). Every base matters: assessing small subunit rRNA primers for marine microbiomes with mock communities, time series and global field samples. *Environmental Microbiology*, *18*(5), 1403–1414. https://doi.org/10.1111/1462-2920.13023

Parkes, R. J., Cragg, B., Roussel, E., Webster, G., Weightman, A., & Sass, H. (2014). A review of prokaryotic populations and processes in sub-seafloor sediments, including biosphere:geosphere interactions. *Marine Geology*, *352*, 409–425. https://doi.org/10.1016/j.margeo.2014.02.009

Pearson, F. J., Arcos, D., Bath, A., Boisson, J.-Y., Fernández, A. M., Gaebler, H.-E., Gaucher, E., Gautschi, A., Griffault, L., Hernan, P., & Waber, H. N. (2003). *Mont Terri Project - Geochemistry of Water in the Opalinus Clay Formation at the Mont Terri Rock Laboratory* (Vol. 5). Bern.

Pedersen, K., Motamedi, M., Karnland, O., & Sandén, T. (2000). Mixing and sulphate-reducing activity of bacteria in swelling, compacted bentonite clay under high-level radioactive waste repository conditions. *Journal of Applied Microbiology*, *89*(6), 1038–1047. https://doi.org/10.1046/j.1365-2672.2000.01212.x

Pedersen, K., Bengtsson, A., Blom, A., Johansson, L., & Taborowski, T. (2017). Mobility and reactivity of sulphide in bentonite clays – Implications for engineered bentonite barriers in geological repositories for radioactive wastes. *Applied Clay Science*, *146*, 495–502. https://doi.org/10.1016/j.clay.2017.07.003

Pedersen, K., Hallbeck, L., Arlinger, J., Erlandson, A.-C., & Jahromi, N. (1997). Investigation of the potential for microbial contamination of deep granitic aquifers during drilling using 16S rRNA gene sequencing and culturing methods. *Journal of Microbiological Methods*, *30*(3), 179–192. https://doi.org/10.1016/S0167-7012(97)00066-3

Quast, C., Pruesse, E., Yilmaz, P., Gerken, J., Schweer, T., Yarza, P., Peplies, J., & Glöckner, F. O. (2013). The SILVA ribosomal RNA gene database project: improved data processing

and web-based tools. *Nucleic Acids Research*, *41*(Database issue), D590–D596. https://doi.org/10.1093/nar/gks1219

Rättö, M., & Itävaara, M. (2012). *Microbial activity in bentonite buffers: Literature study*. VTT Technical Research Centre of Finland. Retrieved September 30, 2019, from https://cris.vtt.fi/en/publications/microbial-activity-in-bentonite-buffers-literature-study

Ravel, B., & Newville, M. (2005). ATHENA, ARTEMIS, HEPHAESTUS: data analysis for X-ray absorption spectroscopy using IFEFFIT [Number: 4 Publisher: International Union of Crystallography]. *Journal of Synchrotron Radiation*, *12*(4), 537–541. https://doi.org/10.1107/S0909049505012719

Reasoner, D., & Geldreich, E. (1985). A new medium for the enumeration and subculture of bacteria from potable water. *Applied and Environmental Microbiology*, *49*(1), 1–7.

Reddy, B., & Burzan, N. (2018). Preparation of Modules for Mont Terri Microbial Corrosion Experiments (ICA-4), Wood PLC Ref 208233/001.

Rickard, D. (1997). Kinetics of pyrite formation by the H2S oxidation of iron (II) monosulfide in aqueous solutions between 25 and 125°C: The rate equation. *Geochimica et Cosmochimica Acta*, *61*(1), 115–134. https://doi.org/10.1016/S0016-7037(96)00321-3

Rouquerol, J., Avnir, D., Fairbridge, C. W., Everett, D. H., Haynes, J. M., Pernicone, N., Ramsay, J. D. F., Sing, K. S. W., & Unger, K. K. (1994). Recommendations for the characterization of porous solids (Technical Report) [Publisher: De Gruyter Section: Pure and Applied Chemistry]. *Pure and Applied Chemistry*, *66*(8), 1739–1758. https://doi.org/10.1351/pac199466081739

Ruijter, J. M., Ramakers, C., Hoogaars, W. M. H., Karlen, Y., Bakker, O., van den Hoff, M. J. B., & Moorman, A. F. M. (2009). Amplification efficiency: linking baseline and bias in the analysis of quantitative PCR data. *Nucleic Acids Research*, *37*(6), e45. https://doi.org/10.1093/nar/gkp045

Salter, S. J., Cox, M. J., Turek, E. M., Calus, S. T., Cookson, W. O., Moffatt, M. F., Turner, P., Parkhill, J., Loman, N. J., & Walker, A. W. (2014). Reagent and laboratory contamination can critically impact sequence-based microbiome analyses. *BMC Biology*, *12*. https://doi.org/10.1186/s12915-014-0087-z

Sánchez-Castro, I., Ruiz-Fresneda, M. A., Bakkali, M., Kämpfer, P., Glaeser, S. P., Busse, H. J., López-Fernández, M., Martínez-Rodríguez, P., & Merroun, M. L. (2017). Stenotrophomonas bentonitica sp. nov., isolated from bentonite formations. *International Journal of Systematic and Evolutionary Microbiology*, *67*(8), 2779–2786. https://doi.org/10.1099/ijsem.0.002016

Schindelin, J., Arganda-Carreras, I., Frise, E., Kaynig, V., Longair, M., Pietzsch, T., Preibisch, S., Rueden, C., Saalfeld, S., Schmid, B., Tinevez, J.-Y., White, D. J., Hartenstein, V., Eliceiri, K., Tomancak, P., & Cardona, A. (2012). Fiji: an open-source platform for biological-image analysis [Number: 7 Publisher: Nature Publishing Group]. *Nature Methods*, *9*(7), 676–682. https://doi.org/10.1038/nmeth.2019

SFOE. (2020). Geothermal energy. Retrieved December 12, 2020, from https://www.bfe.admin.ch/bfe/en/home/versorgung/erneuerbare-energien/geothermie.html

Slon, V., Hopfe, C., Weiss, C. L., Mafessoni, F., Rasilla, M. d. l., Lalueza-Fox, C., Rosas, A., Soressi, M., Knul, M. V., Miller, R., Stewart, J. R., Derevianko, A. P., Jacobs, Z., Li, B., Roberts, R. G., Shunkov, M. V., Lumley, H. d., Perrenoud, C., Gusic, I., … Meyer, M. (2017). Neandertal and Denisovan DNA from Pleistocene sediments. *Science*, eaam9695. https://doi.org/10.1126/science.aam9695

Smart, N. R., Reddy, B., Rance, A. P., Nixon, D. J., Frutschi, M., Bernier-Latmani, R., & Diomidis, N. (2017). The anaerobic corrosion of carbon steel in compacted bentonite exposed to natural Opalinus Clay porewater containing native microbial populations. *Corrosion Engineering, Science and Technology*, *52*(sup1), 101–112. https://doi.org/10.1080/1478422X.2017.1315233

Stamenković, V., Lynch, K., Boston, P. J., Tarnas, J., & Rivera-Valentín, E. G. (2020). *Deep Trek: Science of Subsurface Habitability & Life on Mars : A Window into Subsurface Life in the Solar System* (Working Paper) [Accepted: 2020-08-11T20:46:09Z Journal Abbreviation: Deep Trek: Science of Subsurface Habitability and Life on Mars]. Accepted: 2020-08-11T20:46:09Z Journal Abbreviation: Deep Trek: Science of Subsurface Habitability and Life on Mars. Retrieved December 16, 2020, from https://repository.hou.usra.edu/handle/20.500.11753/1678

Stevens, T. O., & McKinley, J. P. (1995). Lithoautotrophic Microbial Ecosystems in Deep Basalt Aquifers. *Science*, *270*(5235), 450–455. https://doi.org/10.1126/science.270.5235.450

Stookey, L. L. (1970). Ferrozine—a new spectrophotometric reagent for iron. *Analytical Chemistry*, *42*(7), 779–781. https://doi.org/10.1021/ac60289a016

Stroes-Gascoyne, S., Frutschi, M., & Hamon, C. (2013). Microbiological analysis of samples from the engineered barrier experiment at Mont Terri Rock Laboratory TN2013-56. Mont Terri Technical Note.

Stroes-Gascoyne, S., Hamon, C. J., Maak, P., & Russell, S. (2010). The effects of the physical properties of highly compacted smectitic clay (bentonite) on the culturability of indigenous microorganisms. *Applied Clay Science*, *47*(1), 155–162. https://doi.org/10.1016/j.clay.2008.06.010

Takai, K., Abe, M., Miyazaki, M., Koide, O., Nunoura, T., Imachi, H., Inagaki, F., & Kobayashi, T. (2013). Sunxiuqinia faeciviva sp. nov., a facultatively anaerobic organoheterotroph of the Bacteroidetes isolated from deep subseafloor sediment [Publisher: Microbiology Society,]. *International Journal of Systematic and Evolutionary Microbiology*, *63*(Pt_5), 1602–1609. https://doi.org/10.1099/ijs.0.044065-0

Twing, K. I., Brazelton, W. J., Kubo, M. D. Y., Hyer, A. J., Cardace, D., Hoehler, T. M., McCollom, T. M., & Schrenk, M. O. (2017). Serpentinization-Influenced Groundwater Harbors Extremely Low Diversity Microbial Communities Adapted to High pH. *Frontiers in Microbiology*, *8*. https://doi.org/10.3389/fmicb.2017.00308

Vinsot, A., Appelo, C. a. J., Lundy, M., Wechner, S., Lettry, Y., Lerouge, C., Fernandez, A. M., Labat, M., Tournassat, C., Canniere, P. D., Schwyn, B., Mckelvie, J., Dewonck, S., Bossart, P., & Delay, J. (2014). In situ diffusion test of hydrogen gas in the Opalinus Clay. *Geological Society, London, Special Publications*, *400*, SP400.12. https://doi.org/10.1144/SP400.12

Wanner, C., Eggenberger, U., Kurz, D., Zink, S., & Mäder, U. (2012). A chromate-contaminated site in southern Switzerland – Part 1: Site characterization and the use of Cr isotopes to delineate fate and transport. *Applied Geochemistry*, *27*(3), 644–654. https://doi.org/10.1016/j.apgeochem.2011.11.009

Webb, S. M. (2011). The MicroAnalysis Toolkit: X-ray Fluorescence Image Processing Software [Publisher: American Institute of Physics]. *AIP Conference Proceedings*, *1365*(1), 196–199. https://doi.org/10.1063/1.3625338

Wells, J. (1976). A guide to the prognosis for survival in mammals following the acute effects of inhaled radioactive particles. *Journal of the Institution of Nuclear Engineers*, *17*(5), 126–131. Retrieved April 12, 2017, from https://inis.iaea.org/search/searchsinglerecord.aspx?recordsFor=SingleRecord&RN=8293340

Whitman, W. B., Coleman, D. C., & Wiebe, W. J. (1998). Prokaryotes: The unseen majority. *Proceedings of the National Academy of Sciences*, *95*(12), 6578–6583. Retrieved April 11, 2017, from http://www.pnas.org/content/95/12/6578

Wickham, H. (2009). *Ggplot2: Elegant Graphics for Data Analysis*. New York, Springer-Verlag. https://doi.org/10.1007/978-0-387-98141-3

WolframAlpha. (2020a). 16.45 m^3 - Wolfram|Alpha. Retrieved December 15, 2020, from https://www.wolframalpha.com

WolframAlpha. (2020b). 2.6*10^7 m^3 - Wolfram|Alpha. Retrieved December 14, 2020, from https://www.wolframalpha.com

Zalasiewicz, J. (2016). *Rocks - A Very Short Introduction*. Oxford, UK, Oxford University Press. Retrieved April 3, 2017, from http://www.veryshortintroductions.com/view/10.1093/actrade/9780198725190.001.0001/actrade-9780198725190

Zgonnik, V. (2020). The occurrence and geoscience of natural hydrogen: A comprehensive review. *Earth-Science Reviews*, *203*, 103140. https://doi.org/10.1016/j.earscirev.2020.103140

Niels Burzan, Rue des Terreaux 21, 1003 Lausanne, 079 961 66 11, nielsburzan@yandex.com
https://ch.linkedin.com/in/nielsburzan

Curriculum Vitae

- Highly interdisciplinary background in microbiology, material sciences and nanotechnologies
- 17 years working experience in scientific, private and social sector

Citizenship	German
Residence permit CH	B
Date of birth	13th June 1987
Civil status	Single
Languages	German (mother tongue) English (C2) French (A2) Dutch (A1)
IT skills	MS Office, profound knowledge in Excel Strong experience in Unix/GNU, Data analysis & statistics in R, Bioinformatics (USEARCH) Basics in Bash-scripting, Fortran, LabView

Leading experience

03/2008 – 09/2010	Deputy Platoon Leader, German Federal Agency of Technical and Disaster Relief (THW), Rostock

Extra-curricular activities

2016-2019	Social event manager, Doctoral School of EPFL faculty of Architecture, Civil and Environmental Engineering
2012-2014	Financial auditor of the Society of Nanoscience students at the University of Basel
09/2013 – 12/2013	Selected participant for Start-Up-Idea Workshop "Venture Challenge", responsible for sales planning

Education

06/2016 – ongoing	**Doctoral Candidate** in *Environmental Engineering*, Prof. Rizlan Bernier-Latmani group, École Polytechnique Fédérale de Lausanne
09/2013 – 01/2016	**Master of Science** in *Nanoscience* Masterthesis in Computational Chemistry University of Basel
09/2010 - 08/2013	**Bachelor of Science** in *Nanoscience* University of Basel
08/2007 – 07/2010	**General qualification for university entrance** Evening College Rostock (DE)
09/2003 – 02/2007	**Biological technical assistant**, professional training at Leibniz-Institute for Farm Animal Biology, Dummerstorf (DE)

Niels Burzan, Rue des Terreaux 21, 1003 Lausanne, 079 961 66 11,
nielsburzan@yandex.com
https://ch.linkedin.com/in/nielsburzan

Project & Employment history

02/2016 – 05/2016 & 10/2014 – 11/2014
Graduate Researcher (100%)
Dübendorf, Switzerland
EMPA, Swiss Federal Laboratories for Material Science and Technology

01/2014 – 02/2014
Graduate Researcher (100%)
Munich, Germany
TUM, Technische Universität München Klinkum rechts der Isar

07/2014 – 08/2014
Graduate Researcher (100%)
Utrecht, The Netherlands
Hubrecht Institut for Developmental Biology and Stem Cell Biology

02/2007-06/2010
Biological technical assistant (100%)
Dummerstorf, Germany
FBN, Leibniz-Institute for Farm Animal Biology

Student jobs

08/2011 – 03/2015	Technical assistant (10%) at Volkshochschule beider Basel
01/2015 – 10/2015	Child daycare for 4-8 children (10%)
03/2015	VIP Service & Chauffeur, European Product Launch Event Zurich "Cadillac Escalade 2015", Nyou AG, Nidau
01/2018	VIP Service & Chauffeur, "World of Web 2018" Conference in Zurich, Nyou AG, Nidau

Further skills

1993 – 2003	Music university-study enabling Conservatory-degree in piano, Conservatory "Rudolf Wagner-Regeny", Rostock